Low-dimension functional nanomaterials for the detection of pressure and strain

Chang-Bo Huang

UNIVERSITÉ DE STRASBOURG

ÉCOLE DOCTORALE DES SCIENCES CHIMIQUES

UMR 7006 Institut de Science et d'Ingénierie Supramoléculaires

THÈSE

présentée par :

Chang-Bo HUANG

soutenue le : **20 MAIS 2020**

pour obtenir le grade de : **Docteur de l'université de Strasbourg**

Discipline/ Spécialité : Chimie-Chimie

Nanomatériaux fonctionnels à faible dimensionnalité pour la détection de pression et de tension

THÈSE dirigée par :

M. SAMORÌ Paolo	Professeur, Université de Strasbourg, Strasbourg, France
M. CIESIELSKI Artur	Ingénieur de recherche-HDR, Université de Strasbourg, Strasbourg, France

RAPPORTEURS :

M. BELJONNE David	Professeur, Center for Innovation and Research on Materials and Polymers (CIRMAP), Mons, Belgium
MMe. MAS-TORRENT Marta	Directeur de recherches, Institut de Ciència de Materials de Barcelona (ICMAB-CSIC), Barcelona, Spain

---

AUTRES MEMBRES DU JURY :

M. H. GEERTS Yves	Professeur, Laboratoire de Chimie des Polymères, Faculté des Sciences, Université libre de Bruxelles (ULB), Bruxelles, Belgique
M. BIANCO Alberto	Professeur, Institut de Biologie Moléculaire et Cellulaire, CNRS, UPR3572, Strasbourg, France

Résumé de thèse

L'Internet des objets (*IoT*), sans aucun doute considéré parmi les technologies les plus importantes et les plus prometteuses aujourd'hui, a été estimé comme étant un énorme marché pour les prochaines décennies. Cela comprend des milliards d'appareils connectés tels que les smartphones, les PC, les appareils portables, les tablettes et autres appareils synergiques.[1-4] Que ce soit pour l'utilisation d'infrastructures urbaines, d'usines, de soins personnels ou dans d'autres scénarios d'application, les capteurs (sous forme de matrice) sont connectés directement ou indirectement aux réseaux *IoT* servant d'interface frontale pour collecter les données de l'environnement telles que la température, l'humidité, la pression, le mouvement, l'accélération, la présence de gaz, des image, *etc.*[2, 4] Par conséquent, la conception de capteurs possédant des propriétés intéressantes est d'une importance capitale pour le développement de l'*IoT*.

Les capteurs ont été traditionnellement définis comme des appareils capables de convertir des variables physiques en signaux électriques ou de modifier les propriétés électriques de matériaux actifs. Pour répondre aux exigences des technologies modernes telles que l'*IoT*, diverses propriétés doivent être présentes, telles que l'habilité à traiter des informations complexes, le faible coût de production, la transmission sans fil, la flexibilité, la faible puissance de fonctionnement, la robustesse, l'auto-étalonnage, *etc.*[5]

Cette thèse se concentre sur la conception et la fabrication de capteurs de pression et de déformation en utilisant des nanomatériaux fonctionnels préprogrammés, appliqués à la surveillance via des appareils portatif analysant la santé. Ainsi, du graphène et des nanoparticules d'or (AuNPs) ont été utilisés comme nanomatériaux fonctionnels pour fabriquer des capteurs de pression et des capteurs de contraintes mécaniques, respectivement. La puissance électrique (résistance électrique en général) a été collectée lors de pression/déformation. En raison de la compressibilité/extensibilité limitée du matériau lui-même, un ressort moléculaire a été introduit dans les matériaux actifs pour la détection, via une fonctionnalisation chimique pour améliorer la sensibilité de ces capteurs de pression/déformation.

L'utilisation de ressorts moléculaires intégrés dans les matériaux de détection est une nouveauté fondamentale dans ce travail, il est donc nécessaire d'introduire cette approche sous la forme d'un chapitre indépendant (chapitre 2). Les ressorts (supra)moléculaires sont des objets nanométriques artificiels possédant des structures bien définies et des propriétés physico-chimiques modulables. Comme les ressorts macroscopiques, les ressorts supramoléculaires sont capables de changer leur conformation à l'échelle nanométrique en réponse à des stimuli externes (lumière, ions, chaleur, pH, solvant, redox, *etc.*), induisant alors des mouvements mécaniques de type ressort.[6-9] Une telle action dynamique offre des opportunités intéressantes pour l'ingénierie des nanomachines moléculaires, en traduisant les mouvements nanoscopiques sensibles aux stimuli en un travail macroscopique. [10-11] Ces objets nanoscopiques sont des architectures multifonctionnelles dynamiques réversibles qui peuvent exprimer une variété de nouvelles propriétés et se comporter comme des systèmes nanoscopiques adaptatifs. Dans ce chapitre, la conception et la relation structure/fonction des ressorts supramoléculaires ont été discutées. De plus, leur (auto)assemblage en tant que prérequis pour la génération de nouveaux matériaux dynamiques comportant des mouvements contrôlés, facilement intégrables dans des dispositifs macroscopiques pour des applications en détection, en robotique et *IoT*, a également été démontré.

Dans le chapitre 3, une introduction sur les capteurs de pression et de contrainte a été discutée, comprenant les aspects fondamentaux (tels que la définition, les mécanismes de détection, les paramètres clés, *etc.*) et les matériaux actifs pour la détection (par exemple les nanoparticules d'or, les nanotubes de carbone, le graphène, *etc.*). Le capteur de pression et le capteur de contrainte ont été des sujets de recherche extrêmement attrayants ces dernières années du fait de leurs vastes applications dans des domaines tels que la surveillance de la santé humaine via un appareil portatif, la peau électronique (e-skin), l'interface homme-machine, la robotique, l'automatisation, *etc.*[1, 5, 12-15] Ce chapitre offre au lecteur le contexte de recherche de cette thèse et décrit la conception de la recherche développée dans ce travail de thèse, ainsi que l'importance du développement d'un capteur de pression/déformation basé sur ces nouveaux matériaux hybrides.

Dans le chapitre 4, nous avons discuté des méthodes et techniques expérimentales utilisées dans la réalisation de ce travail de thèse, telles que la synthèse de matériaux actifs, les méthodes de fabrication de dispositifs, ainsi que diverses techniques de caractérisation. Une méthode de synthèse efficace (par exemple via un processus simple, avec un rendement élevé, un faible coût des matières premières, *etc.*) et propre (faible toxicité, respectueuse de l'environnement, traitement facile des déchets, *etc.*) des matières actives est la condition préalable à la production de masse pour des applications futures. Dans ce chapitre, nous avons discuté de la synthèse efficace des matériaux de détection et de la fabrication du dispositif plus élaboré, afin de le rendre plus adapté à la fabrication à grande échelle. De plus, une introduction complète de diverses méthodes de caractérisation comprenant les mesures électriques, la configuration du dynamomètre, les caractérisations spectroscopiques (la spectroscopie Raman, la spectroscopie photonique aux rayons X, la diffraction des rayons X sur poudre) et les caractérisations de surface (la microscopie à force atomique et la microscope électronique à balayage) a été fourni pour acquérir une connaissance précise et intrinsèque de la structure et de la composition chimique des matériaux et des dispositifs.

Les capteurs de pression représentent une catégorie d'appareils qui peuvent donner des informations de pression via un signal électrique. Sur la base des mécanismes de fonctionnement, ils peuvent être divisés en capteur de pression piézorésistif, capteur de pression piézoélectrique, capteur de pression capacitif, *etc.* Le capteur de pression piézorésistif, dont la résistance change avec la pression, a été largement rapporté dans la littérature, en raison de sa haute sensibilité, de sa réponse rapide, et de sa facilité de fabrication. Dans le chapitre 5, nous avons discuté d'un type radicalement nouveau de capteur de pression piézorésistif basé sur une architecture de type millefeuille, composé de couches d'oxyde de graphène réduit (rGO) intercalé par des piliers moléculaires attachés de manière covalente (R1: aminotriéthylène glycol (TEG), R2: 1-octylamine et R3: 4-aminobiphényle) possédant des propriétés mécaniques modulables. En appliquant une petite pression sur la structure multicouche, le courant tunnel régissant le transport de charge entre les feuillets de rGO successifs entraîne une diminution colossale de la résistance électrique du matériau. De manière significative, la rigidité intrinsèque des piliers moléculaires utilisés permet un réglage fin de la sensibilité du capteur, atteignant des sensibilités aussi élevées que 0,82 kPa^{-1} dans une région de basse pression (0-0,6 kPa), avec des temps de réponse courts (≈ 24 ms) et une limite de détection faible (7 Pa). Nos capteurs de pression permettent une surveillance efficace du rythme cardiaque et peuvent être facilement transposés à une matrice capable de fournir une carte 3D de la pression exercée par différents objets.

Le capteur de déformation basé sur le réseau AuNPs-TEG a été discuté dans le chapitre 6. En nous inspirant des capteurs de pression modulant le courant d'effet tunnel décrit dans le chapitre 5, nous avons conçu un nouveau modèle de détecteur qui utilise des nanoparticules d'or d'une dizaine de nanomètres comme unités de transmission d'électrons, qui est donc le matériau actif du capteur de déformation. Les nanoparticules d'or sont interconnectées par des molécules de dithioltétra(éthylène glycol) formant des réseaux 3D déposés directement sur des électrodes interdigitées flexibles (substrat en polyimide). Sans contrainte appliquée, les AuNP sont séparées par les ligands organiques isolés qui définissent un transfert de charge efficace entre les nanoparticules d'or dans une certaine gamme de distance. Lors de l'application d'une

contrainte, le matériau actif est soit comprimé (sous contrainte de compression) soit étiré (sous contrainte de traction), remodelant ainsi les ligands organiques en raison de leur nature flexible. La distance interparticulaire, qui peut être considérée comme la barrière de potentiel de l'onde électronique, sera respectivement diminuée/augmentée sous la contrainte de compression/traction, augmentant/diminuant ainsi le courant tunnel de façon exponentielle. D'après ces résultats, le capteur de déformation a démontré un facteur de jauge élevéet une réponse très fine à la contrainte de traction, à la contrainte de compression, au mouvement mixte et même aux vibrations. D'intenses efforts ont été consacrés à la conception de la structure de l'appareil pour réaliser une détection du signal sans fil. Au cours des dernières années, les antennes d'identification par radiofréquence (RFID) ont fait l'objet de nombreuses recherches dans le domaine de l'Internet des objets et des systèmes cyber-physiques (CPS) en raison de leurs propriétés intéressantes telles que la passivité de l'objet, fonctionnant sans fil, simple et compacte, et de nature multimodale.[12, 16] Dans ce projet, la méthode de transmission de données sans fil, c'est-à-dire une puce passive RFID, a été utilisée pour construire un système de détection de contrainte sans fil avec des réseaux AuNPs-TEG comme matériau de détection actif. Le système est composé de deux circuits, qui sont respectivement le circuit à puce et le circuit de mesure. Grâce à l'inductance mutuelle, ces circuits peuvent établir une communication et échanger des informations. Le circuit de mesure est un circuit d'initiative avec une entrée d'alimentation alternative, alors que le circuit à puce est un circuit passif qui répond par inductance mutuelle. Le capteur de contrainte a été intégré dans le circuit à puce en tant que résistance, dans laquelle la résistance changera avec la contrainte, affectant ainsi le courant dans le circuit de mesure. La fabrication et la mesure du capteur de déformation ont été réalisées, alors que la détection sans fil est toujours en cours de test.

Le capteur de pression hybride de type résistif à base de graphène est décrit au chapitre 7. Un nouveau type de capteur de pression dont la sensibilité peut être réglée avec la lumière UV a également été conçu dans ce projet. Le principe consiste à greffer un polymère photosensible sur des feuillets de graphène, dont la rigidité augmentera avec la lumière UV due à la polymérisation de celui-ci. Le courant tunnel passant à travers les feuillets de graphène est

directement régi par la distance entre les couches de graphène. Cette dernière est ainsi contrôlée par la pression appliquée au dispositif. En irradiant le dispositif à l'aide d'une lumière UV avec une puissance ou pendant un temps différent, le composite présentera une compressibilité différente. De ce fait, la sensibilité du dispositif sera modulée via cette méthode. Dans ce travail, la résine photosensible négative SU-8 2002 a été choisie pour former un matériau composite avec du graphène. La résine photosensible négative est largement utilisée en photolithographie et sa rigidité augmente en raison de la polymérisation déclenchée par les UV. Le SU-8 2002 est un photorésiste à base d'époxy à contraste élevé, conçu pour le micro-usinage et pour d'autres applications en microélectroniques. Les parties du film exposées et réticulées thermiquement sont rendues insolubles aux révélateurs liquides. Lors de l'exposition, la réticulation se déroule en deux étapes : (1) un acide fort est formé pendant l'étape d'exposition, puis (2) la réticulation des époxy est catalysée par l'acide et accélérée thermiquement pendant l'étape de recuit finale (PEB). Dans ce projet, le composite tel qu'il a été préparé a été mélangé avec SU-8 2002 et irradié avec de la lumière UV pour former un polymère entre les feuillets de graphène. La synthèse du matériau actif et la fabrication de dispositifs ont été réalisées, mettant en évidence une potentiel application comme capteur de pression.

En conclusion, l'objectif de cette thèse a été la conception chimique et la fabrication de capteurs de pression/déformation avec des matériaux actifs pour une détection fine afin de surveiller la santé humaine. L'ingénierie de la compressibilité du matériau actif à travers des molécules modulables (telles un ressort moléculaire ou un polymère photorésistant) est la principale nouveauté de cette thèse. L'hybride graphène-molécule a d'abord été utilisé comme matériau actif de détection de pression dans lequel la sensibilité peut être réglée en modifiant la rigidité des ressorts moléculaires. Une stratégie de conception similaire a été appliquée au capteur de déformation basé sur le réseau AuNPs-TEG, dans lequel le signal de détection peut être transmis via un système RFID sans fil. Dans le dernier projet, la résine photosensible a été utilisée pour fabriquer un capteur de pression hybride à base de graphène possédant une sensibilité réglable par irradiation UV. Dans l'ensemble, cette nouvelle conception de matériau de détection de pression/déformation a fourni une méthode efficace pour fabriquer des capteurs

de pression/déformation très sensibles. Les caractéristiques supplémentaires de l'appareil telles que la faible consommation énergétique (tension de fonctionnement de 0,2 V), le processus de fabrication à grande échelle, les matières premières disponibles commercialement, le faible coût de production et, plus important encore, la détection sans fil, en font un candidat attrayant pour les applications technologiques portatives contrôlant la santé, pour des dispositif de surveillance, dans la robotique de détection multi-mouvement et pour l'*IoT*.

Abstract

The Internet of Things (*IoT*), undoubtedly considered among the most important and promising technologies today, has been estimated an enormous market within the next decades including billions of connected devices such as smartphones, PCs, wearables, tablets and other synergetic devices.[1-4] Whether for the use of urban infrastructures, factories, personal cares or other application scenarios, sensors (array) are connected directly or indirectly to *IoT* networks serving as front end to collect data from the surrounding environment including temperature, humidity, pressure, motion, acceleration, gas, image *etc.*[2, 4] Therefore, the design of sensors possessing intriguing properties is of great importance for the development of *IoT*.

Sensors have been traditionally defined as devices which can convert physical variables to electrical signals or changes in electrical properties. To meet the requirement of modern technology such as *IoT*, various properties should be rendered such as intelligence, low cost, wireless transmission, flexibility, low operation power, robustness, self-calibration, *etc.* [5]

This thesis is focused on the design and fabrication of pressure and strain sensors by making use of programed functional nanomaterials applied for health monitoring wearables. To this end, graphene and gold nanoparticles (AuNPs) have been employed as functional nanomaterials to fabricate pressure sensors and strain sensors, respectively. The electrical output (resistance

in general) has been collected under implied pressure/strain. Due to the limited compressibility/stretchability of the material itself, molecular spring has been introduced into the active sensing materials through chemical functionalization to improve the sensitivity of the pressure/strain sensor.

The utilization of molecular spring integrated in sensing materials is a core novelty in this work, thus it is worth giving a comprehensive introduction to this approach in the form of an independent chapter (Chapter 2). (Supra-)molecular springs are artificial nanoscale objects possessing well-defined structures and tunable physico-chemical properties. Like a macroscopic spring, supramolecular springs are capable of switching their nanoscale conformation as a response to external stimuli (light, ions, heat, pH, solvent, redox, *etc.*) by undergoing mechanical spring-like motions.[6-9] Such dynamic action offers intriguing opportunities for engineering molecular nanomachines by translating the stimuli-responsive nanoscopic motions into macroscopic work.[10-11] These nanoscopic objects are reversible dynamic multifunctional architectures which can express a variety of novel properties and behave as adaptive nanoscopic systems. In this chapter, the design and structure vs. function relationship of supramolecular springs has been discussed. Moreover, their (self-)assembly as a prerequisite towards the generation of novel dynamic materials featuring controlled movements to be readily integrated into macroscopic devices for applications in sensing, robotics and *IoT* has also been demonstrated.

In Chapter 3, an introduction of pressure sensor and strain sensor has been discussed respectively, including the fundamental aspects (*e.g.* definition, sensing mechanisms, key parameters, *etc.*) and active sensing materials (*e.g.* gold nanoparticles, carbon nanotubes, graphene, *etc.*). Both pressure sensor and strain sensor are extremely appealing research topics in recent years due to their wide applications such as wearable human health monitoring, e-skin, human-machine interface, robotics, automation, *etc.*[1, 5, 12-15] This chapter offers to the reader to fully understand the research background of this thesis and outlines the research

design and significance of the development of pressure/strain sensor based on novel hybrid materials.

In Chapter 4, we have discussed the experimental methods and techniques including the synthesis of active materials, device fabrication methods, as well as various characterization techniques used in this thesis. An efficient (*e.g.* simple process flow, high yield, low cost of starting materials, *etc.*) and clean (*e.g.* low toxicity, environmentally friendly, easy waste treatment, *etc.*) synthesis method of active materials is the precondition for mass production in the upcoming real application. In this chapter, we have discussed the efficient synthesis of sensing materials and the evolved device fabrication flow to make it more suitable for the large-scale fabrication. Meanwhile, a comprehensive introduction of various characterization methods including electrical measurements, force gauge setup, spectroscopic characterizations (*i.e.* Raman Spectroscopy, X-ray Photon Spectroscopy, X-ray powder diffraction), and surface characterizations (*i.e.* Atomic Force Microscopy and Scanning Electron Microscope) has been provided to acquire an accurate and intrinsic cognition of the structure and chemical composition of the materials and devices.

Pressure sensor represents devices that can transfer pressure information to electrical readout. Based on the working mechanisms, it can be divided into piezoresistive pressure sensor, piezoelectric pressure sensor, and capacitive pressure sensor *etc.* Piezoresistive pressure sensor, the resistance of which changes with pressure, has been widely reported due to its high sensitivity, fast response, ease of fabrication. In Chapter 5, we will discuss a radically new type of piezoresistive pressure sensor based on a millefeuille-like architecture of reduced graphene oxide (rGO) intercalated by covalently tethered molecular pillars (*i.e.* R1: triethylene glycol (TEG) amine, R2: 1-octylamine and R3: 4-aminobiphenyl) holding on-demand mechanical properties. By applying a tiny pressure to the multilayer structure, the electron tunnelling ruling the charge transport between successive rGO sheets yields a colossal decrease in the material's electrical resistance. Significantly, the intrinsic rigidity of the molecular pillars employed enables the fine-tuning of the sensor's sensitivity, reaching sensitivities as high as 0.82 kPa-1

at low pressure region (0-0.6 kPa), with short response times (≈24 ms) and detection limit (7 Pa). Our pressure sensors enable the efficient heartbeat monitoring and can be easily transformed into a matrix capable of providing a 3D map of the pressure exerted by different objects.

Strain sensor based on AuNPs-TEG network has been discussed in Chapter 6. Inspired by the tunneling current ruling pressure sensors described in Chapter 5, we have designed a novel model which utilized gold nanoparticles featuring a size of dozens of nanometers as electron transmission units within active material of the strain sensor. Gold nanoparticles are interconnected by tetra (ethylene glycol) (TEG) dithiol to form 3D networks deposited directly on the flexible interdigitated electrode (polyimide substrate). Without applied strain, AuNPs are separated by insulated organic ligands which can effectively define the charge transfer among gold nanoparticles at a certain range. Upon applied strain, the active material is either compressed (under compressive strain) or stretched (under tensile strain) thus reshaping the organic ligands due to its flexible nature. The interparticle distance, which can be seen as the barrier of electron wave, will be decreased/increased under compressive/tensile strain respectively, thus increasing/decreasing the tunneling current exponentially. According to the result, the strain sensor has demonstrated high gauge factor and highly sensitive response to tensile strain, compressive strain, the mixed motion and even vibration. Intensive effort has been paid to the exploration of the structure design of device to achieve wireless sensing. In recent few years, Radio Frequency IDentification (RFID) tag antennas have been widely researched in the field of internet of things and cyber-physical systems (CPS) due to their superior properties such as passive, wireless, simple, compact size, and multimodal nature.[12, 16] In this project, the wireless data transmission method, *i.e.* RFID passive chip, has been employed to construct a wireless strain sensing system with AuNPs-TEG networks being active sensing material. The system is consisting of two circuits, which are the chip circuit and the measure circuit respectively. Through mutual inductance they can achieve the information communication between the two circuits. The measure circuit is an initiative circuit with an alternative power supply input, while the chip circuit is a passive circuit which responds by the

mutual inductance. Strain sensor has been integrated in the chip circuit as a resistor, in which the resistance will change with strain thus affecting the current in the measure circuit through mutual inductance. The fabrication and measurement of strain sensor have been accomplished while the wireless sensing is under testing.

Graphene-resist hybrid pressure sensor is described in Chapter 7. A new type of pressure sensor of which the sensitivity can be tuned with UV light has been designed in this project. The design principle is by grafting photosensitive polymer to graphene flakes, the rigidity of which will increase with UV light due to polymerization. The tunneling current passing through graphene flakes is directly ruled by the inter-layer distance, which is controlled by pressure. By irradiating UV light with different power/time, the composite will exhibit different compressibility thus the sensitivity will be tuned with this method. In this work, negative photoresist SU-8 2002 was chosen to form composite material with graphene. Negative photoresist is widely used in photo lithography, and its rigidity will increase due to the polymerization triggered by UV. SU-8 2002 is a high contrast, epoxy-based photoresist designed for micromachining and other microelectronic applications. The exposed and subsequently thermally cross-linked portions of the film are rendered insoluble to liquid developers. Upon exposure, cross-linking proceeds in two steps (1) formation of a strong acid during the exposure step, followed by (2) acid-catalyzed, thermally driven epoxy cross-linking during the post exposure bake (PEB) step. In this project, the as-prepared composite has been blended with SU-8 2002 and irradiated with UV light to form polymer between graphene flakes. The synthesis of active material and the fabrication of devices have been accomplished, highlighting a potential for application of pressure sensor.

In conclusions, the aim of this Thesis is the chemical design and fabrication of pressure/strain sensor with delicately designed active sensing materials for human health monitoring applications. Engineering of compressibility of active material through tunable molecules (*e.g.* molecular spring, photoresist polymer) is the main novelty in this thesis. Graphene-molecule hybrid has been firstly employed as active pressure sensing material in which the sensitivity

can be tuned by changing the rigidity of molecular springs. Similar design strategy has been applied on the AuNPs-TEG network-based strain sensor, in which the sensing signal can be transmitted through RFID system in a wireless manner. In the last project, photoresist has been utilized to fabricate hybrid graphene material-based pressure sensor possessing tunable sensitivity by UV irradiation. Overall, this novel design of pressure/strain sensing material has provided an effective method to fabricate highly sensitive pressure/strain sensors. The additional device features such as low power consumption (0.2 V operating voltage), large-scale fabrication process, commercially available raw material, low cost, and more importantly, the wireless sensing, make it an appealing candidate for the technological applications in wearable health monitoring device, multimotion detection robotic and *IoT*.

References

[1] T. Q. Trung, N. E. Lee, *Adv. Mater.* **2016**, *28*, 4338.

[2] E. Borgia, *Comput. Commun.* **2014**, *54*, 1

[3] Y. Khan, A. E. Ostfeld, C. M. Lochner, A. Pierre, A. C. Arias, *Adv. Mater.* **2016**, *28*, 4373.

[4] B. L. R. Stojkoska, K. V. Trivodaliev, *J. Clean. Prod.* **2017**, *140*, 1454.

[5] A. M. Almassri, W. Z. W. Hasan, S. A. Ahmad, A. J. Ishak, A. M. Ghazali, D. N. Talib, C. Wada, *J. Sens.* **2015**, *2015*, 846487.

[6] E. Yashima, N. Ousaka, D. Taura, K. Shimomura, T. Ikai, K. Maeda, *Chem. Rev.* **2016**, *116*, 13752.

[7] H. J. Kim, Y. B. Lim, M. Lee, *J. Polym. Sci., Part A: Polym. Chem.* **2008**, *46*, 1925.

[8] B. L. Feringa, *Nat. Chem.* **2010**, *2*, 429.

[9] M. J. Marsella, S. Rahbarnia, N. Wilmot, *Org. Biomol. Chem.* **2007**, *5*, 391.

[10] S. Iamsaard, S. J. Asshoff, B. Matt, T. Kudernac, J. J. L. M. Cornelissen, S. P. Fletcher, N. Katsonis, *Nat. Chem.* **2014**, *6*, 229.

[11] V. Percec, J. G. Rudick, M. Peterca, P. A. Heiney, *J. Am. Chem. Soc.* **2008**, *130*, 7503.

[12] S. Sikarwar, S. S. Singh, B. C. Yadav, *Photonic Sens.* **2017**, *7*, 294.

[13] S. Stassi, V. Cauda, G. Canavese, C. F. Pirri, *Sensors.* **2014**, *14*, 5296.

[14] T. T. Yang, D. Xie, Z. H. Li, H. W. Zhu, *Mat. Sci. Eng. R* **2017**, *115*, 1.

[15] Y. Zang, F. Zhang, C.-A. Di, D. Zhu, *Mater. Horiz.* **2015**, *2*, 140.

[16] J. Zhang, G. Y. Tian, A. M. J. Marindra, A. I. Sunny, A. B. Zhao, *Sensors.* **2017**, *17*, 265.

Table of contents

Résumé de thèse I

Abstract VIII

Table of contents XV

Symbols and abbreviations XIX

1. Introduction
   1.1. Context····1
   1.2. Structure of the thesis····3
   1.3. References ····5
2. Supramolecular springs
   2.1. Introduction····7
   2.2. Supramolecular spring in solution and in single crystals····10
      2.2.1. Coordination driven helicates as supramolecular springs····10
      2.2.2. Thermally driven supramolecular springs····14
      2.2.3. pH-triggered supramolecular springs····15
      2.2.4. Solvent driven supramolecular springs····16
      2.2.5. Redox-responsive supramolecular springs····18
   2.3. Self-assembled springs based dynamic materials····19
      2.3.1. Light-responsive dynamic materials····19
      2.3.2. Thermal fueled dynamic materials····21
   2.4. Spring-like macroscopic devices····23
      2.4.1. Spring-like materials based on 0D nanomaterials····23
      2.4.2. 1D-based spring-like materials····24
   2.5. Conclusion and perspectives····26
   2.6. References····27
3. Concepts of pressure sensors and strain sensors
   3.1. Introduction····33
   3.2. Pressure sensors····34
      3.2.1. Fundamental aspects of pressure sensor····34
         3.2.1.1. Definition and key parameters
         3.2.1.2. Sensing mechanisms
      3.2.2. Active sensing materials····41

3.2.2.1. 0D materials
3.2.2.2. 1D materials
3.2.2.3. 2D materials
3.2.2.4. 3D materials
3.3. Strain sensors····49
3.3.1.Fundamental aspects of strain sensor····49
3.3.1.1. Definition and key parameters
3.3.1.2. Sensing mechanisms
3.3.2.Active sensing materials····54
3.3.2.1. 0D materials
3.3.2.2. 1D materials
3.3.2.3. 2D materials
3.3.2.4. 3D materials
3.4. Applications and Development····60
3.5. References····63
4. Experimental techniques
4.1. General information····70
4.2. Synthesis of active materials····71
4.2.1.Functionalization of graphene····71
4.2.2.Synthesis and functionalization of gold nanoparticles (AuNPs) ····72
4.3. Characterization techniques····73
4.3.1.Electrical measurement····73
4.3.2.Force gauge setup····80
4.3.3.Spectroscopic characterization····81
4.3.3.1. RAMAN spectroscopy
4.3.3.2. XPS
4.3.3.3. UV-Vis spectroscopy
4.3.3.4. DLS
4.3.4.Surface characterization····89
4.3.4.1. AFM
4.3.4.2. SEM
4.4. References····94
5. Graphene-molecules hybrid materials based pressure sensor for human health monitoring
5.1. Introduction····98
5.2. Results and discussion····99

5.3. Experimental methods·····107
5.3.1.Material·····107
5.3.1.1. Synthesis of Triethylene glycol amine
5.3.1.2. Synthesis of functionalized graphene rGO-R_{1-3}
5.3.2.Device fabrication·····109
5.3.2.1. Pressure sensor fabrication process
5.3.2.2. Pressure sensor matrix fabrication process
5.3.3.Characterization·····110
5.3.3.1. XPS spectra of GO, GO-R_{1-3}, rGO-R_{1-3}
5.3.3.2. XRD spectra GO, rGO, GO-R_{1-3}, rGO-R_{1-3}
5.3.3.3. RAMAN spectra of GO, rGO, GO-R_{1-3}, rGO-R_{1-3}
5.3.3.4. IR spectra of GO, rGO, rGO-R_{1-3}
5.3.3.5. BET analysis of rGO, rGO-R_{1-3}
5.3.3.6. LSCM analysis of rGO-R_1
5.3.3.7. Transmittance spectra of PET film after spray coating of rGO-R_{1-3}
5.3.3.8. SEM images of rGO and rGO-R_{1-3}
5.3.3.9. Temperature dependent electrical conductivity measurement
5.3.3.10. Fatigue test of pressure sensor rGO-R_1
5.4. Conclusion·····128
5.5. References·····129
6. AuNPs-TEG network based strain sensor
6.1. Introduction·····134
6.2. Results and discussion·····137
6.2.1.Analysis of gold nanoparticles·····137
6.2.2.Fabrication of AuNPs-TEG network·····142
6.2.3.Temperature dependent electrical conductivity measurement·····145
6.2.4.Electrical sensing properties of strain sensor·····146
6.2.4.1. Dynamic response measurement
6.2.4.2. Statistic response measurement
6.3. Experimental methods·····150
6.3.1.Material·····150
6.3.2.Device fabrication·····153
6.3.2.1. Electrode fabrication
6.3.2.2. AuNPs-TEG network fabrication
6.3.2.3. Electrical connection
6.3.3.Characterization·····157

6.3.3.1. Temperature dependent electrical conductivity measurement
6.3.3.2. Electrical characterization
6.4. Conclusion····159
6.5. References····160
7. Graphene-photoresist hybrid based pressure sensor with tunable sensitivity by UV
7.1. Introduction····164
7.2. Results and discussions····165
7.3. Experimental methods····171
7.3.1.Materials····171
7.3.2.Device fabrication····173
7.3.3.Characterization····174
7.3.3.1. SEM
7.3.3.2. AFM
7.3.3.3. XPS
7.3.3.4. RAMAN
7.4. Conclusion····181
7.5. References····182
8. Conclusions and perspectives
8.1. Conclusions····184
8.2. Perspectives····187
8.2.1.Short-term perspectives····187
8.2.2.Long-term perspectives····188
8.3. References····190
Closing remarks····191
List of publications····192
List of presentations····193
Acknowledgements····194

Symbols and Abbreviations

AFM	atomic force microscopy
AI	artificial intelligence
AI_r	augmentation index
APTES	(3-Aminopropyl) triethoxysilane
AuNPs	gold nanoparticles
BET	Brunauer–Emmett–Teller
BST	backscattered electron detector
CCD	charge coupled device
CD	circular dichroism
CMGO	chemically modified graphene oxide
CNTs	carbon nanotubes
CVD	chemical vapor deposition
DCM	dichloromethane
DLS	dynamic light scattering
ε	strain
EDA	ethylene diamine
EtOH	ethanol
GBL	gamma-butyrolactone
GF	gauge factor
GO	graphene oxide
IDEs	interdigitated electrodes
IoT	internet of things
IPA	isopropanol
IR	infrared spectroscopy
ITO	indium tin oxide
λ	wavelength
LSCM	laser scanning confocal microscopy
MEMS	microelectromechanical systems
OFET	organic field-effect transistor
PCB	printed circuit board
PDMS	polydimethylsiloxane
PE	polyethylene

PEB	post exposure bake
PEG	polyethylene glycol
PET	polyethylene terephthalate
PGMEA	propylene glycol methyl ether acetate
PI	polyimide
PPP	poly-(p-phenylene)
PSSNa	poly(4-styrenesulfonic acid) sodium salt
PU	polyurethane
PVD	physical vapour deposition
PVDF	polyvinylidene difluoride
PVP	poly (4-vinyl phenol)
ρ	electrical resistivity
RFID	radio frequency identification
rGO	reduced graphene oxide
SD	standard deviation
SED	secondary electron detector
SEM	scanning electron microscope
SH-TEG-SH	tetra (ethylene glycol) dithiol
Si	silicon
SiO_2	silicon dioxide
SPR	surface plasmon resonance
STEM	scanning transmission electron microscope
TEG	triethylene glycol
THF	tetrahydrofuran
TPE	thermoplastic elastomer
υ	Poisson's ratio
UV	ultraviolet
Vis	visible light
VR	virtual reality
WAXS	wide-angle X-ray scattering
Wi-Fi	wireless fidelity
XPS	X-ray photoelectron spectroscopy
XRD	X-ray powder diffraction

Chapter 1

Introduction

1.1. Context

Since few years we are witnessing a major progress in smart wearables solutions with the development of the advanced technologies such as AI (Artificial Intelligence) and VR (Virtual Reality) being integrated into wearable devices including smart watches, smart bands, smart glasses, smart rings, smart clothes, *etc.* These smart electronic devices are used to collect information on subject and/or environment and can give corresponding feedback based on the data analyzed either by the devices themselves or by the center network through wireless data transmission techniques such as Wi-Fi (Wireless Fidelity), Bluetooth, RFID (Radio Frequency IDentification), *etc.* Smart watch (commercialized by Apple, Huawei, *etc.*) for example consists of multiple built-in sensors including accelerometer, magnetometer, barometric pressure sensor, ambient temperature sensor, heart rate monitor, oximetry sensor, *etc.*[1, 2] These sensors can refactor a virtual environment based on the collected ambient parameters and monitor the health conditions of the subject. After the overall analysis of the subject, the smart watch can provide personalized instructions such as reminding a break during sedentary work, alert of bedtime, making a suggestion of medical examinations, *etc.* to promote a healthier lifestyle.

Electronic sensing devices are among the key components of the smart wearable electronics, in which pressure and strain sensors are one of the most popular research directions in recent

years for their wide applications in motion detection, health monitoring, robotics, human-machine interaction, electronic skin, *etc.*[3-6] In addition to basic pressure/strain sensing properties such as high sensitivity, fast response, good robustness, *etc.*, unique characteristics including mechanical durability, stretchability, and biodegradability have been imparted to novel sensing devices to improve the device-human body integration through the development of new materials and fabrication strategies.[7-10]

A very important space-interval engineering concept, supramolecular springs, has been introduced (Chapter 2) before the general overview of pressure and strain sensors (Chapter 3). This concept has been employed in the design principle of pressure and strain sensors (Chapter 5, 6, and 7) discussed in this thesis. Supramolecular springs are artificial nanoscale objects possessing well-defined structures and tunable physico-chemical properties. Like a macroscopic spring, supramolecular springs are capable of switching their nanoscale conformation as a response to external stimuli such as light, humidity, pH, pressure, *etc.* by undergoing mechanical spring-like motions. In this thesis, oligomer-based molecular springs have been used to fabricate pressure and strain sensors in which the dynamic motion of molecular springs triggered by external pressure or strain can be monitored by the tunneling current change under bias voltage.

Overall, this Thesis is dedicated to the design and fabrication of flexible pressure and strain sensors featuring superior sensing properties by using low-dimensional hybrid nanomaterials as active components, such as graphene and gold nanoparticles based networks. These novel sensing devices holding superior sensing properties offer unique opportunities for the emerging classes of smart wearable electronics.

1.2. Structure of the thesis

This thesis is given in 8 chapters as follows:

Chapter 1: Brief introduction of the Thesis has been discussed including the inspiration of the projects, the design principle of pressure/strain sensor, and the outline of the Thesis.

Chapter 2: The core concept utilized in the Thesis, supramolecular spring, has been thoroughly discussed including the concept, structure *vs.* property relationship, and novel dynamic materials featuring controlled movements for applications in sensing, robotics, *etc.*

Chapter 3: An introduction of pressure and strain sensors has been discussed including the fundamental aspects (*e.g.* definition, sensing mechanisms, key parameters, *etc.*) and active sensing low-dimensional materials. Research background information and significance of this thesis has also been discussed, which is helpful for readers to gain a better understanding of this Thesis.

Chapter 4: Experimental techniques of synthesis process of active materials involved in this thesis (*i.e.* graphene and gold nanoparticles) have been discussed. In addition, working principles of different characterization methods including SEM, AFM, Raman, and XPS *etc.* have been discussed in order to have an accurate and comprehensive understanding of the novel functional materials.

Chapter 5: Graphene-molecules hybrid materials based pressure sensors have been devised and fabricated. The working principle, synthesis and characterization of functionalized graphene materials, fabrication of pressure sensing device, electrical test of pressure sensing performance, and the demonstration of health monitoring applications have been discussed thoroughly.

Chapter 6: A novel strain sensor based on gold nanoparticle network has been devised. Gold nanoparticles are interconnected by tetra (ethylene glycol) dithiol (TEG) to form 3D networks and have been employed as strain sensing materials. Synthesis and characterization of active materials and fabrication of strain sensing device have been discussed thoroughly. The strain sensor has demonstrated high gauge factor and highly sensitive response to tensile strain, compressive strain, the mixed motion and even vibration. Extensive effort has been paid to the exploration of the structure design of device to achieve wireless sensing for broader applications, and the optimization of data transmission is underway.

Chapter 7: In this chapter, a new type of pressure sensor of which the sensitivity can be tuned with UV light irradiation has been devised by using a negative photoresist (SU-8 2002) to form composite material with graphene. Graphene composite materials have been synthesized and fully characterized by XPS, RAMAN, SEM, *etc.* Electrical tests of the pressure sensing performance have been preliminarily carried out.

Chapter 8: Draws the conclusions of this thesis project and put this in the context of short-term and long-term perspectives.

1.3. References

1. Alam, R.; Anderson, M.; Bankole, A.; Lach, J. In *Inferring physical agitation in dementia using smartwatch and sequential behavior models*, 2018 IEEE EMBS International Conference on Biomedical & Health Informatics (BHI), 4-7 March 2018; 2018; pp 170-173.
2. Weiss, G. M.; Yoneda, K.; Hayajneh, T., Smartphone and Smartwatch-Based Biometrics Using Activities of Daily Living. *IEEE Access* **2019,** *7*, 133190-133202.
3. Yamada, T.; Hayamizu, Y.; Yamamoto, Y.; Yomogida, Y.; Izadi-Najafabadi, A.; Futaba, D. N.; Hata, K., A stretchable carbon nanotube strain sensor for human-motion detection. *Nat. Nanotechnol.* **2011,** *6*, 296-301.
4. Amjadi, M.; Kyung, K. U.; Park, I.; Sitti, M., Stretchable, Skin-Mountable, and Wearable Strain Sensors and Their Potential Applications: A Review. *Adv. Funct. Mater.* **2016,** *26*, 1678-1698.
5. Stoppa, M.; Chiolerio, A., Wearable Electronics and Smart Textiles: A Critical Review. *Sensors* **2014,** *14*, 11957-11992.
6. Meng, Y. N.; Zhao, Y.; Hu, C. G.; Cheng, H. H.; Hu, Y.; Zhang, Z. P.; Shi, G. Q.; Qu, L. T., All-Graphene Core-Sheath Microfibers for All-Solid-State, Stretchable Fibriform Supercapacitors and Wearable Electronic Textiles. *Adv. Mater.* **2013,** *25*, 2326-2331.
7. Chortos, A.; Liu, J.; Bao, Z., Pursuing prosthetic electronic skin. *Nat. Mater.* **2016,** *15*, 937-950.
8. Chen, D.; Pei, Q., Electronic Muscles and Skins: A Review of Soft Sensors and Actuators. *Chem. Rev.* **2017,** *117*, 11239-11268.
9. Yang, T.; Xie, D.; Li, Z.; Zhu, H., Recent advances in wearable tactile sensors: Materials, sensing mechanisms, and device performance. *Mater. Sci. Eng. R Rep.* **2017,** *115*, 1-37.
10. Hammock, M. L.; Chortos, A.; Tee, B. C. K.; Tok, J. B. H.; Bao, Z. N., 25th Anniversary Article: The Evolution of Electronic Skin (E-Skin): A Brief History, Design Considerations, and Recent Progress. *Adv. Mater.* **2013,** *25*, 5997-6037.

Chapter 2

Supramolecular springs

(Supra) molecular springs are artificial nanoscale objects possessing well-defined structures and tunable physico-chemical properties. Like a macroscopic spring, supramolecular springs are capable of switching their nanoscale conformation as a response to external stimuli by undergoing mechanical spring-like motions. Such dynamic action offers intriguing opportunities for engineering molecular nanomachines by translating the stimuli-responsive nanoscopic motions into macroscopic work. These nanoscopic objects are reversible dynamic multifunctional architectures which can express a variety of novel properties and behave as adaptive nanoscopic systems. In this chapter, we focus on the design and structure *vs.* property relationship of supramolecular springs and their (self-) assembly as a prerequisite towards the generation of novel dynamic materials featuring controlled movements to be readily integrated into macroscopic devices for applications in sensing, robotics and IoT (*Internet of Things*).

2.1. Introduction

During the last three decades, a great effort has been devoted to the design and synthesis of more and more complex supramolecular architectures[1-3] relying on the use of non-covalent interactions to assemble individual chemical entities with a sub-nanometer precision as elements for the generation of systems and materials with unprecedented and often unique chemical and physical properties.[4, 5] Supramolecular chemistry, which combines reversibility, directionality, specificity and cooperativity, offers highest control over the process of molecular assembly.[6, 7] Among the various architectures which have been realized, there has been recently an increasing interest on the fabrication of functional supramolecular structures with a nanoscale control over their mechanical properties, targeting at the development of supramolecular machines such as shuttles,[8-10] rotors,[11-14] switches,[15-17] ratchets,[18-20] springs[21, 22] *etc.*, to mimic biological activities via the implementation of controllable molecular-level motions. While the development of supramolecular shuttles, rotors *etc.* have been the subject of comprehensive review articles,[23-27] only a few works discuss the progress in the field of (supra) molecular springs.[27-30] In the macroscopic Hooke's helical springs, the spring constant, which indicates the resistance to elongation, is ruled by several parameters such as material shear modulus, the spring diameter, the number of coils, and the thickness of the coiled wire. At the nanoscale, helically coiled and folded molecular conformations are well-known and have attracted significant attention. However, the potential likeness between the supramolecular springs and Hooke's springs is still largely unexplored, except for DNA. In this chapter we highlight the advances in design, synthesis and structure *vs.* property relationship of supramolecular springs (Section 2.2). (Self-) assembled springs based dynamic materials, in which the motion was controlled by stimuli like light and heat have been discussed in Section 2.3. We also extended the scope of supramolecular spring concept to spring-like macroscopic devices which are highly relevant for practical applications such as actuators, pressure sensing, humidity sensing *etc.* (Section 2.4).

Supramolecular springs widely exist in biological systems to serve as engines for motility.[21] Conformational energy is stored (contracted conformation) in such active mechanochemical systems and released (extended conformation) with certain non-covalent bonds broken to trigger mechanical movement or other functions such as infection and mitosis. In biological systems, supramolecular springs are generally constructed with proteins (*e.g.* actin bundle in a Limulus sperm,[31, 32] *etc.*) and DNAs.[33-35] The research on a spring-like protein complex NOMPC,[36-39] changing its conformation under pressure to control the ion channel for electromechanical signal transferring, has attracted significant attention due to the potential

mechanism interpretation of mechanoreceptor, which is related to the detection of touch, hearing or even the blood pressure.

In chemistry, (supra)molecular springs have been widely reported in the form of (single or double) helicates,[22, 29, 40] π-expanded helicenes,[41] rotaxanes,[42] catenanes,[43] clathrates,[44] peptides,[45] helices,[46, 47] helical (coordination) polymers,[48, 49] and other molecules assemblies,[50-52] which can reversibly extend or/and contract their conformations upon external stimuli accompanied with energy storage and release process.[22, 27, 53] First of all, it is worth pointing out that the contraction/extension motion of a (supra)molecular spring can be fueled either by means of a mechanical input, *i.e.* a force applied, or of a physical/chemical stimulus such as light irradiation, heat, change of pH, ion complexation, solvation, *etc.* Under applied force, supramolecular springs are extended or contracted, and the conformational equilibrium is lost to reach a high energy state. Once the applied force is released, the springs automatically recover to the initial equilibrium state.[27] Depending on the chemical system and stimuli employed to trigger its spring-like motion from helical to non-helical conformation, the equilibrium state could either be the helical or the non-helical state. It should be noted that supramolecular springs differ from the largely existing "spring-like" molecules,[54] which exhibit the spring-like structure, but do not undergo directional contraction-extension movements. Moreover, molecules or assemblies thereof,[55] whose conformations can be extended and/or contracted as a response to external stimuli should not be considered as supramolecular springs. Therefore, several supramolecular foldamers,[56] supramolecular polymerized helical structures,[57] and coordination helical structures,[58] which can be controllably assembled/disassembled into helical conformations by changing the solvent or other conditions are not within the discussion scope of supramolecular springs. Finally, based on the definition of spring structure, supramolecular springs should also be distinguished from (supra) molecular muscle[55, 59, 60] or actuators,[61, 62] even though both of them feature contraction-extension motion under stimuli.

The subtle design of molecular structure makes it possible to control the structural transformations of supramolecular springs in terms of relative position, motion speed, frequency, *etc.*, as a result of different inputs such as ion coordination,[22, 40, 53, 63, 64] light irradiation,[51, 65] pH,[40, 50] heat,[48, 66, 67] and solvent.[44, 45] Even though the mechanistic details and kinetics of conformational changes have been comprehensively studied by means of NMR, UV-Vis, CD, STM and even X-ray crystallography, most of the research have been conducted in the solution and at the single crystal level thus limiting to a large extent the application in real macroscopic devices.[23, 26] To fill this gap, in this chapter, in addition to the discussion of the chemistry of supramolecular springs we will reveal the challenging, yet valuable

connection between molecular scale supramolecular springs and macroscopic functional entities according to a few enlightening reports.

2.2. Supramolecular spring in solution and in single crystals

In analogy with natural proteins which (typically) possess folded structure, the design and synthesis of molecules that can adopt helical conformations or assemble into helical architectures has attracted considerable attention. These artificial molecules can form supramolecular spring-like helical structures which are held together through different intra- or inter-molecular non-covalent interactions such as metal-ligand coordination, hydrogen bonding, solvophobic effects, *etc.* The responsive nature of non-covalent interactions to external stimuli has provided tools to tune the extension-contraction mechanism of the helical structure in a well-controlled manner, yielding a modification of the properties of supramolecular springs. In this section, the chemistry of supramolecular springs has been discussed based on the different inputs exploited to activate the spring's mechanochemical motion at the molecular level, in order to shed light onto their working principle.

2.2.1. Coordination driven helicates as supramolecular springs

In 1987 the term helicate was introduced by Lehn and co-workers to describe the discrete oligo-nuclear supramolecular complexes, in which at least two metal ions are wrapped by two or more oligo-dentate ligands along the helical axis.[68] Since then, helicates have been intensively studied and became the most important supramolecular springs due to the versatile ligand design with different self-assembly strategies.[69-71]

In 2000, Jung and co-workers reported the first example of supramolecular spring[72] whose helical pitch could be reversibly modulated by incorporating guest anions with a different size. As portrayed in Figure 2-1, the Py_2O (3, 3'-oxybispyridine) ligands (curve stripe in Figure 2-1a) are linearly coordinated with the silver (I) ion (black and white squares in Figure 2-1b) to form self-assembled cylindrical helices with counteranions pinched in the helical pitch of the single strand column. Each turn consists of two Py_2O units and two silver ions to form the infinite helical structure. Interestingly, the skeletal structures constructed by different counteranions exhibit similar helical motif only differing in their pitch, which is proportional to the volume of the counteranion guest (NO_3^-, 36.0 cm^3/mol; BF_4^-, 51.0 cm^3/mol; ClO_4^-, 52.1 cm^3/mol; and PF_6^-, 56.2 cm^3/mol). Upon using counteranions having a different size, the spring pitch can be reversibly tuned from 7.430 to 9.621 Å (as revealed by X-ray crystallographic characterization), meaning that the supramolecular spring can feature anion dependent contraction-extension movement.

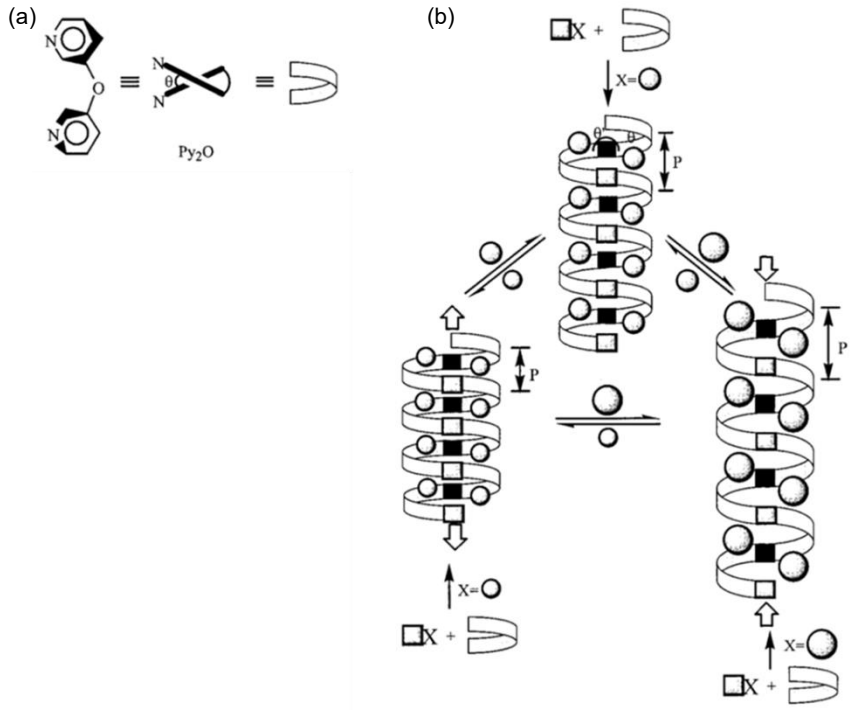

Figure 2-1. (a) Schematic diagram of the stable skewed conformational Py_2O. (b) Design for the molecular spring from combination of the linear geometric silver (I) ion and the skewed Py_2O spacer. Reproduced from Ref.[72].

In addition to the anion dependent regulation, supramolecular springs can also be triggered by metal cations such as sodium,[22] potassium,[52] lithium,[53, 63] *etc.* In 2010, Yashima *et al.*[22] Reported the enantiomeric double helical molecule, in which two tetraphenol strands are intertwined with each other through two spiroborate bridges (Figure 2-2a). Coordinated by four oxygen atoms of the spiroborate moieties, a Na^+ ion is inlayed inside the two strands and electrostatically attracted with the negatively charged spiroborate moieties, enabling the spring to adopt a contracted conformation. Na^+ ions can be removed by addition of cryptand [2.2.1] to the solution, resulting the release, *i.e.* extension, of the supramolecular spring to its initial equilibrium state. The anisotropic extension-contraction dynamic motion can be controlled by adding and removing the sodium ions reversibly (Figure 2-2b).

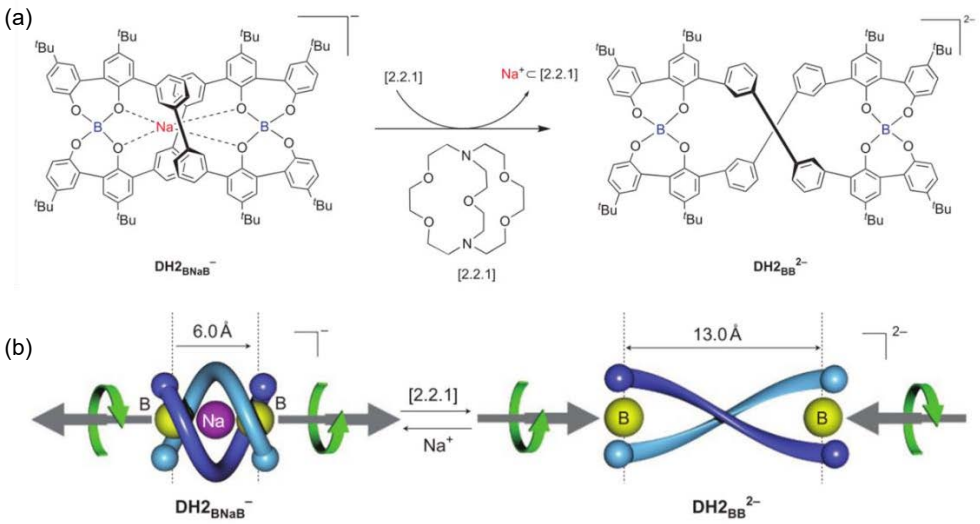

Figure 2-2. (a) Schematic illustration of the removal of the central Na^+ ion from $DH2_{BNaB}^-$ ·Na^+ by cryptand [2.2.1]; (b) Schematic representation of anisotropic twisting motion observed in a right-handed double helical helicate. Reproduced from Ref. [22].

Similarly, Albrecht and co-workers[63] reported on a triple strands helicate prepared from titanoyl bisacetylacetonate and Li_2CO_3, in which two titanium (IV) centers have been bound with two groups of catechol units to form the discrete helicate while lithium ions are bound with the catechol oxygens at both ends to trigger the contraction. As illustrated in Figure 2-3, three states of the helicate, *i.e.* compressed left-handed, expanded right-handed, and expanded left-handed, can be toggled reversibly by introduction, exchange, and removal of counter ions. The switching process can be easily monitored by 1H NMR as well as CD spectroscopy.

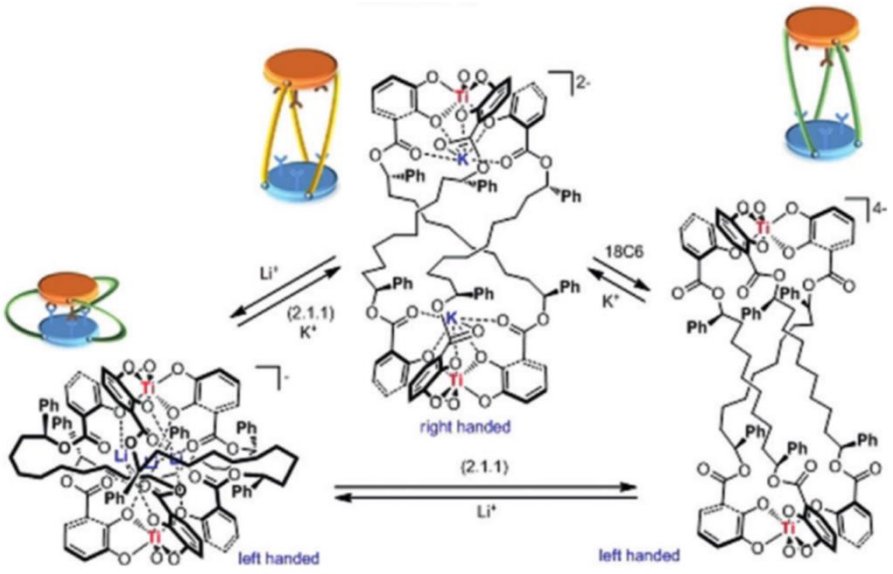

Figure 2-3. Schematic representation of different states of $[(\mathbf{4})_3Ti_2]^{4-}$. Reproduced from Ref. [63]

A very interesting strategy to control the supramolecular spring conformation through coordination driven interaction has been developed by Numata and co-workers[49] in 2013. A semi-artificial curdlan (α β-1,3-glucan) featuring a dendritic amphiphilic Zn-chlorophyll unit attached to each glucose residue (CUR-Chl) (Figure 2-4a) has been prepared to form a one-dimensional right-handed helical structure with a helical pitch of approximately 1.8 nm. Regulated by precise molecular recognition events through Zn-N coordination, the helical polysaccharide was endowed with spring-like motion, in which the degree of elongation could be tuned by varying the contour length of the added ligand (Figure 2-4b-c).

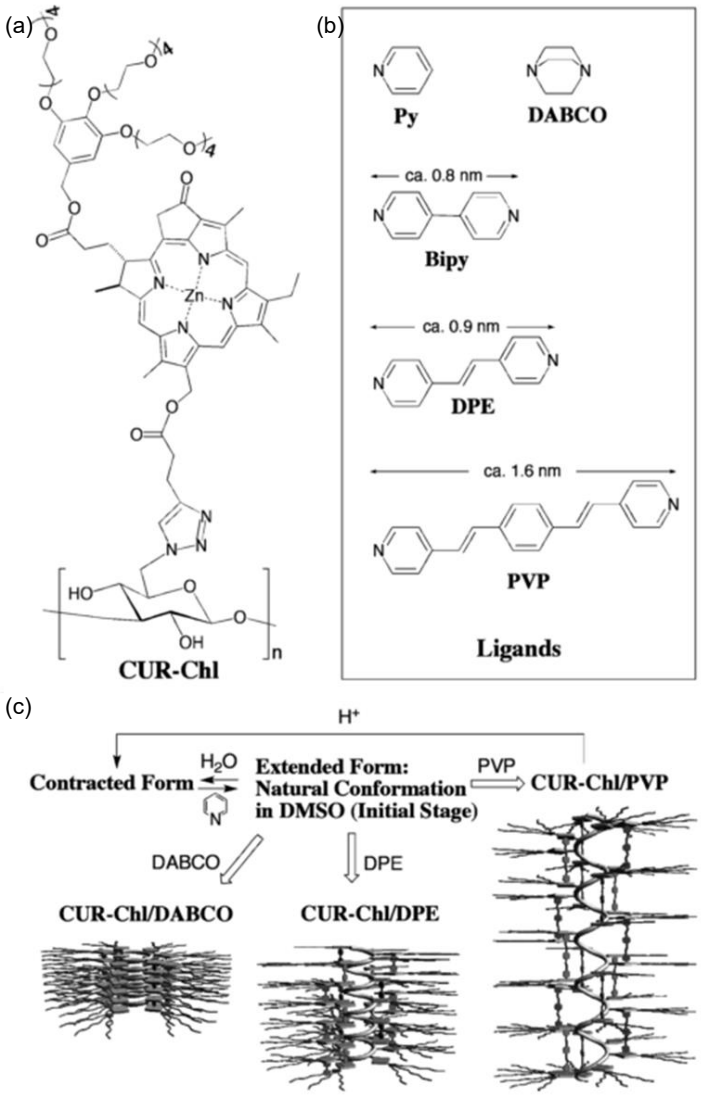

Figure 2-4. (a) Chemical structure of CUR-Chl and (b) potential ligands for coordination with its chlorophyll units. (c) Schematic representation of the controllable motion (contraction/expansion) of CUR-Chl through molecular recognition of its peripheral moieties. Reproduced from Ref. [49].

2.2.2. Thermally driven supramolecular springs

Temperature is also a common stimulus for triggering the motion in supramolecular springs. In 2007 Lee *et al*.[48] reported a supramolecular spring exhibiting thermally tunable pitch in aqueous solution. Cylindrical helical aggregates with a uniform diameter of about 6.5 ± 0.4 nm and lengths of several micrometers have been self-assembled through the coordination of Ag(I) ion and pyridine ligands. The reversible extension-contraction of such helical supramolecular coordination polymers was demonstrated by varying the temperature (Figure 2-5a). In particular, at room temperature, the peripheral ethylene oxide chains were fully hydrated and thus adopted a random coil conformation. Upon heating over 38 °C, the conformational transformation of the lateral ethylene oxide chains into a dehydrated molecular globule took place, rendering the π-stacked helical structure unstable due to steric hindrance between the globules with greater cross-section area. In order to relieve the steric hindrance, the supramolecular spring was extended to allow a larger interfacial area, thus lowering the total free energy. The reversibility of the contraction mode was proven by cooling the samples to room temperature and the switching motion was monitored by ^{1}H NMR. Interestingly, the extension-contraction process was accompanied by the fluorescence switching as shown in Figure 2-5b-c.

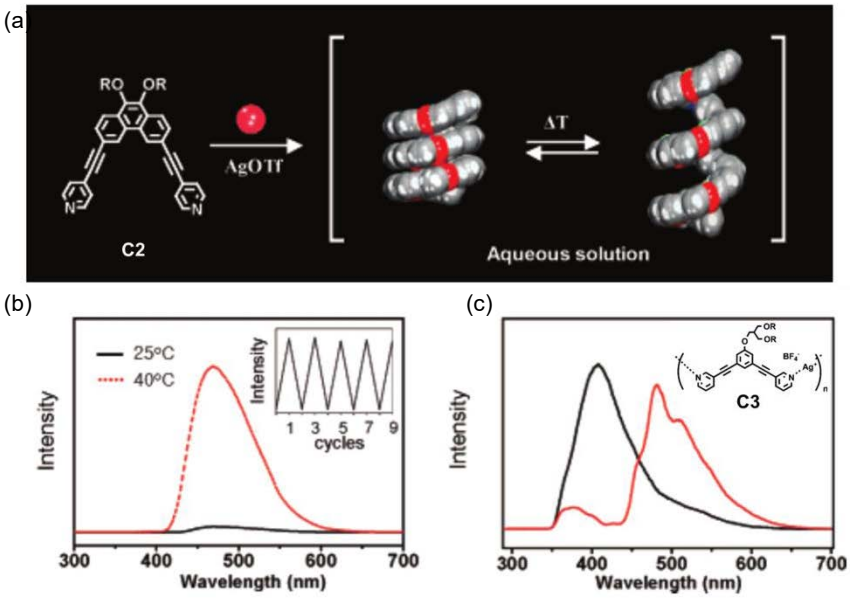

Figure 2-5. (a) Schematic representation of a reversible helical spring. (b) Fluorescence spectra and reversible switching cycles of emission intensity in aqueous solution of C2 (0.1wt%, excited at 280 nm) with temperature variation. (c) Fluorescence spectra of C3 (1wt% aqueous solution) in the absence (black, solid line) and in the presence (red, dashed line) of 5 equiv of perylene at 40 °C (excited at 280 nm). Reproduced from Ref. [48].

2.2.3. pH-triggered supramolecular springs

pH-responsive supramolecular systems such as supramolecular vesicles based on novel amphiphiles[73] have gained particular attention due to their potential applications for example for controlled drug encapsulation/release. In 2016, Yashima *et al.*[40] reported two intelligent supramolecular springs, $DH3_{TBA2}$ and $DH4_{TBA2}$ (TBA=tetrabutylammonium), which are composed of two tetraphenol strands bearing 4,4'-linked 6,6-linked 2,2-bipyridine (bpy) and its bpy N,N'-dioxide units in the middle as shown in Figure 2-6a. The cooperative binding and release of protons (and/or metal ions) to the bipyridine or its N,N'-dioxide units triggered the anti-syn isomerization of the bipyridine units which was accompanied with the reversible switching of the double strand helicates between the contracted and extended conformations (Figure 2-6b). The reversible elastic motions were monitored by NMR, CD, X-ray analysis and theoretical calculations. Similarly, the elastic motions of $DH3_{TBA2}$ could also be controlled by the binding and release of Cu^{2+} ions to the bipyridine units.

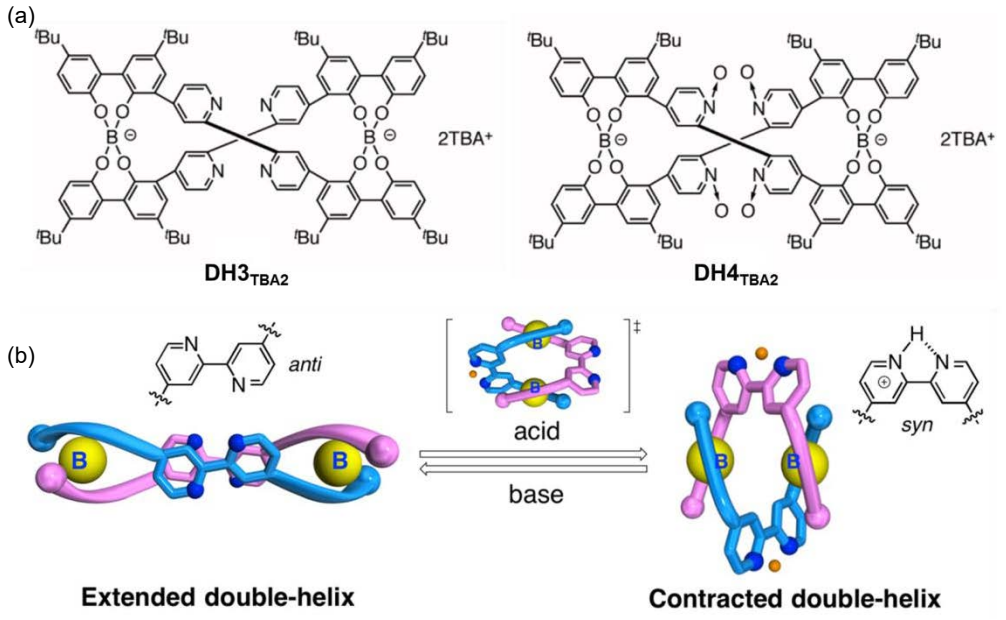

Figure 2-6. (a) Chemical structures of the helicates bearing 4.4'-linked 2,2'-bipyridine and its N,N'-dioxide units. (b) Schematic representation of acid/base-triggered reversible extension-contraction motion of $DH3^{2-}$ through the positive cooperative H^+ binding that induces anti-to-syn isomerization of the 2,2'-bipyridine units of $DH3^{2-}$. Reproduced from Ref. [40].

2.2.4. Solvent driven supramolecular springs

A supramolecular spring formed by self-assembled helicenediol has been reported by Tanaka and co-workers[44] The helicenediol 2,13-bis(hydroxymethyl)dithieno[3,2-e:3',2'-e']benzo[1,2-b:4,3-b']- bis[1]benzothiophene has been recrystallized into racemic mixtures (PM-1) (Figure 2-7a) from ethanol or 1,2-dichloroethane yielding different host-guest stoichiometric ratios, *i.e.* (PM-1)·EtOH and $(PM\text{-}1)_2$, respectively (Figure 2-7b-c). As shown in Figure 2-7b, two homochiral stacked columns, *i.e.* a right-handed strand of (P-1)·EtOH and a left-handed strand of (M-1)·EtOH, are formed by intermolecular hydrogen bonding of host molecules, in which the ethanol molecules are locked with the homochiral columns by hydrogen bonds. As governed by the interaction of π-π forces between the neighboring benzothiophene rings (ring 4-5) and by the hydrogen bond, the interplanar angle between two terminal thiophene rings of (PM-1)·EtOH results 38.0°. When the racemic helicenediol was recrystallized from 1,2-dichloroethane, $(PM\text{-}1)_2$·(1,2-dichloroethane) was formed with a 2:1 host-to-guest stoichiometry as displayed in Figure 2-7c. The terminal hydroxyl groups of a single molecule are located between two hydroxyl groups of the opposite enantiomer and held by hydrogen bonding, which extends the interplanar angle from 38.0° to 54.5° as an extension mode. This helicenediol is among the earliest reported supramolecular springs though the solvent dependent contraction-extension modes are modulated in the crystalline state.

Scrimin and co-workers have reported a peptide made with seven amino acids which exhibit solvent dependent spring like motion.[45] The peptide was reversibly switched between contracted mode (α-helix, 15 Å) and extended mode (310 helix, 17 Å) according to the solvent polarity. The molecular calculation results suggested that the hydrophobic interactions between the side arms of the amino acids provide a major driving force for the stabilization of the α helix in aqueous solution.

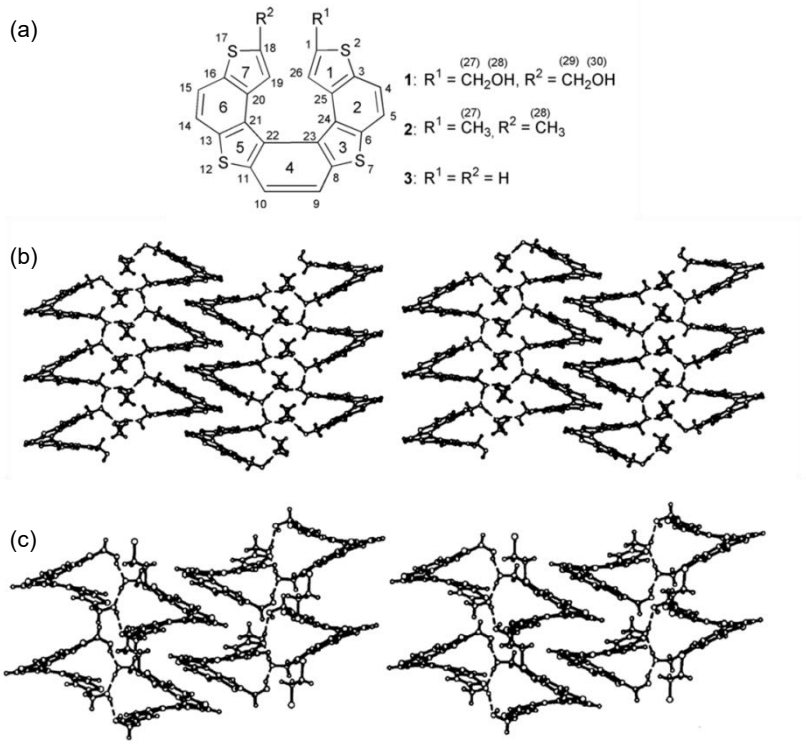

Figure 2-7. (a) Chemical structure of heterohelicenes. (b) Stereo view of the hydrogen bonding network of (PM-1)·(EtOH). Ethanol molecules join two stacking columns of the same helicity to form two stacking columns of (P-1)·(EtOH) (left side) and (M-1)·(EtOH) (right side). (c) Stereo view of the heterochiral dimer of P- and M-helicenediols in the clathrate $(PM\text{-}1)_2$·(1,2-dichloroethane). Reproduced from Ref. [44].

2.2.5. Redox-responsive supramolecular springs

An oligomeric o-phenylene with highly condensed π-cloud that undergoes a redox-responsive dynamic motion has been reported by Aida *et al*.[47] As shown in Figure 2-8, the polymeric *o*-phenylenes are forced to adopt a helical structure as dictated by the heavily angled aromatic connection. Different from the solid-state in which enantiomerically pure crystals are formed due to the chiral symmetry-breaking process, the helices have a rapid helical inversion as an extended conformation with interplanar distances *ca.* 3.2 Å in solution. Once oxidized by one-electron oxidant such as tris(4-bromophenyl) ammoniumyl hexachloroantimonate [(4-$BrC_6H_4)_3N^{\bullet+}SbCl_6^-$], the helices adopt a more compact conformation with interplanar distances of ca. 3.1 Å. and feature a slower switching speed thus allowing a long-lasting chiroptical memory due to a decreased π-electronic repulsion. The reversible contraction-extension mode can be switched by oxidation and reduction with [(4-$BrC_6H_4)_3N^{\bullet+}SbCl_6^-$] and Zn respectively.

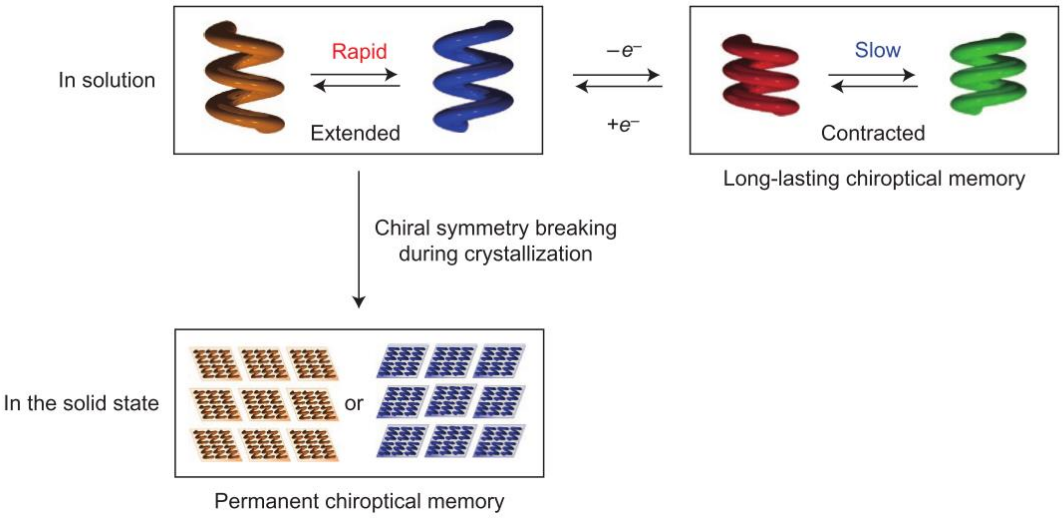

Figure 2-8. Schematic representation of the helical inversion dynamics of OP_8NO_2 in solution and in the solid state. Reproduced from Ref. [47].

By and large, in solution, supramolecular springs can be constructed in various forms (*e.g.* helicates, helicene assemblies, *etc.*) and their elastic motion can be controlled via different stimuli such as metal ions, temperature, pH, solvent, redox processes, *etc.* The contraction-extension motion can be reversibly triggered in a highly controlled manner, which renders supramolecular springs extremely appealing for various applications such as nanoscale mechanical devices[22] or in the separation of chiral compounds.[47]

2.3. Self-assembled springs based dynamic materials

The chemistry of supramolecular springs, introduced in the previous section, enables the precise control over the contraction-extension dynamics as a response to different external stimuli to tune intra- and intermolecular interactions such as metal-ligand coordination, hydrogen bond, π-π stacking, solvophobic effect, *etc.* Although versatile tools have been developed to modulate the supramolecular spring motions, most of the research has been conducted in solutions or single crystals, thus representing a severe limitation for their further applications in everyday life. The exploitation of supramolecular machines including molecular springs in the macroscopic world, by controlling the contraction-extension motions at the molecular level, represents a grand challenge.[23, 26] Integrating supramolecular springs in macroscopic materials is a mandatory step for the development of novel functions with high-level control over the macroscopic movements under the effect of different stimuli. Hitherto, very few examples on the solid-state supramolecular spring macroscopic materials have been reported and are discussed in this section.

2.3.1. Light-responsive dynamic materials

Light is a straightforward and attractive stimulus to trigger macroscopic motions because it is a non-invasive and controllable energy source featuring a high spatio-temporal resolution which can be used to drive different nanoscale molecular systems. A spring-like material capable of converting light energy into macroscopic mechanical movement has been reported by Katsonis *et al*.[51] The prototypical photochromic molecule, *i.e.* an azobenzene-based molecular switch, (Figure 2-9a) has been embedded in the prototypical nematic liquid crystal E7 together with chiral (S) or (R) octan-2-yl 4-((4-(hexyloxy)benzoyl)oxy)benzoate (S-811 and R-811 in Figure 2-9b) to confer a chiral nature to the polymeric ribbons. The mixture was then introduced into a glass cell to promote a twist geometry, in which the orientation of the liquid-crystal director changed smoothly by 90° from the bottom surface to the top surface. The polymer film was cut into ribbons with different angular offset (*i.e.* angle between the orientation of the molecules at mid-plane and the cutting direction). The as prepared ribbons intrinsically adopt different coiling modes, *i.e.* winding, unwinding, and twisting, in which the pitch and handedness as well as the photoresponsive motion is determined by the angular offset.

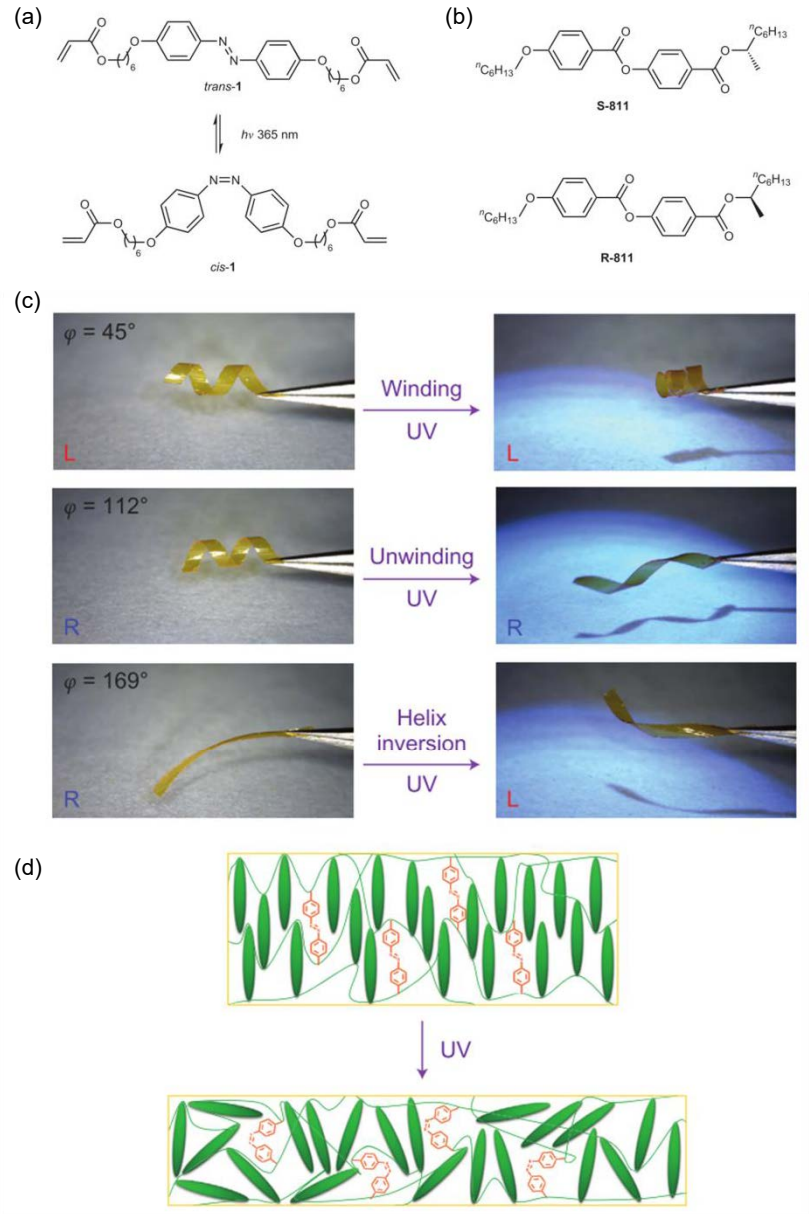

Figure 2-9. A photoresponsive liquid crystal in a twist-nematic molecular organization. (a) The molecular photoswitch 1 used in this study is an azobenzene derivative. (b) Chiral dopants S-811 and R-811 induce a left-handed and right-handed twist in the liquid crystal, respectively. (c) Spiral ribbons irradiated for two minutes with UV (365 nm) display isochoric winding, unwinding and helix inversion as dictated by their initial shape and geometry. (d) Under UV irradiation, the ribbons contract along the director and expand in the perpendicular directions. Reproduced from Ref. [51].

The use of UV irradiation to trigger the contraction-extension behavior of the twisted ribbon was explored at room temperature. As portrayed in Figure 2-9c, the left-handed ribbon exhibit contraction whereas the right-handed ribbon showed extension under UV light. Noteworthy,

the right-handed ribbon with certain angular offset showed helix inversion under the same condition. All the photoresponsive motions above were fully reversible within a few seconds upon exposure to visible light. The mechanism of the reversible contraction-extension was found to depend on the handedness of the director twist and their angular offset. As displayed in Figure 2-9d, the isomerization of azobenzene under UV light induces disorder and causes contraction along the direction of the director and elongation in perpendicular direction. As the top and bottom surfaces adopt different orientation of the director due to the helical twisting, the ribbons need to deform in order to accommodate the anisotropic deformation of both sides. The deformation types (winding, unwinding, and helix inversion) are determined by the orientation of the molecules, which is in turn ruled by the cutting direction.

A proof-of-concept for a photomechanical engine has also been demonstrated to prove the capability of molecular spring material to execute useful work. The detailed device fabrication process[74] relying on a more delicate composition and micropattern design[65] have been reported to demonstrate this bio-inspired strategy could be widely employed for the design of novel light-driven smart materials.

2.3.2. Thermal fueled dynamic materials

Dendronized polymers are a class of linear polymers exposing dendrons in the side groups.[75] The shape-inducing effect of dendritic substituents can be explored to create nanoobjects with a cylindrical shape, which not only considerably widens the range of applications for dendrimers but also opens up new perspectives for various applications. In particular, their self-organization into helical motifs has been reported as a novel strategy for constructing supramolecular spring materials capable of undergoing large-scale motion under external stimuli, such as the thermal treatment.[66] The thermoreversible cisoid-to-transoid conformational isomerism between hexagonal columnar phase (ϕ_{hio}) and a hexagonal columnar (ϕ_h) liquid crystal phase has been observed in dendronized helical polyarylacetylenes by means of differential scanning calorimetry (DSC) and XRD. As displayed in Figure 2-10a, macroscopic samples of the cylindrical polymers are produced by extrusion of the liquid crystalline melt, with the fiber axis being aligned with the cylinder axis. The extruded fiber obtained from the self-organized dendronized helical polymer undergoes extension along its fiber axis upon heating above certain temperature (Figure 2-10b), which is caused by the ϕ_{hio}-to-ϕ_h phase transition. Conversely, upon successive cooling down to room temperature, the fiber contracts back to its original length.

The collective thermal responsive elastic motion of the cylindrical dendronized polymer actuators on the macroscopic scale were demonstrated by object lifting experiment as reveled

in Figure 2-10c. An extruded fiber weighting 1.26 mg was fixed on an inclined (8 ± 0.5°) hot plate with a length of 6.5 mm at room temperature (25°C). Upon heating to 80°C, the fiber underwent expansion with its length increasing about 15% to 7.5 mm, thus lifting a dime weighting 2265 mg along the inclined surface. This self-organizable dendronized polymer has been proven to be an effective strategy to amplify extension-contraction motion of molecular level into large scale to perform real tasks.

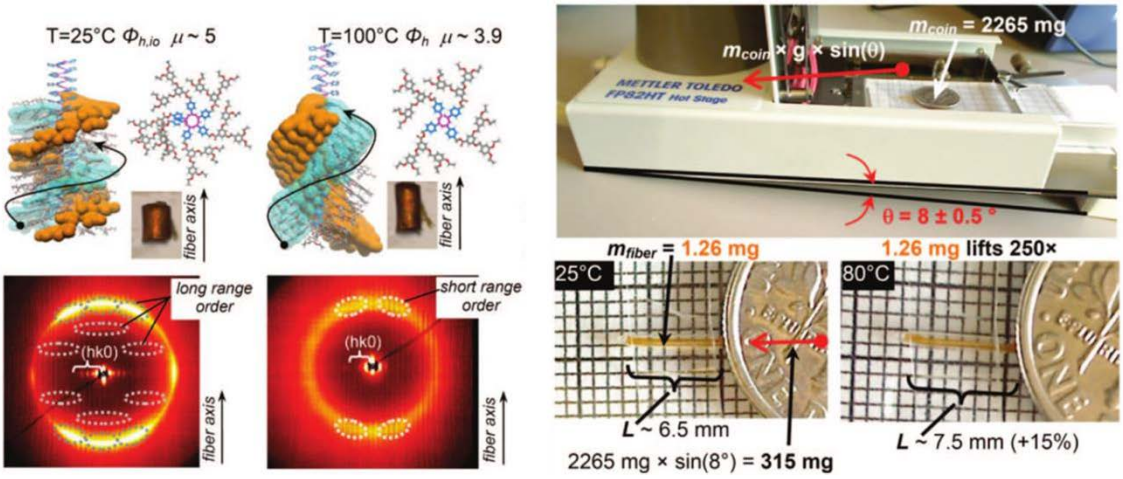

Figure 2-10. Schematic of the self-organizable dendronized helical cis-transoidal polyphenylacetylenes (cis-PPAs) n the (a) cisoid and (b) transoid conformations. (c) Experimental setup that demonstrates the macroscopic scale expansion and contraction of the oriented fiber by the lifting of a dime on the inclined plane of a Mattler hot stage. Reproduced from Ref. [66].

In this section, we have discussed the supramolecular spring based (self-) assembled materials, in which the reversible macroscopic contraction-extension motion could be controlled by light irradiation or by temperature modulation. The aforementioned assemblies demonstrate that self-assembly is an efficient strategy to integrate molecular springs into materials capable of expressing unprecedented functions. These novel functional materials possessing highly controllable macroscopic movement will open a new pathway towards clean, electrode-less actuators.

2.4.Spring-like macroscopic devices

While hitherto supramolecular or self-assembled springs have not been yet integrated in macroscopic devices, spring-like composites and hybrid structures comprising molecular springs and low-dimensional functional nanostructures, including 0D (like nanoparticles and networks thereof), 1D (*e.g.* nanotubes, nanorods, nanoribbons and nanofibers) and 2D (such as graphene and related layered materials) have attracted a great attention due to their structural and functional versatility which opens perspective towards different technological applications. In particular, their superior electrical, optical and mechanical properties of these starting low-dimensional nanomaterials, their controlled functionalization and the possibility of producing them in the bulk quantities make them key components for the generation of functional hybrid material at both lab and industrial scale. Inspired by the supramolecular springs generated via self-assembly at the molecular level, the elastic spring-like motion can also be achieved by the integration of molecular springs and materials, in which macroscale motions or effects of practical applications can be achieved. In this section we will briefly discuss the use of molecular spring containing materials capable to accomplish macroscopic tasks which are integrated into devices such as electromechanical actuators, pressure sensor, and humidity sensor.

2.4.1. Spring-like materials based on 0D nanomaterials

Gold nanoparticles are unique building blocks exhibiting a wide variety of electrical and optical characteristics resulting from their size and electronic interactions.[76, 77] Molecular springs can be co-assembled with gold nanoparticles (AuNPs) to form 2D networks capable of sensing humidity in air.[78] In this case, 8 nm sized AuNPs are covalently interconnected by dithiol PEGs (Figure 2-11a-b), which are organic hygroscopic molecular springs that can sense humidity change through plasmonic coupling, when PEG chains with a contour length of ca. 7 nm are used. The molecular springs play a key role in the sensing process, since they can absorb water molecules and cause swelling of the network. As a result, the interparticle distance increases with increasing humidity (Figure 2-11c), whereas the shift of SPR (surface plasmon resonance) band has been observed in a short time (ca. 200 ms). Noteworthy, the band shift is within the visible light region thus the reversible humidity change process can be observed by naked eyes. The same network swelling phenomena can also be observed with the same two components based network, when shorter dithiol PEG chains (with a contour length of 1.5 or 2.2. nm) are employed. In this case, the humidity ruled contraction and expansion of the PEG chains can be read out electrically with full reversibility, a high

sensitivity and a response as fast as <30 ms, by exploiting the distance dependent electron tunneling process.[79]

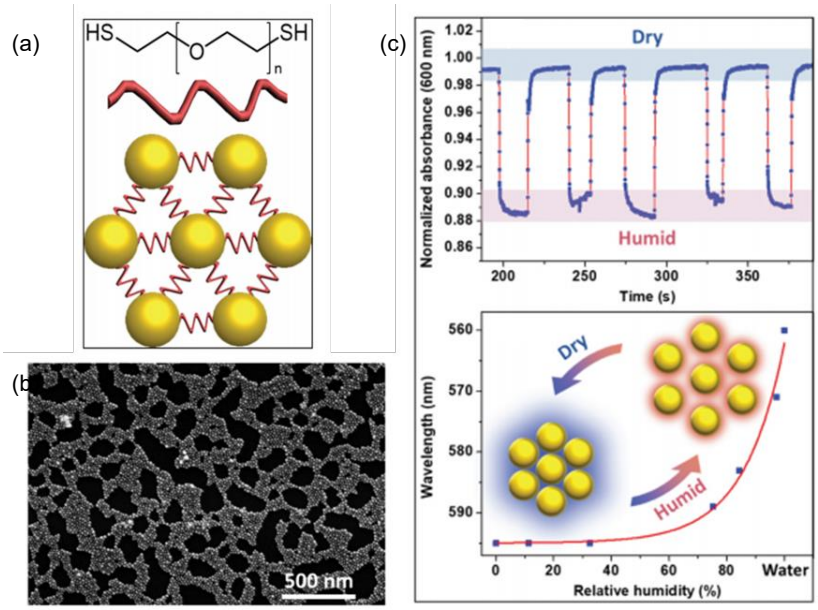

Figure 2-11. (a) Cartoon of the covalently tethered 2D network of AuNPs with di-thiolated PEG; (b) SEM image of the network; (c) reversibility of the sensing process by monitoring the absorbance at a fixed wavelength of 600 nm over time. Reproduced from Ref. [78].

2.4.2. 1D-based spring-like materials

CNTs have been widely utilized to fabricate spring-like materials due to its remarkable properties[80] such as high tensile strengths, electrical conductivities, and most importantly, the ability to further assemble into macroscopic structure in a highly aligned manner. Single-layer fabric ribbons with tunable electromechanical actuations have been reported by Peng *et al.*,[81] in which spring-like CNT fibers were integrated through a sewing method. The CNT fibers were dry-spun from spinnable CVD CNT arrays with a helical structure as shown in Figure 2-12a, in which the chirality depended on the spinning direction during preparation. By applying a voltage, electromechanically contractive and rotary actuations had been generated by the CNT fibers, in which the rotary direction could be tuned by varying the helical chirality. The contractive actuation could be enhanced by increasing the number of fibers to leverage the electromagnetic effects among the electrically conducting fibers. In order to demonstrate the macroscopic motion control, these spring-like fibers were woven into Kapton film which produces reversibly electromechanical bending-recovery motion resembling crawling robot upon current. Furthermore, these fiber-integrated fabric ribbons could be reshaped into helical structures with different chirality by heat setting as shown in Figure 2-

12b. Reversible contraction-extension motion can be triggered with a voltage input (Figure 2-12c-d), in which the actuations were modulated by the chirality of the ribbon helix and helical fibers collectively (*i.e.* contraction for the same chirality and extension for the reverse chirality). This strategy has provided an effective protocol to the design and fabrication of electromechanical spring-like actuators with CNT as active materials towards potential applications like stretchable conductors,[82] and artificial muscle,[83] *etc.*

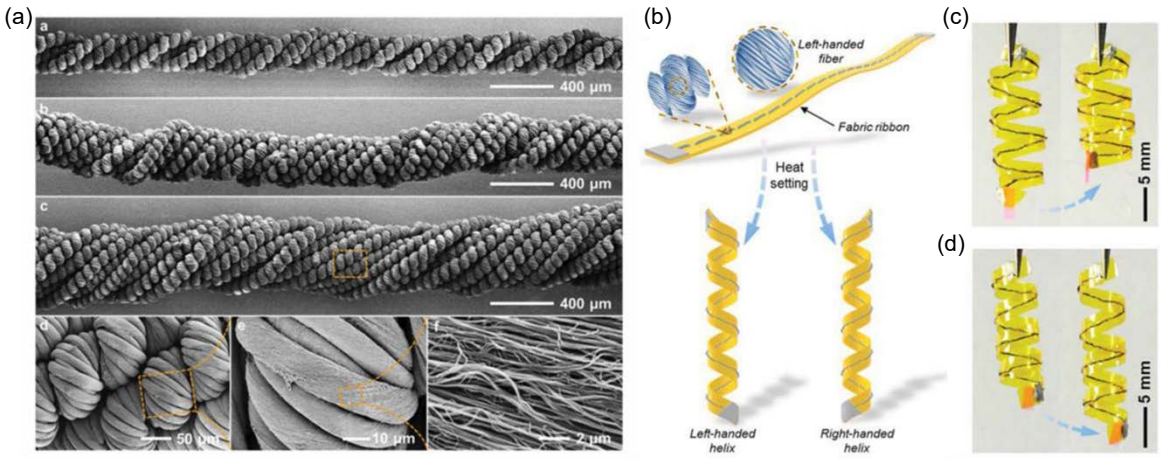

Figure 2-12. (a) SEM images of twisted spring-like fibers; (b) Schematic illustration to the preparation of helical Kapton fabric ribbons with an opposite helical chirality; photographs of the electromechanical contraction motion generated by a (c) left-handed and (d) right-handed Kapton fabric ribbon respectively. Reproduced from Ref. [81].

2.5. Conclusion and perspectives

Spring-like structures are very common in Nature and include systems like DNA and tendrils, yet, mimicking the spring-like function at the nanoscale in artificial molecules is highly challenging. Since the first report on supramolecular spring appeared in 2000, increasing efforts have been dedicated to the use of different external stimuli such as light, heat, ion, pH, solvent, *etc.*, to control of the elastic extension-contraction motion in solution and single crystal. Various stimuli-responsive characteristics have been encoded in the helical molecules or assemblies through supramolecular interactions (*e.g.* metal-ligand coordination, π-π, hydrogen bonding, van der Waals interaction, *etc.*). A few attempts have been made to integrate molecular springs into polymers and aggregates to perform extension-contraction on the macroscopic scale for real applications, *e.g.* actuators and molecular muscles. Self-assembly provides promising way to create smart materials possessing stimuli-response behaviors in micro/macroscopic scale, in which individual motions could be harnessed to orient the nanomechanical actuators thus accomplishing tasks in the macroscopic world. Spring-like materials, constructed by the integration of molecular springs and low-dimensional nanostructures (*e.g.* CNT, graphene, *etc.*), have also been discussed in this chapter as a route to realize functional (nano) devices. The combination of adaptive (supra) molecular springs and materials with versatile properties offers a multitude of potential solutions towards the development of a broadest arsenal of smart materials for sensing, chemical separation and other applications. In the future, the development of artificial machines which can convert molecular movement into macroscopic work will be the greatest challenge in the field, by taming functional complexity in chemical programming of dynamic materials to be readily integrated in functional devices.

2.6. References

1. Lehn, J.-M., Supramolecular Chemistry - Scope and Perspectives Molecules, Supermolecules, and Molecular Devices. *Angew. Chem. Int. Ed.* **1988,** *27*, 89-112.
2. Chakrabarty, R.; Mukherjee, P. S.; Stang, P. J., Supramolecular Coordination: Self-Assembly of Finite Two- and Three-Dimensional Ensembles. *Chem. Rev.* **2011,** *111*, 6810-6918.
3. Lehn, J.-M., Toward complex matter: Supramolecular chemistry and self-organization. *Proc. Natl. Acad. Sci. U.S.A* **2002,** *99*, 4763-4768.
4. Philp, D.; Stoddart, J. F., Self-assembly in natural and unnatural systems. *Angew. Chem. Int. Ed.* **1996,** *35*, 1154-1196.
5. Lee, C. C.; Grenier, C.; Meijer, E. W.; Schenning, A. P. H. J., Preparation and characterization of helical self-assembled nanofibers. *Chem. Soc. Rev.* **2009,** *38*, 671-683.
6. Lehn, J.-M., Perspectives in Chemistry - Steps towards Complex Matter. *Angew. Chem. Int. Ed.* **2013,** *52*, 2836-2850.
7. van Dongen, S. F. M.; Cantekin, S.; Elemans, J. A. A. W.; Rowan, A. E.; Nolte, R. J. M., Functional interlocked systems. *Chem. Soc. Rev.* **2014,** *43*, 99-122.
8. Anelli, P. L.; Spencer, N.; Stoddart, J. F., A Molecular Shuttle. *J. Am. Chem. Soc.* **1991,** *113*, 5131-5133.
9. Lane, A. S.; Leigh, D. A.; Murphy, A., Peptide-based molecular shuttles. *J. Am. Chem. Soc.* **1997,** *119*, 11092-11093.
10. Benniston, A. C.; Harriman, A., A Light-Induced Molecular Shuttle Based on a [2]Rotaxane-Derived Triad. *Angew. Chem. Int. Ed.* **1993,** *32*, 1459-1461.
11. Leigh, D. A.; Wong, J. K. Y.; Dehez, F.; Zerbetto, F., Unidirectional rotation in a mechanically interlocked molecular rotor. *Nature* **2003,** *424*, 174-179.
12. Feringa, B. L., In control of motion: From molecular switches to molecular motors. *Acc. Chem. Res.* **2001,** *34*, 504-513.
13. Kottas, G. S.; Clarke, L. I.; Horinek, D.; Michl, J., Artificial molecular rotors. *Chem. Rev.* **2005,** *105*, 1281-1376.
14. Krajnik, B.; Chen, J. W.; Watson, M. A.; Cockroft, S. L.; Feringa, B. L.; Hofkens, J., Defocused Imaging of UV-Driven Surface-Bound Molecular Motors. *J. Am. Chem. Soc.* **2017,** *139*, 7156-7159.
15. Zehm, D.; Fudickar, W.; Linker, T., Molecular switches flipped by oxygen. *Angew. Chem. Int. Ed.* **2007,** *46*, 7689-7692.
16. Liu, Y.; Flood, A. H.; Stoddart, J. F., Thermally and electrochemically controllable self-complexing molecular switches. *J. Am. Chem. Soc.* **2004,** *126*, 9150-9151.
17. Russew, M. M.; Hecht, S., Photoswitches: From Molecules to Materials. *Adv. Mater.* **2010,** *22*, 3348-3360.
18. Gabrys, B. J.; Pesz, K.; Bartkiewicz, S. J., Brownian motion, molecular motors and ratchets. *Physica A* **2004,** *336*, 112-122.
19. Kelly, T. R.; Tellitu, I.; Sestelo, J. P., In search of molecular ratchets. *Angew. Chem. Int. Ed.* **1997,** *36*, 1866-1868.
20. Serreli, V.; Lee, C. F.; Kay, E. R.; Leigh, D. A., A molecular information ratchet. *Nature* **2007,** *445*, 523-527.
21. Mahadevan, L.; Matsudaira, P., Motility powered by supramolecular springs and ratchets. *Science* **2000,** *288*, 95-99.
22. Miwa, K.; Furusho, Y.; Yashima, E., Ion-triggered spring-like motion of a double helicate accompanied by anisotropic twisting. *Nat. Chem.* **2010,** *2*, 444-449.
23. Erbas-Cakmak, S.; Leigh, D. A.; McTernan, C. T.; Nussbaumer, A. L., Artificial Molecular Machines. *Chem. Rev.* **2015,** *115*, 10081-10206.

24. Barboiu, M.; Stadler, A. M.; Lehn, J.-M., Controlled Folding, Motional, and Constitutional Dynamic Processes of Polyheterocyclic Molecular Strands. *Angew. Chem. Int. Ed.* **2016,** *55*, 4130-4154.
25. Browne, W. R.; Feringa, B. L., Making molecular machines work. *Nat. Nanotechnol.* **2006,** *1*, 25-35.
26. Kay, E. R.; Leigh, D. A.; Zerbetto, F., Synthetic molecular motors and mechanical machines. *Angew. Chem. Int. Ed.* **2007,** *46*, 72-191.
27. Marsella, M. J.; Rahbarnia, S.; Wilmot, N., Molecular springs, muscles, rheostats, and pressing gyroscopes: from review to preview. *Org. Biomol. Chem.* **2007,** *5*, 391-400.
28. Kim, H. J.; Lim, Y. B.; Lee, M., Self-assembly of supramolecular polymers into tunable helical structures. *J. Polym. Sci. Pol. Chem.* **2008,** *46*, 1925-1935.
29. Feringa, B. L., Molecular Machines Springing into Action. *Nat. Chem.* **2010,** *2*, 429-430.
30. Yashima, E.; Ousaka, N.; Taura, D.; Shimomura, K.; Ikai, T.; Maeda, K., Supramolecular Helical Systems: Helical Assemblies of Small Molecules, Foldamers, and Polymers with Chiral Amplification and Their Functions. *Chem. Rev.* **2016,** *116*, 13752-13990.
31. Sun, S. J.; Footer, M.; Matsudaira, P., Modification of Cys-837 identifies an actin-binding site in the beta-propeller protein scruin. *Mol. Biol. Cell* **1997,** *8*, 421-430.
32. Way, M.; Sanders, M.; Garcia, C.; Sakai, J.; Matsudaira, P., Sequence and Domain Organization of Scruin, an Actin Cross-Linking Protein in the Acrosomal Process of Limulus Sperm. *J. Cell Biol.* **1995,** *128*, 51-60.
33. Wang, C. Y.; Huang, Z. Z.; Lin, Y. H.; Ren, J. S.; Qu, X. G., Artificial DNA Nano-Spring Powered by Protons. *Adv. Mater.* **2010,** *22*, 2792-2798.
34. Zocchi, G., Controlling Proteins Through Molecular Springs. *Annu. Rev. Biophys.* **2009,** *38*, 75-88.
35. Saghatelian, A.; Guckian, K. M.; Thayer, D. A.; Ghadiri, M. R., DNA detection and signal amplification via an engineered allosteric enzyme. *J. Am. Chem. Soc.* **2003,** *125*, 344-345.
36. Jin, P.; Bulkley, D.; Guo, Y. M.; Zhang, W.; Guo, Z. H.; Huynh, W.; Wu, S. P.; Meltzer, S.; Cheng, T.; Jan, L. Y.; Jan, Y. N.; Cheng, Y. F., Electron cryo-microscopy structure of the mechanotransduction channel NOMPC. *Nature* **2017,** *547*, 118-122.
37. Saotome, K.; Murthy, S. E.; Kefauver, J. M.; Whitwam, T.; Patapoutian, A.; Ward, A. B., Structure of the mechanically activated ion channel Piezol. *Nature* **2018,** *554*, 481-486.
38. Shi, Y. S.; Polat, B.; Huang, Q.; Sirbuly, D. J., Nanoscale fiber-optic force sensors for mechanical probing at the molecular and cellular level. *Nat. Protoc.* **2018,** *13*, 2714-2739.
39. Zhao, Q. C.; Zhou, H.; Chi, S. P.; Wang, Y. F.; Wang, J. H.; Geng, J.; Wu, K.; Liu, W. H.; Zhang, T. X.; Dong, M. Q.; Wang, J. W.; Li, X. M.; Xiao, B. L., Structure and mechanogating mechanism of the Piezol channel. *Nature* **2018,** *554*, 487-492.
40. Suzuki, Y.; Nakamura, T.; Iida, H.; Ousaka, N.; Yashima, E., Allosteric Regulation of Unidirectional Spring-like Motion of Double-Stranded Helicates. *J. Am. Chem. Soc.* **2016,** *138*, 4852-4859.
41. Nakakuki, Y.; Hirose, T.; Matsuda, K., Synthesis of a Helical Analogue of Kekulene: A Flexible pi-Expanded Helicene with Large Helical Diameter Acting as a Soft Molecular Spring. *J. Am. Chem. Soc.* **2018,** *140*, 15461-15469.
42. Hannak, R. B.; Farber, G.; Konrat, R.; Krautler, B., An organometallic B-12-rotaxane and a B-12-dimer, relaxed and loaded forms of a molecular spring. *J. Am. Chem. Soc.* **1997,** *119*, 2313-2314.
43. Leontiev, A. V.; Serpell, C. J.; White, N. G.; Beer, P. D., Cation-induced molecular motion of spring-like [2]catenanes. *Chem. Sci.* **2011,** *2*, 922-927.
44. Tanaka, K.; Osuga, H.; Kitahara, Y., Clathrate formation by and self-assembled supramolecular structures of a "molecular spring". *J. Chem. Soc. Perk. T 2* **2000**, 2492-2497.

45. Pengo, P.; Pasquato, L.; Moro, S.; Brigo, A.; Fogolari, F.; Broxterman, Q. B.; Kaptein, B.; Scrimin, P., Quantitative correlation of solvent polarity with the alpha-/3(10)-helix equilibrium: A heptapeptide behaves as a solvent-driven molecular spring. *Angew. Chem. Int. Ed.* **2003,** *42*, 3388-3392.
46. Berl, V.; Huc, I.; Khoury, R. G.; Krische, M. J.; Lehn, J. M., Interconversion of single and double helices formed from synthetic molecular strands. *Nature* **2000,** *407*, 720-723.
47. Ohta, E.; Sato, H.; Ando, S.; Kosaka, A.; Fukushima, T.; Hashizume, D.; Yamasaki, M.; Hasegawa, K.; Muraoka, A.; Ushiyama, H.; Yamashita, K.; Aida, T., Redox-responsive molecular helices with highly condensed pi-clouds. *Nat. Chem.* **2011,** *3*, 68-73.
48. Kim, H. J.; Lee, E.; Park, H. S.; Lee, M., Dynamic extension-contraction motion in supramolecular springs. *J. Am. Chem. Soc.* **2007,** *129*, 10994-10995.
49. Numata, M.; Kinoshita, D.; Hirose, N.; Kozawa, T.; Tamiaki, H.; Kikkawa, Y.; Kanesato, M., Controlled Stacking and Unstacking of Peripheral Chlorophyll Units Drives the Spring-Like Contraction and Expansion of a Semi-Artificial Helical Polymer. *Chem. Eur. J.* **2013,** *19*, 1592-1598.
50. Zhang, X. J.; Zou, J. H.; Tamhane, K.; Kobzeff, F. F.; Fang, J. Y., Self-Assembly of pH-Switchable Spiral Tubes: Supramolecular Chemical Springs. *Small* **2010,** *6*, 217-220.
51. Iamsaard, S.; Asshoff, S. J.; Matt, B.; Kudernac, T.; Cornelissen, J. J. L. M.; Fletcher, S. P.; Katsonis, N., Conversion of light into macroscopic helical motion. *Nat. Chem.* **2014,** *6*, 229-235.
52. Luo, D. P.; Zhang, X. M.; Shen, Y. T.; Xu, J.; Shu, L. J.; Zeng, Q. D.; Wang, C., Two-dimensional supramolecular spring: coordination driven reversible extension and contraction of bridged half rings. *Chem. Commun.* **2014,** *50*, 9369-9371.
53. Chen, X. F.; Baumert, M.; Frohlich, R.; Albrecht, M., Cation triggered spring-like helicates based on ketone-substituted bis-catechol ligands. *J. Incl. Phenom. Macro.* **2019,** *94*, 133-140.
54. Berl, V.; Huc, I.; Khoury, R. G.; Lehn, J. M., Helical molecular programming: Folding of oligopyridine-dicarboxamides into molecular single helices. *Chem. Eur. J.* **2001,** *7*, 2798-2809.
55. Takashima, Y.; Hatanaka, S.; Otsubo, M.; Nakahata, M.; Kakuta, T.; Hashidzume, A.; Yamaguchi, H.; Harada, A., Expansion-contraction of photoresponsive artificial muscle regulated by host-guest interactions. *Nat. Commun.* **2012,** *3*, 1270.
56. Prince, R. B.; Saven, J. G.; Wolynes, P. G.; Moore, J. S., Cooperative conformational transitions in phenylene ethynylene oligomers: Chain-length dependence. *J. Am. Chem. Soc.* **1999,** *121*, 3114-3121.
57. Inouye, M.; Waki, M.; Abe, H., Saccharide-dependent induction of chiral helicity in achiral synthetic hydrogen-bonding oligomers. *J. Am. Chem. Soc.* **2004,** *126*, 2022-2027.
58. Heo, J.; Jeon, Y. M.; Mirkin, C. A., Reversible interconversion of homochiral triangular macrocycles and helical coordination polymers. *J. Am. Chem. Soc.* **2007,** *129*, 7712-7713.
59. Jimenez, M. C.; Dietrich-Buchecker, C.; Sauvage, J. P., Towards synthetic molecular muscles: Contraction and stretching of a linear rotaxane dimer. *Angew. Chem. Int. Ed.* **2000,** *39*, 3284-3287.
60. Bruns, C. J.; Stoddart, J. F., Rotaxane-Based Molecular Muscles. *Acc. Chem. Res.* **2014,** *47*, 2186-2199.
61. Mauro, M., Gel-based soft actuators driven by light. *J. Mater. Chem. B* **2019,** *7*, 4234-4242.
62. Zhang, Q.; Rao, S. J.; Xie, T.; Li, X.; Xu, T. Y.; Li, D. W.; Qu, D. H.; Long, Y. T.; Tian, H., Muscle-like Artificial Molecular Actuators for Nanoparticles. *Chem* **2018,** *4*, 2670-2684.
63. Chen, X. F.; Gerger, T. M.; Rauber, C.; Raabe, G.; Gob, C.; Oppel, I. M.; Albrecht, M., A Helicate-Based Three-State Molecular Switch. *Angew. Chem. Int. Ed.* **2018,** *57*, 11817-11820.

64. Barboiu, M.; Lehn, J.-M., Dynamic chemical devices: Modulation of contraction/extension molecular motion by coupled-ion binding/pH change-induced structural switching. *Proc. Natl. Acad. Sci. U.S.A* **2002,** *99*, 5201-5206.
65. Asshoff, S. J.; Lancia, F.; Iamsaard, S.; Matt, B.; Kudernac, T.; Fletcher, S. P.; Katsonis, N., High-Power Actuation from Molecular Photoswitches in Enantiomerically Paired Soft Springs. *Angew. Chem. Int. Ed.* **2017,** *56*, 3261-3265.
66. Percec, V.; Rudick, J. G.; Peterca, M.; Heiney, P. A., Nanomechanical function from self-organizable dendronized helical polyphenylacetylenes. *J. Am. Chem. Soc.* **2008,** *130*, 7503-7508.
67. Lee, J.; Govorov, A. O.; Kotov, N. A., Nanoparticle assemblies with molecular springs: A nanoscale thermometer. *Angew. Chem. Int. Ed.* **2005,** *44*, 7439-7442.
68. Lehn, J. M.; Rigault, A.; Siegel, J.; Harrowfield, J.; Chevrier, B.; Moras, D., Spontaneous Assembly of Double-Stranded Helicates from Oligobipyridine Ligands and Copper(I) Cations - Structure of an Inorganic Double Helix. *Proc. Natl. Acad. Sci. U.S.A* **1987,** *84*, 2565-2569.
69. Albrecht, M.; Chen, X. F.; Van Craen, D., From Hierarchical Helicates to Functional Supramolecular Devices. *Chem. Eur. J.* **2019,** *25*, 4265-4273.
70. Piguet, C.; Bernardinelli, G.; Hopfgartner, G., Helicates as versatile supramolecular complexes. *Chem. Rev.* **1997,** *97*, 2005-2062.
71. Piguet, C.; Borkovec, M.; Hamacek, J.; Zeckert, K., Strict self-assembly of polymetallic helicates: the concepts behind the semantics. *Coordin. Chem. Rev.* **2005,** *249*, 705-726.
72. Jung, O. S.; Kim, Y. J.; Lee, Y. A.; Park, J. K.; Chae, H. K., Smart molecular helical springs as tunable receptors. *J. Am. Chem. Soc.* **2000,** *122*, 9921-9925.
73. Duan, Q. P.; Cao, Y.; Li, Y.; Hu, X. Y.; Xiao, T. X.; Lin, C.; Pan, Y.; Wang, L. Y., pH-Responsive Supramolecular Vesicles Based on Water-Soluble Pillar[6]arene and Ferrocene Derivative for Drug Delivery. *J. Am. Chem. Soc.* **2013,** *135*, 10542-10549.
74. Iamsaard, S.; Villemin, E.; Lancia, F.; Asshoff, S. J.; Fletcher, S. P.; Katsonis, N., Preparation of biomimetic photoresponsive polymer springs. *Nat. Protoc.* **2016,** *11*, 1788-1797.
75. Schlüter, A. D.; Rabe, J. P., Dendronized polymers: Synthesis, characterization, assembly at interfaces, and manipulation. *Angew. Chem. Int. Ed.* **2000,** *39*, 864-883.
76. Grzelczak, M.; Perez-Juste, J.; Mulvaney, P.; Liz-Marzan, L. M., Shape control in gold nanoparticle synthesis. *Chem. Soc. Rev.* **2008,** *37*, 1783-1791.
77. Liz-Marzan, L. M.; Giersig, M.; Mulvaney, P., Synthesis of nanosized gold-silica core-shell particles. *Langmuir* **1996,** *12*, 4329-4335.
78. Squillaci, M. A.; Zhong, X.; Peyruchat, L.; Genet, C.; Ebbesen, T. W.; Samorì, P., 2D hybrid networks of gold nanoparticles: mechanoresponsive optical humidity sensors. *Nanoscale* **2019,** *11*, 19315-19318.
79. Squillaci, M. A.; Stoeckel, M.-A.; Samorì, P., 3D hybrid networks of gold nanoparticles: mechanoresponsive electrical humidity sensors with on-demand performances. *Nanoscale* **2019,** *11*, 19319-19326.
80. Singh, P.; Campidelli, S.; Giordani, S.; Bonifazi, D.; Bianco, A.; Prato, M., Organic functionalisation and characterisation of single-walled carbon nanotubes. *Chem. Soc. Rev.* **2009,** *38*, 2214-2230.
81. Chen, P. N.; He, S. S.; Xu, Y. F.; Sun, X. M.; Peng, H. S., Electromechanical Actuator Ribbons Driven by Electrically Conducting Spring-Like Fibers. *Adv. Mater.* **2015,** *27*, 4982-4988.
82. Shang, Y. Y.; He, X. D.; Li, Y. B.; Zhang, L. H.; Li, Z.; Ji, C. Y.; Shi, E. Z.; Li, P. X.; Zhu, K.; Peng, Q. Y.; Wang, C.; Zhang, X. J.; Wang, R. G.; Wei, J. Q.; Wang, K. L.; Zhu, H. W.; Wu, D. H.; Cao, A. Y., Super-Stretchable Spring-Like Carbon Nanotube Ropes. *Adv. Mater.* **2012,** *24*, 2896-2900.

83. Xu, L. L.; Peng, Q. Y.; Zhu, Y.; Zhao, X.; Yang, M. L.; Wang, S. S.; Xue, F. H.; Yuan, Y.; Lin, Z. S.; Xu, F.; Sun, X. X.; Li, J. J.; Yin, W. L.; Li, Y. B.; He, X. D., Artificial muscle with reversible and controllable deformation based on stiffness-variable carbon nanotube spring-like nanocomposite yarn. *Nanoscale* **2019,** *11*, 8124-8132.

Chapter 3

Pressure sensors and strain sensors

This chapter provides an introduction to pressure and strain sensors by discussing the fundamental aspects (*e.g.* definition, sensing mechanisms, key parameters, *etc.*) and active sensory materials. Both pressure sensor and strain sensor are extremely appealing research topics holding a true potential for technological applications in wearable human health monitoring, e-skin, human-machine interface, robotics, automation, *etc.* This chapter will guide the reader to fully understand the research background of this thesis and to outline the research design and significance of the development of pressure/strain sensor with novel hybrid materials.

3.1. Introduction

Pressure is one of the most frequently used physical parameter either in industrial production or personal electronic devices as an indicator of the physical environment of vapor, liquid, and contact *etc.* In the past few decades, considerable attention has been paid to the design and fabrication of pressure sensor for actual electronic applications such as touch display,[1, 2] e-skin,[3-5] real time human health monitoring,[6-8] motion detection,[9] and others. Together with strain sensor, pressure sensors have been widely integrated into wearable devices to monitor physiological parameters such as pulse, blood pressure, temperature, heart rate, sleeping quality, oxygen saturation *etc.*[10-12] With the development of nanomaterials, novel pressure sensors and strain sensors have been developed with superior properties such as light weight, flexible, robust, high sensitivity, fast response, biocompatibility, low power consumption *etc.*[13-16] In this chapter, we will briefly introduce the fundamental aspects of pressure sensors and strain sensors as well as the most widely used active sensing materials within different dimensions.

3.2. Pressure sensors

3.2.1. Fundamental aspects of pressure sensor

3.2.1.1. Definition and key parameters

Pressure sensors are devices which capable to quantify a pressure change through an electrical readout. Pressure sensors are extensively used in our daily life either directly (*e.g.* touch screen, microphone, *etc.*) or indirectly (*e.g.* altitude, speed of fluid/gas flow, *etc.*). To evaluate the performance of pressure sensors, key parameters need to be taken consideration including sensitivity, linearity, detection range, response time, power consumption, flexibility *etc.*

Among all the parameters, sensitivity is the most important one because it quantifies the effectiveness of pressure sensor. Sensitivity is defined as the ratio between the change of output electrical signal and the change of input pressure of the device. The output signal might be different based on the sensing mechanisms. For examples, relative capacitance change ($\Delta C/C_0$) is used for capacitive pressure sensor. For the most common reported piezoresistive pressure sensor, the sensitivity is defined as:

$$S\ (sensitivity) = \frac{\Delta R/R_0}{\Delta P} \qquad (3-1)$$

where $\Delta R/R_0$ represents the relative resistance change and ΔP represents the pressure change.[13]

Linearity is also an important parameter to determine a pressure sensor's static characteristics. The pressure sensor has a good linearity if the output signal can fit the input pressure change in a straight line, and it is more reliable and accurate in the linear response range. For certain applications, linearity would be considered as the priority parameter such as weight balance.[14]

The design of detection range of pressure sensor is usually related to specific applications. For the daily activities of human beings like touch, object manipulation *etc.*, the pressure mainly located below 100 kPa.[17] As shown in the Figure 3-1, normally the pressure can be divided into four ranges, which are the ultra-low-pressure (below 1 Pa), subtle-pressure (1 Pa-1 kPa), low-pressure (1 kPa-10 kPa), and medium-pressure (10 kPa-100 kPa).[14] To design pressure sensor devices with specific applications, one must consider the relevant detection range. Noteworthy, the ultra-low-pressure range is normally related to sound. The development of microelectromechanical system (MEMS) based ultra-sensitive pressure sensor is of great importance to microphones, hearing aids, and other intelligent products.[18]

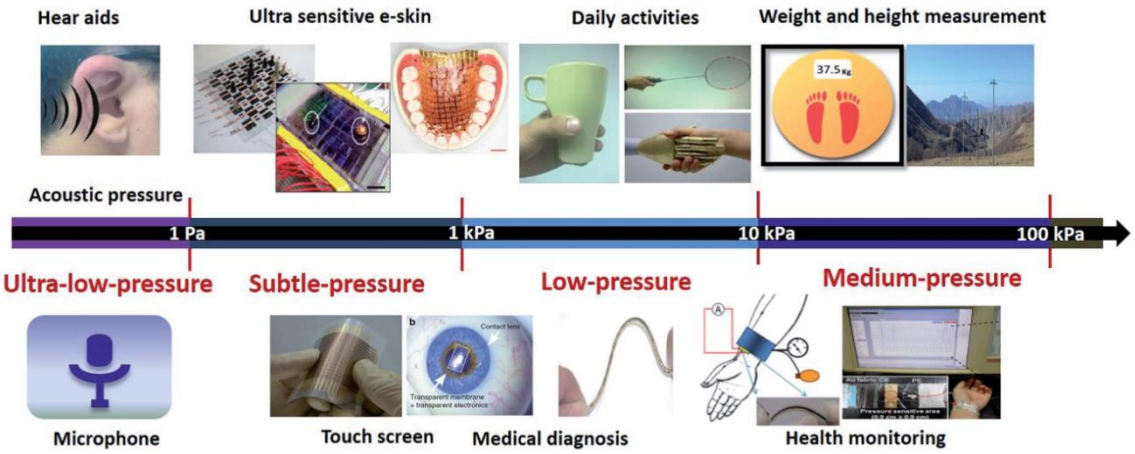

Figure 3-1. The detection range and relevant applications. Reproduced from Ref.[14].

The response time is an important parameter to evaluate a pressure sensor, especially for dynamic real-time sensing devices. The time requires by device once received the input pressure to generating a stable output signal is defined as response time. The smaller is the value, the faster is the response. Normally a response time below 100 ms is widely acceptable, while a shorter response time is necessary for certain applications such as touch screen or health monitoring systems.

Other parameters to assess pressure sensor such as power consumption, flexibility, stability *etc.* are also important and need to be taken careful consideration by researchers when choosing suitable materials (active sensing materials, electrode materials *etc.*) and configurations to get access to various practical applications with comprehensive and balanced qualities.

3.2.1.2. Sensing mechanisms

The "leit motiv" of the pressure sensors, regardless the mechanism employed, is the existence of compressible active materials whose properties are changed when they are subjected to a pressure. Various transduction mechanisms have been employed in pressure sensors including the most frequently reported piezoresistive sensing, capacitive sensing, piezoelectric sensing, and other sensing mechanisms such as resonant sensing, optical sensing, and triboelectric sensing. The difference and characteristics have been summarized below.

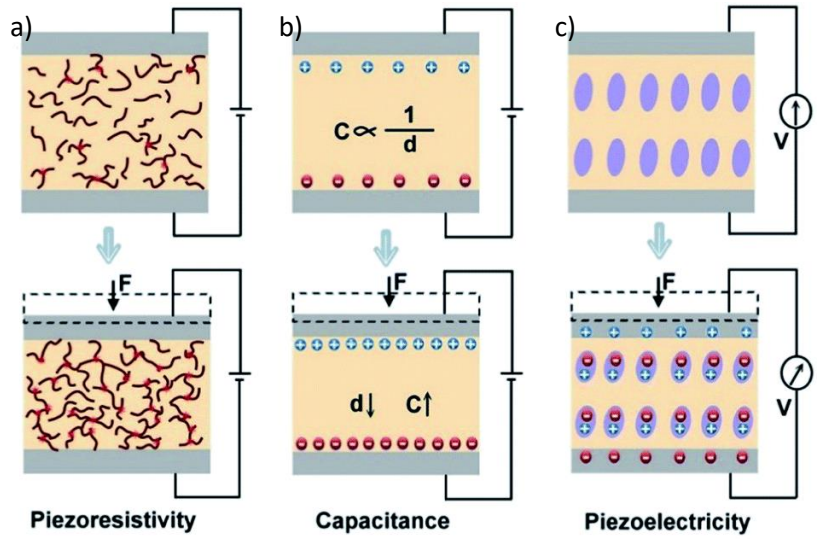

Figure 3-2. The major pressure sensing mechanism. a) piezoresistive pressure sensor; b) capacitive pressure sensor; c) piezoelectric pressure sensor. Reproduced from Ref.[14].

1) **Piezoresistive pressure sensor**, which can convert the pressure change information into resistance change, has been intensively reported due to the ease of fabrication, simple device structure and fast response speed. As shown in Figure 3-2a, under external pressure, either the resistance of active sensing material or the contact resistance between two conductive modules will change accordingly. The most widely used materials for piezoresistive pressure sensor are metal NPs (nanoparticles),[19, 20] PDMS (polydimethylsiloxane) /SWNTs,[12, 21, 22] (functional) graphene (composites),[23, 24] polypyrrole,[25] *etc.*

   A very simple yet effective piezoresistive pressure sensor has been reported by Suh and coworkers.[26] The highly flexible device is consisting of two interlocked arrays of high-aspect-ratio Pt-coated polymeric nanofibers and thin PDMS supporting layers (Figure 3-3). Under applied pressure, the degree of interconnection of the conductive nanofibers changes, in which the contact resistance decreases reversibly. When

pressure is released, the device recovers to its initial state and this process can be repeated over 10000 times.

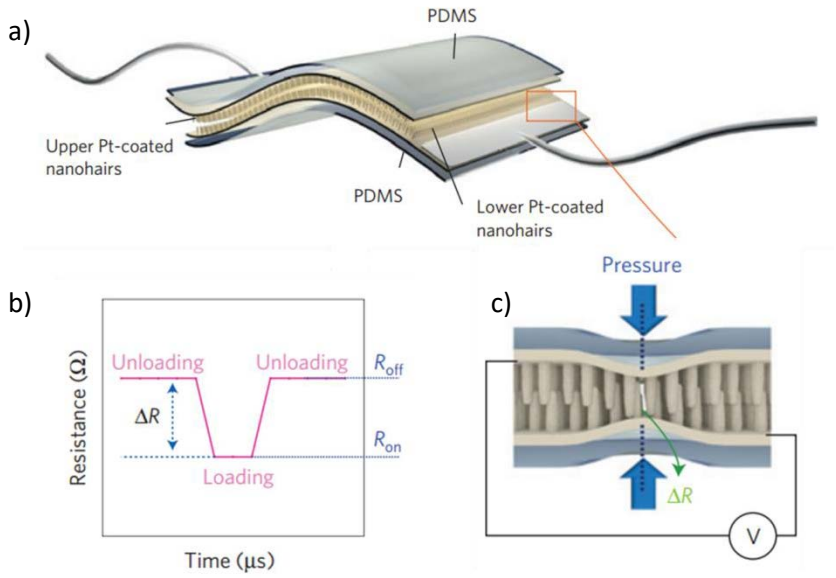

Figure 3-3. a) Schematic of the assembly and operation of a flexible sensor layer sandwiched between thin PDMS supports (~500 μm thickness each); b) Operation of a flexible sensor layer by means of recording of resistance change (R_{off}: unloading, R_{on}: loading); c) Schematic illustrations of the possible geometric distortion of the paired hairs under pressure. Reproduced from Ref.[26].

2) **Capacitive pressure sensing** is another important sensing mechanism which has been widely reported (Figure 3-2b). Capacitance refers the ability of storing electrical charge, the value of which is defined as the equation below:

$$C = \frac{\varepsilon_r \varepsilon_0 A}{d} \qquad (3-2)$$

where C is the capacitance, ε_r is the relative static permittivity of the material between the plates, ε_0 is the electric constant, A is the area of overlap of the two plates in square meters, and d is the separation distance between the plates in meters. In the design of capacitive pressure sensor, the separation distance between the plates has been mostly employed as the variable because it is easily affected by pressure. As shown in Figure 3-2b, the separation distance d decreases with applied pressure thus increasing the capacitance of the device under bias voltage. Most commonly used materials for capacitive pressure sensor are PDMS,[6, 17] polyimide (PI),[27] hydrogel

ionic conductive layer,[28] air-dielectric graphene transistor,[29, 30] AgNWs/polyurethane (PU) composite,[31] *etc.*

In 2010, a highly sensitive flexible pressure sensor with a microstructured rubber dielectric layer has been reported by Bao and coworkers.[17] Micrometer scale pyramid like structures have been duplicated on the dielectric layer by casting PDMS in the silicon mould with inverse features (Figure 3-4). This novel capacitor features microstructure dielectric layers has shown high sensitivity (0.55 kPa^{-1}) and much faster response time (millisecond timescale) compared to the one with unstructured dielectric layer.

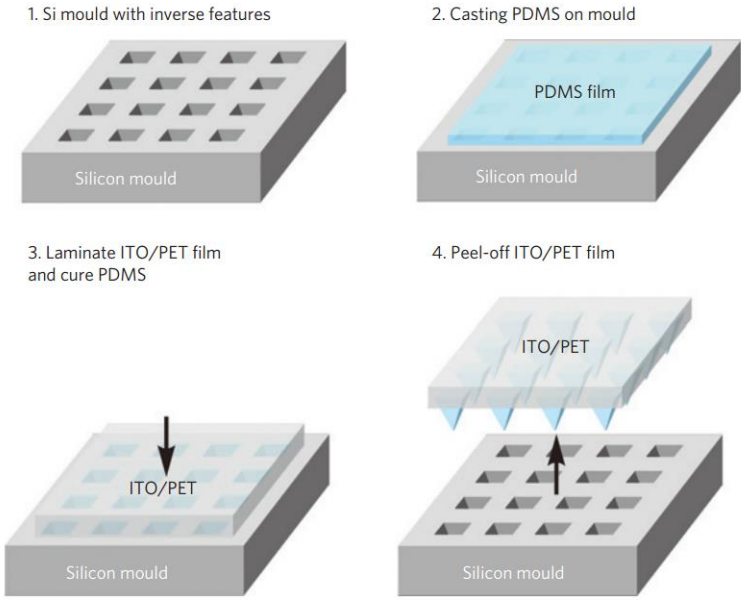

Figure 3-4. Schematic process for the fabrication of microstructured PDMS films. Reproduced from Ref.[17].

The change of capacitance is usually very small (~picofarads), so it is usually integrated into organic field-effect transistors (OFET) to amplify its sensing signal. A typical OFET structure consists of a semiconductor layer, a gate dielectric layer, source-drain electrodes, and a gate electrode. The dielectric layer sandwiched by semiconductor layer and the gate electrode can be seen as a capacitor in which the charge status is affected by external pressure. The subtle capacitance change will be amplified by the integration of capacitive pressure sensor with OFET.[32]

3) The third most commonly reported pressure sensing mechanism is **piezoelectric sensing**. Under applied mechanical stresses, certain inorganic materials like crystals,

ceramics or other piezoelectric polymers can generate electrical charge which is called piezoelectricity. The working principle of piezoelectric pressure sensors is based on the dipole moments generated under external pressure stimuli in the anisotropic crystalline materials (Figure 3-2c). This kind of sensing mechanism features a high sensitivity to dynamic pressure change, fast response, low power consumption while suffering from the poor stretchability, temperature sensitivity. Polyvinylidene fluoride or polyvinylidene difluoride (PVDF) nanofibers[33], ZnO nanoplatelets[34, 35] and other inorganic piezoelectric materials such as BaTiO3, $Pb[Zr_x,Ti_{1-x}]O_3$ (PZT)[36] have been widely used as active sensing materials for piezoelectric sensing.

In 2013, Rogers and coworkers[33] have reported a high performance piezoelectric devices based on aligned arrays of nanofibers of poly(vinylidenefluoride-co-trifluoroethylene) [P(VDF-TrFe)]. As shown in Figure 3-5, free standing films with highly aligned copolymer fibers have been acquired by electro spun process, in which the polymer chains adopt strongly preferential orientations. The obtained films are mechanically robust and respond to both compressive and bending forces. It shows high sensitivity even in the low-pressure region (0.1 Pa) by simply contact the ends of the aligned fibers. This method (electro spun) has provided an effective way to well align the polymer fibers as well as the main molecular chains along the fiber longitudinal axis, in which the active dipoles (C-F) have been aligned thus enhancing the piezoelectric properties of the film. This flexible, robust, and piezoelectric freestanding film is attractive for the fabrication of large area devices for human motion monitoring or robotics.

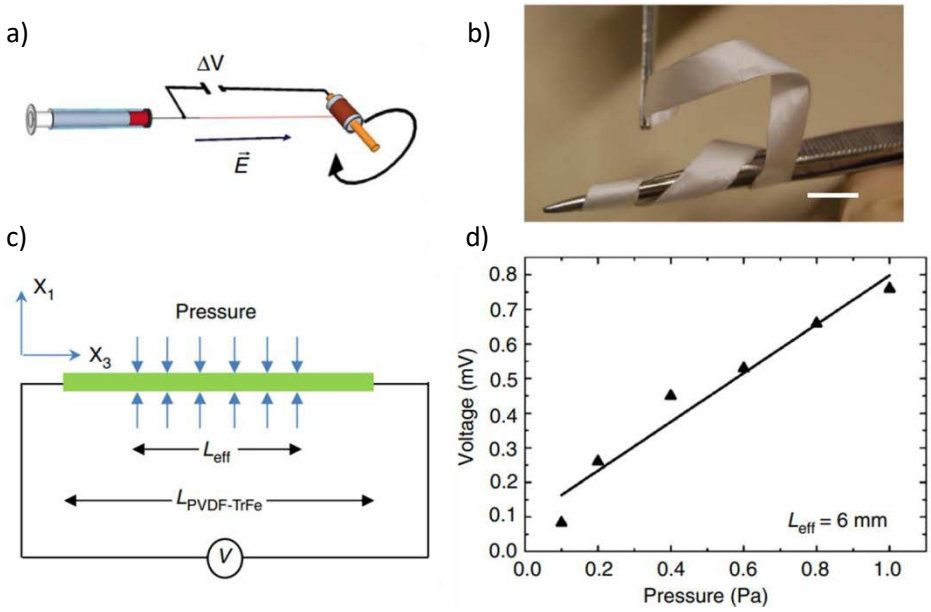

Figure 3-5. a) Schematic illustration of the experimental setup for electrospinning highly aligned arrays of oriented nanofibers of aligned polymer chains of poly(vinylidenefluoride-cotrifluoroethylene); b) Photograph of a free-standing film of highly aligned piezoelectric fibers. Scale bar, 1 cm; c) Schematic illustration of an analytical model for the response of arrays of P(VDF-TrFe) fibers under applied compression p along x_1 direction over the effective contact length (L_{eff}). LPVDF-TrFe is the total length of the P(VDF-TrFe) fiber array; d) Experimental (symbols) pressure response curve in the low-pressure regime (0.1–1 Pa) at L_{eff} = 6 mm. The line corresponds to a linear fit. Reproduced from Ref.[33].

4) Other transducing mechanisms such as **optical pressure sensing**[37-41] has also attracted great interests in the recent years due to their good flexibility, high electronic noise resistance *etc.* The intensity of the output optical power can be adjusted dynamically by the change of optical waveguide exerted by pressure. In 2018, Kim and coworkers[37] have reported a graphene based optical waveguide tactile sensor for dynamic response. As shown in Figure 3-6a, the graphene integrated waveguide platform was covered by a PDMS superstrate with straight prism-like microstructures. The working principle of this pressure sensor is based on the interaction of graphene and light. Upon vertical pressure to the PDMS superstrate, the lateral deformation area of graphene increases thus the graphene-light interaction increases as well. The output optical power at the end of the waveguide decreases with the increase of applied pressure, in which the relation between pressure and optical intensity has been formed as shown in Figure 3-6b. Meanwhile the output optical signal was accurately matched to the input pressure signal thus exhibiting a

real-time response to multi-stepped mechanical pressing and releasing stimuli. This graphene-based optical pressure sensor might attract great attention in the field of electronic skins, displays and other applications.

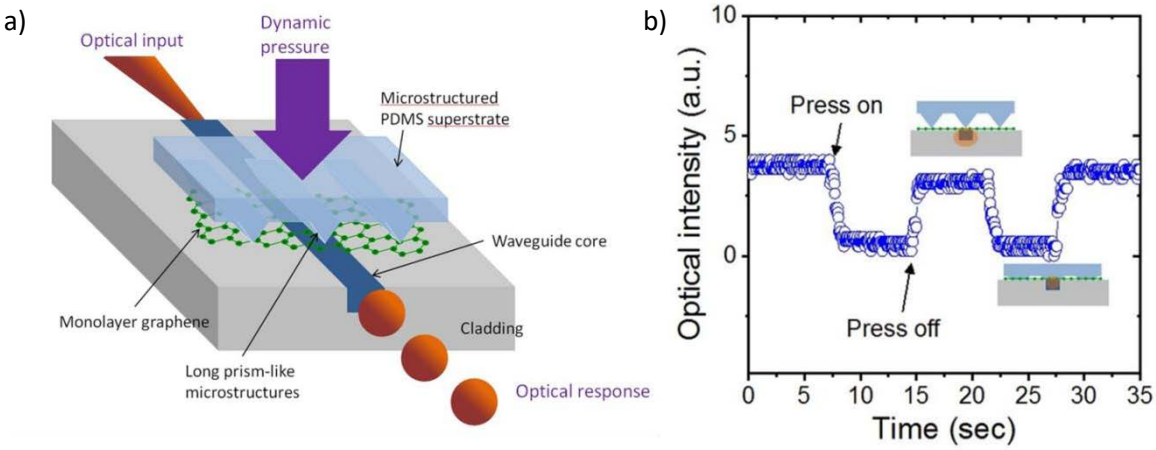

Figure 3-6. a) Bird's eye view of the graphene-based optical waveguide tactile sensor; b) Temporal behavior of the mechanical-to-optical transducer according to the dynamic mechanical force. Reproduced from Ref.[37].

3.2.2. Active materials for pressure sensing

The selection of suitable active sensing material is of crucial importance for designing new pressure sensors. All-aspects intrinsic properties of the selected materials like conductivity, dielectricity, porosity, flexibility and others have to be taken into consideration to fit different sensing mechanisms. Commonly used active materials in the fabrication of pressure sensors are discussed in this section according to their dimensionality (*i.e.* 0-3 dimensions). This classification method is helpful for constructing a clear framework of pressure sensing materials and it will inspire ideas of the fabrication and design of novel active material for pressure sensing.

Nanomaterials have received enormous attention by scientists due to their fascinating physical, chemical, and biological properties which might not be seen in the macroscale forms. By definition, nanomaterials refer to the materials with at least one dimension in the range of 1-100 nm. In this case, nanomaterials have been well summarized[42] in the table below:

Table 3-1. Dimensional classification of nanostructures

Dimensionality (D)	**Description**	**Examples**
Zero-dimensional (0D)	All dimensions in nanoscale	Nanoparticles, C_{60}, Quantum Dots
One-dimensional (1D)	One dimension not in nanoscale	Nanorods, Nanotubes, Carbon Fibers
Two-dimensional (2D)	Two dimensions not in nanoscale	Thin nanolayers, graphene
Three-dimensional (3D)	Three dimensions not in nanoscale	Nanocomposites

For pressure sensing materials, metal nanoparticles,[20] CNTs,[43, 44] carbon fibers,[45] graphene,[46-49] microstructured rubber,[17] conductive composites[50-52] *etc.* have been widely reported and nicely reviewed[14, 53-55] in recent years. In the following sections, typical and highly cited works will be discussed based on the dimensionality of active sensing materials.

3.2.2.1. 0D materials

0D materials usually consist of metal nanoparticles, quantum dots, C_{60}, *etc.* Among them, gold nanoparticles (AuNPs) have attracted large amount of attention due to its stability in air, the easiness to tune its size/shape/composition and characteristics. The size-related electronic, magnetic and optical properties, which are also known as quantum size effect, make it attractive in the applications of catalysis and biology. In 2016, Lee and coworkers[20] have reported a highly sensitive, transparent and durable pressure sensor based on sea-urchin shaped metal (gold and silver) nanoparticles (SSNPs) as shown in Figure 3-7a. The SSNPs and polyurethane composite, used as active sensing material, exhibited excellent pressure sensing performance with a high sensitivity of 2.46 kPa^{-1} and fast response/relaxation time of 30 ms. The high sensitivity of this piezoresistive pressure sensor is based on the quantum tunneling effect among the SSNPs. As shown in Figure 3-7b, the nanoparticles are separated from each other in the relax state and electrons are not prone to pass from one particle to adjacent ones. Conversely, under pressure the interparticle distance decreases enabling a more efficient quantum tunneling effect. By using ITO-PET as electrodes, the pressure sensor

showed outstanding optical transmittance (84.8% at 550 nm) and mechanical flexibility, which make it suitable for the detection of human motion.

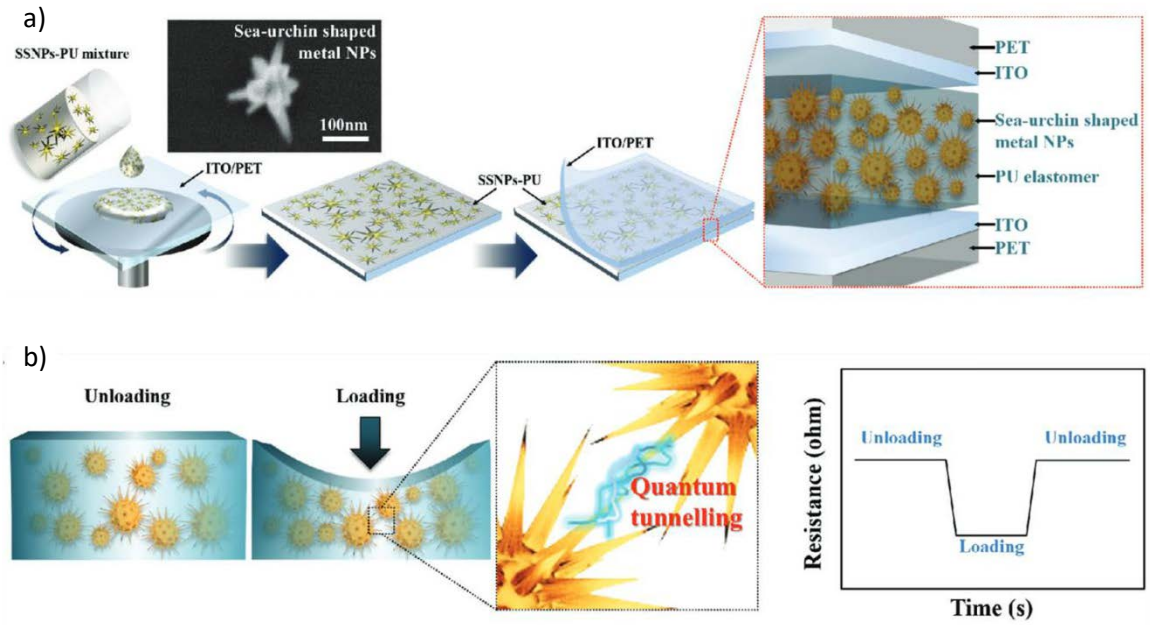

Figure 3-7. a) Schematic illustration for fabrication of a pressure sensor composed of SSNPs and PU. b) Schematic illustration for proposed sensing mechanism of the pressure sensor composed of SSNPs and PU. Reproduced from Ref.[20].

Metal NPs themselves can also serve as active materials in pressure sensing devices. In 2019, Han and co-workers[19] have reported a sensitive pressure sensor which consists of a piezoresistive strain transducer fabricated from closely spaced nanoparticle films deposited on a flexible membrane. Pd NPs were generated from a magnetron plasma gas aggregation cluster source and impacted on the substrate surface with a high kinetic energy which is high enough to create a reactive site that pins the nanoparticles to the polymer surface. These nanoparticles formed a discontinuous film in a disordered manner on the prepatterned interdigital electrodes on PET substrate. The percolation pathways that conduct electric current were deformation-dependent, in which the external pressure induces a change in the inter-particle spacing, enabling more conductive percolation pathways. This pressure sensor has demonstrated high resolution (~0.5 Pa), high sensitivity (0.13 kPa^{-1}) thus can be operated as a barometric altimeter with an altitude resolution of ~ 1m.

Mono-component 0D nanomaterial is typically combined with polymers or other higher dimensional materials like graphene *etc.*[13] to form composite materials in pressure sensing devices. Due to their tunable physical and chemical properties, 0D nanomaterials like nanoparticles play an important role as active materials in the field of pressure sensing.

3.2.2.2. 1D materials

Carbon nanotubes (CNTs) and nanowires (NWs) are the most commonly explored 1D materials for pressure sensing purposes. Usually CNTs serve as electrode materials for its superior conductivity and flexibility.[56] As active pressure sensing materials, CNTs are often integrated into polymer composite[22, 57] to increase the sensitivity and cycling ability. In 2014, Zhang and coworkers[44] have reported a silk-molded flexible, ultrasensitive, and highly stable electronic skin for monitoring human physiological signals. The microstructure of natural silk tissue is transferred to a PDMS film by casting the uncured polymer in the silk mold (Figure 3-8b-i). CNTs film is transferred on top of the structured PDMS film to form the conductive layer. As shown in Figure 3-8a, the pressure sensor was fabricated by face-to-face assembling two CNTs-PDMS substrates together and wiring out with silver paste. Meanwhile the pressure sensor has demonstrated high sensitivity (1.8 kPa^{-1}) in the low-pressure range (< 300 Pa) and very low detection limit (0.6 Pa). Combined with fast response time (< 10 ms) and excellent cycling stability (>67500 cycles), the pressure sensor can effectively detect the human physiological signals such as voice recognition and real time wrist pulse detection, which makes it a good candidate as e-skin.

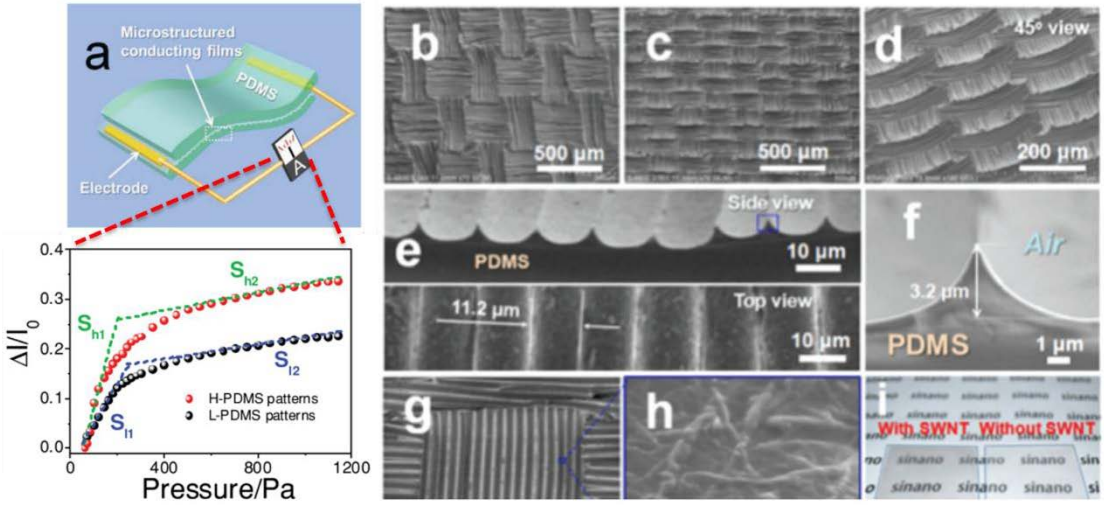

Figure 3-8. a) Schematic of a typical E-skin and sensitivities of pressure sensors constructed with H-PDMS and L-PDMS; b, c) SEM images of patterned L-PDMS and H-PDMS films, respectively; d–f) 45° view, top view, and side view of H-PDMS (c); f) High magnification SEM image from the box (e); g, h) The typical SEM images of patterned PDMS films covered with SWNTs ultrathin film at different magnifications; i) Photographs of patterned PDMS film with and without SWNT ultrathin film. Reproduced from Ref.[44].

Ultrathin metal nanowires featuring superior conductivity, robust and flexible mechanical properties, are novel building blocks for the fabrication of pressure sensor. In 2014, Cheng and co-workers[58] have reported a highly sensitive and flexible pressure sensor by sandwiching ultrathin gold nanowire-impregnated tissue paper between two thin PDMS sheets. More conductive pathways between AuNWs and finger electrodes were formed upon applied pressure, leading to an increasing of current. This piezoresistive pressure sensor has a high sensitivity (>1.14 kPa^{-1}), fast response time (<17 ms), high stability (>50000 loading cycles) and can be applied in the real-time blood pulses monitoring and the detection of small vibration from sound.

3.2.2.3. 2D materials

2D materials such as 2D flakes like graphene which can be obtained by vacuum filtration, CVD, chemical synthesis are the most widespread pressure sensing building blocks for all transduction mechanisms.[47, 59-62] Most 2D materials based sensor display negligible hysteresis, good linearity, and above-average sensitivity.[54] In 2017, Wu and coworkers[49] have reported an ultrafast dynamic pressure sensors based on graphene hybrid structure. As shown in Figure 3-9a, the GO/graphene composite film is obtained by vacuum filtration of graphene oxide and graphene mixture solution. In this case, the 2D graphene layers are the conductive element and GO is served as surfactant to prevent the restacking and aggregation of graphene in aqueous solution. The pressure sensor adopts a lateral structure, in which the planar film of GO/Graphene is placed on top of the electrodes surface as shown in Figure 3-9b. The working principle is based on the conductive graphene layers in the composite film being squeezed under pressure, in which more contacting points are created thus leading a decreasing of resistance. The pressure sensor has demonstrated good sensitivity (0.032 kPa^{-1}) in the low-pressure range (<1kPa) with a very low detection limit (~0.15 g) (Figure 3-9c). It also showed excellent cycling stability (>8000 cycles) and impressive response time which can detect the dynamic pressure signal as high as 10 kHz. This graphene based resistive pressure sensor can be applied in many fields including health monitoring or robotic arms.

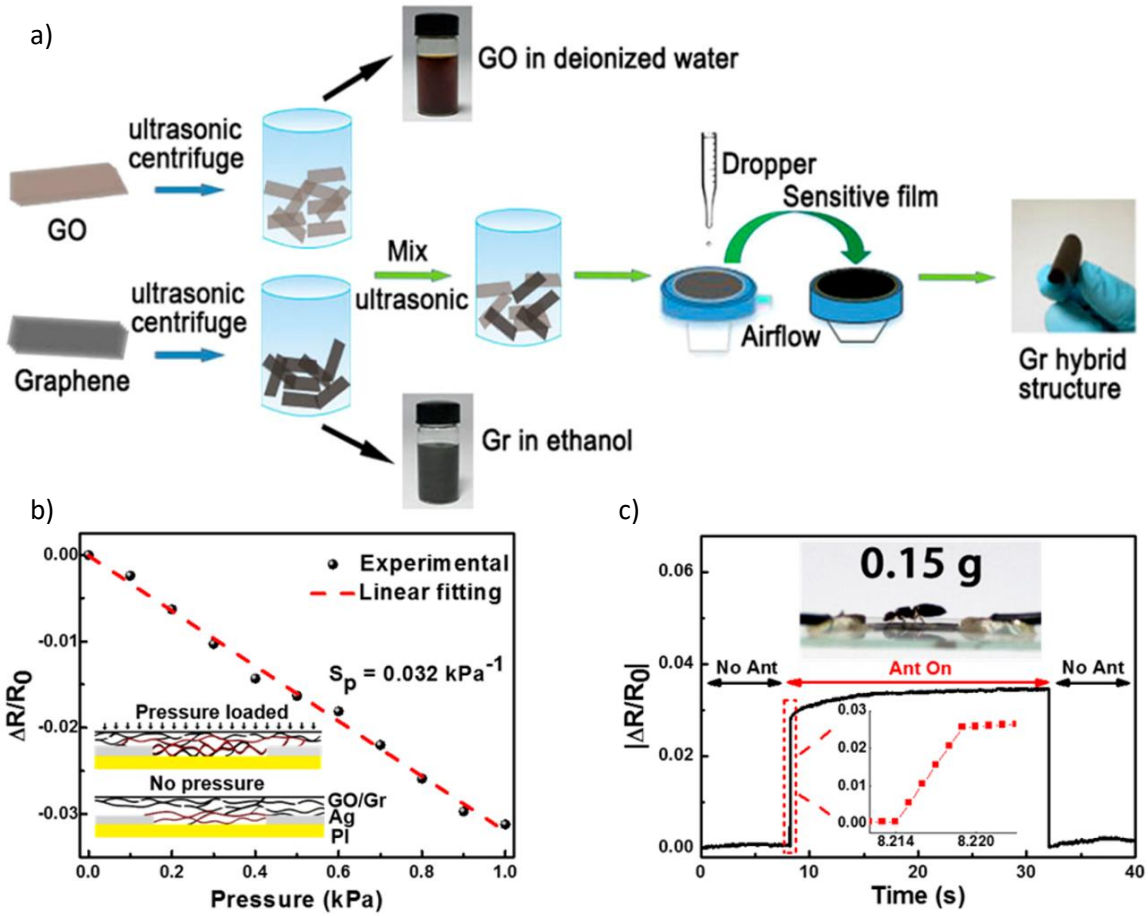

Figure 3-9. Schematics of the synthesis procedure of the GO/Graphene composite film. The as-prepared film is sufficiently flexible such that it can be bent easily without cracking; b) Resistive variation as a function of applied pressure. From 0 to 1000 Pa, the deformation changed linearly. Insets are the sketches of resistance changes of the film with and without pressure; c) Detecting the very slight pressure and subtle motions of an ant, which reflects the low detection limit of the GO/Graphene composite film and its fast response. Reproduced from Ref.[49].

3.2.2.4. 3D materials

3D porous structures, usually obtained by freeze drying, skeleton erosion, elastomer casting, represent another widely used pressure sensing materials. [23, 48, 63] The intrinsic porous and elastic structure makes is compressible under pressure, in which the electrical properties have changed to form the pressure-electrical signal relationship. Normally the 3D structures can be produced in a large quantity and be used in all the transduction mechanisms.[54] In 2013, Yu and coworkers[23] have reported a flexible and highly sensitive graphene-polyurethane sponge based pressure sensor with fractured microstructure design. The fabrication process has been shown in Figure 3-10 a-e. PU sponge was immersed into GO solution to have a coating of GO, after which the GO-PU sponge was reduced by immersing into hot hydrogen iodide (HI) solution to form a conductive rGO layer on the sponge backbone. The final fractured microctructured design, which has been shown in Figure 3-10 f-h, was achieved by the further hydrothermal treatment and compression (95% strain) for 2 hours. The intact adhesion of rGO on the PU microfibers has been demonstrated in the insets. As shown in Figure 3-10i, the working principle of the 3D framework is based on the pressure dependent resistance. Larger contact area of the fiber network was form under pressure and recovered while the pressure is released. This fractured structure can effectively improve the sensitivity (0.26 kPa^{-1}, 0-2 kPa) compared the RGO-PU sponge without fracture design (0.001 kPa^{-1}, 0-10 kPa). The pressure sensor also demonstrated good cycling stability (>10000 cycles) and large area fabrication, which make it promising in the field of e-skin applications.

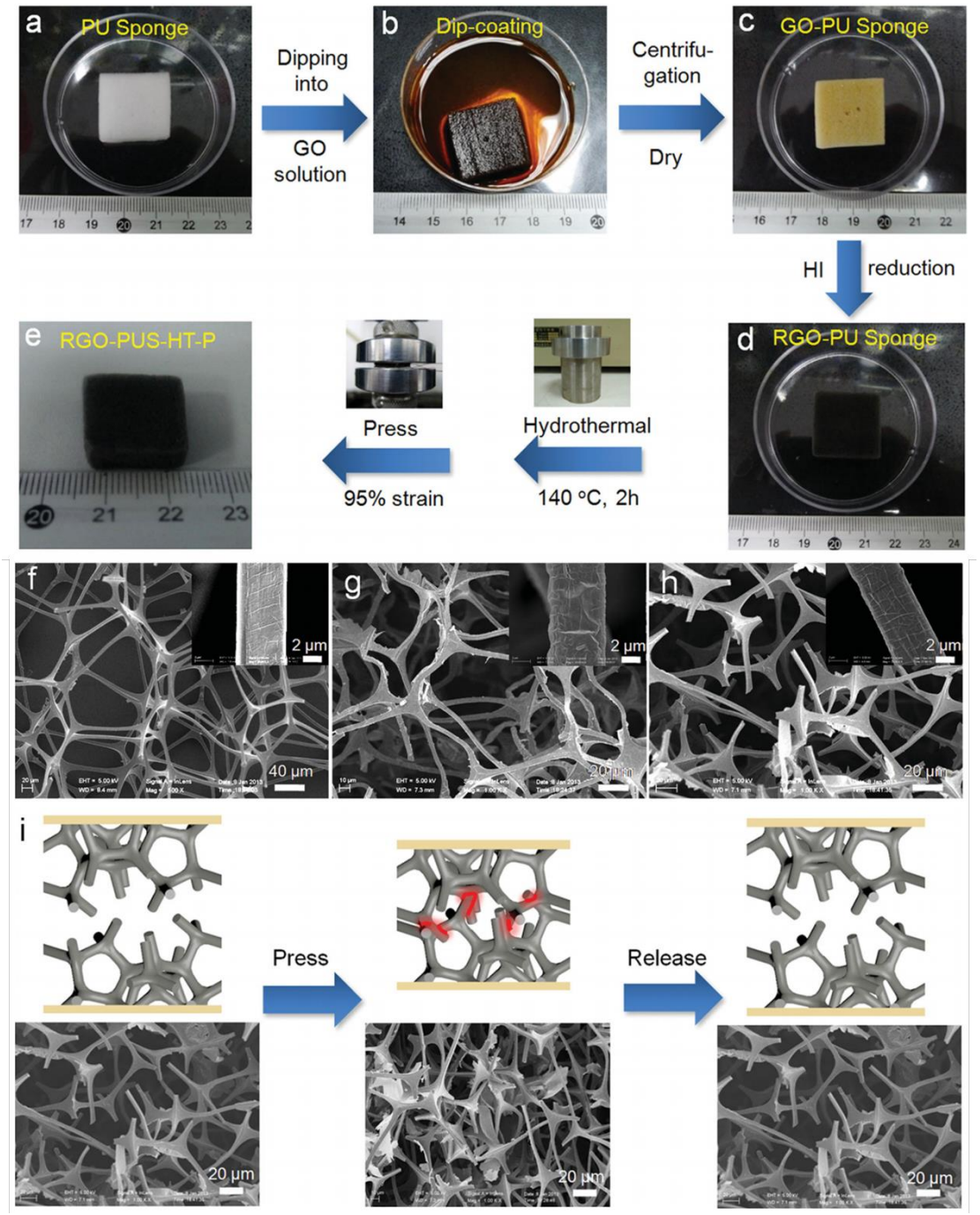

Figure 3-10. a–e) Schematic illustration of the fabrication procedure of fractured RGO–PU sponges; f–h) SEM images of the RGO–PU sponge, hydrothermally treated RGO–PU sponge (RGO–PU–HT), and the compressed treated RGO–PU–HT sponge (RGO–PU–HT–P); i) Pressure-sensing models of as-prepared RGO–PU–HT–P sponge pressure sensors, showing the contact area variation of fiber network with compressive deformation. Reproduced from Ref.[23].

3.3. Strain sensors

3.3.1. Fundamental aspects of strain sensor

3.3.1.1. Definition and key parameters

Strain, defined as extension per unit length (as shown in Figure 3-11), is another important physical parameter[64] describing the resistance of an object to deformation. It can be divided into compressive strain and tensile strain depending on if the applied forced triggering an increase or decrease of the object length compared to the original one. Usually compressive strain is defined as negative while tensile strain is defined as positive.[65-67]

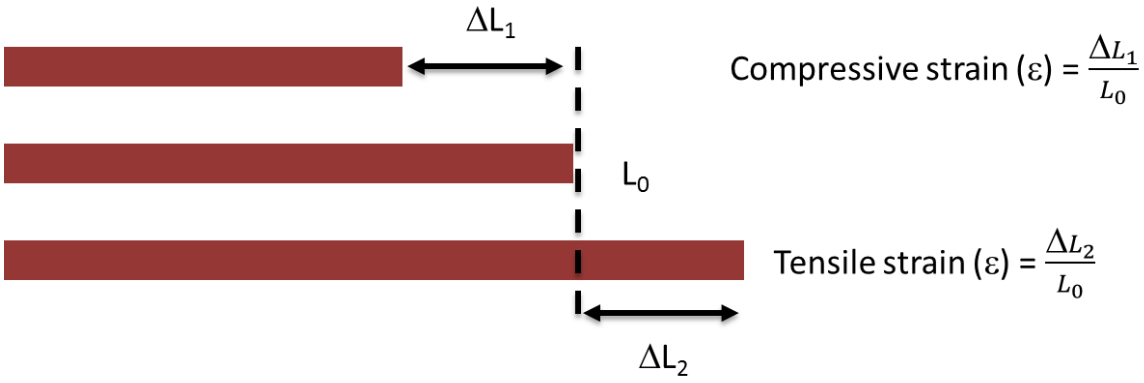

Figure 3-11. Illustration and definition of compressive strain and tensile strain.

Like pressure sensors, strain sensors are also widely used in health monitoring, human motion detection, human-machine interface *etc.* by utilizing flexible, stretchable, mechanically robust (composite) nanomaterials as sensing materials.[26, 68-71] Strain sensors and pressure sensors share the same key performance indicators for the evaluation of the sensing properties such as linearity, response time, detection range, cycling stability *etc.* except sensitivity, which essentially represents the effectiveness of the sensing device. Normally we use gauge factor (GF) instead of sensitivity as the major parameter to evaluate the strain sensor. The GF of strain sensor is the ratio of the relative resistance change ($\Delta R/R_0$) to the mechanical strain (ε), which is represented as follows:

$$GF = \left|\frac{\Delta R/R_0}{\varepsilon}\right| \qquad (3-3)$$

3.3.1.2. Sensing mechanisms

The sensing mechanisms of strain sensor can be mainly divided into 5 categories: geometrical effect, piezoresistive effect, disconnection mechanism, crack propagation and tunneling effect.[64] The working principle and differences of these sensing mechanisms will be discussed briefly in the following paragraphs.

1) **Geometrical effect** is the main working principle of piezoresistive and piezo capacitive strain sensor, in which the resistance or capacitance change due to the size changes caused by the strain. The resistance of a conductor is calculated as:

$$R = \frac{\rho L}{A} \qquad (3-4)$$

where ρ is the electrical resistivity, L is the length and A is the cross-sectional area. L increases and A decreases upon stretching which increases the resistance of the conductor. While for capacitor, the capacitance can be expressed as:

$$C = \varepsilon \frac{A}{d} \qquad (3-5)$$

where ε is the electric constant, A is the overlap area of the two plates and d is the separation distances. A increases and d decreases upon stretching which increases the capacitance of the capacitor.

2) **Piezoresistivity** refers to the resistance change (ΔR) of materials caused by structural deformations. The relative resistance change can be expressed as:

$$\frac{\Delta R}{R_0} = (1 + 2\upsilon)\varepsilon + \frac{\Delta\rho}{\rho_0} \qquad (3-6)$$

where υ is Poisson's ratio, $\Delta\rho/\rho_0$ is the relative change of electrical resistivity. In this equation, the former term is caused by geometrical change while the latter one means the piezoresistivity of the material. Piezoresistivity of metal materials could be increased of a few fold while some semiconductor materials like silicon can be increased by several orders of magnitudes.[72, 73] However, these semiconducting materials and other nanoscale materials like CNTs and zinc oxide nanowires (ZnONWs) featuring high piezoresistivity exhibit a very narrow strain sensing range. For this reason, composites of functional materials and stretchable polymers are commonly employed for strain sensing.[74, 75]

3) **Disconnection mechanism** is often employed in the conductive thin films made of nanomaterial network, in which electrons can travel through percolation pathways. Upon stretching the thin films, the percolation pathways get worsen yielding an increase in resistance. Nanowires networks[76-78] and graphene[79, 80] based thin films are widely exploited as stretchable and flexible strain sensors employing this detection mechanism.

4) **Crack propagation** is very similar to the disconnection mechanism. Conductive brittle thin film such as metal film,[81] CNT,[71] AuNWs,[82] AgNPs,[83] graphene[84, 85] are adsorbed onto stretchable substrates and (microscale) cracks are formed and spread upon stretching. As a result, the electrical conduction of the conductive film decreases due to the separation of conductive element. Noteworthy, the resistance usually decreases dramatically under strain thus leading a very high gauge factor of the strain sensor. As shown in Figure 3-12, cracks are generated and enlarged in the silver nanoparticle thin film under increasing strain,[83] thus increasing the electrical resistance of the film. Upon releasing the strain, the opened cracks of the film are gradually closed, and the resistance is decreased accordingly.

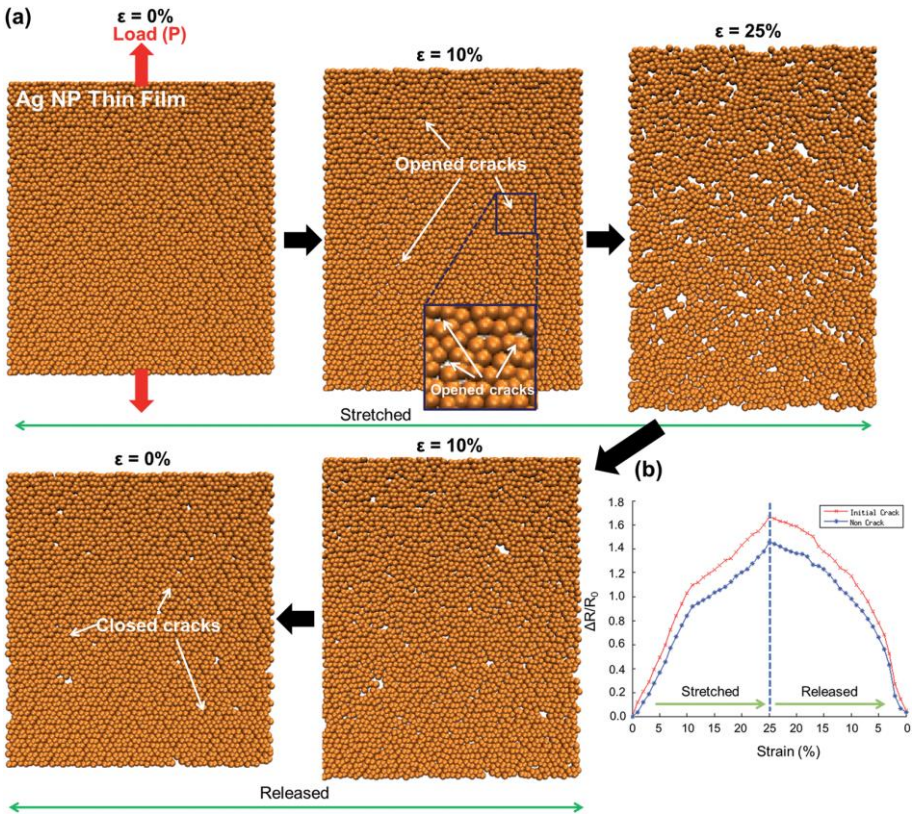

Figure 3-12. (a) Results of molecular dynamics based numerical simulation for the Ag NPs thin film under elongation/relaxation processes; during the elongation process by the external load, micro-cracks were opened and propagated at higher strains. During the relaxation process, opened micro-cracks become smaller and closed with decreasing strains; (b) relative change of electrical resistance of the Ag NP thin film with and without initial micro-cracks under the stretching/releasing process calculated by numerical simulation. Reproduced from Ref.[83].

5) **Tunneling effect** is different from the previously discussed mechanisms. Electrons can overcome a certain barrier between neighboring nanostructures yielding a tunneling current. The tunneling distance can be approximately calculated by Simmons's theory[86, 87] as follows:

$$R_{tunnel} = \frac{V}{AJ} = \frac{h^2 d}{Ae^2\sqrt{2m\lambda}} exp\left(\frac{4\pi d}{h}\sqrt{2m\lambda}\right) \qquad (3-7)$$

where V is the electrical potential difference, A is the cross sectional area of the tunneling junction, J is the tunneling current density, h is Plank's constant, d is the distance between adjacent nanomaterials, e is the single electron charge, m is the mass of electron, and λ is the height of energy barrier for polymers. For example, in the CNT-polymer composite materials,[88] electron can pass through very close

distance between CNTs (as shown in Figure 3-13), in which the tunneling current is affected by the inter nanotube distance modulated by strain.

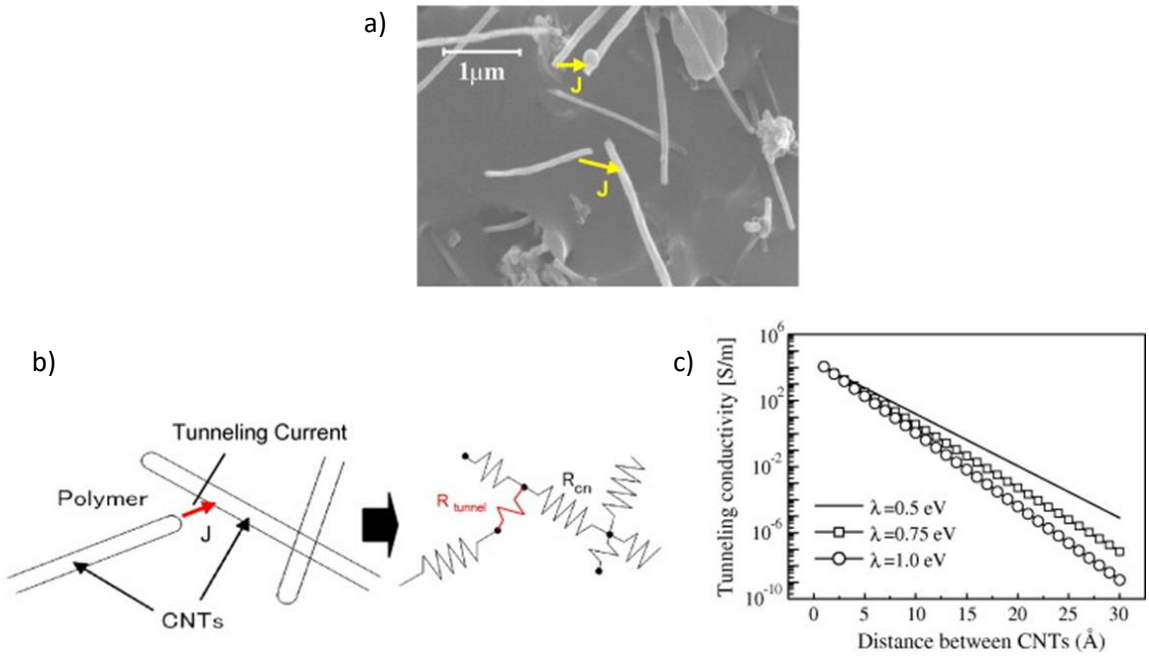

Figure 3-13. Modeling of tunneling effect in the resistor network: a) SEM image of possible tunneling effect among CNTs in the nanocomposites; b) modeling of tunneling resistance in the resistor network; and c) tunneling conductivity for various distances. Reproduced from Ref.[88].

3.3.2. Active materials for strain sensing

3.3.2.1. 0D materials

Nanoparticles are commonly used as sensing materials for resistive type strain sensors.[66, 83, 89, 90] In 2012, Ressier and co-workers[66] have reported a tris(2,4-dimethyl-5-sulfonatophenyl)phosphine (TDSP) coated gold nanoparticle based strain sensor fabricated by consecutive self-assembly. As shown in Figure 3-14a, gold nanoparticles have been assembled into the multilayered wire arrays on a flexible substrate. While bending the substrate, the distance between particles decreases (bending inward) or increases (bending outward). Ruled by the tunneling mechanism, the resistance of the strain sensor changes exponentially with the interparticle distance (Figure 3-14b). Interestingly, the authors claimed the gauge factor increases linearly with the nanoparticle size, which means the larger nanoparticle, the higher gauge factor (Figure 3-14c). The reason for this result is mainly due to the increasing interparticle distance in networks made with larger nanoparticles.

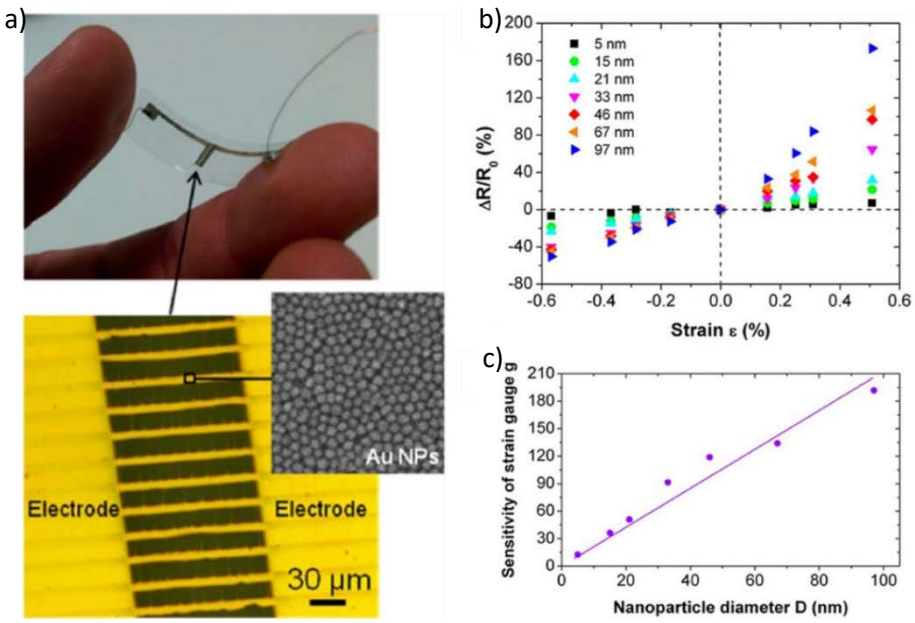

Figure 3-14. a) Photograph of a typical AuNPs-based strain gauge (top) and optical microscopy image of the active area consisting of a NP wire array between interdigitated gold electrodes (bottom). Inset in the bottom panel shows a scanning electron microscopy image of the assembled 15 nm gold colloidal NPs within the NP wires. b) Relative resistance variation as a function of strain for the strain gauges based on different sized gold NPs and c) plot showing the linear dependence of strain gauge sensitivity *g* with the diameter *D* of the gold NPs. Reproduced from Ref.[66].

3.3.2.2. 1D materials

Nanowires (or nanofibers)[26, 74, 76, 77, 91-93] and carbon nanotubes[43, 71, 94-96] are the most widely used materials for strain sensing because of the flexibility and stretchability to develop wearable devices. These 1D structures can be integrated into the strain sensing devices in different ways. Common fabrication methods of 1D strain sensing materials have been summarized as follows. Pt-coated polymer nanofibers[26] were placed in a reversible interlocking way, in which the resistance changes differently under the effect of pressure, shear, and torsion as shown in Figure 3-15a. The nanowires can also be integrated with polymer to form conductive composite,[93] in which the resistance will change with strain ruled by the tunneling effect as shown in Figure 3-15b. CNTs can be directly spray coated onto flexible substrate[43] as conductive electrodes to fabricate capacitive strain sensor as shown in Figure 3-15c, in which the separation distance *d* decreases under lateral strain thus increasing the capacitance. Another way to fabricate strain sensor is by using well-aligned CNTs as strain sensing materials,[71] in which the CNTs film fractures into gaps and islands with bundles bridging the gaps as shown in Figure 3-15d. This method has increased the sensing range effectively up to 280%, 50 times higher than conventional metal strain gauges.

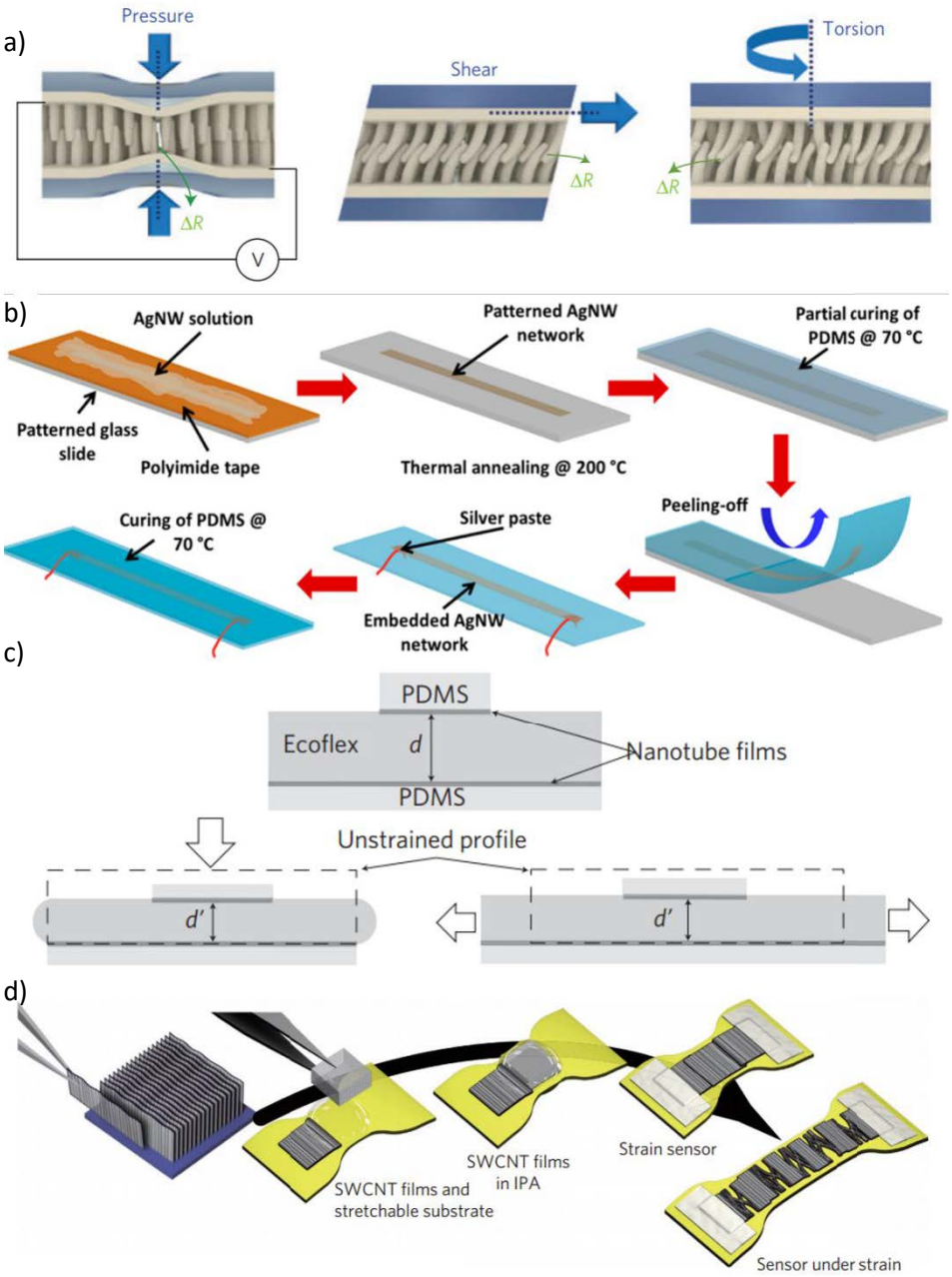

Figure 3-15. a) Schematic illustrations of the pressure, shear and torsion loads and their possible geometric distortions of the paired hairs. Reproduced from Ref.[26]. b) Fabrication processes of the sandwich structured PDMS/AgNW/PDMS nanocomposite strain sensor. Reproduced from Ref.[93]. c) Schematic showing a stretchable capacitor with transparent electrode (top), and the same capacitor after being placed under pressure (left) and being stretched (right). Reproduced from Ref.[43]. d) Key steps in fabricating the SWCNT strain sensor. Reproduced from Ref.[71].

3.3.2.3. 2D materials

Ultrathin metal films[81, 97] and graphene[98-100] represent the most commonly reported 2D materials based strain sensors. The metal film based strain sensors normally take advantage of crack propagation mechanism as shown in Figure 3-16a. Inspired by the geometry of spider's slit organ,[81] the nanoscale crack of the platinum film can detect very subtle strain change with a gauge factor over 2000 in the 1-2% strain range. In addition, graphene represents a major 2D strain sensing material for multiple applications. It can form reduced graphene oxide (rGO)-PDMS composite film (Figure 3-16b) serving as piezoresistive strain sensor possessing a high gauge factor over 630.[100] The graphene material itself can also be integrated into strain sensing devices[98, 99] due to its high electrical conductivity and flexibility (Figure 3-16c-d).

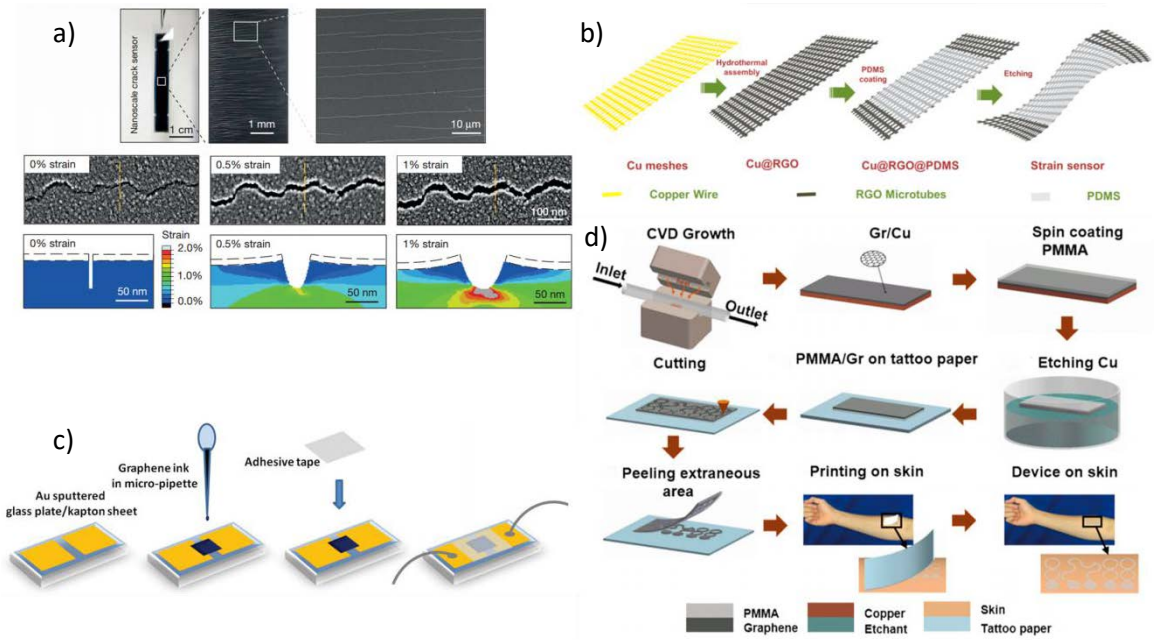

Figure 3-16. a) SEM images and finite-element method modelling of crack interfacial deformation under different strain. Reproduced from Ref.[81]. b) Fabrication steps of rGO microtubes−elastomer strain sensor. Reproduced from Ref.[100]. c) Fabrication process of a taped rGO strain/pressure sensor. Reproduced from Ref.[98]. d) Fabrication of graphene electronic tattoo. Reproduced from Ref.[99].

3.3.2.4. 3D materials

3D strain sensing materials normally refer the composite materials consisting conductive fillers (*e.g.* graphene, CNTs, *etc.*) and elastic frameworks.[79, 101] These polymer frameworks not only strengthen the flexibility and stretchability of the conductive fillers, but also improve the compressibility thus broaden the sensing region dramatically. In 2014, Coleman and coworkers[79] have reported a graphene-rubber composites based strain sensor which has a high gauge factor and the ability of detecting high frequency dynamic strain (Figure 3-17a). This cheap, lightweight, mechanically compliant strain sensor has been used as body motion detectors which can effectively monitor human motions such as joint and muscle motion, breathing and pulse. CNTs composites also play an important role of constructing strain sensing devices due to its high conductivity and flexibility. In 2017, Zhang and coworkers[101] have reported a CNTs- thermoplastic elastomer (TPE) based strain sensor which can detect stretching, bending as well as torsion sensitively. The resistance increases under stretching due to the disconnection of CNTs as shown in Figure 3-17b. The special gradient TPE structure not only renders the composite high sensitivity and fast response, but also hydrophobize the material surface, which make the CNT-TPE composite suitable for water-proof strain sensing coating materials.

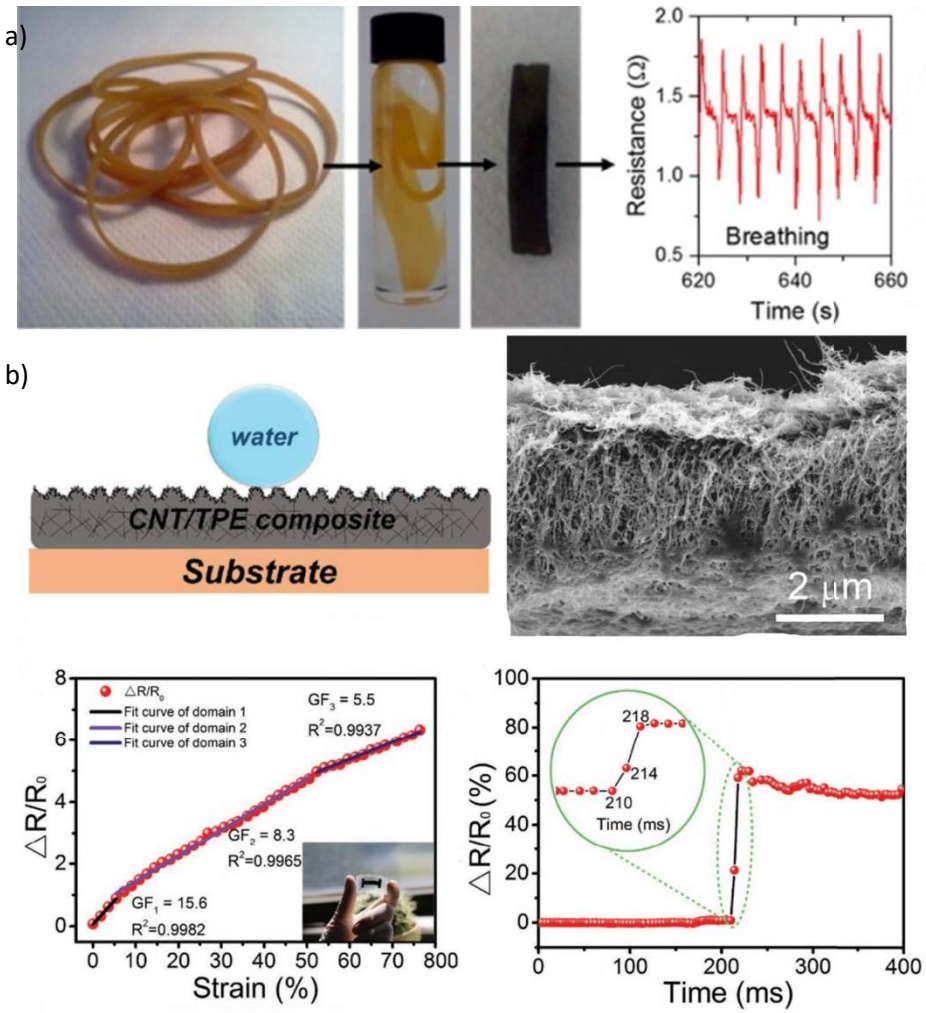

Figure 3-17. a) graphene-infused band preparation and the resistance change of slow breathing. Reproduced from Ref.[79]. b) (up) Schematic illustration and the SEM image of cross-sectional structure of the CNT-TPE composite structure. (bottom) Normalized relative resistance as a function of tensile strain and the time response of the sensor upon applying a quasi-transient step strain from ε = 0% to ε = 5%. Reproduced from Ref.[101].

3.4. Applications and Development

Both pressure sensors and strain sensors have very broad applications in health monitoring (*e.g.* heartbeat,[26, 84] artery pulse,[36, 60, 68] respiration,[58, 71] *etc.*), motion detection (by attaching on limbs,[91] joints,[61] fingers,[102] face,[84, 103] *etc.*), human-machine interface (*e.g.* robotics,[92] artificial limb, smart glove,[93, 104] virtual reality and interactive gaming,[105] *etc.*). Flexible and wearable pressure sensors and strain sensors for sure will be fully integrated into our daily electronic gadgets in the near future just as smart watch/band nowadays. Wearable personal health monitoring system has been widely believed as the key solution of next generation of health care technology. The sensing devices can continually sense, analysis, store, and transmit the health data of our body, providing accurate and long-term health evaluation. To achieve this goal, on-skin, light weight, non-invasive and wireless sensing devices will be the best option. The trend of personalized health monitoring will push forward the research, more importantly, commercial implementation of new materials-based sensing devices with high sensitivity, high flexibility, and high accuracy.

However, with such high expectation on the new materials (*e.g.* graphene, CNTs, nanowires, nanoparticles, *etc.*) based sensing devices for health monitoring and the endless effort of global research institutes and numerous start-ups, the dominant products in the market is still silicon-based MEMS devices. Insufficient accuracy and lack of long-term stability of these novel material based pressure/strain sensors are nowadays the main limitations. Normally the accuracy of commercial pressure sensors for industrial applications (*e.g.* LPS33W-STMicroelectronics™, MLH series-Honeywell™, *etc.*) should be controlled below ± (0.1-0.5%). While the accuracy of the novel materials based pressure sensors can easily reach over 5-10%, which is too large for any practical applications.

The reason for this is largely depends on the quality of the active sensing materials and the fabrication methods. If one considering graphene for an example, most of the superior properties such as high conductivity, high mechanical strength, and high thermal conductivity are depending on the crystal structure. But it is difficult to scale up the production while maintaining the high quality. For example, mechanical exfoliated graphene flakes possess perfect single-layer crystal structure yet the size of it is usually small. Solution exfoliation process (*e.g.* reduced graphene oxide *etc.*) can increase the yield effectively while defects are inevitable. CVD method produces the highest quality graphene, but it suffers high cost, low efficiency, and inevitable grain boundaries. Graphene is undoubtedly a great material regarding of all its superior properties, and tremendous efforts have been devoted in the last

15 years (as shown in Figure 3-18) to unravel and exploits its outstanding properties. After an 8-years hysteresis, graphene-based pressure sensors have been reported exponentially.

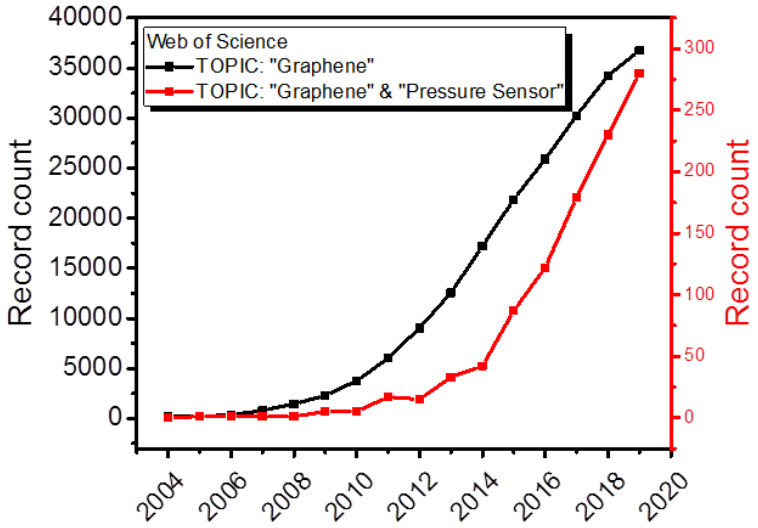

Figure 3-18. Web of Science record counts of published papers from 2004 to 2019 with the topic of "Graphene" and "Graphene & Pressure Sensor".

According to the hype cycle theory (Figure 3-19), it seems that the research of graphene has arrived the peak while apparently graphene-based pressure sensor is still on the rise. Even though the practical application has been largely affected before the emergence of production method which can produce graphene with perfect crystal structure in a large quantity yield, we still believe these new materials based sensing devices will pass through the "Disillusionment phase" and reach the "Slope of Enlightenment" to make a difference in our daily life.

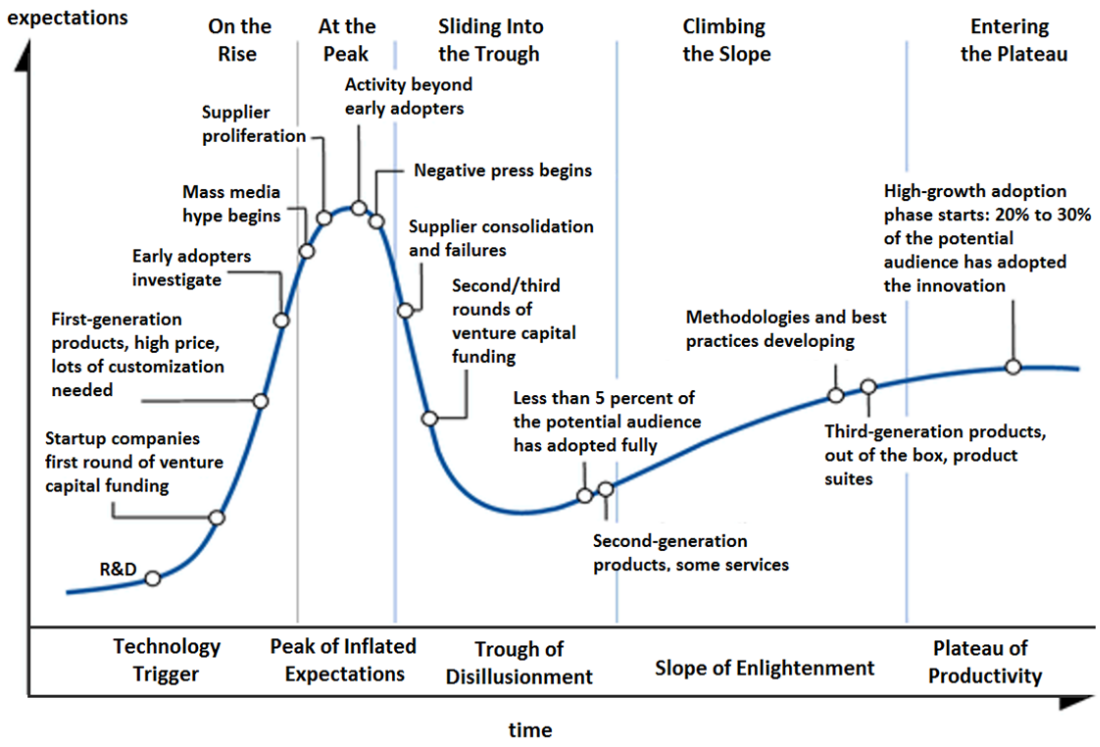

Figure 3-19. General hype cycle for technology. Free Copyright from https://commons.wikimedia.org/wiki/File:Hype-Cycle-General.png.

3.5. References

1. Kim, H. K.; Lee, S.; Yun, K. S., Capacitive tactile sensor array for touch screen application. *Sens. Actuator A Phys.* **2011,** *165*, 2-7.
2. Khan, U.; Kim, T.-H.; Ryu, H.; Seung, W.; Kim, S.-W., Graphene Tribotronics for Electronic Skin and Touch Screen Applications. *Adv. Mater.* **2017,** *29*, 1603544.
3. Hammock, M. L.; Chortos, A.; Tee, B. C. K.; Tok, J. B. H.; Bao, Z. N., 25th Anniversary Article: The Evolution of Electronic Skin (E-Skin): A Brief History, Design Considerations, and Recent Progress. *Adv. Mater.* **2013,** *25*, 5997-6037.
4. Wang, C.; Hwang, D.; Yu, Z.; Takei, K.; Park, J.; Chen, T.; Ma, B.; Javey, A., User-interactive electronic skin for instantaneous pressure visualization. *Nat. Mater.* **2013,** *12*, 899-904.
5. Lou, Z.; Chen, S.; Wang, L.; Jiang, K.; Shen, G., An ultra-sensitive and rapid response speed graphene pressure sensors for electronic skin and health monitoring. *Nano Energy* **2016,** *23*, 7-14.
6. Schwartz, G.; Tee, B. C. K.; Mei, J.; Appleton, A. L.; Kim, D. H.; Wang, H.; Bao, Z., Flexible polymer transistors with high pressure sensitivity for application in electronic skin and health monitoring. *Nat. Commun.* **2013,** *4*, 1859.
7. Chen, L. Y.; Tee, B. C. K.; Chortos, A. L.; Schwartz, G.; Tse, V.; J. Lipomi, D.; Wong, H. S. P.; McConnell, M. V.; Bao, Z., Continuous wireless pressure monitoring and mapping with ultra-small passive sensors for health monitoring and critical care. *Nat. Commun.* **2014,** *5*, 5028.
8. Gao, Y.; Ota, H.; Schaler, E. W.; Chen, K.; Zhao, A.; Gao, W.; Fahad, H. M.; Leng, Y.; Zheng, A.; Xiong, F.; Zhang, C.; Tai, L.-C.; Zhao, P.; Fearing, R. S.; Javey, A., Wearable Microfluidic Diaphragm Pressure Sensor for Health and Tactile Touch Monitoring. *Adv. Mater.* **2017,** *29*, 1701985.
9. Yao, S. S.; Zhu, Y., Wearable multifunctional sensors using printed stretchable conductors made of silver nanowires. *Nanoscale* **2014,** *6*, 2345-2352.
10. Bingger, P.; Zens, M.; Woias, P., Highly flexible capacitive strain gauge for continuous long-term blood pressure monitoring. *Biomed. Microdevices.* **2012,** *14*, 573-581.
11. Lou, Z.; Li, L.; Wang, L. L.; Shen, G. Z., Recent Progress of Self-Powered Sensing Systems for Wearable Electronics. *Small* **2017,** *13*.
12. Wang, X.; Gu, Y.; Xiong, Z.; Cui, Z.; Zhang, T., Silk-Molded Flexible, Ultrasensitive, and Highly Stable Electronic Skin for Monitoring Human Physiological Signals. *Adv. Mater.* **2014,** *26*, 1336-1342.
13. Luo, Z. W.; Hu, X. T.; Tian, X. Y.; Luo, C.; Xu, H. J.; Li, Q. L.; Li, Q. H.; Zhang, J.; Qiao, F.; Wu, X.; Borisenko, V. E.; Chu, J. H., Structure-Property Relationships in Graphene-Based Strain and Pressure Sensors for Potential Artificial Intelligence Applications. *Sensors* **2019,** *19*.
14. Zang, Y.; Zhang, F.; Di, C.-A.; Zhu, D., Advances of flexible pressure sensors toward artificial intelligence and health care applications. *Mater. Horiz.* **2015,** *2*, 140-156.
15. Li, J.; Bao, R. R.; Tao, J.; Peng, Y. Y.; Pan, C. F., Recent progress in flexible pressure sensor arrays: from design to applications. *J. Mater. Chem. C* **2018,** *6*, 11878-11892.
16. Almassri, A. M.; Hasan, W. Z. W.; Ahmad, S. A.; Ishak, A. J.; Ghazali, A. M.; Talib, D. N.; Wada, C., Pressure Sensor: State of the Art, Design, and Application for Robotic Hand. *J. Sens.* **2015,** *2015*, 846487.
17. Mannsfeld, S. C. B.; Tee, B. C. K.; Stoltenberg, R. M.; Chen, C. V. H. H.; Barman, S.; Muir, B. V. O.; Sokolov, A. N.; Reese, C.; Bao, Z., Highly sensitive flexible pressure sensors with microstructured rubber dielectric layers. *Nat. Mater.* **2010,** *9*, 859-864.
18. Graz, I.; Kaltenbrunner, M.; Keplinger, C.; Schwödiauer, R.; Bauer, S.; Lacour, S. P.; Wagner, S., Flexible ferroelectret field-effect transistor for large-area sensor skins and microphones. *Appl. Phys. Lett.* **2006,** *89*, 073501.

19. Chen, M. R.; Luo, W. F.; Xu, Z. Q.; Zhang, X. P.; Xie, B.; Wang, G. H.; Han, M., An ultrahigh resolution pressure sensor based on percolative metal nanoparticle arrays. *Nat. Commun.* **2019,** *10*.
20. Lee, D.; Lee, H.; Jeong, Y.; Ahn, Y.; Nam, G.; Lee, Y., Highly Sensitive, Transparent, and Durable Pressure Sensors Based on Sea-Urchin Shaped Metal Nanoparticles. *Adv. Mater.* **2016,** *28*, 9364-9369.
21. Chou, H. H.; Nguyen, A.; Chortos, A.; To, J. W. F.; Lu, C.; Mei, J. G.; Kurosawa, T.; Bae, W. G.; Tok, J. B. H.; Bao, Z. A., A chameleon-inspired stretchable electronic skin with interactive colour changing controlled by tactile sensing. *Nat. Commun.* **2015,** *6*.
22. Park, J.; Lee, Y.; Hong, J.; Ha, M.; Jung, Y. D.; Lim, H.; Kim, S. Y.; Ko, H., Giant Tunneling Piezoresistance of Composite Elastomers with Interlocked Microdome Arrays for Ultrasensitive and Multimodal Electronic Skins. *ACS Nano* **2014,** *8*, 4689-4697.
23. Yao, H. B.; Ge, J.; Wang, C. F.; Wang, X.; Hu, W.; Zheng, Z. J.; Ni, Y.; Yu, S. H., A Flexible and Highly Pressure-Sensitive Graphene-Polyurethane Sponge Based on Fractured Microstructure Design. *Adv. Mater.* **2013,** *25*, 6692-6698.
24. Chen, W. J.; Gui, X. C.; Liang, B. H.; Yang, R. L.; Zheng, Y. J.; Zhao, C. C.; Li, X. M.; Zhu, H.; Tang, Z. K., Structural Engineering for High Sensitivity, Ultrathin Pressure Sensors Based on Wrinkled Graphene and Anodic Aluminum Oxide Membrane. *ACS Appl. Mater.* **2017,** *9*, 24111-24117.
25. Pan, L.; Chortos, A.; Yu, G.; Wang, Y.; Isaacson, S.; Allen, R.; Shi, Y.; Dauskardt, R.; Bao, Z., An ultra-sensitive resistive pressure sensor based on hollow-sphere microstructure induced elasticity in conducting polymer film. *Nat. Commun.* **2014,** *5*, 3002.
26. Pang, C.; Lee, G.-Y.; Kim, T.-i.; Kim, S. M.; Kim, H. N.; Ahn, S.-H.; Suh, K.-Y., A flexible and highly sensitive strain-gauge sensor using reversible interlocking of nanofibres. *Nat. Mater.* **2012,** *11*, 795-801.
27. Huang, X.; Liu, Y. H.; Cheng, H. Y.; Shin, W. J.; Fan, J. A.; Liu, Z. J.; Lu, C. J.; Kong, G. W.; Chen, K.; Patnaik, D.; Lee, S. H.; Hage-Ali, S.; Huang, Y. G.; Rogers, J. A., Materials and Designs for Wireless Epidermal Sensors of Hydration and Strain. *Adv. Funct. Mater.* **2014,** *24*, 3846-3854.
28. Lei, Z. Y.; Wang, Q. K.; Sun, S. T.; Zhu, W. C.; Wu, P. Y., A Bioinspired Mineral Hydrogel as a Self-Healable, Mechanically Adaptable Ionic Skin for Highly Sensitive Pressure Sensing. *Adv. Mater.* **2017,** *29*.
29. Shin, S. H.; Ji, S.; Choi, S.; Pyo, K. H.; An, B. W.; Park, J.; Kim, J.; Kim, J. Y.; Lee, K. S.; Kwon, S. Y.; Heo, J.; Park, B. G.; Park, J. U., Integrated arrays of air-dielectric graphene transistors as transparent active-matrix pressure sensors for wide pressure ranges. *Nat. Commun.* **2017,** *8*.
30. Zang, Y.; Zhang, F.; Huang, D.; Gao, X.; Di, C.-a.; Zhu, D., Flexible suspended gate organic thin-film transistors for ultra-sensitive pressure detection. *Nat. Commun.* **2015,** *6*, 6269.
31. Hu, W. L.; Niu, X. F.; Zhao, R.; Pei, Q. B., Elastomeric transparent capacitive sensors based on an interpenetrating composite of silver nanowires and polyurethane. *Appl. Phys. Lett.* **2013,** *102*.
32. Kang, B. S.; Kim, J.; Jang, S.; Ren, F.; Johnson, J. W.; Therrien, R. J.; Rajagopal, P.; Roberts, J. C.; Piner, E. L.; Linthicum, K. J.; Chu, S. N. G.; Baik, K.; Gila, B. P.; Abernathy, C. R.; Pearton, S. J., Capacitance pressure sensor based on GaN high-electron-mobility transistor-on-Si membrane. *Appl. Phys. Lett.* **2005,** *86*, 253502.
33. Persano, L.; Dagdeviren, C.; Su, Y.; Zhang, Y.; Girardo, S.; Pisignano, D.; Huang, Y.; Rogers, J. A., High performance piezoelectric devices based on aligned arrays of nanofibers of poly(vinylidenefluoride-co-trifluoroethylene). *Nat. Commun.* **2013,** *4*, 1633.

34. Liu, S.; Wang, L.; Feng, X.; Wang, Z.; Xu, Q.; Bai, S.; Qin, Y.; Wang, Z. L., Ultrasensitive 2D ZnO Piezotronic Transistor Array for High Resolution Tactile Imaging. *Adv. Mater.* **2017,** *29*, 1606346.
35. Wang, L.; Liu, S.; Feng, X.; Xu, Q.; Bai, S.; Zhu, L.; Chen, L.; Qin, Y.; Wang, Z. L., Ultrasensitive Vertical Piezotronic Transistor Based on ZnO Twin Nanoplatelet. *ACS Nano* **2017,** *11*, 4859-4865.
36. Park, D. Y.; Joe, D. J.; Kim, D. H.; Park, H.; Han, J. H.; Jeong, C. K.; Park, H.; Park, J. G.; Joung, B.; Lee, K. J., Self-Powered Real-Time Arterial Pulse Monitoring Using Ultrathin Epidermal Piezoelectric Sensors. *Adv. Mater.* **2017,** *29*.
37. Kim, J. T.; Choi, H.; Shin, E.; Park, S.; Kim, I. G., Graphene-based optical waveguide tactile sensor for dynamic response. *Sci. Rep.* **2018,** *8*.
38. Dai, X. L.; Mihailov, S. J.; Blanchetiere, C., Optical evanescent field waveguide Bragg grating pressure sensor. *Opt. Eng.* **2010,** *49*.
39. Poeggel, S.; Tosi, D.; Duraibabu, D.; Leen, G.; McGrath, D.; Lewis, E., Optical Fibre Pressure Sensors in Medical Applications. *Sensors* **2015,** *15*, 17115-17148.
40. Rothmaier, M.; Luong, M. P.; Clemens, F., Textile pressure sensor made of flexible plastic optical fibers. *Sensors* **2008,** *8*, 4318-4329.
41. Ramuz, M.; Tee, B. C. K.; Tok, J. B. H.; Bao, Z. N., Transparent, Optical, Pressure-Sensitive Artificial Skin for Large-Area Stretchable Electronics. *Adv. Mater.* **2012,** *24*, 3223-3227.
42. Jamdagni, P.; Sidhu, P.; Khatri, P.; Nehra, K.; Rana, J. S., Metallic Nanoparticles: Potential Antimicrobial and Therapeutic Agents. 2018; pp 143-160.
43. Lipomi, D. J.; Vosgueritchian, M.; Tee, B. C. K.; Hellstrom, S. L.; Lee, J. A.; Fox, C. H.; Bao, Z., Skin-like pressure and strain sensors based on transparent elastic films of carbon nanotubes. *Nat. Nanotechnol.* **2011,** *6*, 788-792.
44. Wang, X. W.; Gu, Y.; Xiong, Z. P.; Cui, Z.; Zhang, T., Silk-Molded Flexible, Ultrasensitive, and Highly Stable Electronic Skin for Monitoring Human Physiological Signals. *Adv. Mater.* **2014,** *26*, 1336-1342.
45. Han, Z. Y.; Cheng, Z. Q.; Chen, Y.; Li, B.; Liang, Z. W.; Li, H. F.; Ma, Y. J.; Feng, X., Fabrication of highly pressure-sensitive, hydrophobic, and flexible 3D carbon nanofiber networks by electrospinning for human physiological signal monitoring. *Nanoscale* **2019,** *11*, 5942-5950.
46. Yao, H.-B.; Ge, J.; Wang, C.-F.; Wang, X.; Hu, W.; Zheng, Z.-J.; Ni, Y.; Yu, S.-H., A Flexible and Highly Pressure-Sensitive Graphene–Polyurethane Sponge Based on Fractured Microstructure Design. *Adv. Mater.* **2013,** *25*, 6692-6698.
47. Wei, Y. H.; Qiao, Y. C.; Jiang, G. Y.; Wang, Y. F.; Wang, F. W.; Li, M. R.; Zhao, Y. F.; Tian, Y.; Gou, G. Y.; Tan, S. Y.; Tian, H.; Yang, Y.; Ren, T. L., A Wearable Skinlike Ultra-Sensitive Artificial Graphene Throat. *ACS Nano* **2019,** *13*, 8639-8647.
48. Zhu, B.; Niu, Z.; Wang, H.; Leow, W. R.; Wang, H.; Li, Y.; Zheng, L.; Wei, J.; Huo, F.; Chen, X., Microstructured Graphene Arrays for Highly Sensitive Flexible Tactile Sensors. *Small* **2014,** *10*, 3625-3631.
49. Liu, S.; Wu, X.; Zhang, D.; Guo, C.; Wang, P.; Hu, W.; Li, X.; Zhou, X.; Xu, H.; Luo, C.; Zhang, J.; Chu, J., Ultrafast Dynamic Pressure Sensors Based on Graphene Hybrid Structure. *ACS Appl. Mater.* **2017,** *9*, 24148-24154.
50. Park, J.; Lee, Y.; Hong, J.; Ha, M.; Jung, Y.-D.; Lim, H.; Kim, S. Y.; Ko, H., Giant Tunneling Piezoresistance of Composite Elastomers with Interlocked Microdome Arrays for Ultrasensitive and Multimodal Electronic Skins. *ACS Nano* **2014,** *8*, 4689-4697.
51. Shao, Q.; Niu, Z.; Hirtz, M.; Jiang, L.; Liu, Y.; Wang, Z.; Chen, X., High-Performance and Tailorable Pressure Sensor Based on Ultrathin Conductive Polymer Film. *Small* **2014,** *10*, 1466-1472.

52. Roh, E.; Lee, H.-B.; Kim, D.-I.; Lee, N.-E., A Solution-Processable, Omnidirectionally Stretchable, and High-Pressure-Sensitive Piezoresistive Device. *Adv. Mater.* **2017,** *29*, 1703004.
53. Almassri, A. M.; Wan Hasan, W. Z.; Ahmad, S. A.; Ishak, A. J.; Ghazali, A. M.; Talib, D. N.; Wada, C., Pressure Sensor: State of the Art, Design, and Application for Robotic Hand. *J. Sens.* **2015,** *2015*, 12.
54. Luo, Z.; Hu, X.; Tian, X.; Luo, C.; Xu, H.; Li, Q.; Li, Q.; Zhang, J.; Qiao, F.; Wu, X.; Borisenko, V. E.; Chu, J., Structure-Property Relationships in Graphene-Based Strain and Pressure Sensors for Potential Artificial Intelligence Applications. *Sensors* **2019,** *19*, 1250.
55. Li, J.; Bao, R.; Tao, J.; Peng, Y.; Pan, C., Recent progress in flexible pressure sensor arrays: from design to applications. *J. Mater. Chem. C* **2018,** *6*, 11878-11892.
56. Kim, S. H.; Song, W.; Jung, M. W.; Kang, M.-A.; Kim, K.; Chang, S.-J.; Lee, S. S.; Lim, J.; Hwang, J.; Myung, S.; An, K.-S., Carbon Nanotube and Graphene Hybrid Thin Film for Transparent Electrodes and Field Effect Transistors. *Adv. Mater.* **2014,** *26*, 4247-4252.
57. Li, J.; Orrego, S.; Pan, J.; He, P.; Kang, S. H., Ultrasensitive, flexible, and low-cost nanoporous piezoresistive composites for tactile pressure sensing. *Nanoscale* **2019,** *11*, 2779-2786.
58. Gong, S.; Schwalb, W.; Wang, Y.; Chen, Y.; Tang, Y.; Si, J.; Shirinzadeh, B.; Cheng, W., A wearable and highly sensitive pressure sensor with ultrathin gold nanowires. *Nat. Commun.* **2014,** *5*, 3132.
59. Amirhosseini, S. A.; Safian, R., Graphene-based optical photodetector exploiting hybrid plasmonic waveguide to enhance photo-thermoelectric current. *J. Phys. D Appl. Phys.* **2017,** *50*.
60. Huang, C.-B.; Witomska, S.; Aliprandi, A.; Stoeckel, M. A.; Bonini, M.; Ciesielski, A.; Samorì, P., Molecule-Graphene Hybrid Materials with Tunable Mechanoresponse: Highly Sensitive Pressure Sensors for Health Monitoring. *Adv. Mater.* **2019,** *31*, 1804600.
61. Tao, L. Q.; Zhang, K. N.; Tian, H.; Liu, Y.; Wang, D. Y.; Chen, Y. Q.; Yang, Y.; Ren, T. L., Graphene-Paper Pressure Sensor for Detecting Human Motions. *ACS Nano* **2017,** *11*, 8790-8795.
62. Ren, H.; Zheng, L.; Wang, G.; Gao, X.; Tan, Z.; Shan, J.; Cui, L.; Li, K.; Jian, M.; Zhu, L.; Zhang, Y.; Peng, H.; Wei, D.; Liu, Z., Transfer-Medium-Free Nanofiber-Reinforced Graphene Film and Applications in Wearable Transparent Pressure Sensors. *ACS Nano* **2019,** *13*, 5541-5548.
63. Luo, N.; Huang, Y.; Liu, J.; Chen, S.-C.; Wong, C. P.; Zhao, N., Hollow-Structured Graphene–Silicone-Composite-Based Piezoresistive Sensors: Decoupled Property Tuning and Bending Reliability. *Adv. Mater.* **2017,** *29*, 1702675.
64. Amjadi, M.; Kyung, K.-U.; Park, I.; Sitti, M., Stretchable, Skin-Mountable, and Wearable Strain Sensors and Their Potential Applications: A Review. *Adv. Funct. Mater.* **2016,** *26*, 1678-1698.
65. Chen, S.; Wei, Y.; Wei, S.; Lin, Y.; Liu, L., Ultrasensitive Cracking-Assisted Strain Sensors Based on Silver Nanowires/Graphene Hybrid Particles. *ACS Appl. Mater.* **2016,** *8*, 25563-25570.
66. Sangeetha, N. M.; Decorde, N.; Viallet, B.; Viau, G.; Ressier, L., Nanoparticle-Based Strain Gauges Fabricated by Convective Self Assembly: Strain Sensitivity and Hysteresis with Respect to Nanoparticle Sizes. *J. Phys. Chem. C* **2013,** *117*, 1935-1940.
67. WangWang; Shi, X.; Kariuki, N. N.; Schadt, M.; Wang, G. R.; Rendeng, Q.; Choi, J.; Luo, J.; Lu, S.; Zhong, C.-J., Array of Molecularly Mediated Thin Film Assemblies of Nanoparticles: Correlation of Vapor Sensing with Interparticle Spatial Properties. *J. Am. Chem. Soc.* **2007,** *129*, 2161-2170.

68. Pang, C.; Koo, J. H.; Nguyen, A.; Caves, J. M.; Kim, M.-G.; Chortos, A.; Kim, K.; Wang, P. J.; Tok, J. B.-H.; Bao, Z., Highly Skin-Conformal Microhairy Sensor for Pulse Signal Amplification. *Adv. Mater.* **2015,** *27*, 634-640.
69. McEvoy, M. A.; Correll, N., Materials that couple sensing, actuation, computation, and communication. *Science* **2015,** *347*, 1261689.
70. Park, S.; Kim, H.; Vosgueritchian, M.; Cheon, S.; Kim, H.; Koo, J. H.; Kim, T. R.; Lee, S.; Schwartz, G.; Chang, H.; Bao, Z., Stretchable Energy-Harvesting Tactile Electronic Skin Capable of Differentiating Multiple Mechanical Stimuli Modes. *Adv. Mater.* **2014,** *26*, 7324-7332.
71. Yamada, T.; Hayamizu, Y.; Yamamoto, Y.; Yomogida, Y.; Izadi-Najafabadi, A.; Futaba, D. N.; Hata, K., A stretchable carbon nanotube strain sensor for human-motion detection. *Nat. Nanotechnol.* **2011,** *6*, 296-301.
72. Lu, N.; Lu, C.; Yang, S.; Rogers, J., Highly Sensitive Skin-Mountable Strain Gauges Based Entirely on Elastomers. *Adv. Funct. Mater.* **2012,** *22*, 4044-4050.
73. He, R.; Yang, P., Giant piezoresistance effect in silicon nanowires. *Nat. Nanotechnol.* **2006,** *1*, 42-46.
74. Amjadi, M.; Pichitpajongkit, A.; Lee, S.; Ryu, S.; Park, I., Highly Stretchable and Sensitive Strain Sensor Based on Silver Nanowire–Elastomer Nanocomposite. *ACS Nano* **2014,** *8*, 5154-5163.
75. Hu, N.; Itoi, T.; Akagi, T.; Kojima, T.; Xue, J.; Yan, C.; Atobe, S.; Fukunaga, H.; Yuan, W.; Ning, H.; Surina; Liu, Y.; Alamusi, Ultrasensitive strain sensors made from metal-coated carbon nanofiller/epoxy composites. *Carbon* **2013,** *51*, 202-212.
76. Hwang, B.-U.; Lee, J.-H.; Trung, T. Q.; Roh, E.; Kim, D.-I.; Kim, S.-W.; Lee, N.-E., Transparent Stretchable Self-Powered Patchable Sensor Platform with Ultrasensitive Recognition of Human Activities. *ACS Nano* **2015,** *9*, 8801-8810.
77. Xiao, X.; Yuan, L.; Zhong, J.; Ding, T.; Liu, Y.; Cai, Z.; Rong, Y.; Han, H.; Zhou, J.; Wang, Z. L., High-Strain Sensors Based on ZnO Nanowire/Polystyrene Hybridized Flexible Films. *Adv. Mater.* **2011,** *23*, 5440-5444.
78. Hempel, M.; Nezich, D.; Kong, J.; Hofmann, M., A Novel Class of Strain Gauges Based on Layered Percolative Films of 2D Materials. *Nano Lett.* **2012,** *12*, 5714-5718.
79. Boland, C. S.; Khan, U.; Backes, C.; O'Neill, A.; McCauley, J.; Duane, S.; Shanker, R.; Liu, Y.; Jurewicz, I.; Dalton, A. B.; Coleman, J. N., Sensitive, High-Strain, High-Rate Bodily Motion Sensors Based on Graphene–Rubber Composites. *ACS Nano* **2014,** *8*, 8819-8830.
80. Pang, Y.; Tian, H.; Tao, L.; Li, Y.; Wang, X.; Deng, N.; Yang, Y.; Ren, T.-L., Flexible, Highly Sensitive, and Wearable Pressure and Strain Sensors with Graphene Porous Network Structure. *ACS Appl. Mater.* **2016,** *8*, 26458-26462.
81. Kang, D.; Pikhitsa, P. V.; Choi, Y. W.; Lee, C.; Shin, S. S.; Piao, L.; Park, B.; Suh, K.-Y.; Kim, T.-i.; Choi, M., Ultrasensitive mechanical crack-based sensor inspired by the spider sensory system. *Nature* **2014,** *516*, 222-226.
82. Gong, S.; Lai, D. T. H.; Su, B.; Si, K. J.; Ma, Z.; Yap, L. W.; Guo, P.; Cheng, W., Highly Stretchy Black Gold E-Skin Nanopatches as Highly Sensitive Wearable Biomedical Sensors. *Adv. Electron. Mater.* **2015,** *1*, 1400063.
83. Lee, J.; Kim, S.; Lee, J.; Yang, D.; Park, B. C.; Ryu, S.; Park, I., A stretchable strain sensor based on a metal nanoparticle thin film for human motion detection. *Nanoscale* **2014,** *6*, 11932-11939.
84. Wang, Y.; Wang, L.; Yang, T.; Li, X.; Zang, X.; Zhu, M.; Wang, K.; Wu, D.; Zhu, H., Wearable and Highly Sensitive Graphene Strain Sensors for Human Motion Monitoring. *Adv. Funct. Mater.* **2014,** *24*, 4666-4670.
85. Park, J. J.; Hyun, W. J.; Mun, S. C.; Park, Y. T.; Park, O. O., Highly Stretchable and Wearable Graphene Strain Sensors with Controllable Sensitivity for Human Motion Monitoring. *ACS Appl. Mater.* **2015,** *7*, 6317-6324.

86. Obitayo, W.; Liu, T., A Review: Carbon Nanotube-Based Piezoresistive Strain Sensors. *J. Sens.* **2012**.
87. Alamusi; Hu, N.; Fukunaga, H.; Atobe, S.; Liu, Y. L.; Li, J. H., Piezoresistive Strain Sensors Made from Carbon Nanotubes Based Polymer Nanocomposites. *Sensors* **2011,** *11*, 10691-10723.
88. Hu, N.; Karube, Y.; Yan, C.; Masuda, Z.; Fukunaga, H., Tunneling effect in a polymer/carbon nanotube nanocomposite strain sensor. *Acta Mater.* **2008,** *56*, 2929-2936.
89. Shi, X.; Liu, S.; Sun, Y.; Liang, J.; Chen, Y., Lowering Internal Friction of 0D–1D–2D Ternary Nanocomposite-Based Strain Sensor by Fullerene to Boost the Sensing Performance. *Adv. Funct. Mater.* **2018,** *28*, 1800850.
90. Zheng, M.; Li, W.; Xu, M.; Xu, N.; Chen, P.; Han, M.; Xie, B., Strain sensors based on chromium nanoparticle arrays. *Nanoscale* **2014,** *6*, 3930-3933.
91. Yao, S.; Zhu, Y., Wearable multifunctional sensors using printed stretchable conductors made of silver nanowires. *Nanoscale* **2014,** *6*, 2345-2352.
92. Gong, S.; Lai, D. T. H.; Wang, Y.; Yap, L. W.; Si, K. J.; Shi, Q.; Jason, N. N.; Sridhar, T.; Uddin, H.; Cheng, W., Tattoolike Polyaniline Microparticle-Doped Gold Nanowire Patches as Highly Durable Wearable Sensors. *ACS Appl. Mater.* **2015,** *7*, 19700-19708.
93. Highly stretchable and sensitive strain sensor based on silver nanowire-elastomer nanocomposite. *ACS Nano* **2014,** *8*, 5154.
94. Shin, U.-H.; Jeong, D.-W.; Park, S.-M.; Kim, S.-H.; Lee, H. W.; Kim, J.-M., Highly stretchable conductors and piezocapacitive strain gauges based on simple contact-transfer patterning of carbon nanotube forests. *Carbon* **2014,** *80*, 396-404.
95. Cohen, D. J.; Mitra, D.; Peterson, K.; Maharbiz, M. M., A Highly Elastic, Capacitive Strain Gauge Based on Percolating Nanotube Networks. *Nano Lett.* **2012,** *12*, 1821-1825.
96. Roh, E.; Hwang, B.-U.; Kim, D.; Kim, B.-Y.; Lee, N.-E., Stretchable, Transparent, Ultrasensitive, and Patchable Strain Sensor for Human–Machine Interfaces Comprising a Nanohybrid of Carbon Nanotubes and Conductive Elastomers. *ACS Nano* **2015,** *9*, 6252-6261.
97. Yang, T.; Li, X.; Jiang, X.; Lin, S.; Lao, J.; Shi, J.; Zhen, Z.; Li, Z.; Zhu, H., Structural engineering of gold thin films with channel cracks for ultrasensitive strain sensing. *Mater. Horiz.* **2016,** *3*, 248-255.
98. Kundu, S.; Sriramdas, R.; Rafsanjani Amin, K.; Bid, A.; Pratap, R.; Ravishankar, N., Crumpled sheets of reduced graphene oxide as a highly sensitive, robust and versatile strain/pressure sensor. *Nanoscale* **2017,** *9*, 9581-9588.
99. Kabiri Ameri, S.; Ho, R.; Jang, H.; Tao, L.; Wang, Y.; Wang, L.; Schnyer, D. M.; Akinwande, D.; Lu, N., Graphene Electronic Tattoo Sensors. *ACS Nano* **2017,** *11*, 7634-7641.
100. Tang, Y.; Zhao, Z.; Hu, H.; Liu, Y.; Wang, X.; Zhou, S.; Qiu, J., Highly Stretchable and Ultrasensitive Strain Sensor Based on Reduced Graphene Oxide Microtubes–Elastomer Composite. *ACS Appl. Mater.* **2015,** *7*, 27432-27439.
101. Li, L.; Bai, Y.; Li, L.; Wang, S.; Zhang, T., A Superhydrophobic Smart Coating for Flexible and Wearable Sensing Electronics. *Adv. Mater.* **2017,** *29*, 1702517.
102. Amjadi, M.; Yoon, Y. J.; Park, I., Ultra-stretchable and skin-mountable strain sensors using carbon nanotubes–Ecoflex nanocomposites. *Nanotechnology* **2015,** *26*, 375501.
103. Ho, M. D.; Ling, Y.; Yap, L. W.; Wang, Y.; Dong, D.; Zhao, Y.; Cheng, W., Percolating Network of Ultrathin Gold Nanowires and Silver Nanowires toward “Invisible” Wearable Sensors for Detecting Emotional Expression and Apexcardiogram. *Adv. Funct. Mater.* **2017,** *27*, 1700845.
104. Highly stretchable piezoresistive graphene–nanocellulose nanopaper for strain sensors. *Adv. Mater.* **2013,** *26*, 2022.
105. Patel, S.; Park, H.; Bonato, P.; Chan, L.; Rodgers, M., A review of wearable sensors and systems with application in rehabilitation. *J. Neuroeng. Rehabil.* **2012,** *9*, 21.

Chapter 4

Experimental techniques

In this Chapter, the experimental techniques employed during synthesis process of active materials described in this thesis (*i.e.* graphene and gold nanoparticles) have been discussed. In addition, working principles of different characterization methods including SEM, AFM, Raman, and XPS *etc.* have been discussed in order to provide an accurate and comprehensive understanding of these novel functional materials.

4.1. General information

Graphene oxide (GO) (4 mg/ml, water dispersion) was purchased from Graphenea. Before the synthesis of functionalized graphene in Chapter 5 and Chapter 7, it was diluted in ethanol and sonicated for 30 min to have a better dispersion.

All the chemicals and reagents were purchased from Sigma-Aldrich and used without further purification.

ITO-PET (surface resistivity: 60 Ω/sq, L × W × thickness 1 ft × 1 ft × 5 mil, thickness of ITO coating: 130 nm) was purchased from Sigma-Aldrich. No further surface treatment was needed due to the protection film, which was removed before using.

Silicon substrate (230 nm ± 10 nm SiO_2, 15×15 mm^2) was purchased from Fraunhofer. Substrate was cleaned with sonication bath in acetone and isopropanol for 20 min respectively, followed by UV ozone treatment to further remove the surface contaminant.

4.2. Synthesis of active materials

4.2.1. Functionalization of graphene oxide

Graphene oxide is a great 2D platform that can be readily functionalized thereby modifying its structural, electronic, chemical properties in view of its applications in the field of catalysis,[1-4] bio-sensing,[5-11] drug-delivery[12-16] *etc.* In recent years, graphene and graphene oxide have been widely functionalized with chromophores,[17-20] organic compounds,[21, 22] polymers,[23, 24] nanoparticles.[25-28] These approaches have been extensively reviewed.[29-34] As shown in Figure 4-1, the functionalization of graphene or graphene oxide can be achieved through covalent bonding (*e.g.* nucleophilic substitution reaction, electrophilic substitution reaction, condensation reaction, addition reaction *etc.*) or noncovalent bonding (*e.g.* π-π interaction, cation-π interaction, anion-π interaction, H-π interaction *etc.*). Substitution reaction, usually through the attack of epoxy groups with amine (-NH_2) containing organic compounds, has been considered as a promising method for large scale production due to its high yield at room temperature, in absence of catalyst in aqueous medium. Therefore, we employed this method to functionalize GO (Chapter 5 and Chapter 7). The related synthesis details are discussed in each chapter.

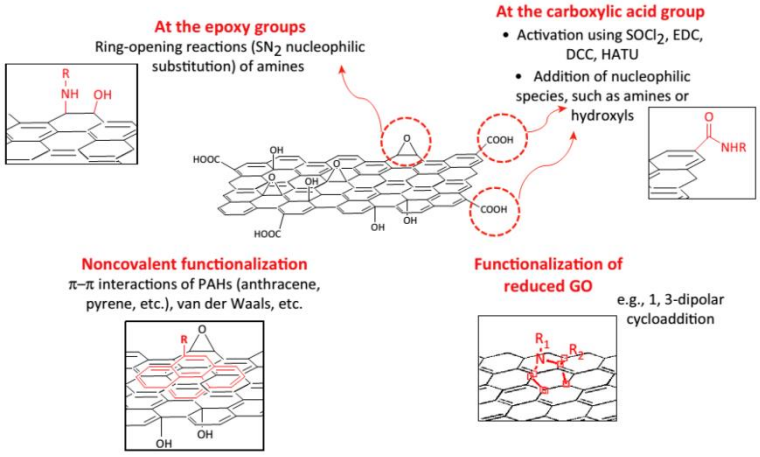

Figure 4-1. Different approaches for the functionalization of GO. Reproduced from Ref.[34]

4.2.2. Synthesis and functionalization of gold nanoparticles (AuNPs)

Gold nanoparticles have attracted great interest for applications in the field of catalysis,[35-39] biosensing,[40-44] biomedicine,[45-48] bioimaging,[49-52] *etc.* (see Figure 4-2) because of their unique optical, electrical, magnetic properties. Although AuNPs has been first synthesized over 100 years ago, much research focus has been so far addressed to its functionalization as well as to the various size and shape controlled synthesis methods to enhance and broaden potential applications in different fields. To meet the requirements for various applications, versatile ligands, polymers, biomolecules, *etc.* can be easily functionalized on AuNPs, thus making it one of the most active dynamic research areas.[53, 54] In this section, experimental details of the synthesis and functionalization of AuNPs utilized in Chapter 6 are discussed.

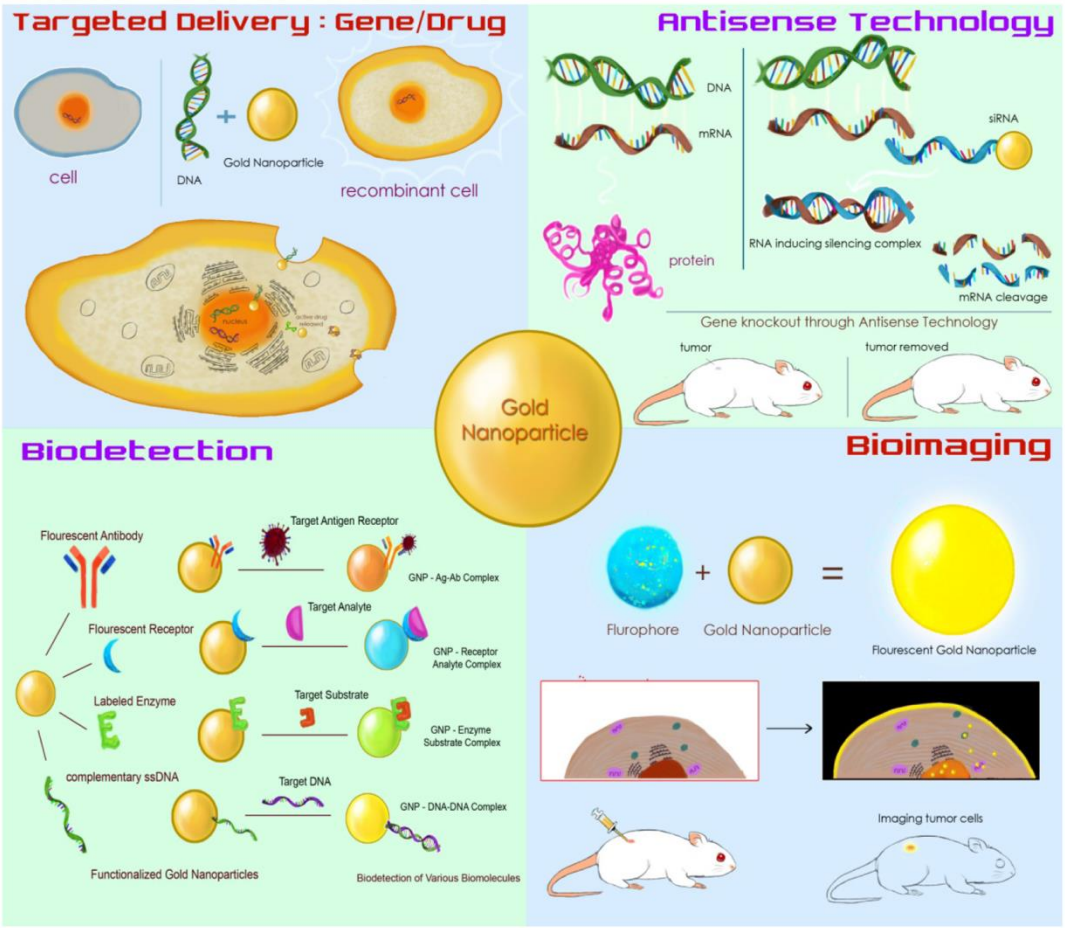

Figure 4-2. Types of functionalization of gold nanoparticles and their potential biomedical applications. Reproduced from Ref.[44]

4.3. Characterization techniques

4.3.1. Electrical measurement

In this thesis, three independent experimental chapters have been discussed to design and fabricate pressure sensors and strain sensors featuring electrical resistive readout in which novel nanomaterials were used as active components. For piezoresistive pressure sensors discussed in Chapter 5 and Chapter 7, functionalized graphene materials were sandwiched in between flexible ITO coated PET electrodes. The latter were further wired out with cooper wires and silver paste, which were then connected with the source meter Keithley 2635B. By applying bias voltage of 0.2 V, the current passing through the vertical junction was collected. The current was directly affected by the interlayer distance among the graphene flakes which depends on the applied pressure. Through the measured currents at given bias voltages, the resistance can be easily calculated according to Ohm law:

$$\mathrm{R} = \frac{V}{I} \qquad (4-1)$$

Where R is the electrical resistance, V is the applied bias voltage and I is the measured current. The working principle of the functionalized graphene based pressure sensors were discussed in the following chapters (Chapter 5 and Chapter 7).

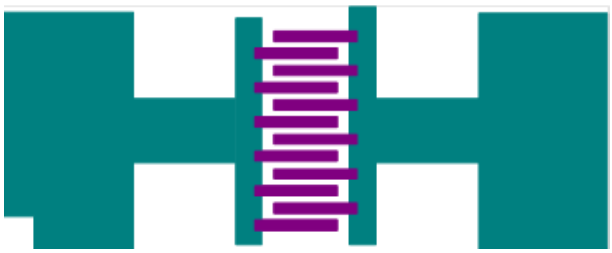

Figure 4-3. Illustration of interdigitated electrode for AuNPs-TEG network based strain sensor. (Green and purple colors stand for different layers; channel length: 5 or 10 μm)

The electrical measurement of Gold nanoparticles based strain sensor (Chapter 6) was similar to the above mentioned method. The major difference is the device structure and corresponding fabrication process. Interdigitated electrode (Figure 4-3) was fabricated by photolithography method before the active material deposition process. The pads at the ends were wired up with cooper wire and silver paste and connected with source meter. Bias voltage of 0.2 V was applied on the device and the current passing through the nanoparticle network was collected at the same time while applying different strain on the PET substrate on which the device was attached.

Apart from the normal electrical connection through conductive wires, the electrical sensing process of AuNPs-TEG network based strain sensor was also designed to achieve wireless reading through Radio Frequency IDentification (RFID). The measured circuit has been constructed by using an alternative supply as power source and the rest components including capacitor, resister and inductor were integrated on a printed circuit board (PCB) according the diagram above. Here, detailed discussion has been focused on the design of chip circuit.

Chip Design A: Single-Film-Multilayer-Circuit

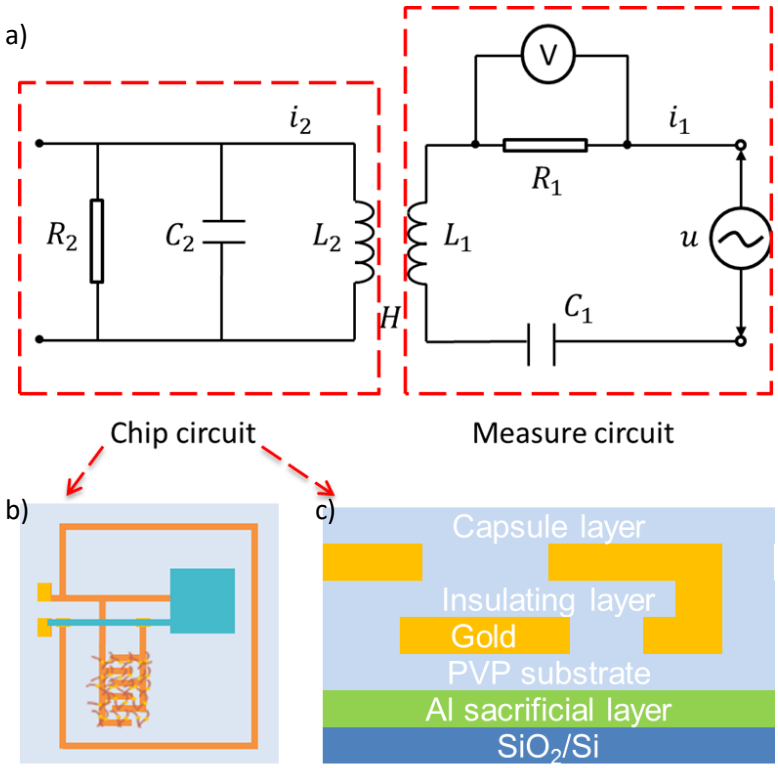

Figure 4-4. Diagram of chip circuit and measure circuit (a); Illustration of chip circuit layout (b) and the side view (c).

Interdigitated electrode, on which the AuNPs-TEG network is deposited serving as the resistance R2, is linked in parallel with capacitor and inductor coil (Figure 4-4a). Two external pads are reserved to measure the resonance frequency of chip circuit. The details of fabrication process have been discussed as below:

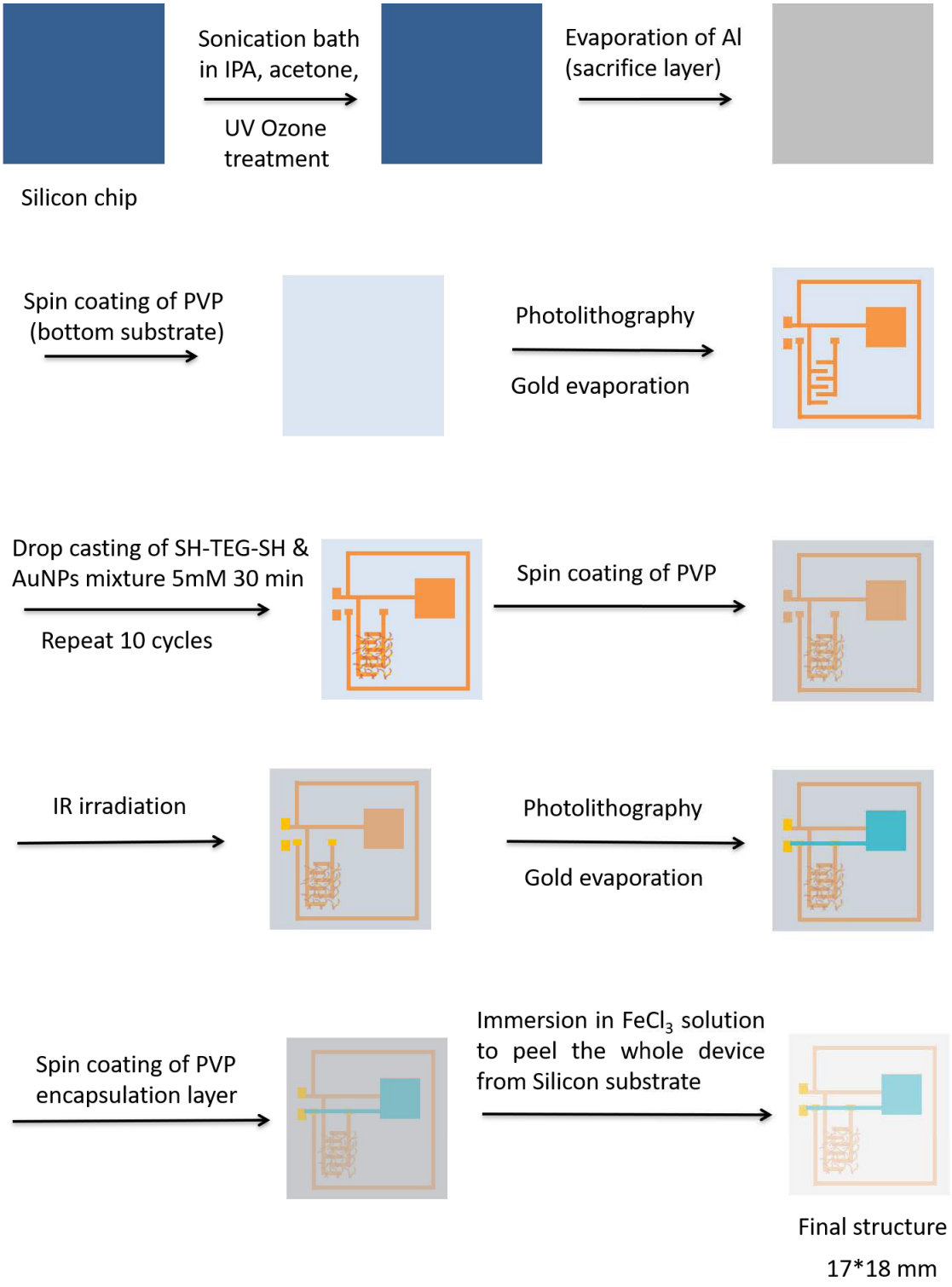

Figure 4-5. Fabrication flow of RFID chip for strain sensor.

As shown in Figure 4-5, after cleaning the SiO_2 chip (sonication bath in acetone and IPA for 20min respectively, UV ozone treatment for 20 min), the fabrication flow started from evaporating Aluminum (160 nm) as sacrificial layer on the SiO_2 chip. Then PVP (poly (4-vinyl phenol)) was spin coated as the substrate. The gold electrodes on the PVP substrate were constructed by photolithography and gold evaporation, followed by spin coating an insulate layer of PVP to separate the two conductive layers. The most challenging step in this fabrication flow was the connection between the two electrode layers, which have to be connected together to form an interconnected circuit. IR laser was used to get through the insulating PVP layer between the two gold electrode layers, which were connected during the evaporation of the top electrode. As shown in Figure 4-6, a square of 120µm × 80µm has been scanned by IR laser with the energy level 30% and pulse rate 60 kHz. The black area indicated that the gold layer beneath the PVP layer is penetrated by IR laser. In addition to the unstable IR laser irradiation, the scanned area (area in the red dash lines) is also checked by AFM and there is no difference in the phase diagram of the scanned area and unscanned one, which means the PVP is not efficiently removed.

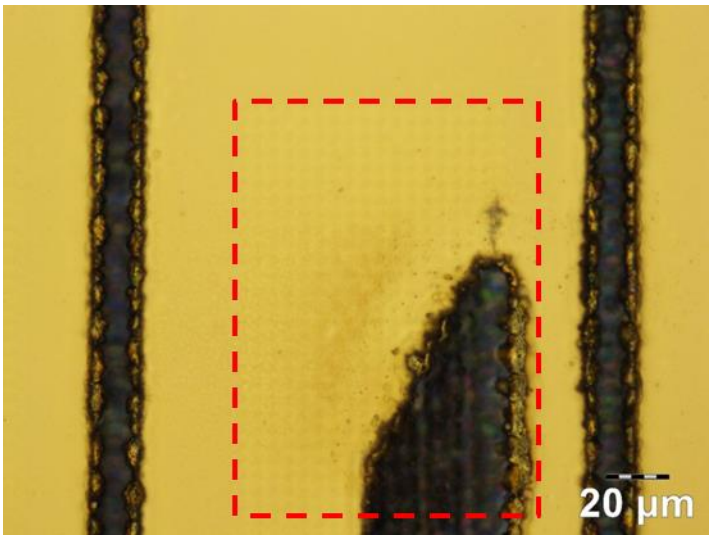

Figure 4-6. Photo of substrate under IR lase scan. (red dash square: scanned area)

To determine the best IR scanning parameters, different combinations of energy level and pulse rate have been checked as shown in Table 4-1, in which the cross symbol (×) means the destroy of the gold layer and the check symbol (√) means no penetration. The best combination of energy level and pulse rate is 30%-40 kHz and 40%-60 kHz (red check) because they possess the highest energy level meanwhile not too strong to destroy the gold layer. But the experiment showed that the IR laser scanning with the two sets of parameters

also did not work well due to the unstable irradiation, which made the IR laser method not suitable in this case.

Table 4-1. PVP layer burned with IR laser under different power lever and pulse rate (kHz)

Pulse rate / Energy level	20	30	40	50	60	70	80	90	100
10%	√	√	√	√	√	√	√	√	√
20%	√	√	√	√	√	√	√	√	√
30%	×	×	√	√	√	√	√	√	√
40%	×	×	×	×	√	√	√	√	√
50%	×	×	×	×	×	×	×	×	×
60%	×	×	×	×	×	×	×	×	×
70%	×	×	×	×	×	×	×	×	×
80%	×	×	×	×	×	×	×	×	×
90%	×	×	×	×	×	×	×	×	×
100%	×	×	×	×	×	×	×	×	×

Due to the failure of IR laser irradiation experiment as well as the multistep of photolithography technique, this fabrication design has been modified to have a more efficient fabrication process. Also, the fully flexible structure might cause unstable electrical performance during the operation process, thus commercially available capacitor and inductor were employed to simplify the fabrication process and to improve the operation stability. The new structure is discussed as below:

Chip Design b: Commercial electric components based structure

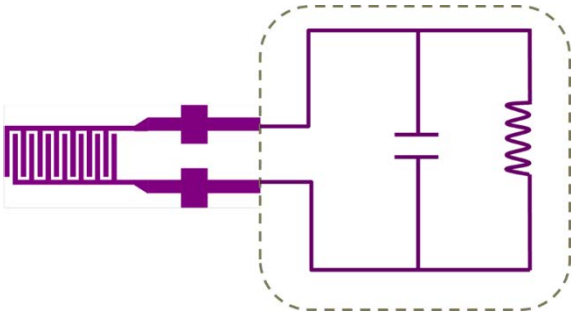

Figure 4-7. Diagram of commercial electric components based chip circuit.

As shown in Figure 4-7, while the interdigitated electrodes remaining the same, the circuit (dash area) including capacitor and inductor were changed by using commercially available electronic components. In this design, we fully focused on the fabrication of the flexible resistor part to get a better performance.

To improve the robustness of the device, polyimide (PI) was utilized as flexible substrate and the gold electrodes were fabricated by photolithography as previously. Water soluble polymer poly(4-styrenesulfonic acid) sodium salt (PSSNa) instead of Aluminum was spin coated onto the SiO_2 as sacrificial layer to facilitate the peeling process. After the fabrication of electrode, aqueous solution of SH-TEG-SH and AuNPs was mixed and drop casted immediately on the electrode to form AuNPs-TEG network. The aqueous solution was removed after 30 min deposition. After 10 cycles of drop casting process, the flexible device was released by putting the whole device on water surface and fished out with PET film. Two pads at the end were connected with commercially available RFID tag (Figure 4-8) to achieve wireless sensing. The alternative input was generated by a signal generator paired with cooper wire coil to induce mutual inductance with the strain sensing device. This wireless reading process involves other electrical engineering techniques such as signal filter, amplifier *etc.* and the RFID system is under testing.

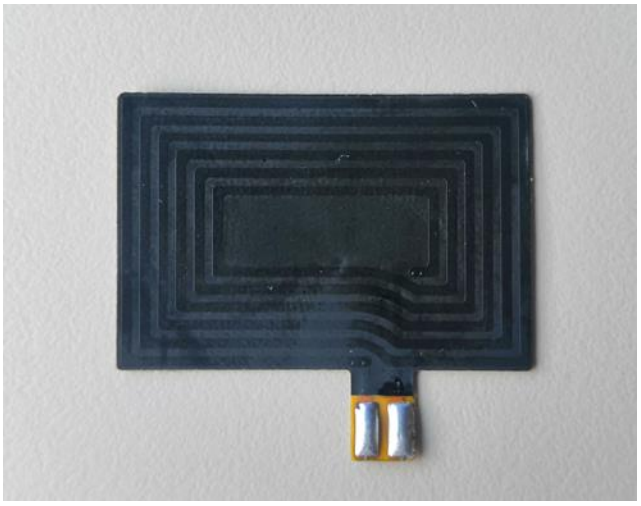

Figure 4-8. Commercially available RFID tag with two connecting pads.

4.3.2. Force gauge setup

Mark-10 force gauge setup was used for the pressure sensing measurement. It comprises of 5 major parts including the force gauge, test stand, sample stage, control panel, and corresponding software (Figure 4-9). During the dynamic pressure test, pressure sensor was fixed on the sample stage and connected with source meter. Certain pressure values can be set through MESUR gauge plus software, after which the force gauge will move downwards under the control of the motorized test stand to reach the certain set point. Current change of the device was recorded by applying different pressure load under bias voltage. The pressing pad can also be programmed to apply a continuous pressure to the device with pre-set pressure value and cycle number, while the current change was recorded and analysed for the evaluation of robustness of pressure sensor.

Figure 4-9. The test system consists of a digital force gauge ① (Mark-10, M7-025E, ~1.0 N), a motorized test stand ② (Mark-10, ESM-303E), sample test platform ③ (sample holder and compression plate with diameter of 1.15 cm), control panel ④, and software ⑤ (MESUR gauge Plus).

4.3.3. Spectroscopic characterization

4.3.3.1. RAMAN spectroscopy

Raman spectroscopy is a powerful technique used to determine the vibrational modes of molecules, in which the structural fingerprint of the sample can be identified. The working principle of Raman spectroscopy is schematized in Figure 4-10. When a sample is exposed in a monochromatic light (*e.g.* visible, near infrared or near ultraviolet), most of the light gets transmitted through the sample with minor part of light being scattered in different directions. When the incident light interacts with an electron of the sample, the electrons absorb energy and rises to the virtual energy state. Afterwards the electron fells back to an energy level by losing energy in the form on scattering light. Depending on the relationship of the energy of incident light and scattering light, the scattering can be divided into Rayleigh Scattering (elastic scattering, $h\nu_1=h\nu_2$), Stocks Raman Scattering (inelastic scattering, $h\nu_1>h\nu_3$), and Anti-Stocks Raman Scattering (inelastic scattering, $h\nu_1<h\nu_4$).

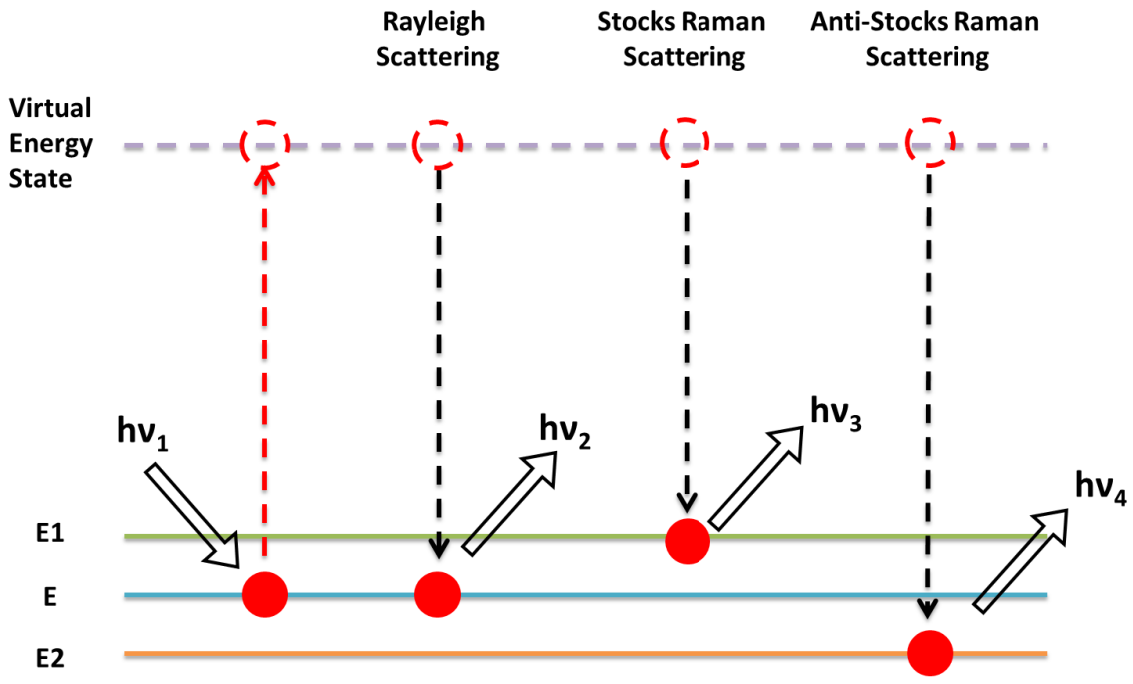

Figure 4-10. Vibrational energy-level diagram showing the states involved in Raman spectra.

As shown in Figure 4-11, the major parts of Raman Spectroscopy include laser source, sample chamber, spectrometer and detectors. In this thesis, the spectra of functionalized graphene materials were recorded by a Renishaw InVia spectrometer combined with a 532 nm laser source. A beam spot of 800 nm was focused on the sample with a confocal microscope. The emitted signal by the sample was collected by the microscope lens and filtered via a rejection filter. After splitting the signal by energy with a grating, the final signal was collected by a CCD camera.

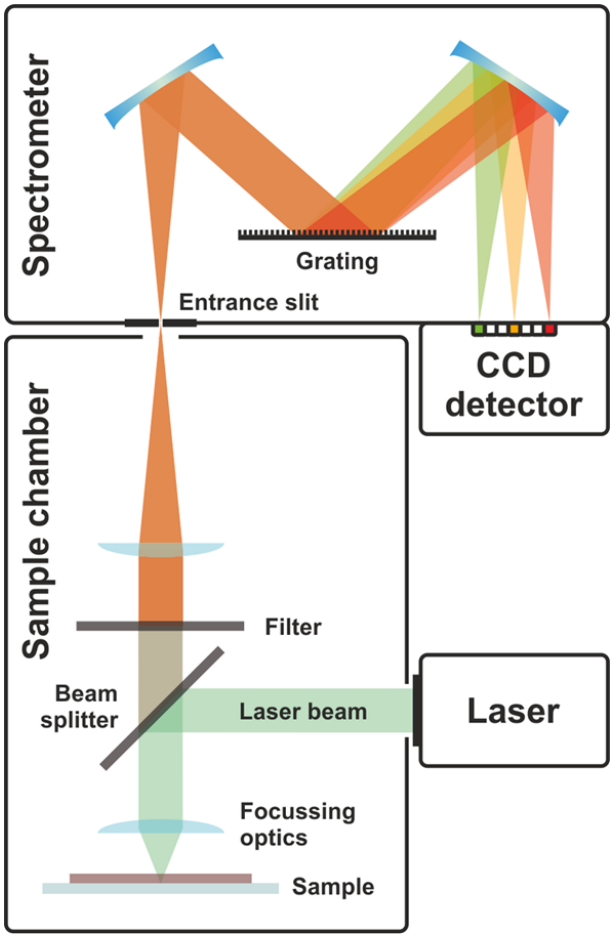

Figure 4-11. Schematic of an upright Raman microscope. Reproduced from Ref.[55]

All the Raman spectra presented in this thesis were acquired with a Renishaw InVia RE04 combined with a MS20 Encoded stage 100 nm and a 532 nm laser maintained at a power excitation below 1 mW. The measurements were carried out in ambient conditions with a 100x lens affording a beam spot of 800 nm.

4.3.3.2. X-ray Photoelectron Spectroscopy

X-ray photoelectron spectroscopy (XPS) is a non-destructive surface spectroscopic technique that can provide information about the elemental composition, chemical or electronic state of each element (except H and He) within the depth of ~10 nm. When a high-energy photon interacts with matter, the photoemission process occurs with an electron removed from the atomic orbital to reach the vacuum level (Figure 4-12). This process can be described in three steps including X-ray excitation (known value, *hv*), electron transport to the matter surface (binding energy, E_b), and escape from the surface (work function Φ, constant instrumental correction factor). With the kinetic energy (as measured by the instrument, E_k) of escaped electron, the binding energy can be calculated based on the energy conservation rule:

$$h\nu = E_B + E_K + \Phi \qquad (4-2)$$

With the calculated binding energy, a typical XPS spectrum can be acquired by plotting the detected electron numbers (Y-axis) versus corresponding binding energy (X-axis).

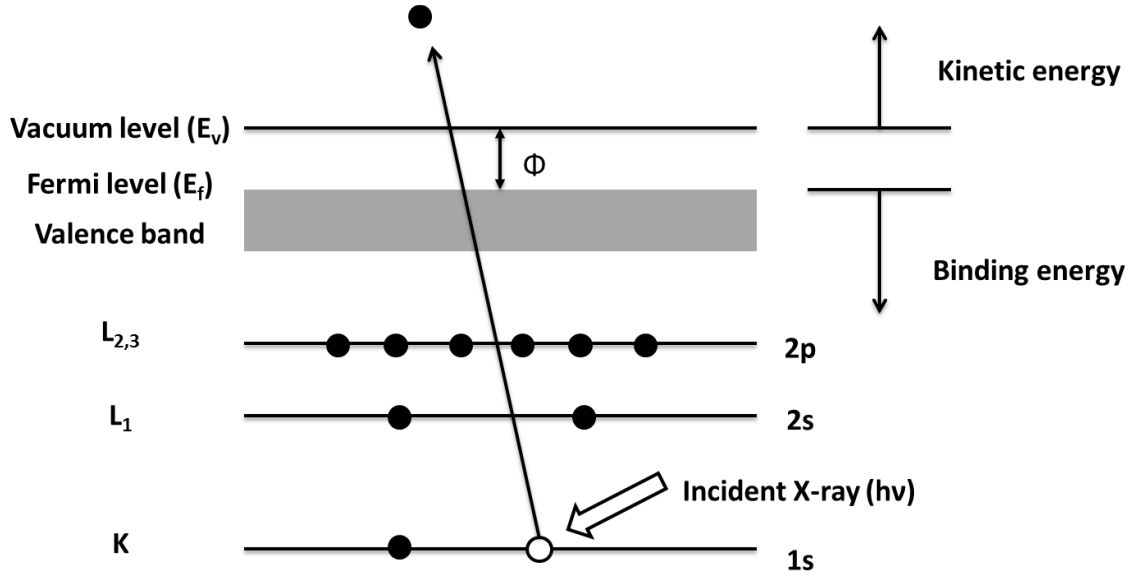

Figure 4-12. Illustration of photoemission process.

As shown in Figure 4-13, the major components of XPS include an X-ray source, a high vacuum chamber, an electron collection lens, an electron energy analyzer, a magnetic field shielding, and electron detector. Produced by bombarding an aluminum anode with an electron beam, X-ray was irradiated on the sample in an ultra-high vacuum chamber to avoid contamination and maximize the photoelectron path length. The photoelectrons were focused by a magnetic lens and then collected and counted with a detector.

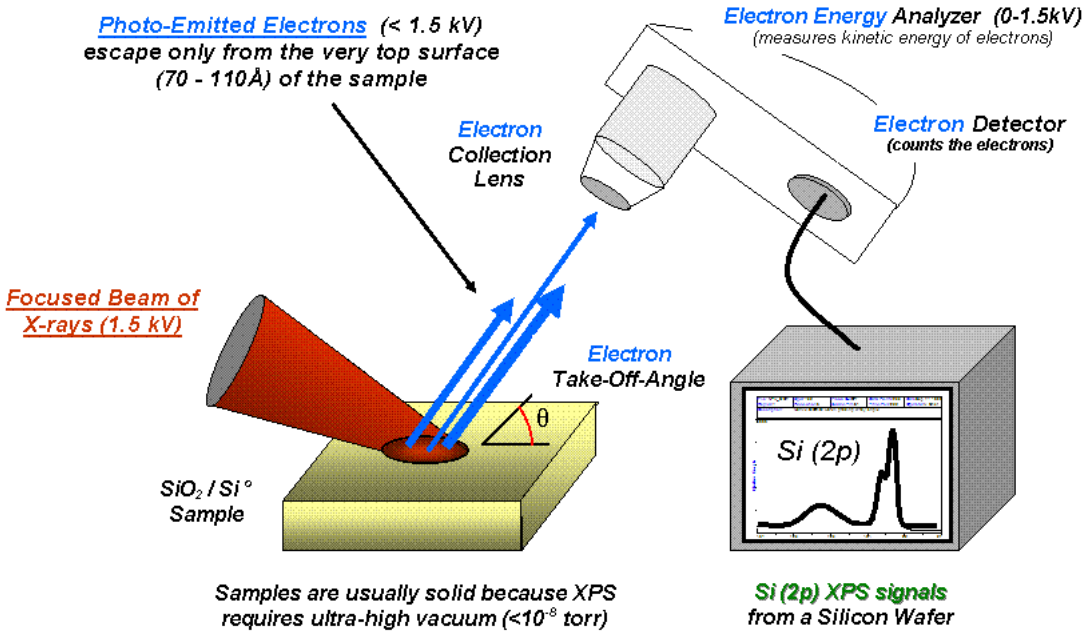

Figure 4-13. Basic components of a monochromatic XPS system. Free copyright from https://commons.wikimedia.org/wiki/File:System2.gif#filelinks.

In this thesis, XPS was used to characterize the functionalized graphene materials in Chapter 5 and Chapter 7. XPS analysis was performed with a Thermo Scientific K-Alpha X-ray photoelectron spectrometer. Details of the materials characterization were discussed in the following chapters.

4.3.3.3. UV-Vis Spectroscopy

Ultraviolet-visible (UV-Vis) spectroscopy is one of the most commonly used techniques in analytical chemistry for the quantitative determination of different organic and inorganic compounds in solution. The principle of UV-Vis spectroscopy is based on the interaction of UV or visible light with molecules, in which the bonding or non-bonding electrons can absorb energy and be excited to higher anti-bonding molecular orbitals (*e.g.* σ–σ*, n–σ*, π–π*, n–π*). UV-Vis spectroscopy follows the Lambert-Beer law, in which the absorbance of a solution is proportional to the concentration of absorbing species (c) and the path length (l):

$$\mathrm{A} = \log_{10}\frac{I_0}{I} = \varepsilon c l \qquad (4-3)$$

Where A is the measured absorbance, I_0 is the intensity of the incident light at a given wavelength, I is the transmitted intensity, and ε is the extinction coefficient. Based on this equation, the concentration of the absorber in a solution can be calculated with a known path length and given extinction coefficient.

As shown in Figure 4-14, major components of the UV-Vis spectrophotometer including light source, filter, monochromator, beam splitter, photodiode, and data processing system have been demonstrated. The UV-Vis spectrophotometer used in this thesis is the model Jasco V670, in which two light sources (*i.e.* a deuterium lamp producing UV light from 200-400 nm, and a halogen lamp producing visible and near-infrared light from 400-2700 nm) have been equipped. Made by a grating and slit, monochromatic light can be generated and selected with a desired wavelength and intensity. Beam splitter is used to send the light signals to the sample and reference (normally made of the same solvent as the sample solution). Light signals passing through the sample and reference are collected by photodiode and analyzed as a plot of optical absorbance of the sample as a function of the wavelength.

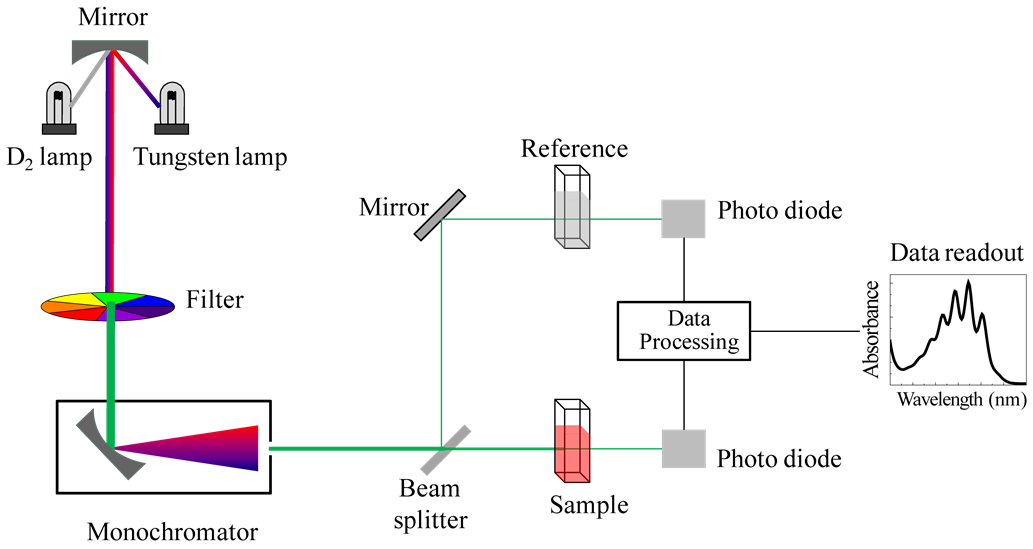

Figure 4-14. Schematic of UV-vis spectrophotometer. Free copyright from https://commons.wikimedia.org/wiki/File:Schematic_of_UV-_visible_spectrophotometer.png.

In this Thesis, UV-Vis spectroscopy has been used to determine the thickness of deposited graphene materials (Chapter 5 and Chapter 7), and gold nanoparticles concentration (Chapter 6). Details of the optical characterization of functionalized materials were discussed in the following chapters.

4.3.3.4. Dynamic Light Scattering

Dynamic light scattering (DLS) is widely used to analysis particles or macromolecules size (normally in the nanometer range) in solutions. The working principle of DLS is based on the Brownian motion, in which particles are randomly moving due to the colliding with surrounded solvent molecules (Figure 4-15). In this process, smaller particles move or diffuse more quickly, vice versa. The rate of Brownian motion is quantified as Translational Diffusion Coefficient (*D*). It is worth noting that the measured particle size is hydrodynamic size, which represents the size of an equivalent sphere which diffuses at the same rate as the tested particles.

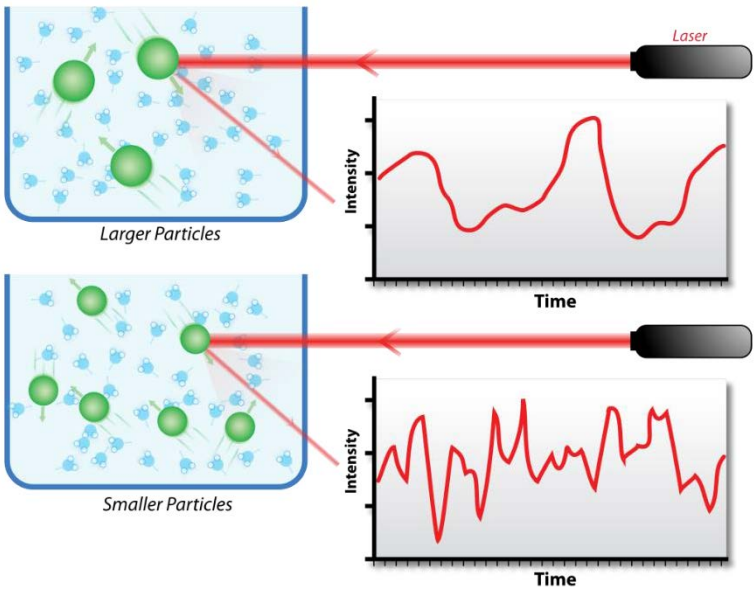

Figure 4-15. Hypothetical dynamic light scattering of larger and smaller particles. Free copyright from https://en.wikipedia.org/wiki/Dynamic_light_scattering#/media/File:DLS.svg.

As shown in Figure 4-16, particles in a solution will scatter the incident light randomly, after which the scattered light is collected by photodetector. Due to the constantly moving particles, the intensity of scattered light is changing with time, in which the changing speed depends on the particle diffusion rate. The hydrodynamic radius can be calculated according to the Stokes-Einstein equation:

$$\mathrm{D} = \frac{k_B T}{6\pi \eta r} \qquad (4-4)$$

Where D is Translational Diffusion Coefficient, k_B is Boltzmann's constant (1.380649×10^{-23} J/K), T is temperature (K), η is dynamic viscosity and r is the particle's

hydrodynamic radius. The Translational Diffusion Coefficient is extracted in the auto-correlation process by the correlator. The size distribution of all the particles in a sample can be acquired with DLS by showing the intensity of scattered light, and the results can also be converted to the volume or number size distribution for different research purposes.

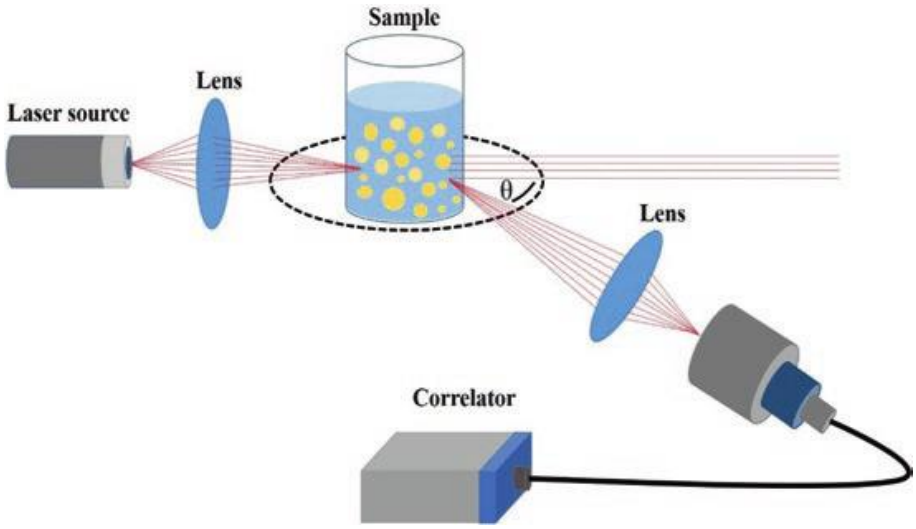

Figure 4-16. Illustration of the dynamic light scattering principle. Reproduced from Ref.[56]

In this Thesis, DLS was used to characterize the size distribution of gold nanoparticles (Chapter 6) with a Malvern "Zetasizer Nano ZS" instrument. A laser source (4W, λ=633 nm) and two PMT detectors placed at 13° (for diluted solutions with low extinction) and 173° (for big particles or highly concentrated solutions) with respect to the beam dump were equipped with the instrument.

4.3.4. Surface characterization

4.3.4.1. Atomic Force Microscopy

Atomic Force Microscopy (AFM) is one of the Scanning Probe Microscopes (SPM) invented in the 1980s.[57, 58] It is an important technique to acquire topographic information of conducting and insulating surfaces with high resolution (atomic resolution in some cases). Not only for the application of surface topography imaging, AFM can also be used to measure local material properties such as elasticity, hardness, adhesion and surface charge densities *etc.* by plotting force curves (*i.e.* force vs distance curves).[59] As shown in Figure 4-17, the major components of a MultiMode AFM head used in this thesis consist of laser, mirror, cantilever, tilt mirror, and photodetector. Apart from those components, three sets of screws are designed to adjust the position of laser, photodiode and stage respectively.

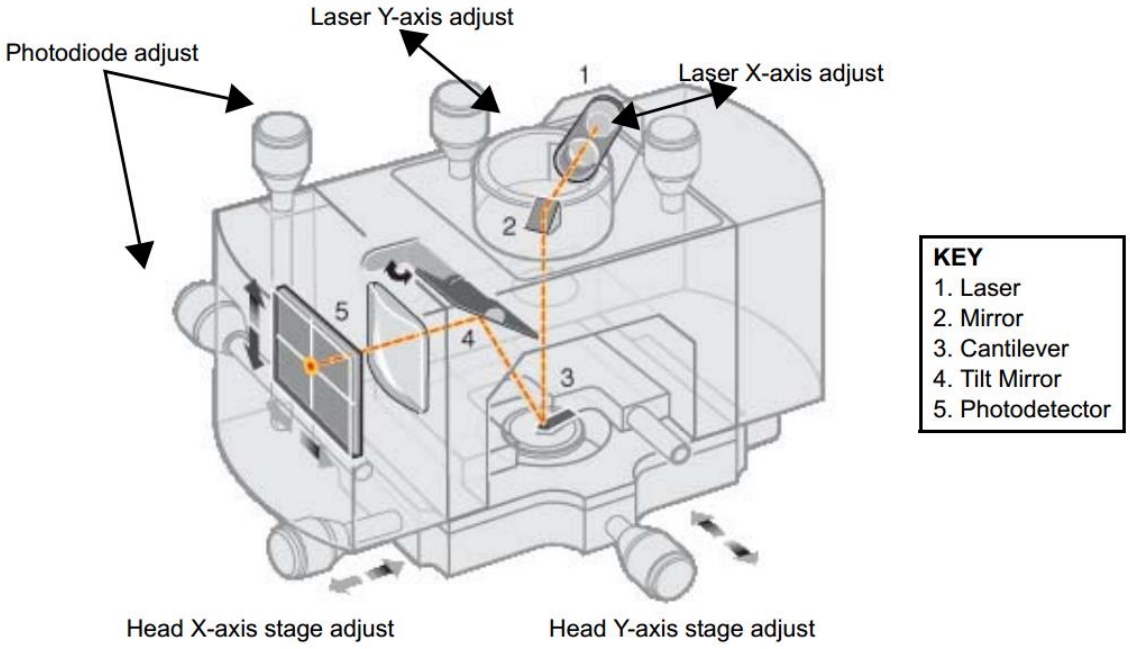

Figure 4-17. MultiMode SPM Head and Major Components. Reproduced from SPM Instruction Manual. Copyright © [2006] Veeco Instruments Inc.

While scanning the sample, the tip micro fabricated of the edge of the cantilever interacts with the sample surface (roughness or nanostructured architectures *etc.*) causing a deflection of the cantilever. The laser reflected by the backside of the cantilever will change its reflection path and be recorded by photodiode. By mapping the deflection information of each scanned point, the sample surface morphology can be acquired. The scanning process is precisely controlled by a scanner which integrate three piezoelectric crystals, each one responsible of displacements along a given axis (x, y, z) as depicted in Figure 4-18. AC signals applied to conductive areas of the tube determines the piezo expansion/restriction along the three axes.

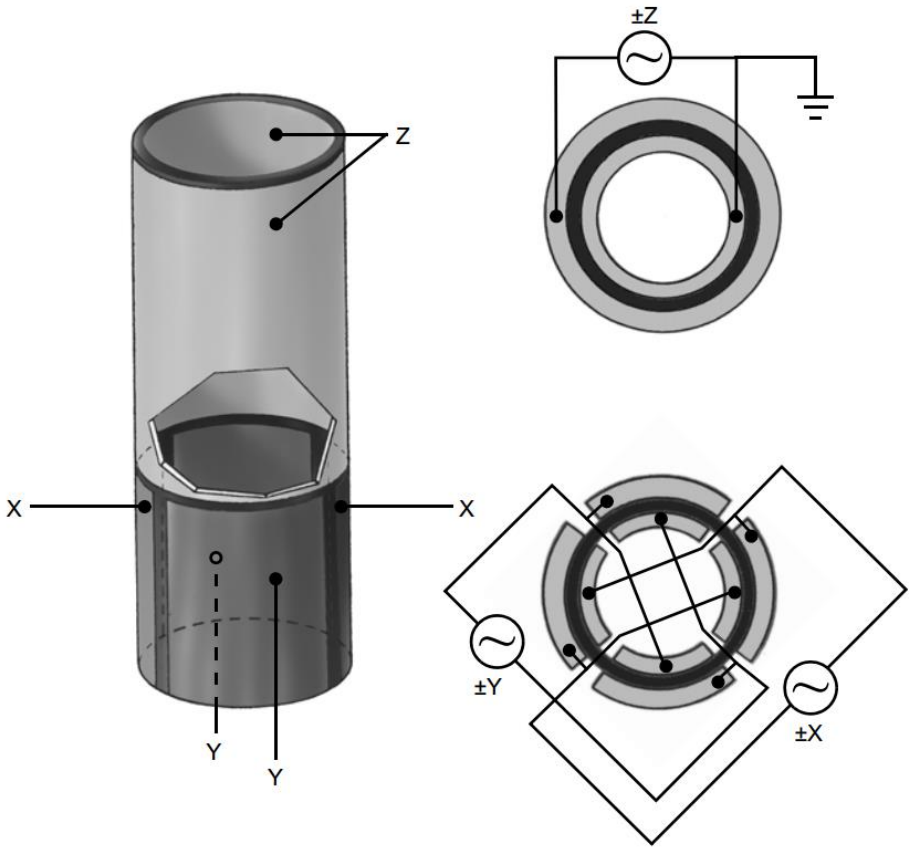

Figure 4-18. Typical Scanner Piezo Tube and X-Y-Z Electrical Configurations. Reproduced from SPM Instruction Manual. Copyright © [2006] Veeco Instruments Inc.

In Chapter 7, contact mode was used to study the elastic properties of photo sensitive polymer (SU-8 2002). During the force measurement, the sample is moved up and down by the piezoelectric translator along the *z* direction while keeping still in the other two directions (*i.e.* planner directions: *x* and *y*). As shown in Figure 4-19a, the cantilever moves downwards by a distance of z while bending into the opposite direction by a distance of *x*, thus giving the value of indention of δ. The cantilever bending distance *x* can be calculated by the following equation:

$$\mathrm{x} = \frac{F}{k} \qquad (4-5)$$

where *F* is the measured force and *k* is spring constant of the cantilever which is normally given by cantilever supplier. The spring constant can be further examined by applying indention measurement on hard samples (*e.g.* Si wafer *etc.*), in which the indention value (δ) is 0 thus bending distance (*x*) equals the measured height (*z*). The subtraction of bending distance (*x*) from measured height (*z*) has done automatically in the build-in software, thus the Young's modulus (*E*) can be calculated with the given value of tip radius (*R*, provided by supplier and examined by SEM) and Poisson's ratio (υ, given value by 6.777J/2.751J Material Property Database) based on the Hertz contact model which is described as below:

$$\mathrm{F} = \frac{4\sqrt{R}}{3}\frac{E}{1-\upsilon^2}\delta^{\frac{3}{2}} \qquad (4-6)$$

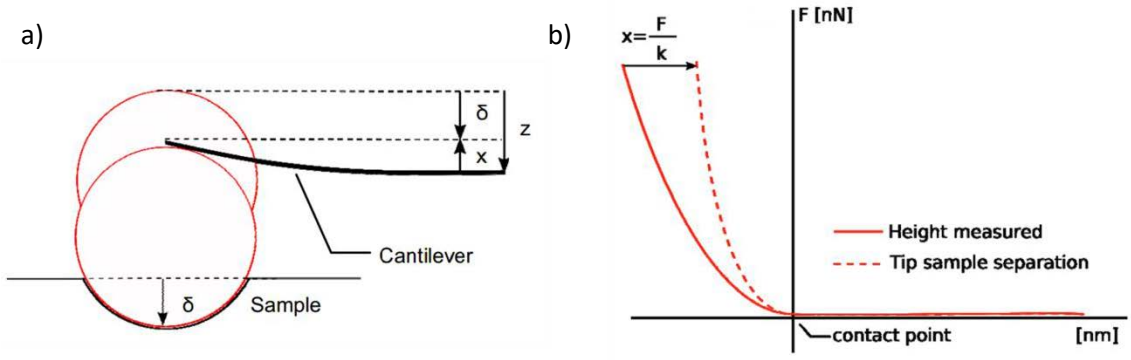

Figure 4-19. a) Sketch of the indentation experiment. b) Schematic of the correction of the height for the cantilever bending (*x*) to derive the tip-sample-separation (force indentation curve). Reproduced from JPK Instruments. Copyright © JPK Instruments AG.

4.3.4.2. Scanning Electron Microscope

Scanning electron microscope (SEM) is widely used for surface morphological characterization. Normally specimens are placed in a high vacuum chamber and irradiated with a focused beam of electrons. Other conditions such as low vacuum, wet conditions, cryogenic or elevated temperatures need specialized instruments to conduct the measurements. As shown in Figure 4-20, SEM consists of several major components including electron gun, anode, electromagnetic lens, scanning coils, backscattered electron detector (BST), secondary electron detector (SED), and stage. For some other models, X-ray detector is equipped to determine the chemical composition of specimen.

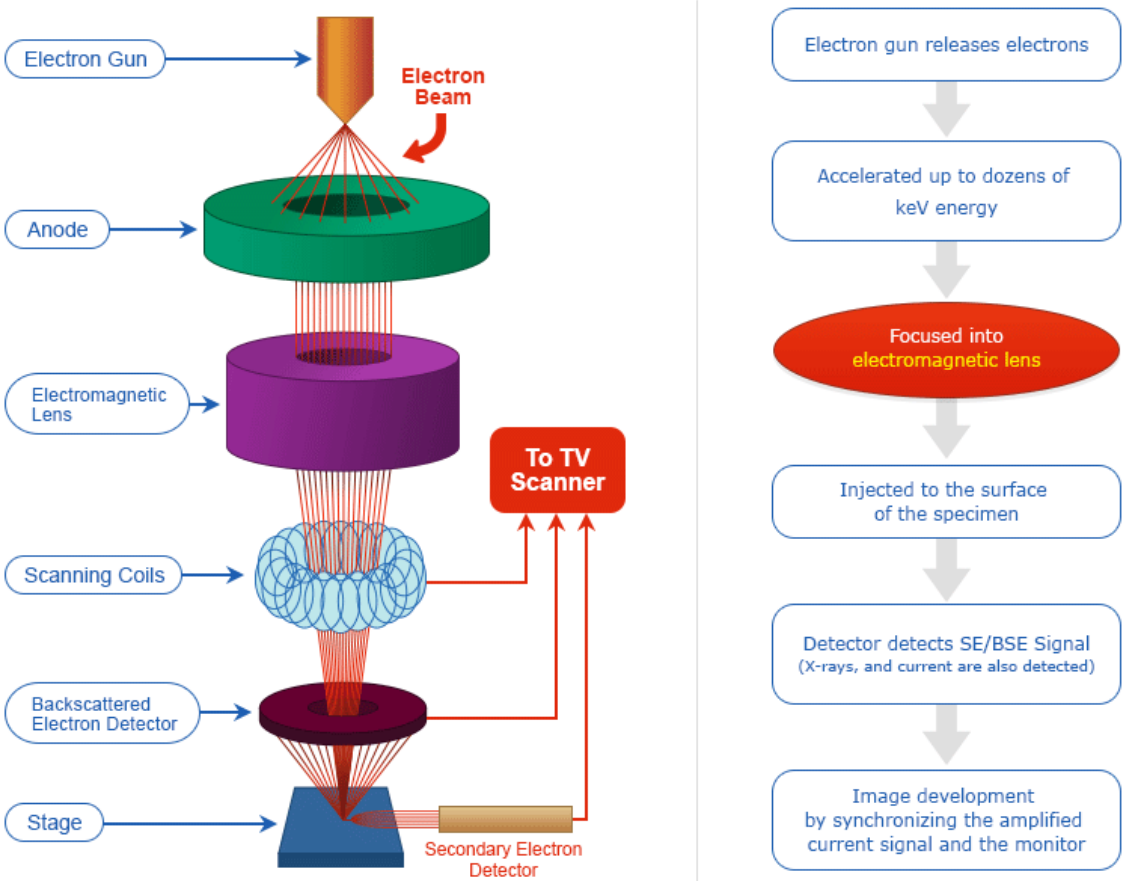

Figure 4-20. Schematic of Scanning Electron Microscope a) internal components and b) working process. Copyright © 2017 NANOIMAGES.

Electron beam is generated by the electron gun mounted in an ultra-high vacuum tube (~10^{-7} Pa) located on top of the vacuum chamber. Thermionic guns, the most common type, and field emission guns are the typical electron source for SEM. The electron beam is focused and controlled by the electromagnetic lenses and then passing through the scanning coil before reaching the sample. While the primary electron (PE) beam interacts with the sample, different electron species (Figure 4-21) are generated by energy exchange such as secondary electron (SE) ejected by inelastic scattering interaction, backscattered electrons (BSE) reflected by elastic scattering interaction, characteristic X-ray generated by the combination of an outer shell electron and an inner shell electron hole. Corresponding electron and X-ray detectors are equipped to collect and map the electron signal.

Scanning Electron Microscopy (SEM) images were recorded with a FEI Quanta FEG 250 instrument S3 (FEI corporate, Hillsboro, Oregon, USA). In Chapter 5, 6, and 7, SEM was used for the surface morphology research of functionalized graphene and gold nanoparticles. Specimens were deposited on Si substrates which were fixed on the sample holder with cooper scotch tape. In order to observe the side-view of multi-layer graphene materials, the sample holder was tilted for 90° inside the vacuum chamber. The morphology details of different materials are discussed in the following chapters.

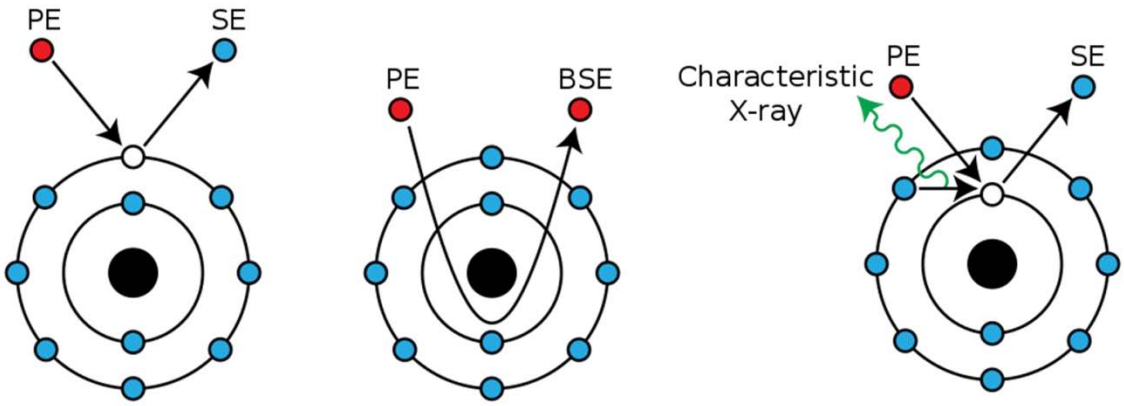

Figure 4-21. Mechanisms of emission of secondary electrons (SE), backscattered electrons (BSE), and characteristic X-rays from atoms of the sample. Free copyright and reproduced from https://commons.wikimedia.org/wiki/File:Electron_emission_mechanisms.svg.

4.4. References

1. Sheng, Z. H.; Shao, L.; Chen, J. J.; Bao, W. J.; Wang, F. B.; Xia, X. H., Catalyst-Free Synthesis of Nitrogen-Doped Graphene via Thermal Annealing Graphite Oxide with Melamine and Its Excellent Electrocatalysis. *ACS Nano* **2011,** *5*, 4350-4358.
2. Wang, S. Y.; Zhang, L. P.; Xia, Z. H.; Roy, A.; Chang, D. W.; Baek, J. B.; Dai, L. M., BCN Graphene as Efficient Metal-Free Electrocatalyst for the Oxygen Reduction Reaction. *Angew. Chem. Int. Ed.* **2012,** *51*, 4209-4212.
3. Chen, D.; Tang, L. H.; Li, J. H., Graphene-based materials in electrochemistry. *Chem. Soc. Rev.* **2010,** *39*, 3157-3180.
4. Lin, Z. Y.; Waller, G.; Liu, Y.; Liu, M. L.; Wong, C. P., Facile Synthesis of Nitrogen-Doped Graphene via Pyrolysis of Graphene Oxide and Urea, and its Electrocatalytic Activity toward the Oxygen-Reduction Reaction. *Adv. Energy Mater.* **2012,** *2*, 884-888.
5. Wang, Y.; Shao, Y. Y.; Matson, D. W.; Li, J. H.; Lin, Y. H., Nitrogen-Doped Graphene and Its Application in Electrochemical Biosensing. *ACS Nano* **2010,** *4*, 1790-1798.
6. Kang, X. H.; Wang, J.; Wu, H.; Aksay, I. A.; Liu, J.; Lin, Y. H., Glucose Oxidase-graphene-chitosan modified electrode for direct electrochemistry and glucose sensing. *Biosens. Bioelectron.* **2009,** *25*, 901-905.
7. Georgakilas, V.; Tiwari, J. N.; Kemp, K. C.; Perman, J. A.; Bourlinos, A. B.; Kim, K. S.; Zboril, R., Noncovalent Functionalization of Graphene and Graphene Oxide for Energy Materials, Biosensing, Catalytic, and Biomedical Applications. *Chem. Rev.* **2016,** *116*, 5464-5519.
8. Shan, C. S.; Yang, H. F.; Song, J. F.; Han, D. X.; Ivaska, A.; Niu, L., Direct Electrochemistry of Glucose Oxidase and Biosensing for Glucose Based on Graphene. *Anal. Chem.* **2009,** *81*, 2378-2382.
9. Pumera, M.; Ambrosi, A.; Bonanni, A.; Chng, E. L. K.; Poh, H. L., Graphene for electrochemical sensing and biosensing. *Trends Anal. Chem.* **2010,** *29*, 954-965.
10. Pumera, M., Graphene in biosensing. *Mater. Today* **2011,** *14*, 308-315.
11. Zhou, M.; Zhai, Y. M.; Dong, S. J., Electrochemical Sensing and Biosensing Platform Based on Chemically Reduced Graphene Oxide. *Anal. Chem.* **2009,** *81*, 5603-5613.
12. Zhang, L. M.; Xia, J. G.; Zhao, Q. H.; Liu, L. W.; Zhang, Z. J., Functional Graphene Oxide as a Nanocarrier for Controlled Loading and Targeted Delivery of Mixed Anticancer Drugs. *Small* **2010,** *6*, 537-544.
13. Yang, X. Y.; Zhang, X. Y.; Ma, Y. F.; Huang, Y.; Wang, Y. S.; Chen, Y. S., Superparamagnetic graphene oxide-Fe3O4 nanoparticles hybrid for controlled targeted drug carriers. *J. Mater. Chem.* **2009,** *19*, 2710-2714.
14. Bitounis, D.; Ali-Boucetta, H.; Hong, B. H.; Min, D. H.; Kostarelos, K., Prospects and Challenges of Graphene in Biomedical Applications. *Adv. Mater.* **2013,** *25*, 2258-2268.
15. Zhang, L. M.; Lu, Z. X.; Zhao, Q. H.; Huang, J.; Shen, H.; Zhang, Z. J., Enhanced Chemotherapy Efficacy by Sequential Delivery of siRNA and Anticancer Drugs Using PEI-Grafted Graphene Oxide. *Small* **2011,** *7*, 460-464.
16. Feng, L. Y.; Wu, L.; Qu, X. G., New Horizons for Diagnostics and Therapeutic Applications of Graphene and Graphene Oxide. *Adv. Mater.* **2013,** *25*, 168-186.
17. Liu, Y.; Zhou, J.; Zhang, X.; Liu, Z.; Wan, X.; Tian, J.; Wang, T.; Chen, Y., Synthesis, characterization and optical limiting property of covalently oligothiophene-functionalized graphene material. *Carbon* **2009,** *47*, 3113-3121.
18. Yu, D.; Yang, Y.; Durstock, M.; Baek, J.-B.; Dai, L., Soluble P3HT-Grafted Graphene for Efficient Bilayer−Heterojunction Photovoltaic Devices. *ACS Nano* **2010,** *4*, 5633-5640.
19. Melucci, M.; Treossi, E.; Ortolani, L.; Giambastiani, G.; Morandi, V.; Klar, P.; Casiraghi, C.; Samorì, P.; Palermo, V., Facile covalent functionalization of graphene oxide using

microwaves: bottom-up development of functional graphitic materials. *J. Mater. Chem.* **2010,** *20*, 9052-9060.
20. Xu, Y.; Liu, Z.; Zhang, X.; Wang, Y.; Tian, J.; Huang, Y.; Ma, Y.; Zhang, X.; Chen, Y., A Graphene Hybrid Material Covalently Functionalized with Porphyrin: Synthesis and Optical Limiting Property. *Adv. Mater.* **2009,** *21*, 1275-1279.
21. Si, Y.; Samulski, E. T., Synthesis of Water Soluble Graphene. *Nano Lett.* **2008,** *8*, 1679-1682.
22. Chen, Y.; Zhang, X.; Yu, P.; Ma, Y., Stable dispersions of graphene and highly conducting graphene films: a new approach to creating colloids of graphene monolayers. *Chem. Commun.* **2009**, 4527-4529.
23. Liu, Z.; Robinson, J. T.; Sun, X.; Dai, H., PEGylated Nanographene Oxide for Delivery of Water-Insoluble Cancer Drugs. *J. Am. Chem. Soc.* **2008,** *130*, 10876-10877.
24. Yang, K.; Zhang, S.; Zhang, G.; Sun, X.; Lee, S.-T.; Liu, Z., Graphene in Mice: Ultrahigh In Vivo Tumor Uptake and Efficient Photothermal Therapy. *Nano Lett.* **2010,** *10*, 3318-3323.
25. Chen, W. F.; Li, S. R.; Chen, C. H.; Yan, L. F., Self-Assembly and Embedding of Nanoparticles by In Situ Reduced Graphene for Preparation of a 3D Graphene/Nanoparticle Aerogel. *Adv. Mater.* **2011,** *23*, 5679-+.
26. Guo, S. J.; Wen, D.; Zhai, Y. M.; Dong, S. J.; Wang, E. K., Platinum Nanoparticle Ensemble-on-Graphene Hybrid Nanosheet: One-Pot, Rapid Synthesis, and Used as New Electrode Material for Electrochemical Sensing. *ACS Nano* **2010,** *4*, 3959-3968.
27. Yin, H. J.; Zhao, S. L.; Wan, J. W.; Tang, H. J.; Chang, L.; He, L. C.; Zhao, H. J.; Gao, Y.; Tang, Z. Y., Three-Dimensional Graphene/Metal Oxide Nanoparticle Hybrids for High-Performance Capacitive Deionization of Saline Water. *Adv. Mater.* **2013,** *25*, 6270-6276.
28. Pan, X.; Zhao, Y.; Liu, S.; Korzeniewski, C. L.; Wang, S.; Fan, Z. Y., Comparing Graphene-TiO2 Nanowire and Graphene-TiO2 Nanoparticle Composite Photocatalysts. *ACS Appl. Mater.* **2012,** *4*, 3944-3950.
29. Kuila, T.; Bose, S.; Mishra, A. K.; Khanra, P.; Kim, N. H.; Lee, J. H., Chemical functionalization of graphene and its applications. *Prog. Mater. Sci.* **2012,** *57*, 1061-1105.
30. Chen, D.; Feng, H.; Li, J., Graphene Oxide: Preparation, Functionalization, and Electrochemical Applications. *Chem. Rev.* **2012,** *112*, 6027-6053.
31. Dreyer, D. R.; Park, S.; Bielawski, C. W.; Ruoff, R. S., The chemistry of graphene oxide. *Chem. Soc. Rev.* **2010,** *39*, 228-240.
32. Georgakilas, V.; Otyepka, M.; Bourlinos, A. B.; Chandra, V.; Kim, N.; Kemp, K. C.; Hobza, P.; Zboril, R.; Kim, K. S., Functionalization of Graphene: Covalent and Non-Covalent Approaches, Derivatives and Applications. *Chem. Rev.* **2012,** *112*, 6156-6214.
33. Yan, L.; Zheng, Y. B.; Zhao, F.; Li, S.; Gao, X.; Xu, B.; Weiss, P. S.; Zhao, Y., Chemistry and physics of a single atomic layer: strategies and challenges for functionalization of graphene and graphene-based materials. *Chem. Soc. Rev.* **2012,** *41*, 97-114.
34. Liu, W.; Speranza, G., Functionalization of Carbon Nanomaterials for Biomedical Applications. *C-Journal of Carbon Research* **2019,** *5*, 72.
35. Stratakis, M.; Garcia, H., Catalysis by Supported Gold Nanoparticles: Beyond Aerobic Oxidative Processes. *Chem. Rev.* **2012,** *112*, 4469-4506.
36. Herves, P.; Perez-Lorenzo, M.; Liz-Marzan, L. M.; Dzubiella, J.; Lu, Y.; Ballauff, M., Catalysis by metallic nanoparticles in aqueous solution: model reactions. *Chem. Soc. Rev.* **2012,** *41*, 5577-5587.
37. Campelo, J. M.; Luna, D.; Luque, R.; Marinas, J. M.; Romero, A. A., Sustainable Preparation of Supported Metal Nanoparticles and Their Applications in Catalysis. *ChemSusChem* **2009,** *2*, 18-45.
38. Wu, S.; Dzubiella, J.; Kaiser, J.; Drechsler, M.; Guo, X. H.; Ballauff, M.; Lu, Y., Thermosensitive Au-PNIPA Yolk-Shell Nanoparticles with Tunable Selectivity for Catalysis. *Angew. Chem. Int. Ed.* **2012,** *51*, 2229-2233.

39. Wunder, S.; Lu, Y.; Albrecht, M.; Ballauff, M., Catalytic Activity of Faceted Gold Nanoparticles Studied by a Model Reaction: Evidence for Substrate-Induced Surface Restructuring. *ACS Catal.* **2011,** *1*, 908-916.
40. Mayer, K. M.; Hafner, J. H., Localized Surface Plasmon Resonance Sensors. *Chem. Rev.* **2011,** *111*, 3828-3857.
41. Anker, J. N.; Hall, W. P.; Lyandres, O.; Shah, N. C.; Zhao, J.; Van Duyne, R. P., Biosensing with plasmonic nanosensors. *Nat. Mater.* **2008,** *7*, 442-453.
42. Jain, P. K.; Huang, X. H.; El-Sayed, I. H.; El-Sayed, M. A., Noble Metals on the Nanoscale: Optical and Photothermal Properties and Some Applications in Imaging, Sensing, Biology, and Medicine. *Acc. Chem. Res.* **2008,** *41*, 1578-1586.
43. Zeng, S. W.; Yong, K. T.; Roy, I.; Dinh, X. Q.; Yu, X.; Luan, F., A Review on Functionalized Gold Nanoparticles for Biosensing Applications. *Plasmonics* **2011,** *6*, 491-506.
44. Tiwari, P. M.; Vig, K.; Dennis, V. A.; Singh, S. R., Functionalized Gold Nanoparticles and Their Biomedical Applications. *Nanomaterials* **2011,** *1*, 31-63.
45. Mout, R.; Moyano, D. F.; Rana, S.; Rotello, V. M., Surface functionalization of nanoparticles for nanomedicine. *Chem. Soc. Rev.* **2012,** *41*, 2539-2544.
46. Jain, P. K.; Lee, K. S.; El-Sayed, I. H.; El-Sayed, M. A., Calculated absorption and scattering properties of gold nanoparticles of different size, shape, and composition: Applications in biological imaging and biomedicine. *J. Phys. Chem. B* **2006,** *110*, 7238-7248.
47. Giljohann, D. A.; Seferos, D. S.; Daniel, W. L.; Massich, M. D.; Patel, P. C.; Mirkin, C. A., Gold Nanoparticles for Biology and Medicine. *Angew. Chem. Int. Ed.* **2010,** *49*, 3280-3294.
48. Dreaden, E. C.; Alkilany, A. M.; Huang, X.; Murphy, C. J.; El-Sayed, M. A., The golden age: gold nanoparticles for biomedicine. *Chem. Soc. Rev.* **2012,** *41*, 2740-2779.
49. Wang, Z. X.; Ma, L. N., Gold nanoparticle probes. *Coordin. Chem. Rev.* **2009,** *253*, 1607-1618.
50. Hainfeld, J. F.; Smilowitz, H. M.; O'Connor, M. J.; Dilmanian, F. A.; Slatkin, D. N., Gold nanoparticle imaging and radiotherapy of brain tumors in mice. *Nanomedicine* **2013,** *8*, 1601-1609.
51. Wu, X.; He, X. X.; Wang, K. M.; Xie, C.; Zhou, B.; Qing, Z. H., Ultrasmall near-infrared gold nanoclusters for tumor fluorescence imaging in vivo. *Nanoscale* **2010,** *2*, 2244-2249.
52. Nicoletti, O.; de la Pena, F.; Leary, R. K.; Holland, D. J.; Ducati, C.; Midgley, P. A., Three-dimensional imaging of localized surface plasmon resonances of metal nanoparticles. *Nature* **2013,** *502*, 80-+.
53. Jain, P. K.; Huang, X.; El-Sayed, I. H.; El-Sayed, M. A., Review of Some Interesting Surface Plasmon Resonance-enhanced Properties of Noble Metal Nanoparticles and Their Applications to Biosystems. *Plasmonics* **2007,** *2*, 107-118.
54. Sperling, R. A.; Rivera Gil, P.; Zhang, F.; Zanella, M.; Parak, W. J., Biological applications of gold nanoparticles. *Chem. Soc. Rev.* **2008,** *37*, 1896-1908.
55. Schmid, T.; Dariz, P., Raman Microspectroscopic Imaging of Binder Remnants in Historical Mortars Reveals Processing Conditions. *Herit.* **2019,** *2*, 1662-1683.
56. Choudhary, R. C.; Kumaraswamy, R. V.; Kumari, S.; Pal, A.; Raliya, R.; Biswas, P.; Saharan, V., Synthesis, Characterization, and Application of Chitosan Nanomaterials Loaded with Zinc and Copper for Plant Growth and Protection. In *Nanotechnology: An Agricultural Paradigm*, Prasad, R.; Kumar, M.; Kumar, V., Eds. Springer Singapore: Singapore, 2017; pp 227-247.
57. Binnig, G.; Rohrer, H.; Gerber, C.; Weibel, E., Surface Studies by Scanning Tunneling Microscopy. *Phys. Rev. Lett.* **1982,** *49*, 57-61.
58. Binnig, G.; Rohrer, H.; Gerber, C.; Weibel, E., 7 \ifmmode\times\else\texttimes\fi{} 7 Reconstruction on Si(111) Resolved in Real Space. *Phys. Rev. Lett.* **1983,** *50*, 120-123.
59. Butt, H.-J.; Cappella, B.; Kappl, M., Force measurements with the atomic force microscope: Technique, interpretation and applications. *Surf. Sci. Rep.* **2005,** *59*, 1-152.

Chapter 5

Graphene-molecules hybrid materials based pressure sensor for human health monitoring

Pressure sensors are devices capable of monitoring and quantifying an applied pressure through an electrical readout. It can be divided into piezoresistive pressure sensor, piezoelectric pressure sensor, capacitive pressure sensor *etc.* based on the working mechanisms. In piezoresistive pressure sensor, the electrical resistance changes as a function of an applied pressure. Due to its high sensitivity, fast response, and ease of fabrication, it has been the subject of various studies. In this chapter, we discuss a radically new type of piezoresistive pressure sensor based on a millefeuille-like architecture of reduced graphene oxide (rGO) intercalated by covalently tethered molecular pillars holding on-demand mechanical properties. By applying a tiny pressure to the multilayer structure, the electron tunneling ruling the charge transport between successive rGO sheets yields a colossal decrease in the material's electrical resistance. Significantly, the intrinsic rigidity of the molecular pillars employed enables the fine-tuning of the sensor's sensitivity, reaching sensitivities as high as 0.82 kPa^{-1} at low pressure region (0-0.6 kPa), with short response times (≈24 ms) and detection limit (7 Pa). Our pressure sensors enable the efficient heartbeat monitoring and can be easily transformed into a matrix capable of providing a 3D map of the pressure exerted by different objects.

5.1. Introduction

The basic concepts and fundamental aspects of pressure sensor have been discussed in Chapter 3. Pressure sensors are devices capable of generating electrical signals in response to a change in pressure.[1, 2] The sensitivity of the pressure sensor, defined as the ratio between the change in the electrical signal output and the applied pressure, is the most important parameter to evaluate the performance of pressure sensor. Sensors featuring high sensitivities are capable of detecting extremely small changes in the pressure, and can be exploited even to transduce muscle movements[3, 4] as well as the subtle vibrations of sound[5-8] into electrical outputs.

Compared to the complicated fabrication methods such as microelectromechanical systems (MEMS)[9, 10] and microfluidics techniques[11], the engineering of the structure of active material represents the simplest and the most straightforward approach for the fabrication of pressure sensors with high sensitivity. For example, upon applying a pressure, cracks and structural defects can be generated, which results in modification of the percolation pathways for charge transport, and can ultimately result in large variations in the electrical output.[12-14] Moreover, the contact resistance at the electrode-active layer interface can be modulated by pressure resulting into an improvement of the sensitivity.[15-18] Furthermore, a change in capacitance can be induced by pressure, which is the working principle of capacitive pressure sensor. In that case the sensitivity can be improved by micro structuration of the dielectric layer between electrodes.[19-21] Although these methods can indeed improve the sensitivity of the device, their applications are generally limited due to the complicated nature of the fabrication process, high production cost and high operating voltage. Conversely, piezoelectric sensors are usually not chosen because they display lower pressure sensitivities and can be hardly integrated into flexible electronic skins.[21]

5.2. Results and discussion

In this chapter, we have developed a novel and simple method to drastically improve the sensitivity of a piezoresistive pressure sensor. The active material has been assembled by reacting commercially available GO with amino functionalized molecules in order to form covalent bonds on the basal plane of GO through the epoxy ring-opening reaction (Figure 5-1a). Three organic molecules characterized by a similar contour length and increasing rigidity, namely triethylene glycol (TEG) amine (**R1**), 1-octylamine (**R2**) and 4-aminobiphenyl (**R3**) were chosen as the molecular units. Upon condensation of **R1**-**R3** with GO, hybrid structures are obtained in the form of ink dispersed in ethanol. In this way the growth of molecular pillars occurs specifically along the axis perpendicular to the graphene basal plane,[22] yet, the amidation of carboxyl groups, present at the edges of GO sheets may occur as a side reaction. Such chemically modified GO (CMGO) has been chemically reduced with hydrazine[23] to restore high electrical conductivities (for details see experimental methods). The as-obtained conducting ink can be deposited onto arbitrary substrates by spray-coating, yielding multilayer structures with spacing between adjacent GO sheets which are dictated by the employed molecular pillars, *i.e.* **R1**-**R3** molecules. Significantly, the latter possess different compressibility, resulting from the intrinsic flexibility of the chosen molecules. The CMGO containing molecules possessing the highest flexibility should display the largest compressibility at a given pressure, thus leading to the highest sensitivity to detect changes of pressure. In analogy to the Hooke's law ruling the compressibility of macroscopic springs, we demonstrate that the sensitivity of the pressure sensor can be improved from **rGO-R$_3$** (0.32 kPa^{-1}) to **rGO-R$_1$** (0.82 kPa^{-1}) by using more flexible linkers acting as molecular springs separating rGO layers (Figure 5-1b). Compared to the other approaches employed so far,[12, 18, 21] this method shows several additional advantages (Table 1) that render it of potential interest for technological applications including the low cost production, simple device fabrication and low operating voltage (0.2 V).

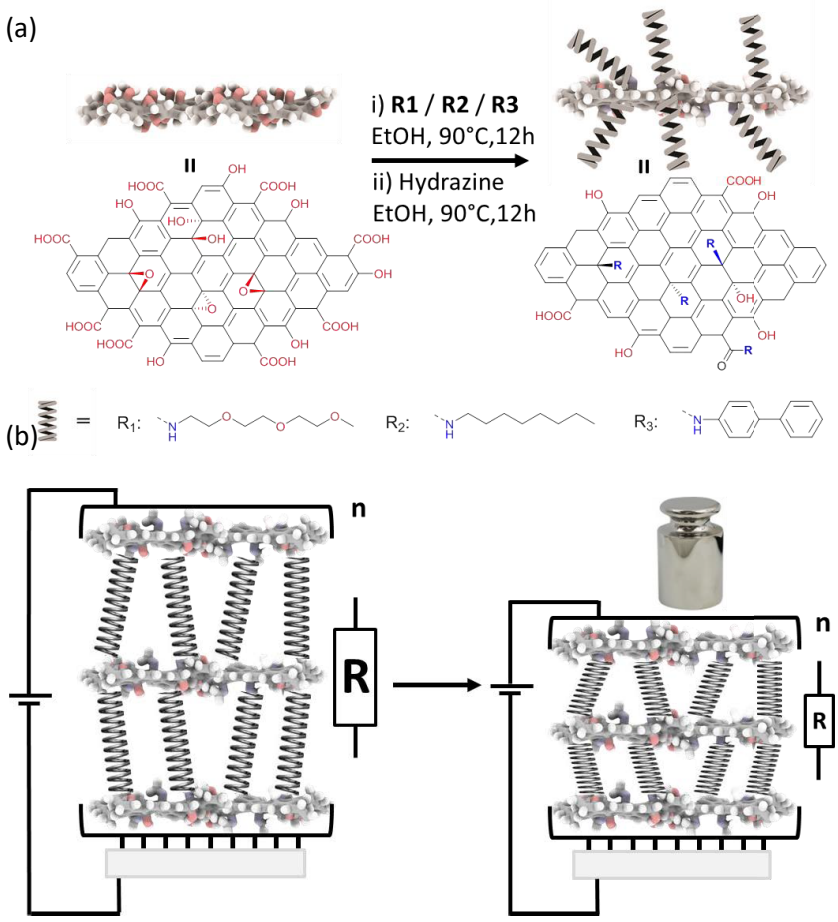

Figure 5-1. (a) Synthesis and architecture of rGO-R_1, rGO-R_2, and rGO-R_3. (b) Schematic of working principle of the pressure sensor.

Table 1: Key parameters of piezoresistive pressure sensor (state of the art)[a]

Active materials [Ref.]	Flexibility	Minimum detection	Response time	Sensitivity[b] (kPa^{-1})	Cyclability
Graphene/PU[12]	flexible	9 Pa	-	0.26	10000
RGO micropyramid[17]	flexible	1.5 Pa	0.1 ms	5.5	8000
SSNPs-PU[24]	flexible	300 Pa	30 ms	2.46	200
Au-PPy[25]	-	2 Pa	100 ms	1.8	-
GO/Graphene[8]	flexible	0.15 g	0.1 ms	0.032	8000
PEDOT:PSS–SWCNT[26]	flexible	28 Pa	77 ms	0.5	2000

[a] Piezoresistive pressure sensors are mainly focused here, and some works[27, 28] are not listed due to the different calculation method of sensitivity. [b] (Sensitivity=$\delta(\Delta R/R_0)/\delta p$)

The multiscale characterization of various physico-chemical properties of the GO based hybrid structures have been carried out using different experimental techniques (detailed information has been discussed in *Experimental Methods*). X-ray photoelectron spectroscopy (XPS) provided quantitative insight into the chemical composition of hybrid material. In particular, the significant difference between the carbon, oxygen and nitrogen peaks provided evidence for the formation of a chemical bond between the oxygen-containing functional groups on the surface of GO and amine groups from **R1**-**R3** molecules (Figure 5-7, Figure 5-8, Figure 5-9). The interlayer distance (d_{002}) between modified GO sheets with **R** molecules is characterized by wide-angle X-ray scattering (WAXS). After functionalization the 2θ peak of **GO-R$_{1\text{-}3}$** shifts toward lower angles compared to pristine GO, which indicates an increase in the interlayer distance (Figure 5-10). The efficiency of the reaction has also been confirmed by Raman spectroscopy (Figure 5-11) and infrared spectroscopy (FTIR) (Figure 5-12). The porosity of functionalized graphene has been investigated by the means of BET measurements (Figure 5-13). Details on the details of analysis and results obtained by XPS, WAXS, Raman, BET and FTIR are provided in the *Experimental Methods*.

The pressure sensors have been fabricated by following the procedure displayed in Figure 5-2a. Functionalized reduced graphene oxide inks (**rGO-R$_1$**, **rGO-R$_2$** or **rGO-R$_3$**) have been spray-coated through a shadow mask onto the surface of ITO-PET. The amount of deposited material was monitored by UV-Vis absorption as shown in Figure 5-15. Images of scanning electron microscopy (SEM, Figure 5-16) display flakes stacked perpendicularly to the surface of the electrode forming a multilayer architecture, which can be further verified by the tilted or side view of spray coated **rGO-R$_1$**. After the removal of the shadow mask, two substrates have been fixed together in face-to-face fashion and sealed with Kapton tape preventing the interference of humidity. Finally, the extremities of the PET film have been contacted with copper wires using silver paste.

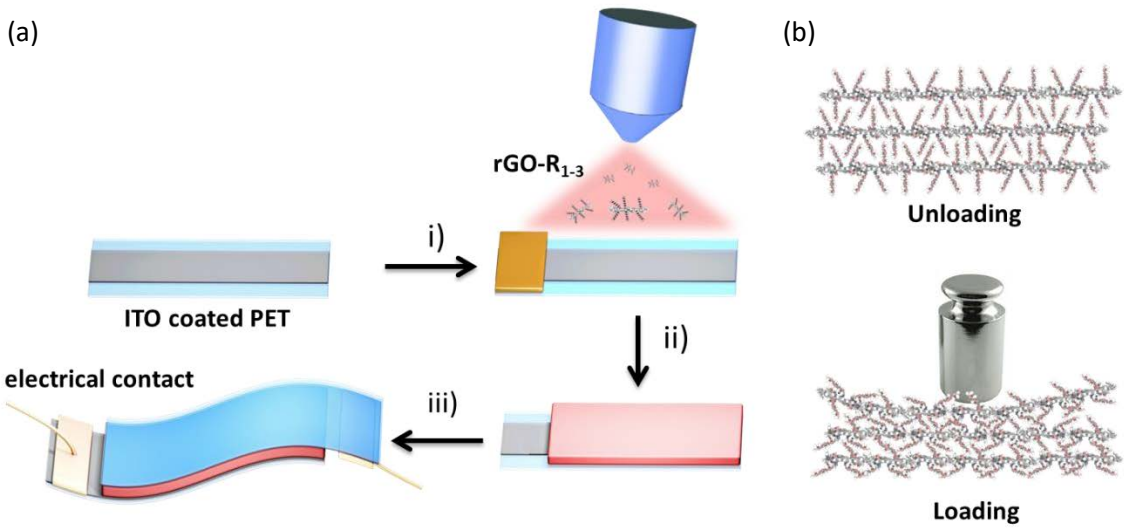

Figure 5-2. (a) Pressure sensor fabrication process: i) spray coating of rGO-R_{1-3} in presence of a shadow mask on commercially available ITO-PET which was cut into stripes (13 mm × 20 mm); ii) mask removal; iii) face-to-face assembly and wire out with copper wire and silver paste. (b) Schematic illustration of the inner structure change of the functionalized graphene upon loading pressure.

The performance of pressure sensors has been investigated by exploiting a force gauge equipped with a movement-control stand combined with a source-meter to offer a steady bias voltage. Step force from 0.005 N to 1 N has been applied on the device (contact area is 1.04 cm^2). The conversion of mechanical displacement into electrical signal is achieved by measuring the current change under different applied forces. The sensitivity of the different pressure sensors can be calculated by using the equation $S=\delta(\Delta R/R_0)/\delta P$, with P being the applied pressure, R and R_0 being the resistance with or without applied pressure, respectively.[12] As shown in Figure 5-3a, the sensitivity of each pressure sensor is defined as S_1, S_2, S_3 and S_4 for **rGO-R_1**, **rGO-R_2**, **rGO-R_3** and unfunctionalized rGO (blank experiment) respectively, in the low-pressure region from 0 to ca. 0.6 kPa. Among all the three functionalized graphene based pressure sensors the one containing **R1** pillars, *i.e.* (**rGO-R_1**) shows the highest sensitivity of 0.82 kPa^{-1}. The pressure sensor made with **rGO-R_2** shows the medium sensitivity of 0.47 kPa^{-1} and the one made with **rGO-R_3** shows the lowest sensitivity of 0.32 kPa^{-1}. Noteworthy, all the three functionalized graphene based pressure sensors display prominently higher sensitivity than the one based on neat rGO, the latter exhibiting a negligible response (0.073 kPa^{-1}).

The detected difference in sensitivities can be explained by the fact that the current passing through the rGO-based vertical junction is strongly affected by extremely small changes of

the interlayer distance between the rGO sheets, which is in turn dictated by the flexibility (or conformation) of the molecular bridges (Figure 5-2b). Laser Scanning Confocal Microscopy (LSCM) measurements revealed that the interlayer distance of functionalized graphene materials decreases when a pressure is applied (Figure 5-14), thus yielding an increase in the tunnelling current. The contribution to resistance variation determined by the contact resistance has been found being negligible as revealed by performing blank experiment with neat rGO as active material (Figure 5-3a, green line) and the effect caused by pore structure has been excluded by BET analysis (Table 2, Figure 5-13). The electron transport mechanism has been proved to be direct electron tunnelling by temperature dependent electrical conductivity measurement (see Figure 5-17 for detailed analysis). The molecular flexibility is related to the intrinsic conformational degree of freedom of carbon and/or oxygen atoms around their chain bonds. Persistence length (L_p) has been widely used to quantify the flexibility or stiffness of polymers, in which the smaller is the L_p, the more flexible is the polymer.[29-31] Here the three molecular linkers **R1**, **R2** and **R3** can be considered as small oligomers of polyethylene glycol (PEG), polyethylene (PE) and poly-(p-phenylene) (PPP) polymers, respectively. Thus, by considering the L_p of each polymer, which amounts to 0.37 nm for PEG[29], 0.65 nm for PE[30] and 28 nm for PPP[31], **R1** should be the most flexible linker while **R3** the most rigid one. The trend we have observed for the sensitivity is in excellent agreement with the different L_n of the molecular linkers suggesting that the more flexible is the linker the higher is the sensitivity. Furthermore, the vertical amplitude of the error bar associated to $\Delta R/R_0$ (Figure 5-3a) is increasing as L_n is decreasing, suggesting that flexible linkers can possess different conformations at the same pressure.

The response of the devices to a dynamic force has also been investigated through finger press, bending test, light object trigger and fatigue test. For these experiments, the pressure sensor containing **rGO-R1** as active material has been employed due to its highest sensitivity. As shown in Figure 5-3b, quick press and release of a finger on the device leads to a quick response, which results in sharp peaks of current. The response time (t_1) and recovery time (t_2) of **rGO-R1** are 24 ms and 10 ms (inset in Figure 5-3b) respectively, which are 3~5 times faster than those reported for pressure sensors made with reduced graphene oxide.[32, 33] Figure 5-3c shows the dynamic response of pressure sensor **rGO-R1** during bending test. During bending cycles (1.5 cm bending radius, 100° bending angle) sharp peaks of current have been recorded demonstrating high flexibility and robustness of the sensor. By taking full advantage of the high sensitivity, the pressure sensor can also detect ultra-small pressure fluctuations as tiny as 7 Pa. A paper-folding star (ca. 70 mg, corresponding to 7 Pa, inset in Figure 5-3d) has been placed-and-removed continuously onto the pressure sensor, causing a distinct change of current. The ability of sensing such small pressures once again represents an unambiguous

evidence of the high sensitivity of this material and device thereof. The excellent cyclability of the device has been verified by fatigue test as shown in Figure 5-18. After 2000 cycles of press-release with the pressure of 3 kPa, the on-state signal is still stable, demonstrating the high robustness of the device which is fundamental for a future commercialization. The negligible upper shift of baseline might be caused by some irreversible deformation of graphene layers between flexible electrodes.

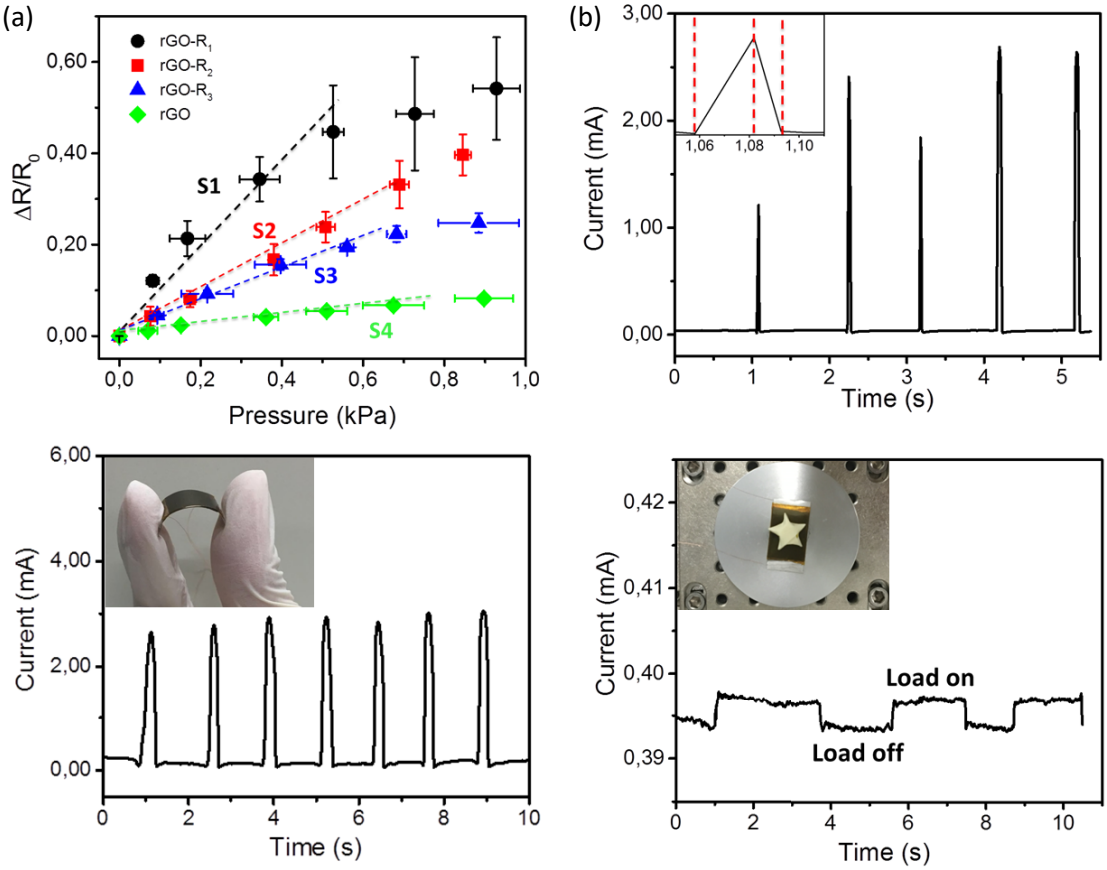

Figure 5-3. (a) Relative resistance as a function of the pressure applied for sensor rGO-R_1 (black circles), rGO-R_2 (red squares), rGO-R_3 (blue triangle), and rGO (green diamond) (error bar: mean±SD). Response of pressure sensor rGO-R_1 to consecutive finger press (b), bending test (c) and light object (d) (inset: a paper folding star, ca. 70 mg, corresponding to the pressure of 7 Pa).

Due to the high sensitivity, fast response to both pressure changes and bending as well as ultralow detection limit and high robustness, such pressure sensor can be implemented into wearable electronic devices for healthcare, human-machine interface, and digital tactile system *etc.* As a proof-of-concept we have employed the pressure sensor (**rGO-R_1**) to

monitor wrist pulse and carotid artery pulse of an adult male, which are generally used to evaluate the health condition of human body.[19, 34] As shown in Figure 5-4a, the pressure sensor has been placed on an adhesive bandage and fixed to the wrist or to the neck of the tested human object, who voluntarily took part in this proof-of-concept demonstration with full understanding of the process and any risks involved. A stationary signal has been recorded from which the radial artery frequency (65 pulses min^{-1}) and carotid artery frequency (61 pulses min^{-1}) can be obtained, indicating that the subject in good health condition as an adult male. More importantly, due to the high resolution of the radial artery pulse curve, we can clearly observe two distinguish peaks, P1 which refers to the sum of ejected wave and reflected wave, and P2 which is the peak of the reflected wave from the lower body minus end-diastolic pressure. Thus we can calculate two important parameters, *i.e.* the radial artery augmentation index (AI_r) and the time between two peaks (ΔT_{DVP}), which are commonly used for arterial stiffness diagnosis.[44] According to the measured results, $AI_r \approx 61\%$, $\Delta T_{DVP} \approx 0.26$ s further verify the good health condition of the subject. All these results indicate that the pressure sensor (**rGO-R$_1$**) can be successfully applied to human health monitoring.

Furthermore, we provide a demonstration of a sensor matrix by assembling the PET-ITO thin strips to a network as shown in Figure 5-6. In this way the sensor can be used not only to measure the pressure, but to capture spatial information. Each cross point will indeed act as a pressure sensor and used as pixel to form a rough 3D mapping. The sensing matrix is made with a similar architecture of the pressure sensors discussed above, which is composed by ITO-PET as electrodes and **rGO-R$_1$** as active material in between. The pressure is determined by measuring the change of relative resistance ($\Delta R/R_0$) of each pixel. As shown in Figure 5-4d, a bolt (mass = 6.1 g) with an annular bottom was placed on the matrix and its contact area (white dash circle) corresponds to the pixels plotted by the electrical output. The highest relative resistance change ($\Delta R/R_0$) occurs in pixel “3D”, which indicates the centre of gravity of the bolt. This pressure sensor matrix is also applicable for objects with irregular contact area. Figure 5-4e reveals the four contact points of a stone (mass = 67.2 g), whose weight is mostly located in position “4C”. By expressing the pressure value in the Z-scale of each pixel, a 3D map of the weight distribution has been obtained as shown in Figure 5-4f. Such results provide clear evidence for the potential of such arrays for being implemented into multi-touch devices.

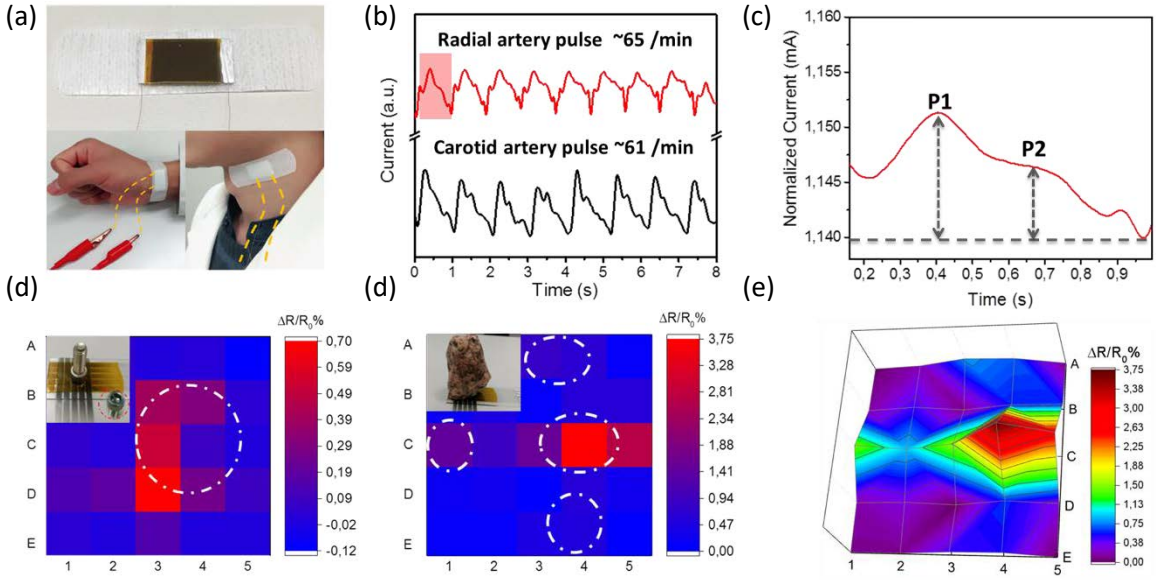

Figure 5-4. Sensing application on human health monitoring (a-c) and sensor matrix for 3D mapping (d-f). (a) radial artery pulse and carotid artery pulse detection assembled by adhesive bandage; (b) The signals of radial artery pulse (top) and carotid artery pulse (bottom). (c) Magnification of a single peak of radial artery pulse (marked with a red square in Figure 5-4b). Relative resistance mapping of pressure sensor matrix when putting a bolt (d) or a stone (e) on the pressure sensor matrix (white circles: actual contact area). (f) 3D map of the pressure distribution of the stone in Figure 5-4e.

5.3. Experimental methods

5.3.1. Material

Graphene oxide (GO) (4 mg/ml, water dispersion) was purchased from Graphenea. Triethylene glycol amine has been synthetized as reported. All the chemicals and reagents were purchased from Sigma-Aldrich and used without further purification.

5.3.1.1. Synthesis of triethylene glycol amine

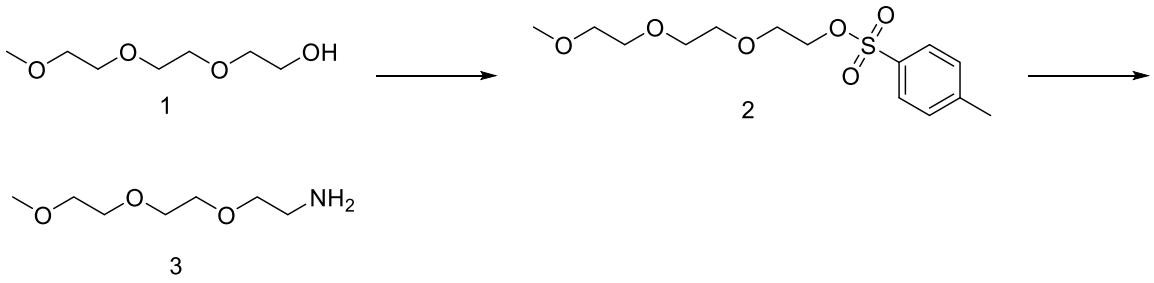

Figure 5-5. Synthesis of triethylene glycol amine.

All the solvents and chemicals were used as received from Aldrich without any further purification. ^{1}H NMR spectra were recorded on a Bruker Avance 400 spectrometer. The ^{1}H NMR chemical shifts (δ) are given in ppm and referred to residual protons on the corresponding deuterated solvent. All deuterated solvents were used as received without any further purification.

2-[2-(2-Methoxyethoxy)ethoxy]ethyl *p*-toluenesulfonate (**2**).[35] Triethylene glycol monomethyl ether (**1**) (8.0 g, 48.7 mmol, 1 eq) was dissolved in 4 mL of THF. An aqueous NaOH (1.8 g, 45 mmol, 0.9 eq) solution (4 mL) was added to the reactant at 0 °C and then a THF solution (15 mL) of *p*-toluenesulfonyl chloride (TosCl) (8.6 g, 46 mmol, 0.9 eq) was added while stirring (1 h). After stirring at 0 °C (2 h), the reaction mixture was diluted with cold water (60 mL). The organic layer was separated, and the aqueous layer was extracted with DCM (3 × 50 mL). The combined organic layers were extracted 3 times with H_2O (50 mL). The organic layer was dried with Na_2SO_4 and evaporated in vacuum to yield 10.45 g (67%) of **2** as a yellow oil. ^{1}H NMR (400 MHz, $CDCl_3$) δ 7.80 (d, J = 8.3 Hz, 2H), 7.34 (d, J = 8.3 Hz, 2H), 4.21 – 4.13 (m, 2H), 3.73 – 3.65 (m, 2H), 3.65 – 3.56 (m, 6H), 3.57 – 3.49 (m, 2H), 3.37 (s, 3H), 2.45 (s, 3H).

Triethylene glycol amine (**3**).[35, 36] 5 g of **2** (15.7 mmol, 1 eq) was dissolved in 70 mL of EtOH, then sodium azide (1.8 g, 25.2 mmol, 2 eq) was added and the solution was stirred under

reflux for 16 h. The solution was concentrated to ca. 1/3 of volume under vacuum and 80 mL of water were added, then the ethanol was completely removed in vacuum. The remaining water solution was extracted with DCM 4 times. The organic layer was dried with Na_2SO_4 and evaporated in vacuum, The obtained yellow oil (2.98 g, 15.7 mmol, 1 eq) was added dropwise to a two neck flask containing 80 mL of anhydrous THF, triphenyilphosphine (5.9 g, 23.6 mmol) under N_2 at 0 °C, and the reaction was stirred overnight under N_2. Then 50 mL of water were added, and the reaction was stirred for 8 hours. Then the organic phase was evaporated, and the water phase was extracted 3 times with toluene. Finally, the water phase was dried under vacuum to obtain **3** as pure colorless oil (1.95 g; 75.9 % yield). ^{1}H NMR (400 MHz, $CDCl_3$) δ 3.68 – 3.62 (m, 6H), 3.55 (dd, *J* = 5.7, 3.6 Hz, 2H), 3.51 (t, *J* = 5.2 Hz, 2H), 3.38 (s, 3H), 2.86 (t, *J* = 5.2 Hz, 2H).

5.3.1.2. Synthesis of functionalized graphene rGO-R_{1-3}

50 ml water dispersion of GO (4 mg/ml) was diluted with 120 ml ethanol in a 250 ml round-bottom flask and sonicated for 30 min. Then 200 mg of the corresponding organic amine compound was weighed into a 10 mL glass vial and dissolved in 5 ml ethanol. The amine solution was then added into the GO dispersion and refluxed while stirring overnight at 90 °C under N_2 atmosphere. After cooling down the solution to room temperature, the dispersion was centrifuged for 10 min at 2000 rpm. Then the supernatant was removed, and 200 ml of ethanol were added to the black sludge. The mixture was sonicated for 10 min and centrifuged again. The sonication-centrifugation process was repeated 3 times. After the last centrifugation the black sludge (**GO-R_{1-3}**) was dispersed in 200 ml ethanol and sonicated 10 min.

The reduction process was carried out by adding 2 ml of hydrazine hydrate to **GO-R_{1-3}** ethanolic dispersion followed by refluxing overnight at 90 °C under N_2 atmosphere. The purification was performed through sonication-centrifugation cycles as described above for **GO-R_{1-3}**. The resulting dispersion was decanted and used for characterization and device fabrication.

5.3.2. Device fabrication

ITO-PET (surface resistivity: 60 Ω/sq, L × W × thickness 1 ft × 1 ft × 5 mil, thickness of ITO coating: 130 nm) was purchased from Sigma-Aldrich.

5.3.2.1. Pressure sensor fabrication process

ITO-PET foil was cut into rectangular pieces (13 mm × 20 mm). A part of the ITO was protected from the rGO deposition with a shadow mask (13 mm × 5 mm) to ensure a good electrical contact. After fixing the PET substrates on the hotplate (80 °C), the ethanolic dispersion of **rGO-R$_{1-3}$** was spray coated onto the surface and the amount of deposited material was monitored by UV-Vis absorption in order to obtain a film transmittance of 20% at the wavelength of 500 nm. Afterwards the mask was removed, and two electrodes were fixed together using polyimide (PI) tape keeping the active layer sandwiched in between. The clean ITO strips were then wired out with cooper wire and silver paste.

5.3.2.2. Pressure sensor matrix fabrication process

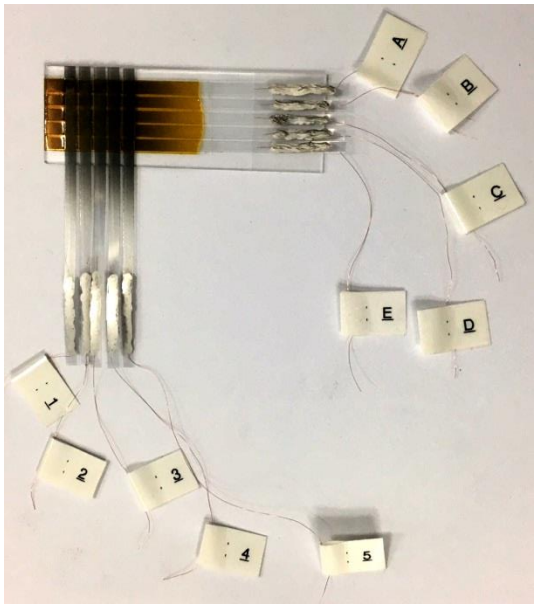

Figure 5-6. Photo of pressure sensor matrix based on rGO-R$_1$.

ITO-PET film was cut into 10 strips with the same width (3 mm), after which the dispersion of **rGO-R$_1$** was spray coated on the ITO surface. 5 ribbons were fixed on glass slide with the same intervals (2 mm) to be bottom electrodes and another 5 ribbons were fixed face to face on the top in a decussation way, thus making a 5×5 matrix with 25 pixels. The ends of the 10 strips were wired out with copper wires and silver paste.

5.3.3. Characterization

XPS analysis was performed with a Thermo Scientific K-Alpha X-ray photoelectron spectrometer. X-ray powder diffraction (XRD) has been acquired on a Bruker ASX D8 Advanced equipped with Cu anode. FT-IR spectra were recorded using a FT-IR-4700 Fourier Transform Infrared Spectrometer (JASCO) equipped with ATR Diamond. Raman spectra were acquired with a Renishaw InVia RE04 combined with a MS20 Encoded stage 100 nm and a 532 nm laser maintained at a power excitation below 1 mW. The measurements were carried out in ambient conditions with a 100x lens affording a beam spot of 800 nm. Scanning Electron Microscopy (SEM) images were recorded with a FEI Quanta FEG 250 instrument S3 (FEI corporate, Hillsboro, Oregon, USA). The sample was prepared by spray coating the **rGO-R$_{1-3}$** ethanol dispersion onto a silicon substrate. The UV-Vis absorption spectra were recorded using a Jasco V-670 UV-Vis spectrophotometer. Thicknesses of the spray-coated layers were determined by means of an Alpha-step KLA-Tencor Alpha-Step IQ Profilometer. The test system consists of a digital force gauge (Mark-10, M7-025E, ~1.0 N), a motorized test stand (Mark-10, ESM-303E), and a system source meter (Keithley, 2635B). Pressure sensor was fixed on the sample stage (diameter of round compression plate: 1.15 cm) and linked with source meter. Set points of pressure and bias voltage were controlled by MESUR gauge Plus software and Labtracer respectively.

5.3.3.1. XPS spectra of GO, GO-R1-3, rGO-R1-3

X-ray photoelectron spectroscopy (XPS) has been used to study the chemical composition of hybrid material by identifying the relevant chemical elements present in the neat and functionalized GO. In the wide energy spectrum of pristine GO, only two peaks at 286.7 eV and 532.3 eV are found, and are attributed to C1s and O1s, respectively (Figure 5-7). In contrast, the appearance of the N1s peak is observed in the wide energy spectrum of functionalized GO. Furthermore, a strong decrease in the oxygen signal is observed upon reduction of the samples with hydrazine.

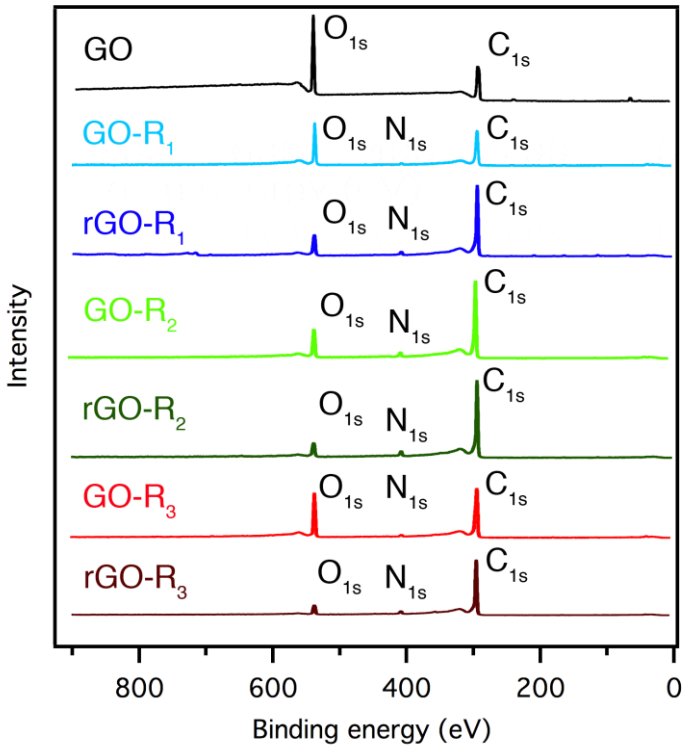

Figure 5-7. XPS spectra of GO, GO-R_{1-3}, rGO-R_{1-3}.

The C1s XPS spectrum of the neat GO (Figure 5-8) shows two main peaks at 284.6 eV (C-C) and 286.8 eV (C-O) and one smaller peak at 288.3 eV, which is ascribed to C=O bonds. Compared to GO, the C1s spectra of the functionalized **GO-R1**, **GO-R2** and **GO-R3** hybrid materials appear differently and feature peaks at 284.8 eV and 285.7 eV and broader peaks at 286.8 eV and 288.6 eV which can be assigned to C-C, C-N, C-O and C=O bonds, respectively. Interestingly, based on the ratio between the C-C and C-O peaks we have concluded that the distinct nature of molecular bridges used to covalently modify GO sheets resulted in different functionalization degree of GO. The highest functionalization degree, *i.e.* the lowest C-O signal intensity, has been observed for **R2** molecules. Furthermore, the C-O signal intensity suggested that **R3** molecules give higher functionalization degree than **R1**. Nevertheless, the initial conclusions based on the C1s spectra analysis have been re-evaluated based on the N1s spectra of all compounds.

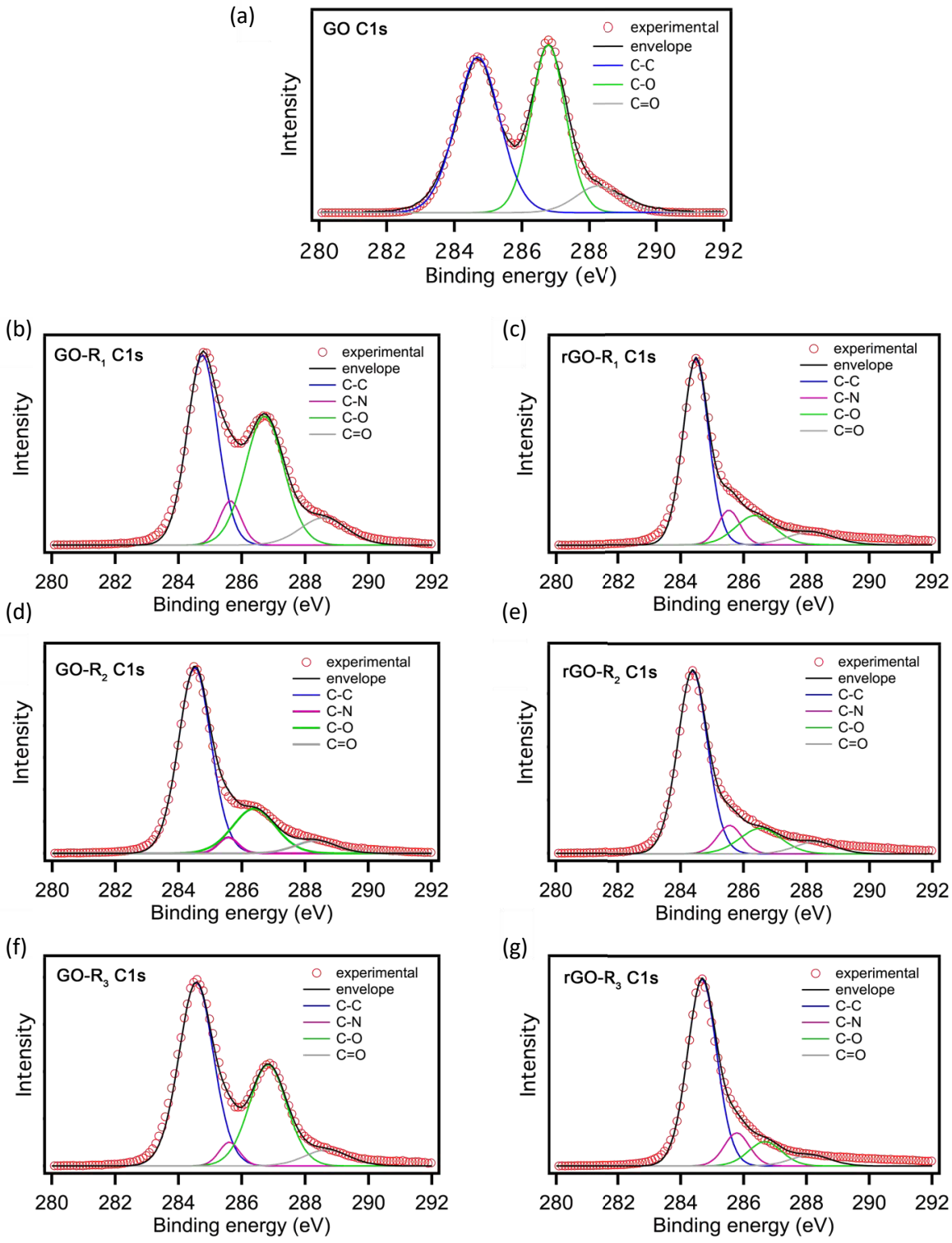

Figure 5-8. C1s XPS spectra of (a) GO; (b), (d), (f), GO-$R_{1\text{-}3}$; (c), (e), (g), rGO-$R_{1\text{-}3}$.

The high-resolution N1s spectrum of GO sample does not show any nitrogen signal (Figure 5-9). Conversely, clear signal is observed in **GO-R$_{1-3}$** samples, and it can be deconvoluted into two peaks, *i.e.* at 399.6 eV and 401.5 eV, which can be ascribed to secondary and protonated primary amines, respectively. Noteworthy, the existence of the latter can be associated with the formation of the ammonium-carboxylate species. Notably, presence peaks at 401.5 eV suggest that not all the molecules undergo the covalent grafting onto GO sheets but instead are physisorbed mostly at the edges of GO surface, where carboxylic groups are being present. Based on the intensity of the 401.5 eV peaks, we concluded that the largest portion of unreacted amine molecules was found in the **GO-R$_1$** samples.

Interestingly, the unreacted molecules were easily removed from the hybrid material during the reduction step. The N1s spectra of all samples display only one signal, which correspond to secondary amines. Interestingly, the C/N ratio, which amounts to 23.3, 16.7 and 20.9 for **rGO-R$_1$**, **rGO-R$_2$** and **rGO-R$_3$**, respectively, supports our initial assessment and proves that the functionalization degree can be presented as following: **rGO-R$_2$** > **rGO-R$_3$** > **rGO-R$_1$**.

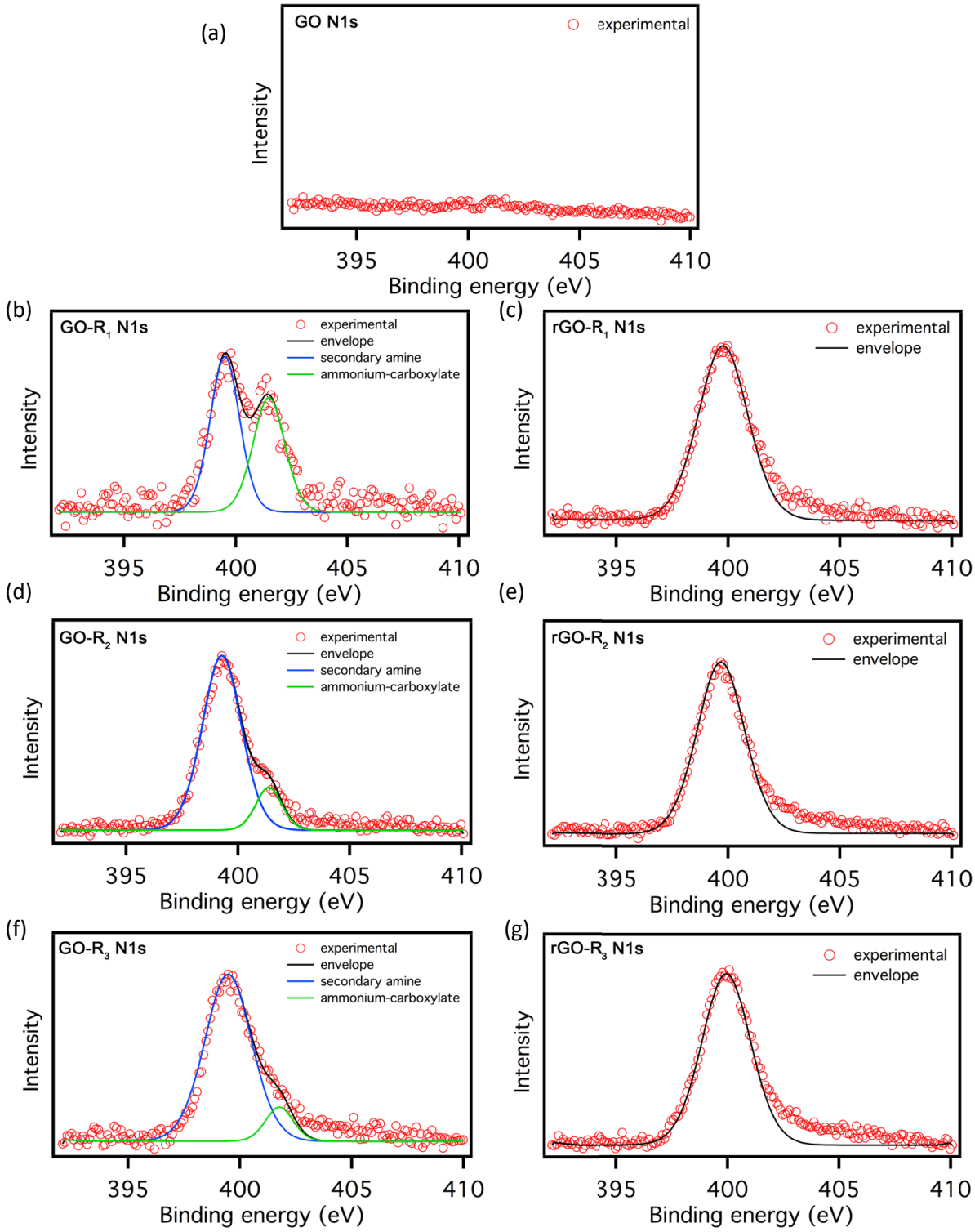

Figure 5-9. N1s XPS spectra of (a) GO; (b), (d), (f), GO-R$_{1-3}$; (c), (e), (g), rGO-R$_{1-3}$.

5.3.3.2. XRD spectra of GO and GO-R_{1-3}, rGO and rGO-R_{1-3}

Wide-angle X-ray scattering (WAXS) of the pristine GO displays only a typical sharp peak at ≈10.01° (see Figure 5-10), corresponding to an interlayer spacing of 0.87 nm due to the (*002*) reflection of stacked GO sheets, in accordance with the previously reported value. Interestingly after reduction with hydrazine, such peak disappears and a new broad peak at 23.94° appears corresponding to an interlayer distance of 0.38 nm, which has been attributed to π-π stacking between the rGO sheets due to the partial restore of the graphitic structure. When GO is reacted with organic aliphatic amines (**R1** and **R2**), a bimodal packing has been observed with the presence of a first broad peak at 18.98° (0.47 nm) and 21.55° (0.41 nm) and a second sharp peak at ≈ 9.55° (0.93 nm) and 8.36° (1.06 nm) for **GO-R_1** and **GO-R_2** respectively. These peaks suggest that the functionalization of GO by aliphatic amines is occurring concomitantly to a partial reduction of the GO sheets thus the spacing is dictated by both the aliphatic amine (≈ 1 nm) and π-π stacking interactions (≈ 0.4 nm) of graphitic domains. Interestingly such bimodal packing is not observed for the case of the aromatic amine (**R3**) which is instead characterized by a single peak at 9.10° (0.97 nm) indicating that the spacing is only dictated by the aromatic molecular spacer (4-aminobiphenyl) while the reduction process is not taking place at a reasonable extent to give rise to observable π-π stacking interactions. Such observations have been further corroborated by WAXS analysis performed on the samples after reduction with hydrazine. Indeed a bimodal packing is observed for all the samples in particular the first peak for **rGO-R_1**, **rGO-R_2** and **rGO-R_3** was observed at 23.74°, 23.12° and 24.71° which correspond an interlayer distance of 0.37 nm, 0.38 and 0.36 nm, respectively and ascribed to π-π interactions[37, 38], while the second peaks are shifted toward lower angles, from 11.38° (0.78 nm) for **rGO-R_1**, 11.98° (0.74 nm) for **rGO-R_2** to 12.51° (0.71 nm) for **rGO-R_3** due to the presence of the organic spacer.

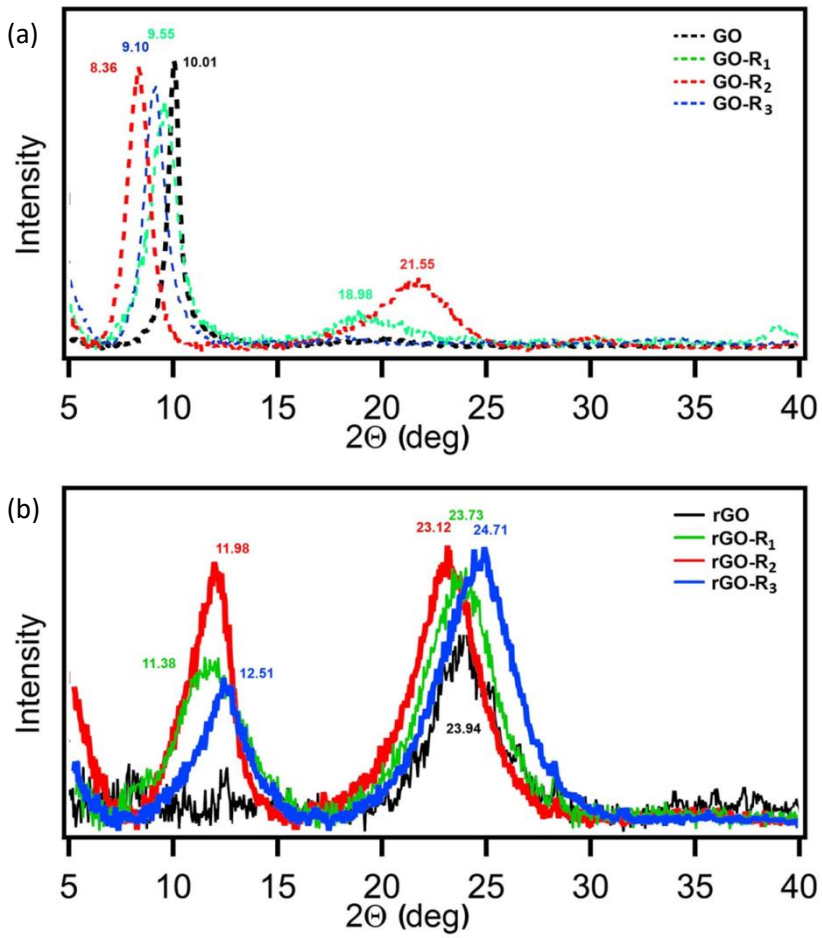

Figure 5-10. XRD spectra of (a) GO and GO-R_{1-3}; (b) rGO and rGO-R_{1-3}.

5.3.3.3. Raman spectra of GO, rGO, GO-R_{1-3} and rGO-R_{1-3}

The proposed mechanism of functionalization has been further supported by Raman spectroscopy (see Figure 5-11) through the analysis of the D and G peaks characteristics[39] around 1350 cm^{-1} and 1600 cm^{-1}. The former provides information on the defect associated to vacancies and grain boundaries of the material,[38] while the latter gives insight into the chemical state of the carbon through the scattering of the E_{2G} phonon of the sp^2 carbon bond.[40] Considering the G-peak of the GO measured at 1604 cm^{-1}, its value shifts to a lower wavenumber, reaching 1591 cm^{-1} for the rGO, which is consistent with the observed effect of the functionalization of graphitic materials.[41, 42] The intensity ratio I_D/I_G is commonly used to quantify the disorder level in graphene.[43] After a certain degree of disorder, which is much lower than the density of defect encountered in GO, the addition of defects lead to an attenuation of the peaks, and consequently, to a decrease of the I_D/I_G ratio.[44] Thus, that value does not change drastically from the GO to the functionalized GO, since the anchoring groups to realize this functionalization are already present on the GO and already count as defects. However, during the reduction step of the functionalized GO, the elimination of defects that have not reacted during the previous step leads to an increase of the I_D/I_G ratio, as observed in the three cases.

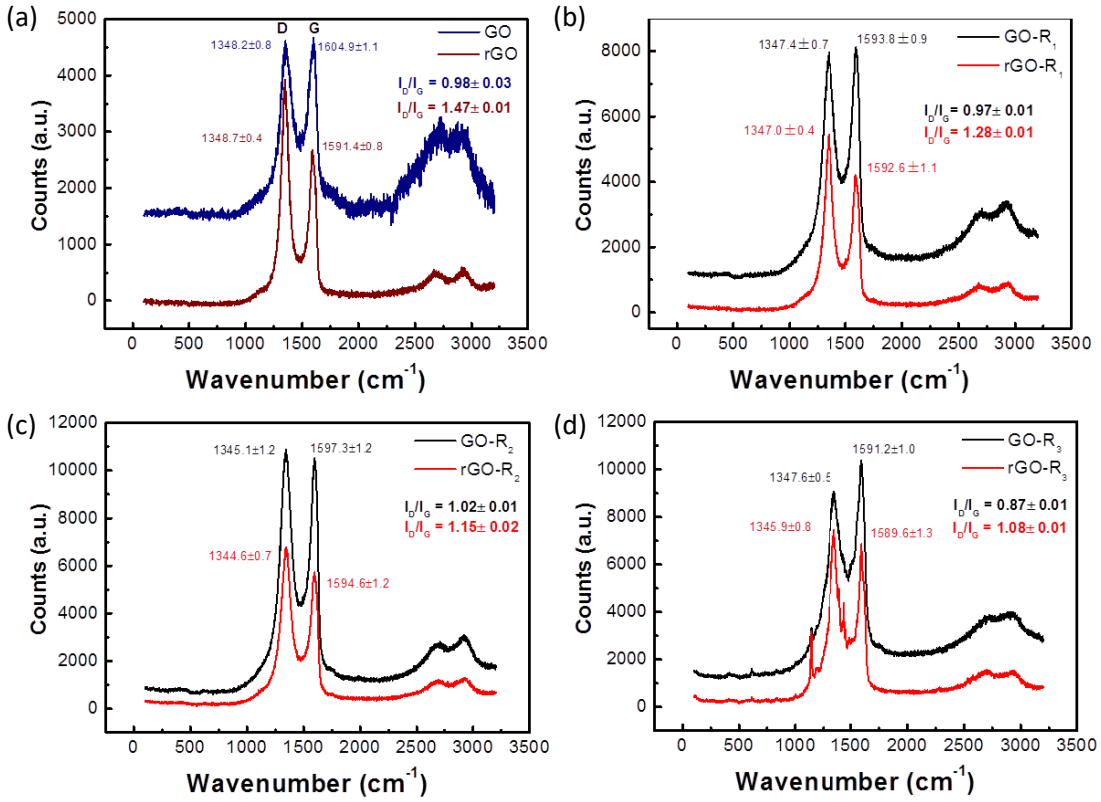

Figure 5-11. Raman spectra of (a) GO and rGO; (b) GO-R_1 and rGO-R_1; (c) GO-R_2 and rGO-R_2; (d) GO-R_3 and rGO-R_3.

5.3.3.4. IR spectra of GO, rGO, rGO-R_{1-3}

The successful functionalization and reduction of GO has been further confirmed by infrared spectroscopy (FTIR). As shown in Figure 5-12, pristine GO displays the typical peaks corresponding to a variety of oxygen-containing functional groups. In particular, the broad band around 3390 cm^{-1} is typical of O–H stretching vibrations, the peak at 1724 cm^{-1} has been attributed to the C=O stretching of carboxylic acid group; the peak at 1624 cm^{-1} to the sp^2 C=C bonds, while the peaks at 1216 cm^{-1} and 1054 cm^{-1} have been attributed to C–O stretching of epoxy and alkoxy groups, respectively. The disappearance of the peak at 1724 cm^{-1} and a significant decrease in peak intensity within 3200–3500 cm^{-1} indicate the successful reduction of the functionalized GO upon hydrazine treatment. The sp^2 C=C (1623 cm^{-1}) and =C-H (999 cm^{-1}) bonds still can be observed. Typically, cross-linking reaction between GO and amine derivatives results in the formation of amides (at the edges of GO flakes) and opening the epoxy groups (located on the plane of GO flakes). After reaction, the epoxy groups in the GO disappear, and a new band at 1169 cm^{-1}, 1192 cm^{-1}, 1163 cm^{-1} appears in **rGO-R_1**, **rGO-R_2** and **rGO-R_3**, respectively. These bands are attributed to the C–N stretching mode. The most important change observed after amine treatment is a strong decrease in intensity of the C=O band of COOH groups along with appearance of strong absorption at 1560–1580 cm^{-1}, which is corresponding to N-H stretching vibration. In the case of **rGO-R_2**, the asymmetric peaks at 2911 and 2842 cm^{-1} are assigned to the C-H stretching vibrations of the alkyl group $–CH_2$ of the alkyl amine.

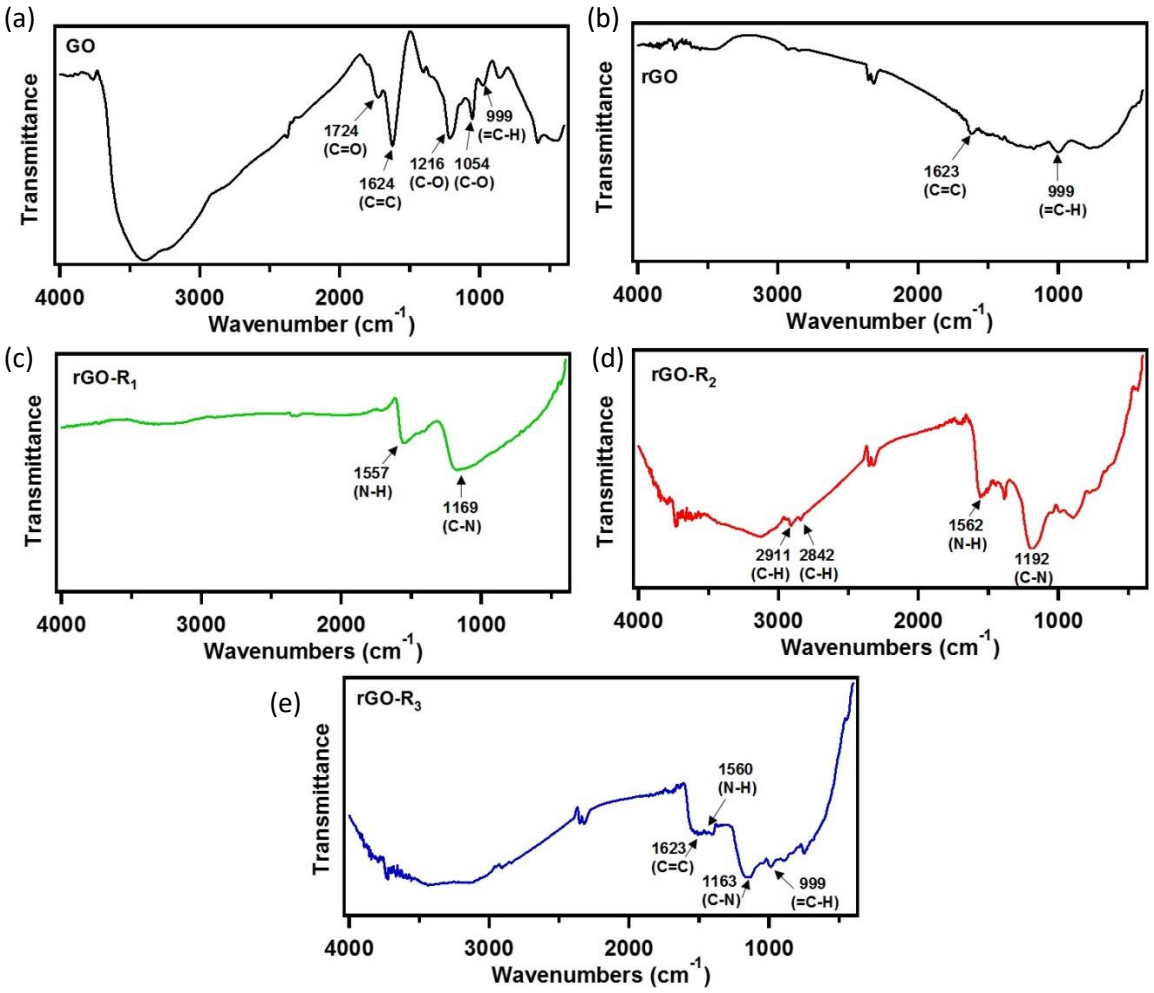

Figure 5-12. IR spectra of (a) GO; (b) rGO; (c) rGO-R_1; (d) rGO-R_2; (e) rGO-R_3.

5.3.3.5. BET analysis of rGO, rGO-R_{1-3}

Figure 5-13a shows the nitrogen sorption isotherms of rGO, rGO-R_1, rGO-R_2 and rGO-R_3 samples, and the gas sorption analysis results are listed in Table S1. All of the four samples are mesopore-structured as observed from the shape of nitrogen sorption isotherms, and the pore size distribution (PSD). The average pore diameter calculated with the Barrett-Joyner-Halenda (BJH) model are amounts to 4.1, 6.2, 5.4 and 6.1 nm for rGO, rGO-R_1, rGO-R_2 and rGO-R_3 respectively (Figure 5-13b). After functionalization and reduction, increase the porosity of the materials is observed and the specific surface area values of rGO-R_1/R_2/R_3 are 123, 119, 128 m^2/g which are all higher than that of rGO (29 m^2/g). The isotherms of N_2 adsorption and desorption of rGO and rGO-R_1/R_2/R_3 are similar to type IV isotherm, which possess a distinct H4 hysteresis loop, revealing a mesoporous structure with narrow slit-like pores with irregular shape and broad size distribution. This type of isotherm is often used to describe adsorption-desorption process for 2D and 3D-carbon based materials.[45] In the present case, the isotherms revealed slow uptake followed by rapid approach to attain equilibrium. This behaviour for gas adsorption may be due to the significant adsorption capacity.

Table 2. Specific surface area calculated from the nitrogen adsorption isotherm using the BET method. Pore volume obtained from Barret-Joyner-Halenda (BJH) desorption cumulative volume of pores and rGO, rGO-R_1, rGO-R_2 and rGO-R_3 results obtained from BJH desorption average pore diameter.

	BET surface area (m^2 g^{-1})	Pore volume (cm^3 g^{-1})	Average pore size (Å)
rGO	29.0 ± 0.8	0.41 ± 0.03	41 ± 4
rGO-R_1	123.0 ± 4.1	0.91 ± 0.06	62 ± 6
rGO-R_2	119.0 ± 3.9	0.86 ± 0.06	54 ± 5
rGO-R_3	128.0 ± 4.2	0.82 ± 0.05	61 ± 6

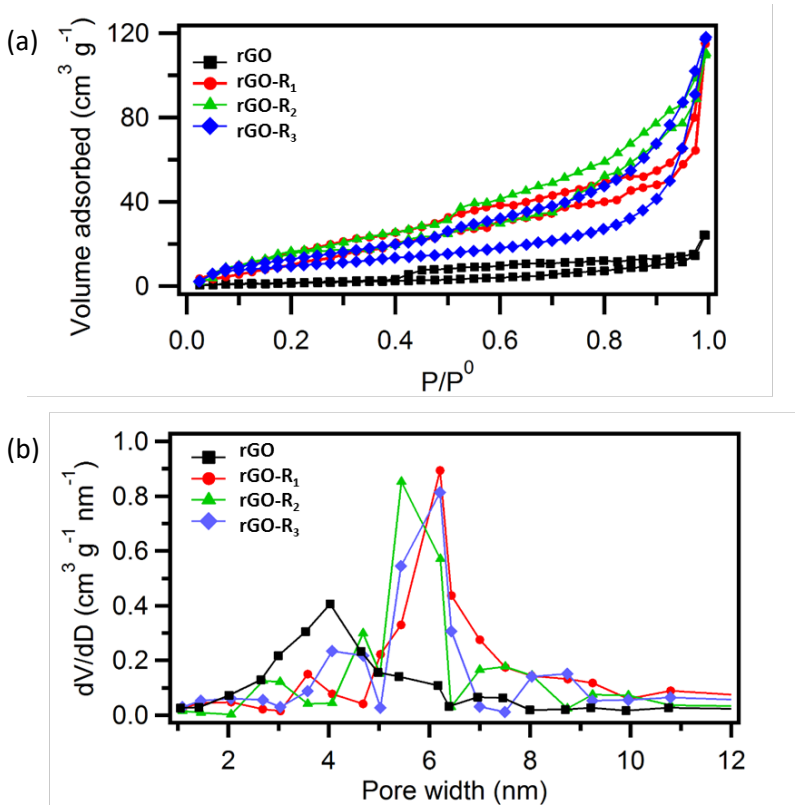

Figure 5-13. (a) BET adsorption-desorption isotherms of rGO, rGO-R_1, rGO-R_2 and rGO-R_3; (b) Pore volume dV/dD plots for mesoporous rGO, rGO-R_1, rGO-R_2 and rGO-R_3.

5.3.3.6. Laser Scanning Confocal Microscopy (LSCM) analysis of rGO-R_1

Film thickness under different loading was measured by means of Laser Scanning Confocal Microscopy (LSCM) with a LEICA DMIRE2 equipped with a 20X objective (vertical resolution: ~650 nm. Two glass coverslips (dimensions: 2.5x2.5 cm^2, thickness: 150 µm) were spray coated with a rGO-R_1 solution and then combined to obtain a film with average thickness around 150 µm. A circular spot in the middle of the coverslips (area: 3.14 mm^2) was not coated and the glass surface was marked on both sides with a solution of Rhodamine 110 chloride in ethanol. A sketch of the film is given in Figure 5-14a. Different weights (with annular shape) were then placed over the top glass coverslip and the distances between the glass surfaces were measured according to the loss of fluorescence emission in a vertical scan in the centre of the sample. The results are shown in Figure 5-14b, showing the significant reduction of thickness as a function of the loading, and once the load was removed, the thickness of the film restored to its starting value (within the experimental error).

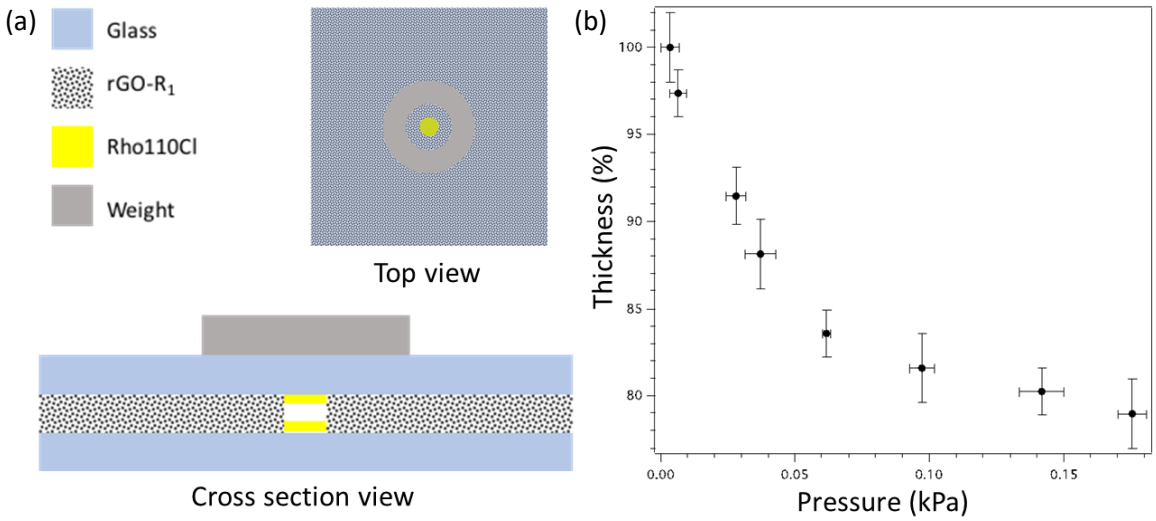

Figure 5-14. (a) Sketch of the sample used for LSCM thickness measurements; (b) Variation of the thickness of rGO-R_1 film as a function of the applied load.

5.3.3.7. Transmittance spectra of PET film after spray coating of rGO-R_{1-3}

To obtain a good control over the amount of active material deposited on the surface of ITO-PET film, the transmittance of each electrode was tested by recording UV-Vis spectra (by means of a Jasco V-670 spectrophotometer). During the spray coating process, the PET films were analysed in real time to control the transmittance, which is also crucial for the good repeatability. As shown in Figure 5-15 all the electrodes show nearly identical transmittance (T% = 20%) at the wavelength at 500 nm, indicating a good film uniformity in-between the electrodes.

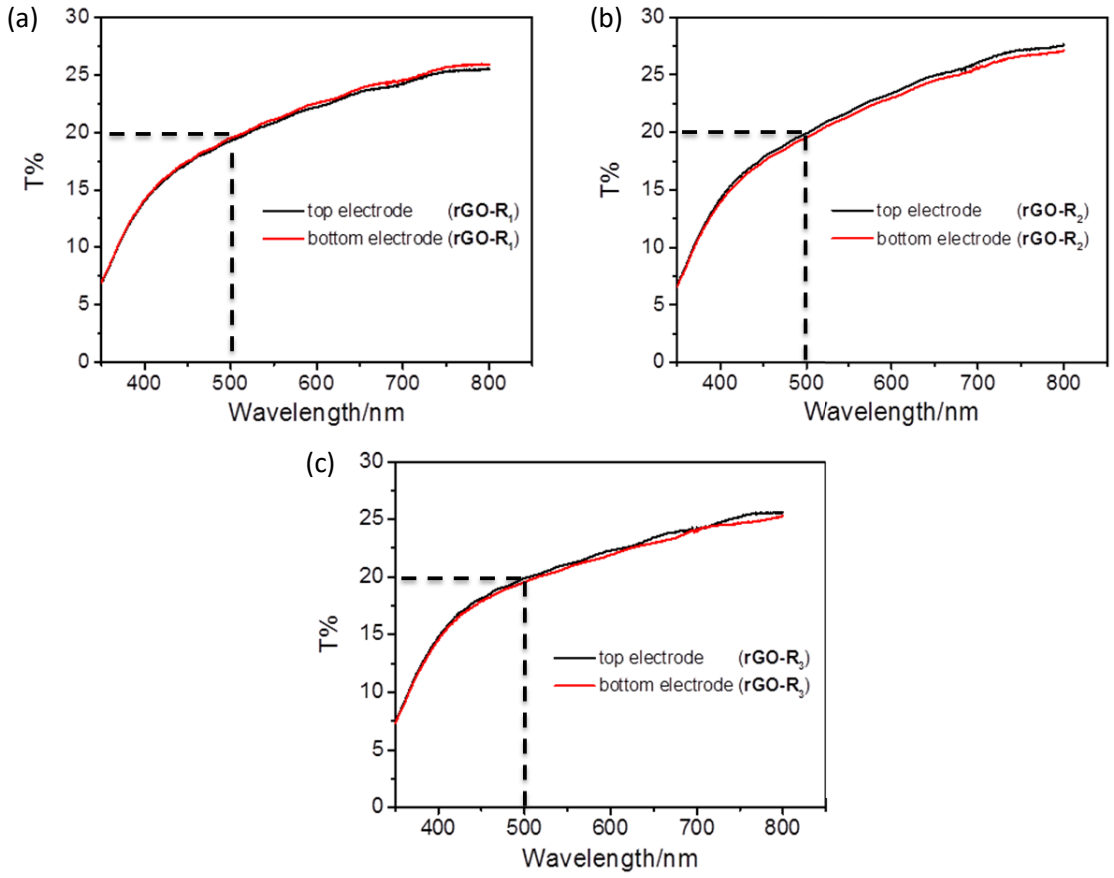

Figure 5-15. Transmittance spectra of ITO-PET film after spray coating of (a) rGO-R_1; (b) rGO-R_2; (c) rGO-R_3.

5.3.3.8. SEM images of rGO and rGO-R_{1-3}

The mophorlogy of electrodes after spray coating was investegated by SEM (FEI Quanta 450 FEG). As shown in Figure 5-16, all the three reduced funtionalized graphene oxides (*i.e.* **rGO-R_1**, **rGO-R_2**, **rGO-R_3**) and rGO show similar multilayer structure as expected. The surface of rGO is more rough than functionalized graphene due to the restore of graphite structure after reduction by hydrazine. The tilted view (Figure 5-16e) and side view (Figure 5-16f) of substrate after spray coating of **rGO-R_1** clearly demonstrate that the functionalized graphene layers stack perpendicularly to substrate without introducing conspicuous pore structure.

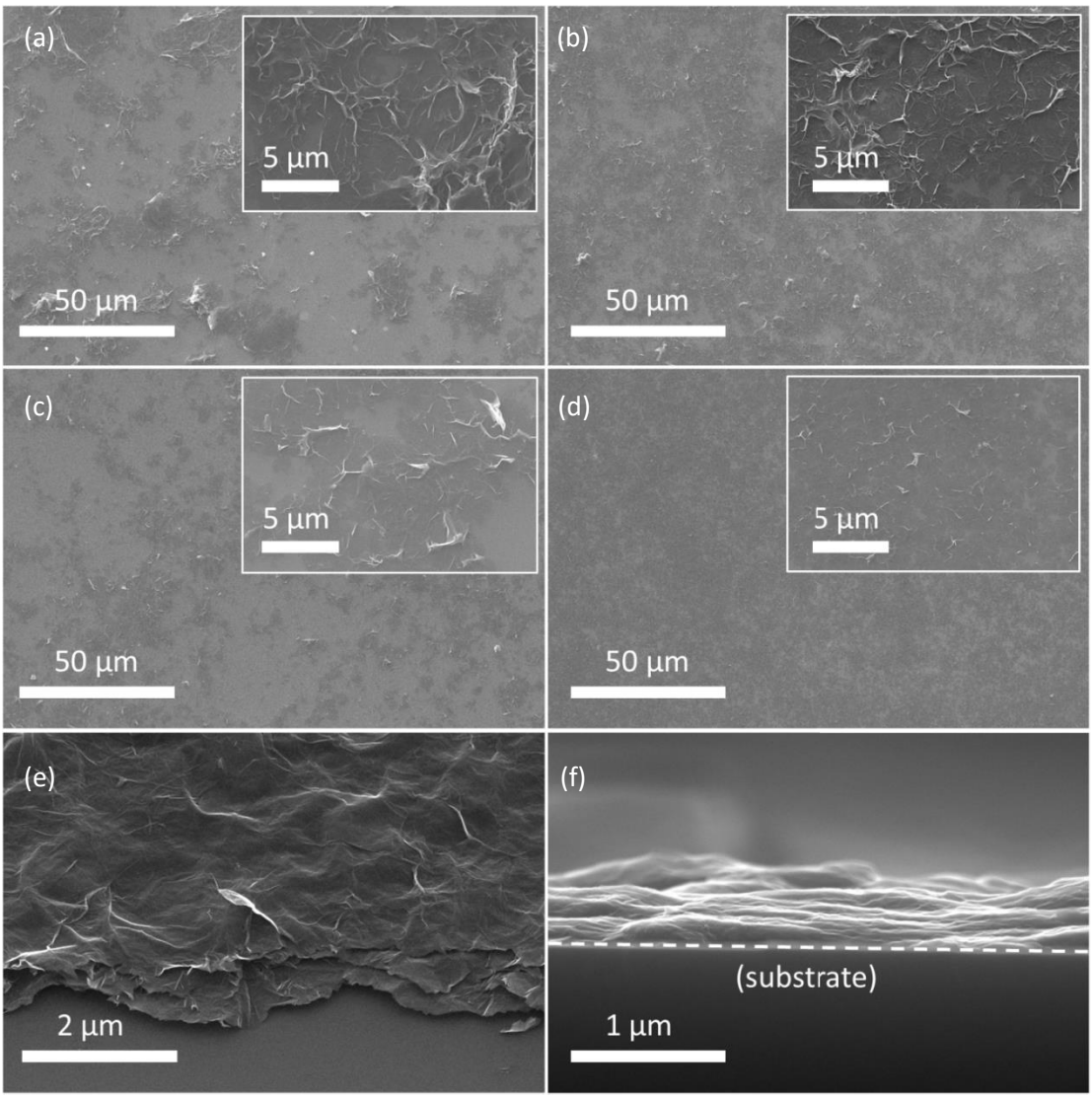

Figure 5-16. SEM images of (a) rGO; (b) rGO-R_1; (c) rGO-R_2; (d) rGO-R_3; (e) tilted view of rGO-R_1; (f) side view of rGO-R_1.

5.3.3.9. Temperature dependent electrical conductivity measurement

Electrical measurements at low temperature were done with a Nitrogen cryostat Oxford Instrument OptistatDN-V from 80 K to 300 K with a step of 10 K, controlled through an ITC503S Cryogenic Temperature Controller and interfaced with a dual channel Keithley 2636A sourcemeter. The electrical conductance of **rGO-R$_1$** has been measured at each temperature, from -0.1 V to 0.1 V (0.005 V steps), in a vertical geometry device based on two rigid quartz substrates covered with ITO. This alternative device was mandatory to get accurate results since the thermal expansion of PET is bigger than the quartz one, which would strongly affect the measurement. As a comparison, a lateral geometry has also been measured between -0.5 V and 0.5 V (0.01 V steps) with interdigitated gold electrodes (W = 1 cm, L = 60 μm).

In both cases, the conductivity is almost stable over the whole temperature range (Figure 5-17), allowing excluding a hopping transport mechanism that usually demonstrates an exponential behavior of the conductivity while increasing the temperature. It indicates a direct tunneling transport due to the small voltage used, because of the low temperature dependence of this mechanism which is driven by the energy barrier width between states, i.e, the distance between reduced graphene sheets.[46]

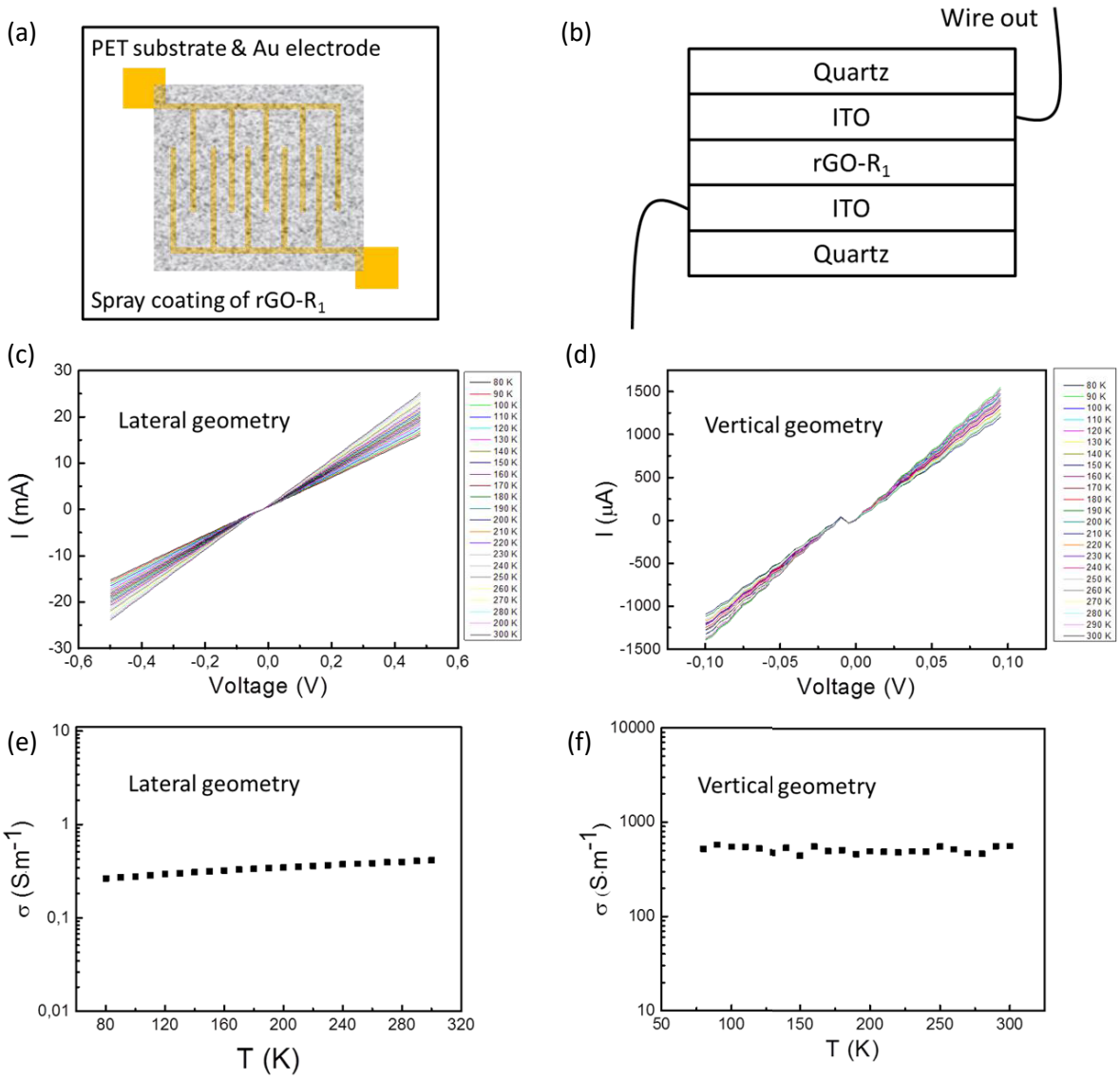

Figure 5-17. Temperature-dependent electrical conductivity measurements of rGO-R_1 suggest a direct tunneling transport mechanism by using (a), (c), (e) a lateral geometry; and (b), (d), (f) a vertical geometry.

5.3.3.10. Fatigue test of pressure sensor rGO-R_1

The stability and the robustness of pressure sensors has been investigated by fatigue tests, in which the periodic press and release on the sensor surface was generated by a digital force gauge (Mark-10, M7-025E, ~25 N) equipped with a motorized test stand (Mark-10, ESM-303E). The result presented in Figure 5-18 clearly shows that the pressure sensor exhibits a superior performance, in which the working current (on-stage) is highly stable even after 2000 times of press-release circles. The high robustness of pressure sensor imparts it a great protential in the field of electronic skins and novel wearable devices.

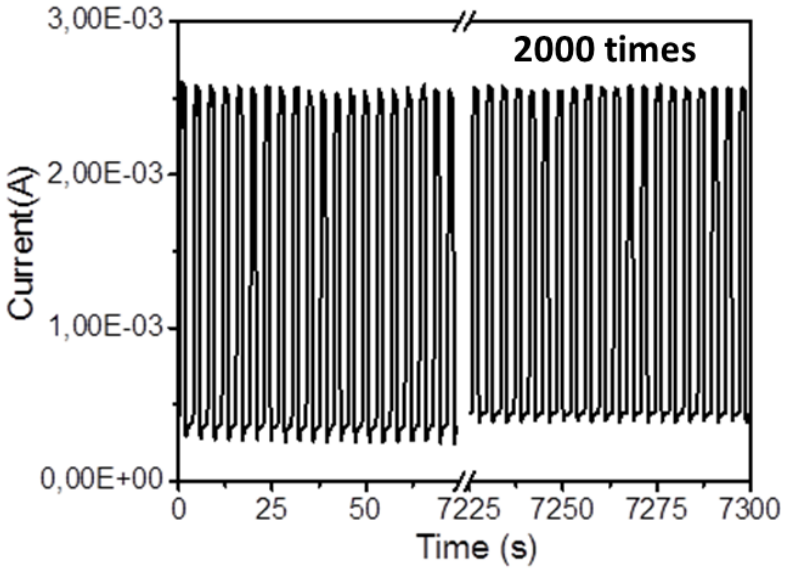

Figure 5-18. Fatigue test of pressure sensor rGO-R_1.

5.4. Conclusion

In summary, we have described a novel method to tune and boost the sensitivity of pressure sensors by using as active component a hybrid architecture comprising a mille-feuille assembly of rGO separated by covalently tethered molecular linkers. In analogy with the Hooke's law, our results clearly demonstrate how the sensitivity is effectively improved when flexible molecular linkers are employed. In particular, the sensitivity of pressure sensor is significantly increased by functionalization of graphene with more flexible molecules. The pressure sensor based on graphene oxide chemically modified with triethylene glycol amine (**rGO-R$_1$**) exhibits a sensitivity as high as 0.82 kPa^{-1}, short response time (24 ms), ultralow detection limit (7 Pa), high durability (over 2000 times) and flexibility. By taking advantage of the compatibility of graphene for on-the-skin applications, we have demonstrated how our hybrid multilayer architecture can be employed for health monitoring and can be easily transformed into a matrix, which allows a 3D mapping of the pressure exerted by different object thus providing also spatial information. The device additional features such low power consumption (0.2 V operating voltage), large-scale fabrication process, commercially available raw material and low cost, makes it an appealing candidate for the technological applications in wearable health monitoring device, multimotion detection robotic and internet of functions. Furthermore, our pressure sensor is fabricated by solution processing, thus it is compatible with printed electronics solutions.

5.5. References

1. Zang, Y. P.; Zhang, F. J.; Di, C. A.; Zhu, D. B., Advances of Flexible Pressure Sensors toward Artificial Intelligence and Health Care Applications. *Mater. Horiz.* **2015,** *2*, 140-156.
2. Hammock, M. L.; Chortos, A.; Tee, B. C. K.; Tok, J. B. H.; Bao, Z. N., 25th Anniversary Article: The Evolution of Electronic Skin (E-Skin): A Brief History, Design Considerations, and Recent Progress. *Adv. Mater.* **2013,** *25*, 5997-6037.
3. Chun, S.; Jung, H.; Choi, Y.; Bae, G.; Kil, J. P.; Park, W., A tactile sensor using a graphene film formed by the reduced graphene oxide flakes and its detection of surface morphology. *Carbon* **2015,** *94*, 982-987.
4. Li, L. H.; Bai, Y. Y.; Li, L. L.; Wang, S. Q.; Zhang, T., A Superhydrophobic Smart Coating for Flexible and Wearable Sensing Electronics. *Adv. Mater.* **2017,** *29*, 1702517.
5. Lou, Z.; Chen, S.; Wang, L. L.; Jiang, K.; Shen, G. Z., An ultra-sensitive and rapid response speed graphene pressure sensors for electronic skin and health monitoring. *Nano Energy* **2016,** *23*, 7-14.
6. Liu, M. M.; Pu, X.; Jiang, C. Y.; Liu, T.; Huang, X.; Chen, L. B.; Du, C. H.; Sun, J. M.; Hu, W. G.; Wang, Z. L., Large-Area All-Textile Pressure Sensors for Monitoring Human Motion and Physiological Signals. *Adv. Mater.* **2017,** *29*, 1703700.
7. Gong, S.; Schwalb, W.; Wang, Y. W.; Chen, Y.; Tang, Y.; Si, J.; Shirinzadeh, B.; Cheng, W. L., A Wearable and Highly Sensitive Pressure Sensor with Ultrathin Gold Nanowires. *Nat. Commun.* **2014,** *5*, 3132.
8. Liu, S. B. A.; Wu, X.; Zhang, D. D.; Guo, C. W.; Wang, P.; Hu, W. D.; Li, X. M.; Zhou, X. F.; Xu, H. J.; Luo, C.; Zhang, J.; Chu, J. H., Ultrafast Dynamic Pressure Sensors Based on Graphene Hybrid Structure. *ACS Appl. Mater.* **2017,** *9*, 24148-24154.
9. Wang, X.; Que, M.; Chen, M.; Han, X.; Li, X.; Pan, C.; Wang, Z. L., Full Dynamic-Range Pressure Sensor Matrix Based on Optical and Electrical Dual-Mode Sensing. *Adv. Mater.* **2017,** *29*, 1605817.
10. Choong, C. L.; Shim, M. B.; Lee, B. S.; Jeon, S.; Ko, D. S.; Kang, T. H.; Bae, J.; Lee, S. H.; Byun, K. E.; Im, J.; Jeong, Y. J.; Park, C. E.; Park, J. J.; Chung, U. I., Highly Stretchable Resistive Pressure Sensors Using a Conductive Elastomeric Composite on a Micropyramid Array. *Adv. Mater.* **2014,** *26*, 3451-3458.
11. Gao, Y. J.; Ota, H.; Schaler, E. W.; Chen, K.; Zhao, A.; Gao, W.; Fahad, H. M.; Leng, Y. G.; Zheng, A. Z.; Xiong, F. R.; Zhang, C. C.; Tai, L. C.; Zhao, P. D.; Fearing, R. S.; Javey, A., Wearable Microfluidic Diaphragm Pressure Sensor for Health and Tactile Touch Monitoring. *Adv. Mater.* **2017,** *29*, 1701985.
12. Yao, H. B.; Ge, J.; Wang, C. F.; Wang, X.; Hu, W.; Zheng, Z. J.; Ni, Y.; Yu, S. H., A Flexible and Highly Pressure-Sensitive Graphene-Polyurethane Sponge Based on Fractured Microstructure Design. *Adv. Mater.* **2013,** *25*, 6692-6698.
13. Kang, D.; Pikhitsa, P. V.; Choi, Y. W.; Lee, C.; Shin, S. S.; Piao, L. F.; Park, B.; Suh, K. Y.; Kim, T. I.; Choi, M., Ultrasensitive Mechanical Crack-Based Sensor Inspired by the Spider Sensory System. *Nature* **2014,** *516*, 222-226.
14. Li, X. M.; Yang, T. T.; Yang, Y.; Zhu, J.; Li, L.; Alam, F. E.; Li, X.; Wang, K. L.; Cheng, H. Y.; Lin, C. T.; Fang, Y.; Zhu, H. W., Large-Area Ultrathin Graphene Films by Single-Step Marangoni Self-Assembly for Highly Sensitive Strain Sensing Application. *Adv. Funct. Mater.* **2016,** *26*, 1322-1329.
15. Wang, X. W.; Gu, Y.; Xiong, Z. P.; Cui, Z.; Zhang, T., Silk-Molded Flexible, Ultrasensitive, and Highly Stable Electronic Skin for Monitoring Human Physiological Signals. *Adv. Mater.* **2014,** *26*, 1336-1342.
16. Pan, L. J.; Chortos, A.; Yu, G. H.; Wang, Y. Q.; Isaacson, S.; Allen, R.; Shi, Y.; Dauskardt, R.; Bao, Z. N., An Ultra-Sensitive Resistive Pressure Sensor Based on Hollow-Sphere Microstructure Induced Elasticity in Conducting Polymer Film. *Nat. Commun.* **2014,** *5*, 3002.

17. Zhu, B. W.; Niu, Z. Q.; Wang, H.; Leow, W. R.; Wang, H.; Li, Y. G.; Zheng, L. Y.; Wei, J.; Huo, F. W.; Chen, X. D., Microstructured Graphene Arrays for Highly Sensitive Flexible Tactile Sensors. *Small* **2014,** *10*, 3625-3631.
18. Pang, C.; Lee, G. Y.; Kim, T. I.; Kim, S. M.; Kim, H. N.; Ahn, S. H.; Suh, K. Y., A Flexible and Highly Sensitive Strain-Gauge Sensor Using Reversible Interlocking of Nanofibres. *Nat. Mater.* **2012,** *11*, 795-801.
19. Schwartz, G.; Tee, B. C. K.; Mei, J. G.; Appleton, A. L.; Kim, D. H.; Wang, H. L.; Bao, Z. N., Flexible Polymer Transistors with High Pressure Sensitivity for Application in Electronic Skin and Health Monitoring. *Nat. Commun.* **2013,** *4*, 1859.
20. Vandeparre, H.; Watson, D.; Lacour, S. P., Extremely Robust and Conformable Capacitive Pressure Sensors Based on Flexible Polyurethane Foams and Stretchable Metallization. *Appl. Phys. Lett.* **2013,** *103*, 204103.
21. Mannsfeld, S. C. B.; Tee, B. C. K.; Stoltenberg, R. M.; Chen, C. V. H. H.; Barman, S.; Muir, B. V. O.; Sokolov, A. N.; Reese, C.; Bao, Z. N., Highly sensitive flexible pressure sensors with microstructured rubber dielectric layers. *Nat. Mater.* **2010,** *9*, 859-864.
22. Zhang, X. Y.; Ciesielski, A.; Richard, F.; Chen, P. K.; Prasetyanto, E. A.; De Cola, L.; Samori, P., Modular Graphene-Based 3D Covalent Networks: Functional Architectures for Energy Applications. *Small* **2016,** *12*, 1044-1052.
23. Chua, C. K.; Pumera, M., Chemical reduction of graphene oxide: a synthetic chemistry viewpoint. *Chem. Soc. Rev.* **2014,** *43*, 291-312.
24. Lee, D.; Lee, H.; Jeong, Y.; Ahn, Y.; Nam, G.; Lee, Y., Highly Sensitive, Transparent, and Durable Pressure Sensors Based on Sea-Urchin Shaped Metal Nanoparticles. *Adv. Mater.* **2016,** *28*, 9364.
25. Shao, Q.; Niu, Z. Q.; Hirtz, M.; Jiang, L.; Liu, Y. J.; Wang, Z. H.; Chen, X. D., High-Performance and Tailorable Pressure Sensor Based on Ultrathin Conductive Polymer Film. *Small* **2014,** *10*, 1466-1472.
26. Roh, E.; Lee, H.-B.; Kim, D.-I.; Lee, N.-E., A Solution-Processable, Omnidirectionally Stretchable, and High-Pressure-Sensitive Piezoresistive Device. *Adv. Mater.* **2017,** *29*, 1703004.
27. Liu, M.; Pu, X.; Jiang, C.; Liu, T.; Huang, X.; Chen, L.; Du, C.; Sun, J.; Hu, W.; Wang, Z. L., Large-Area All-Textile Pressure Sensors for Monitoring Human Motion and Physiological Signals. *Adv. Mater.* **2017,** *29*, 1703700.
28. Bae, G. Y.; Pak, S. W.; Kim, D.; Lee, G.; Kim, D.; Chung, Y.; Cho, K., Linearly and Highly Pressure-Sensitive Electronic Skin Based on a Bioinspired Hierarchical Structural Array. *Adv. Mater.* **2016,** *28*, 5300-5306.
29. Lee, H.; Venable, R. M.; MacKerell, A. D.; Pastor, R. W., Molecular Dynamics Studies of Polyethylene Oxide and Polyethylene Glycol: Hydrodynamic Radius and Shape Anisotropy. *Biophys. J.* **2008,** *95*, 1590-1599.
30. Ramachandran, R.; Beaucage, G.; Kulkarni, A. S.; McFaddin, D.; Merrick-Mack, J.; Galiatsatos, V., Persistence Length of Short-Chain Branched Polyethylene. *Macromolecules* **2008,** *41*, 9802-9806.
31. Petekidis, G.; Vlassopoulos, D.; Galda, P.; Rehahn, M.; Ballauff, M., Determination of chain conformation of stiff polymers by depolarized Rayleigh scattering in solution. *Macromolecules* **1996,** *29*, 8948-8953.
32. Tao, L. Q.; Zhang, K. N.; Tian, H.; Liu, Y.; Wang, D. Y.; Chen, Y. Q.; Yang, Y.; Ren, T. L., Graphene-Paper Pressure Sensor for Detecting Human Motions. *ACS Nano* **2017,** *11*, 8790-8795.
33. Tian, H.; Shu, Y.; Wang, X. F.; Mohammad, M. A.; Bie, Z.; Xie, Q. Y.; Li, C.; Mi, W. T.; Yang, Y.; Ren, T. L., A Graphene-Based Resistive Pressure Sensor with Record-High Sensitivity in a Wide Pressure Range. *Sci. Rep.* **2015,** *5*, 8603.

34. Nichols, W. W., Clinical Measurement of Arterial Stiffness Obtained from Noninvasive Pressure Waveforms. *Am. J. Hypertens* **2005,** *18*, 3S-10S.
35. Park, K. D.; Liu, R.; Kohn, H., Useful Tools for Biomolecule Isolation, Detection, and Identification: Acylhydrazone-Based Cleavable Linkers. *Chem. Biol.* **2009,** *16*, 763-772.
36. Kim, H.; Kong, Y. J.; Jeong, E. S.; Kong, S.; Kim, K. T., Glucose-Responsive Disassembly of Polymersomes of Sequence-Specific Boroxole-Containing Block Copolymers under Physiologically Relevant Conditions. *ACS Macro Lett.* **2012,** *1*, 1194-1198.
37. Cui, P.; Lee, J.; Hwang, E.; Lee, H., One-pot reduction of graphene oxide at subzero temperatures. *Chem. Commun.* **2011,** *47*, 12370-12372.
38. Kim, N. H.; Kuila, T.; Lee, J. H., Simultaneous reduction, functionalization and stitching of graphene oxide with ethylenediamine for composites application. *J. Mater. Chem. A* **2013,** *1*, 1349-1358.
39. Tuinstra, F., Raman spectrum of graphite. *J. Chem. Phys.* **1970,** *53*, 1126.
40. Ferrari, A. C.; Robertson, J., Interpretation of Raman spectra of disordered and amorphous carbon. *Phys. Rev. B* **2000,** *61*, 14095-14107.
41. Li, W. J.; Tang, X. Z.; Zhang, H. B.; Jiang, Z. G.; Yu, Z. Z.; Du, X. S.; Mai, Y. W., Simultaneous surface functionalization and reduction of graphene oxide with octadecylamine for electrically conductive polystyrene composites. *Carbon* **2011,** *49*, 4724-4730.
42. Chakraborty, S.; Saha, S.; Dhanak, V. R.; Biswas, K.; Barbezat, M.; Terrasi, G. P.; Chakraborty, A. K., High yield synthesis of amine functionalized graphene oxide and its surface properties. *RSC Adv.* **2016,** *6*, 67916-67924.
43. Lucchese, M. M.; Stavale, F.; Ferreira, E. H. M.; Vilani, C.; Moutinho, M. V. O.; Capaz, R. B.; Achete, C. A.; Jorio, A., Quantifying ion-induced defects and Raman relaxation length in graphene. *Carbon* **2010,** *48*, 1592-1597.
44. Abdolhosseinzadeh, S.; Asgharzadeh, H.; Seop Kim, H., Fast and fully-scalable synthesis of reduced graphene oxide. *Sci. Rep.* **2015,** *5*, 10160.
45. Lai, L. F.; Chen, L. W.; Zhan, D.; Sun, L.; Liu, J. P.; Lim, S. H.; Poh, C. K.; Shen, Z. X.; Lin, J. Y., One-step synthesis of NH2-graphene from in situ graphene-oxide reduction and its improved electrochemical properties. *Carbon* **2011,** *49*, 3250-3257.
46. Pandey, S.; Biswas, C.; Ghosh, T.; Bae, J. J.; Rai, P.; Kim, G. H.; Thomas, K. J.; Lee, Y. H.; Nikolaev, P.; Arepalli, S., Transition from direct to Fowler-Nordheim tunneling in chemically reduced graphene oxide film. *Nanoscale* **2014,** *6*, 3410-3417.

Chapter 6

AuNPs-TEG network based strain sensor

Inspired by the tunneling current ruled pressure sensor discussed in Chapter 5, we have designed a novel strain sensor based on gold nanoparticles (AuNPs) featuring a size of dozens of nanometers as conductive nanostructures in an active hybrid material of the strain sensor. AuNPs are interconnected by tetra (ethylene glycol) dithiol (SH-TEG-SH) to form 3D networks deposited directly in between flexible interdigitated electrodes. Without applied strain, AuNPs are separated by insulated organic ligands which can effectively define the charge transfer among AuNPs at a certain range. Upon applied strain, the active material is either compressed (under compressive strain) or stretched (under tensile strain) thus having the organic ligands undergoing conformational change ruled by its flexibility. The interparticle distance, which can be seen as the insulating barrier for charge transport, will be decreased/increased under compressive/tensile strain respectively, thus increasing/decreasing the tunneling current exponentially when voltage is applied. Our results show that the developed strain sensor displays high gauge factor (GF) and highly sensitive response both to tensile strain and compressive strain as well as to the mixed motion and even vibrations. Extensive effort has been devoted to the optimization of the structure design of device to achieve wireless sensing. In recent years, Radio Frequency IDentification (RFID) tag antennas have been widely employed in the field of *Internet of Things* (IoT) and cyber-physical systems (CPS) due to their superior properties such as passive, wireless, simple, compact size, and multimodal nature.[1, 2] In this Chapter, the wireless data transmission method, *i.e.* RFID, has been employed to construct a wireless strain sensing system with

AuNPs-TEG networks being active sensing material. Strain sensor has been integrated in the chip circuit as a resistor, in which the resistance was changing with strain thus affecting the current in the measure circuit through mutual inductance. The fabrication and measurement of strain sensor have been accomplished while the wireless sensing is under testing.

6.1. Introduction

Strain sensors, which respond to mechanical deformations providing an electrical output, have been extensively integrated into flexible and wearable electronic devices making it adapt for applications in health monitoring,[3] motion detection,[4] human-machine interface[5-7] and soft robotics[8, 9] *etc.* The definition and the key performance indicators have been fully discussed in Chapter 3.3. Different materials such as metal nanoparticles,[10-12] carbon nanotube[13-15], graphene[16-18] *etc.* have been used to fabricate strain sensors.

Nanoparticles gathered a large amount attention for application in strain sensing due to the easiness in controlling the composition, shape, size and molecular functionalization combined with a simple and cost-effective of fabrication.[19] In this Chapter, AuNPs have been chosen to serve as the active material in strain sensing devices. AuNPs have been already exploited as active sensing material of strain sensor,[10, 20, 21] the mechanism of which lies on the correlation between strain and electron tunneling among nanoparticles. Tunneling is a quantum mechanical effect indicating that electrons are able to move across a barrier (Figure 6-1). According to classical models, if an object doesn't have enough energy to move across a barrier, it will be stopped. However, according to quantum mechanics, electrons are free to move in a conductor, but when they meet a barrier, their wave function decreases exponentially. If the barrier has a finite thickness, the electrons have a finite probability to pass the barrier.

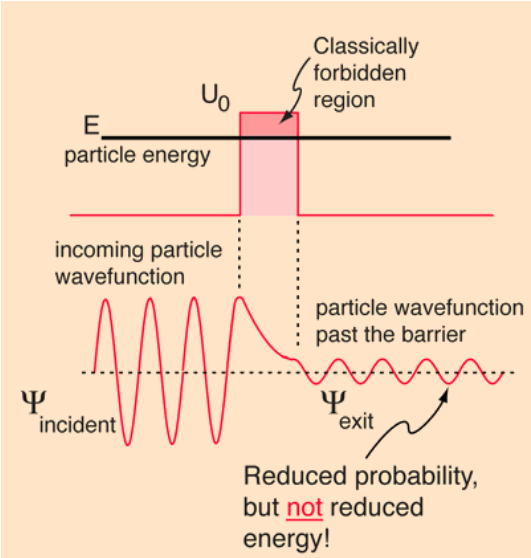

Figure 6-1. Illustration of barrier penetration in classical and quantum field. Free use with reserved copyright from http://hyperphysics.phy-astr.gsu.edu/hbase/quantum/barr.html.

Based on this principle, we have designed a device architecture which utilizes AuNPs featuring a size of dozens of nanometers as electrically conducting nodes within an active hybrid material of the strain sensor. AuNPs are interconnected by SH-TEG-SH to form 3D networks sandwiched by flexible electrodes. The AuNPs-TEG network has been proved to respond to changes in the environment humidity[22, 23] due to the reversible binding and unbinding of water molecules with TEG chains varying the conformation of the latter. In this way the distance between AuNPs is changed affecting the tunneling modulated charge transport through the network. As a strain sensor, the electrical properties of AuNPs-TEG network can also be modulated by strain. Without applied strain, AuNPs are separated by electrically insulating organic ligands which can efficiently limit the charge transfer through the particles network. Upon applied compressive strain, the active material is compressed thus squeezing the organic ligands due to the flexible nature. The interparticle distance which can be seen the barrier for electron transfer will decrease in size yielding to an exponential increase of the tunneling current. On the contrary, the interparticle distance increases under tensile strain, resulting in a decrease of the tunneling current.

To fully exploit such a mechanism in wearable sensing devices, all the components of the device are designed to be flexible. In this way, micro-patterned gold electrode on polyimide (PI) substrate was chosen to make the whole device flexible. Under certain bias voltage, the current passing through the device changes with strain, thus making it a piezoresistive strain sensor.

In addition to design a novel strain sensor featuring high sensitivity and flexibility, the data transmission method has also been intensively investigated to improve the sensing efficiency. Among different wireless data transmission methods, RFID[2] has attracted a notable attention due to its potential for applications in structural health monitoring (SHM)[2, 24] and IoT[25, 26]. These passive RFID tag features a simple structure, a compact size and a large-scale fabrication rendering suitable both for facile large-scale fabrication and adapt for daily life. For this reason, the wireless data transmission method (*i.e.* RFID) has been exploited to construct a sensitive strain sensor that can be in simple contact to the outside world.

The system is consisting of two circuits: the chip circuit and the measure circuit (Figure 6-2). Information can be transferred between the two circuits through mutual inductance. The measure circuit is an initiative circuit with an alternative power supply input. The chip circuit is a passive circuit which responds by the mutual inductance H. R_2 is the functional part, *i.e.* the sensing device with AuNPs-TEG network as the active sensing material.

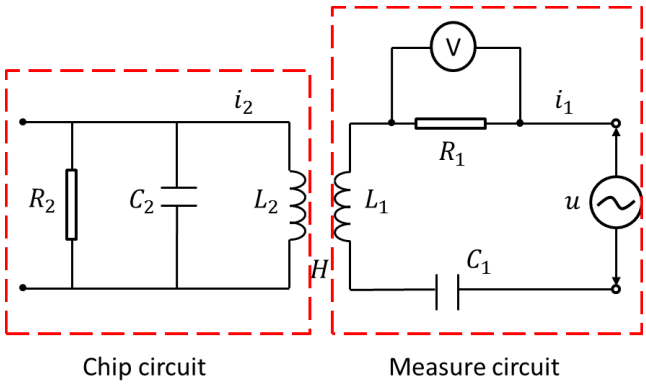

Figure 6-2. Diagram of chip circuit (left) and measure circuit (right).

For the measure circuit:

$$u = i_1\left(R_1 + j\omega L_1 - j\frac{1}{\omega C_1}\right) + i_2 \cdot j\omega H \qquad (6-1)$$

And for the chip circuit:

$$0 = i_1 \cdot j\omega H + i_2\left(\frac{R_2}{j\omega C_2 R_2 + 1} + j\omega L_2\right) \qquad (6-2)$$

where u, i_1 and i_2 are complex number, the final observable is the voltmeter in the measure circuit.

$$\|V\| = \|i_1\|R_1 \qquad (6-3)$$

From equation (6-1) and (6-2), we can see the i_1 is related to the variable R_2 and therefore we can find the relation between V and R_2 which means the amplitude of the voltmeter indicate the value of the resistanceR_2.

To optimize the measurement in terms of sensitivity, the measure circuit should be driven by an alternative voltage in the resonance frequency of chip circuit, which is given by:

$$\omega = \frac{1}{\sqrt{L_2 C_2}} \qquad (6-4)$$

6.2. Results and discussion

6.2.1. Analysis of gold nanoparticles

The consecutive seed growth method[27] was applied to accomplish the synthesis of AuNPs whose details have been provide in the *Experimental methods*. To determine the concentration and the size of the AuNPs, a UV-Vis spectrum of the solution was recorded. The shape and morphology of the particles were investigated by SEM. To determine a distribution of the diameter of the nanoparticles, the image taken by STEM was analysed statistically. DLS was used to study the distribution profile of the hydrodynamic diameter of the nanoparticles.

UV-Vis spectrum is the most direct method to evaluate both the size and concentration of AuNPs based on the optical properties.[28] For spherical particles below 100 nm the Lambert-Beer law was used to calculate the Au(0) concentration:

$$A = \varepsilon_{abs} \cdot c \cdot l \qquad (6-5)$$

where A is the absorption, ε_{abs} the extinction coefficient in $M^{-1}cm^{-1}$, c the concentration in M (mol/L) and l the width of the cuvette in cm. The concentration was determined at 400 nm, where the absorbance is mainly due to interband transition[29, 30] (from 5d band to hybridized 6sp band) and the extinction coefficient is known to be 2.6 $M^{-1}cm^{-1}$ for the estimation of the Au(0) concentration.[28]

A unique photophysical response of gold nanoparticle occurs when it is exposed to light. The free electrons of AuNPs which are located on conduction band oscillate with the oscillating electromagnetic field of the light, causing charge separation and dipole oscillation along the electric field direction (Figure 6-3a). The amplitude of the oscillation reaches a peak at certain frequency, which is called surface plasmon resonance (SPR).[31] The SPR peak correlates with the size of the particles,[32] which allows an estimation of the particle size.[33]

Three cycles of seed growth have been conducted during the synthesis process. As shown in Figure 6-3b, symmetric surface plasmon absorption was observed from the UV-Vis spectrum of the three samples after each cycle of nanoparticle growth. The spectra red-shifts with the increasing size of the nanoparticles, in accordance with reference results.[27] The results of the SPR peak, absorption at 400 nm and the resulting concentration and estimated size have been summarized in Table 6-1.

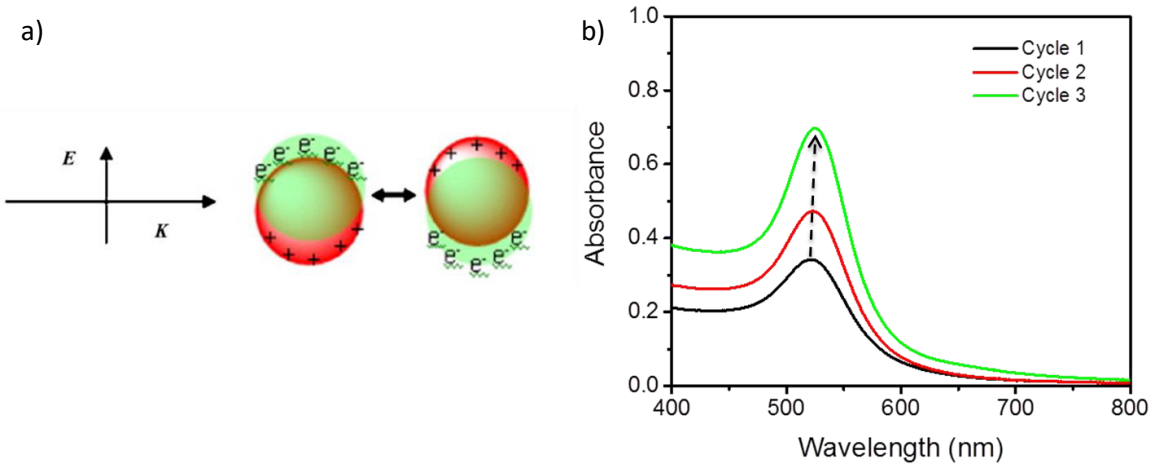

Figure 6-3: a) Schematic illustration of surface plasmon resonance in plasmonic nanoparticles. Reproduced from Ref.[31] b) UV-Vis spectrum of AuNPs following seed growth method after each growth cycle.

Table 6-1: Results UV-Vis measurements and concentration of solutions.

Sample	SPR peak	Reference SPR peak[27]	Expected diameter	Absorption at 400 nm	Concentration
Cycle 1	521 nm	521.5 nm	18.2 nm	0.211	0.406 mM
Cycle 2	523 nm	523.5 nm	24.5 nm	0.273	0.525 mM
Cycle 3	525 nm	525.5 nm	30.4 nm	0.381	0.733 mM

(length of cuvette: 0.2 cm)

The SPR peaks of the three samples correspond well with the values found in literature.[27] The concentration after each cycle of addition increases and the final solution, which was used for the gold nanoparticle ligand network growth, had a concentration of 0.733 mM with an estimated nanoparticle size of 30.4 nm.

The morphology and shape of AuNPs after the 3rd cycle of the seed growth method were investigated by SEM. The as-prepared solution of gold nanoparticle was drop casted on SiO_2/Si substrate as SEM sample. As shown in Figure 6-4, AuNPs have demonstrated the homogenous spherical shape and very good size distribution with slight aggregation on top of the SiO_2/Si surface, which makes it suitable for the determination of nanoparticle

concentration by means of the Lambert-Beer Law. Further morphology information and size distribution has been obtained by STEM.

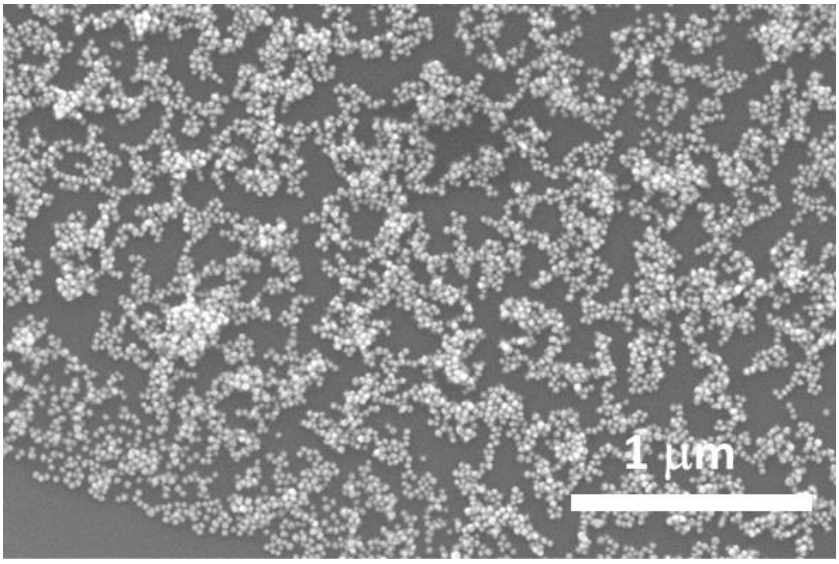

Figure 6-4: AuNPs after 3rd cycle of the seed growth method.

For the STEM measurement, the solution of AuNPs after the 3rd growth cycle has been washed by centrifugation (4000 rpm, 30 min) and rinsing to remove the extra organic salt before drop casting on a TEM grid. Capping molecules were added to form polymer layers thus preventing aggregation for a clear observation and size measurement. The STEM images at two different magnifications can be seen in Figure 6-5 a-b.

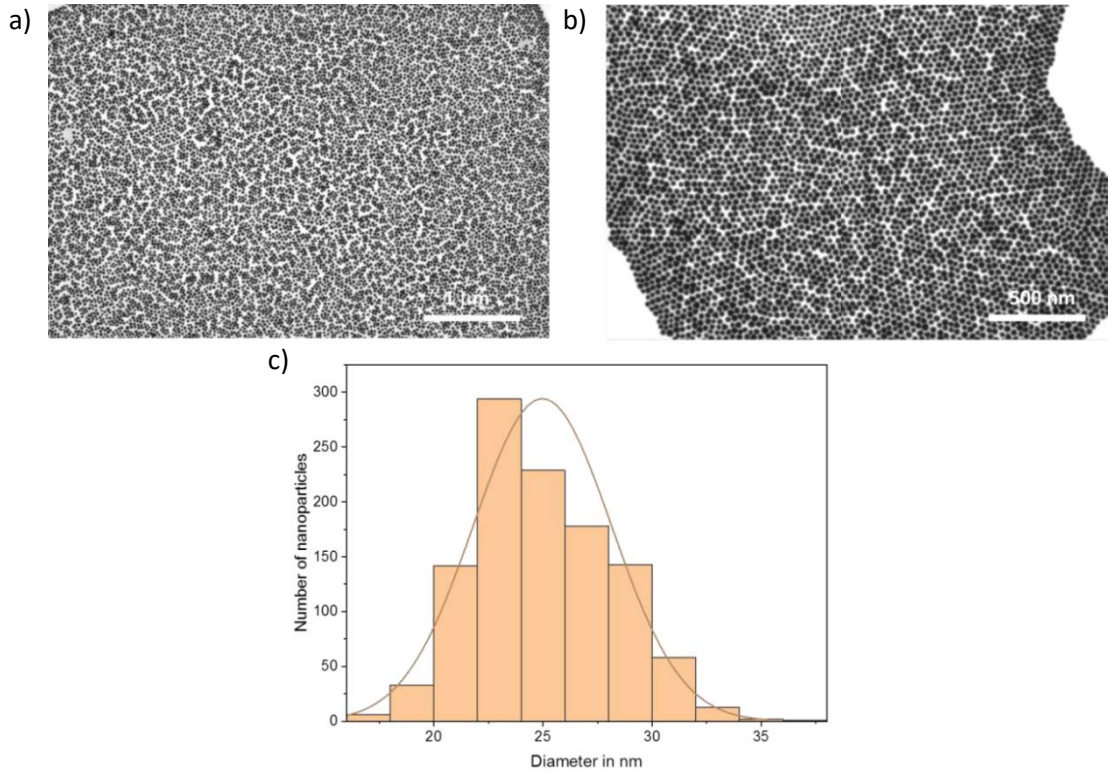

Figure 6-5: a, b) STEM image of AuNPs and c) corresponding size distribution.

High resolution images of the well spread nanoparticles have been recorded to enable a statistical size investigation. The distribution of the size obtained from the STEM images are illustrated in a histogram in Figure 6-5c. The average size of the nanoparticles acquired by STEM is 24.97 nm with a standard deviation of 3.17 nm, which is slightly smaller than the reference value (30 nm) given by UV-Vis. The difference is within the confidence interval and might be caused by resolution of STEM measurement.

DLS was used to determine the hydrodynamic radius and distribution of AuNPs. The solutions were diluted to a concentration of 0.1 mM and each sample has been measured three times in a raw to get an average value. Results of the hydrodynamic diameter and its standard deviation are reported in Table 6-2.

Table 6-2: Results of dynamic light scattering

Sample	Dynamic radius	Standard deviation
Cycle 1	22.33 nm	0.4886 nm
Cycle 2	27.45 nm	0.5447 nm
Cycle 3	35.20 nm	1.2390 nm

The dynamic radius increases with seed growth cycles, in accordance with the previously tested results. The hydrodynamic diameter of the final AuNPs after the 3rd seed growth cycle is 35.20 nm. The hydrodynamic size refers to the size of a sphere that diffuses as the same rate as the particle being measured, and it is generally larger than the real radius of the particles due to the hydration layer attached to the particles in solution. Figure 6-6 shows the size distribution of the AuNPs synthesized with the seed growth method after the 1st, 2nd and 3rd cycle, in which both the size and deviation increase accordingly. This might be caused by the heterogeneity of growth, which broadens the distribution after each cycle of nanoparticle growth.

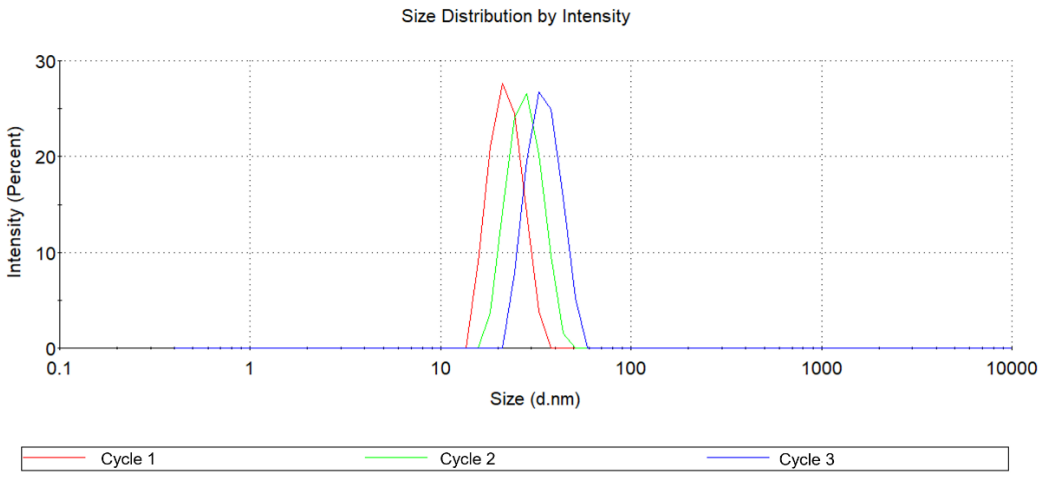

Figure 6-6. Size distribution of AuNPs of cycle 1, 2 and 3.

UV-Vis spectroscopy, STEM and DLS all revealed diameter of the AuNPs between 25 nm and 35 nm with an average size of 30 nm, which is in accordance with the value reported in the literature.[27]

6.2.2. Fabrication of AuNPs-TEG network

To gain insights into the kinetics of AuNPs-TEG network formation process, we have conducted the UV-Vis titration experiment of AuNPs with different stoichiometric portion of SH-TEG-SH in a certain period of time. While adding thiol molecules into AuNPs solution, the intensity of the characteristic peak of AuNPs at 528 nm decreases because of the aggregation caused by the Au-S reaction. As shown in Figure 6-7, while adding different amount of dithiol molecules into AuNPs solution, the reaction started to accelerate in the first 30 min and gradually saturated within 60 min. The molar ratio of AuNPs/dithiol plays an important role in the formation of the covalent network, *i.e.* too low molar ratio will cause over encapsulation of AuNPs, and too high molar ratio will cause lack of interconnection among the nanoparticles. The result below has demonstrated that the third group with a molar ratio of 3.5/1 has the fastest reaction. To have a fully cross linking to form an extended AuNPs-TEG network, 3.5/1 (molar ratio) has been chosen to perform the following network growing process.

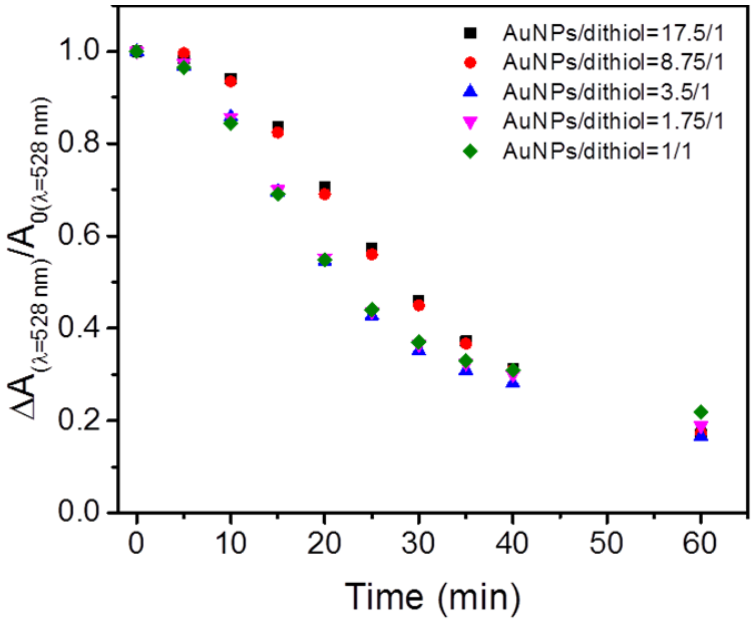

Figure 6-7. UV-Vis titration AuNPs with different portion of SH-TEG-SH.

The fabrication details of AuNPs-TEG network has been provided in the *Experimental methods*. The morphology of the AuNPs-TEG network on the electrode was firstly studied with SEM (Figure 6-8). The AuNPs-TEG network forms a homogenous film over the electrodes. Bridging the latter thereby enable current transmission under bias voltage.

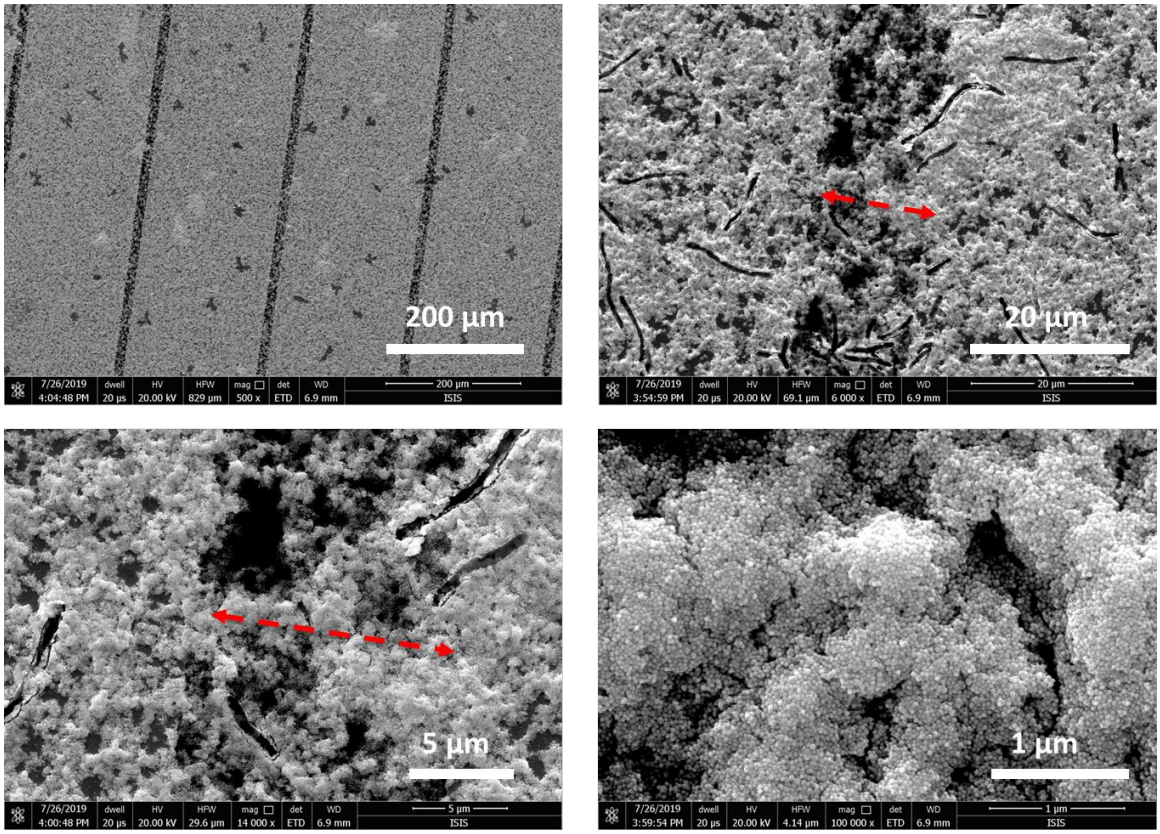

Figure 6-8. SEM images of AuNPs-TEG network on the electrode. (Channel length: 10 µm)

Noteworthy, black lines randomly appeared in the SEM images of AuNPs-TEG network. These are not external impurities but sunken structures as revealed in high magnified images. The formation of sunken structure of AuNPs-TEG network could be caused by N_2 drying process or inner strain inside the AuNPs-TEG network. Firstly, to understand the influence of N_2 blowing during the repeating drop casting process, we have fabricated devices without using N_2 after each casting step. The mixed solution of previous casting was removed and freshly made mixture of AuNPs and SH-TEG-SH was drop casted directly without drying the surface with N_2. The other possible reason is the inner strain formed by the over-aggregated network due to an inappropriate ratio between AuNPs and SH-TEG-SH. The amount of SH-TEG-SH has been increased to 10-fold compared to previous one. The surface structure resulting from both experiments has been examined by SEM (Figure 6-9). As displayed in Figure 6-9a-b, the sunken fiber structure was still observed in both cases. Yet, compared to the normal amount of SH-TEG-SH (Figure 6-9c) which was previously used, the amount of sunken structure lines is much less in the case of increased amount of SH-TEG-SH (Figure 6-9b). This result has clearly demonstrated the inner strain of AuNPs-TEG network could be the reason of formation of the sunken lines. Also, it is easy to find that very few network bridges were formed over the electrodes without N_2 blowing. This might due to the fact that the

network is bonded more tightly after drying with N_2, which will in turn facilitates the growth of the network.

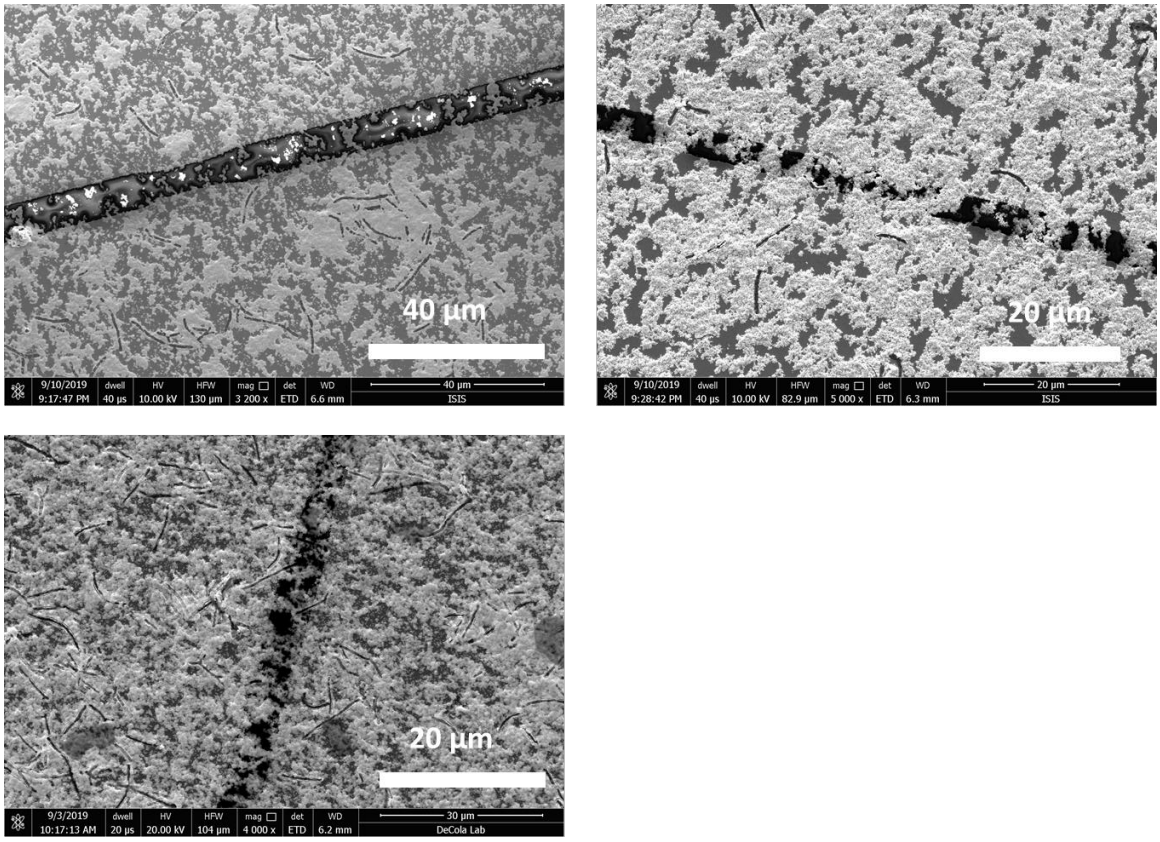

Figure 6-9. SEM images of AuNPs-TEG network formed a) without N_2 blowing, b) increased amount of SH-TEG-SH (3.5/10), and c) normal amount of SH-TEG-SH (3.5/1).

6.2.3. Temperature dependent electrical conductivity measurement

The temperature dependent electrical conductivity of AuNPs-TEG network and bare AuNPs has been measured to investigate the working principle of the strain sensor. Test details are discussed in the *Experimental methods*. While plotting the conductance vs temperature of AuNPs-TEG network, one can see that the device shows very stable behavior, with almost no dependence of the temperature on the conductance (Figure 6-10a). This behavior is characteristic of a tunneling transport mechanism. On the opposite, the same measurement of a sample composed by bare AuNPs demonstrates a linear decrease of the conductance versus the temperature (Figure 6-10b), which is characteristic of the metallic transport mechanism.[23, 34]

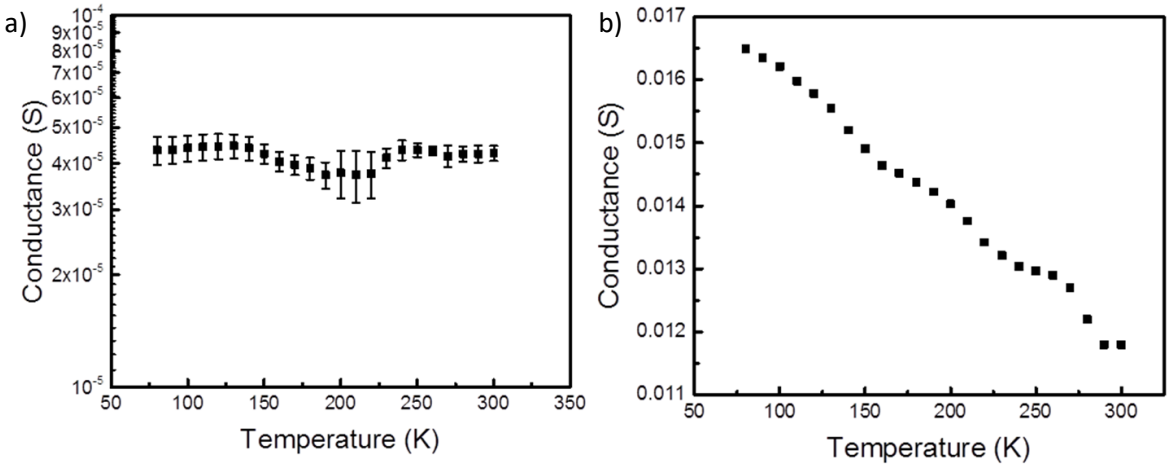

Figure 6-10. Cryostat results of a) AuNPs-TEG network and b) bare AuNPs.

6.2.4. Electrical sensing properties of strain sensor

The above-mentioned results have shown that the electrode channels have been covered by uniform AuNPs-TEG network featuring tunneling transport under bias voltage. This unique structure should endow highly sensitive strain sensing properties to the device. After the fabrication of strain sensor, the strain sensing performance of the device has been tested. Dynamic and statistic response to strain are discussed respectively below. The details of device fabrication including flexible substrate fabrication, AuNPs-TEG network growth, wire connection and encapsulation have been provided in the *Experimental methods*.

6.2.4.1. Dynamic response measurement

As shown in Figure 6-11, strain sensor was fixed on the PET substrate to test the functionality, in which compressive and tensile stress was applied by bending the PET sheet upwards (compressive strain) or downwards (tensile strain).[10, 20] Compressive stress was generated while bending the PET sheet upwards due to the squeezing of the AuNPs-TEG network, vice versa. The calculation of generated strain is discussed in the next section.

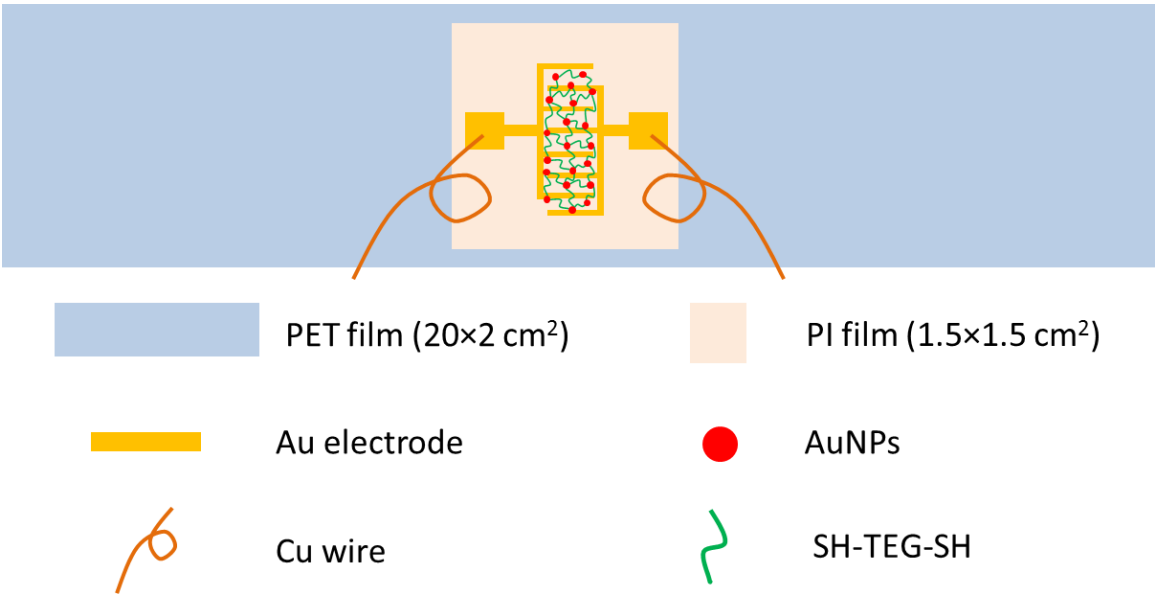

Figure 6-11. Illustration of strain sensor supported by PET film.

The electrical response to tensile strain (Figure 6-12a) and compressive strain (Figure 6-12b) clearly demonstrate the quick response of the device. It also shows the ability to sense the quickly switched signal between compressive and tensile strain (Figure 6-12c). The high strain sensing ability and quick response can also be proved by vibration experiment as shown in Figure 6-12d. With one end fixed, vibration was triggered by tapping the other end of PET substrate. The electrical response was recorded with each damping peak (inset in Figure 6-12d) clearly distinguished. The dynamic strain sensing results have proved that the AuNPs-TEG network based strain sensor has a high sensitivity and fast response speed.

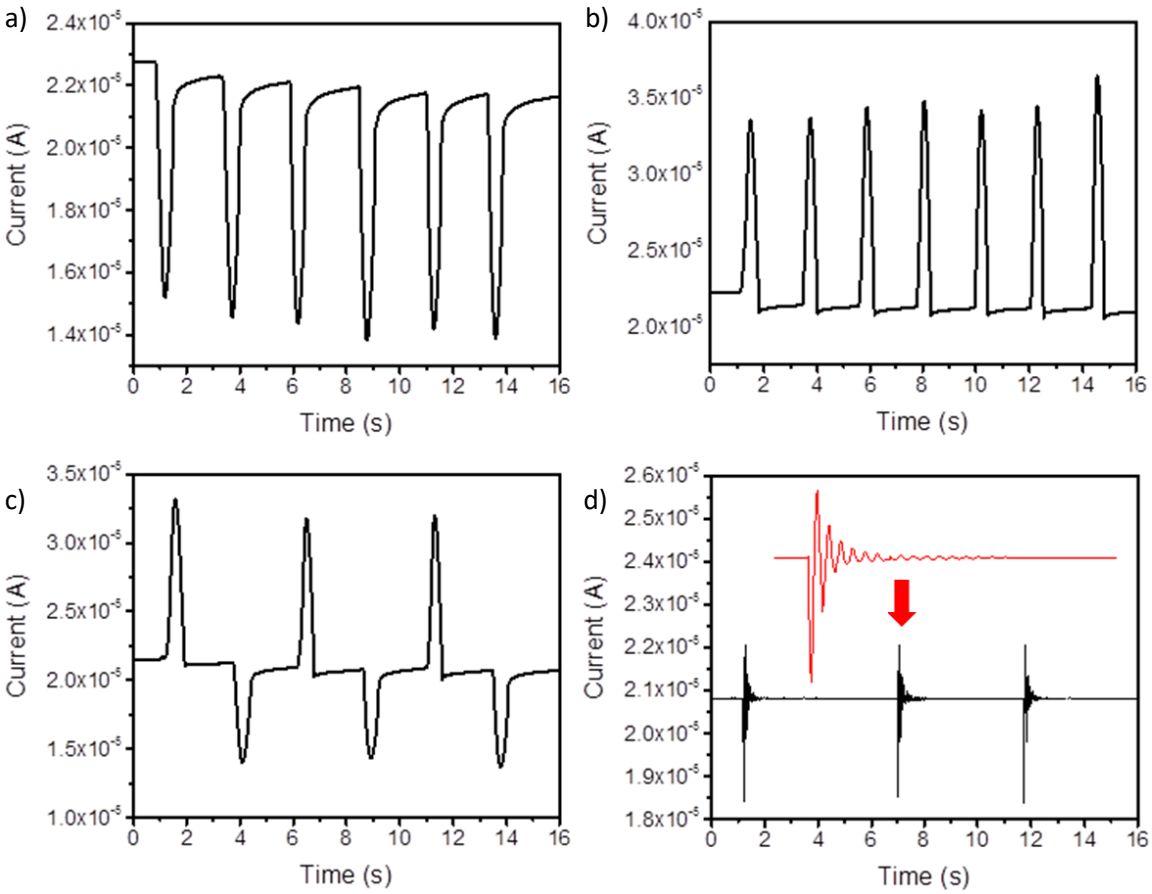

Figure 6-12: Electrical response to the signal of a) tensile strain, b) compressive strain, c) alternative compressive and tensile strain, and d) vibration.

6.2.4.2. Statistic response measurement

Gauge factor is the most important parameter to evaluate the performance of strain sensor. To determine the gauge factor, the relative resistance change $\left(\frac{\Delta R}{R_0} = \frac{R-R_0}{R_0}\right)$ under different strain (ε) has been measured. R_0 is the baseline resistance while the strain sensor is under 0 stresses. The strain ε is calculated by the equation below[35, 36]:

$$\varepsilon = \frac{h}{2r} \qquad (6-6)$$

where h is the thickness of the PET sheet (125 µm) and r is the bending radius of the substrate (Figure 6-13).

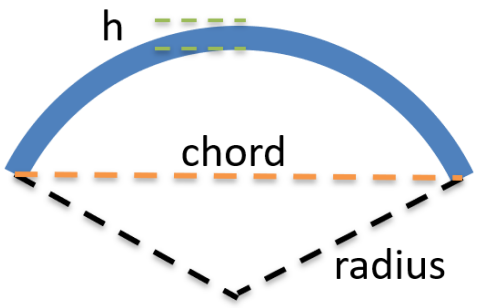

Figure 6-13. Scheme of parameters to determine strain caused by bending.

The resulting gauge factor is calculated as followed:[36]

$$GF = \frac{\Delta R}{R_0} \cdot \frac{1}{\varepsilon} = \frac{\Delta R}{R_0} \cdot \frac{2r}{h} \qquad (6-7)$$

The relative resistance change ($\Delta R/R_0$) is calculated by the current change under different stress. The bending radius (r) is determined by cylinder mould with known radii, on which the PET substrate was attached to form certain bending radius (see Table 6-3). Compressive or tensile stress was generated by attaching the PET substrate inside or outside of the cylinder mould respectively.

Table 6-3: Cylinders with their inner and outer radii and the corresponding compressive and tensile strain.

Cylinder mould	Inner radius $\mathbf{r_1}$ (compressive)	Calculated compressive strain	Outer radius $\mathbf{r_2}$ (tensile)	Calculated tensile strain $\boldsymbol{\varepsilon}$
C1	13 mm	$-4.81\cdot10^{-3}$	15 mm	$4.17\cdot10^{-3}$
C2	18 mm	$-3.47\cdot10^{-3}$	20 mm	$3.13\cdot10^{-3}$
C3	28 mm	$-2.23\cdot10^{-3}$	30 mm	$2.08\cdot10^{-3}$
C4	38 mm	$-1.64\cdot10^{-3}$	40 mm	$1.56\cdot10^{-3}$
C5	48 mm	$-1.30\cdot10^{-3}$	50 mm	$1.25\cdot10^{-3}$
C6	73 mm	$-8.56\cdot10^{-4}$	75 mm	$8.33\cdot10^{-4}$

As shown in Figure 6-14, the relative resistance shows a linear relationship with strain in the range of -0.005 to 0.005. The mean value and standard deviation (SD) of the relative resistance of nine devices were measured, in which the mean gauge factor is 30.29 with a standard deviation of 10.25. The high gauge factor for both compressive and tensile strain demonstrates excellent strain sensing properties of AuNPs-TEG based strain sensor, which makes it promising for the applications in electronic skin, motion detector and health monitoring.

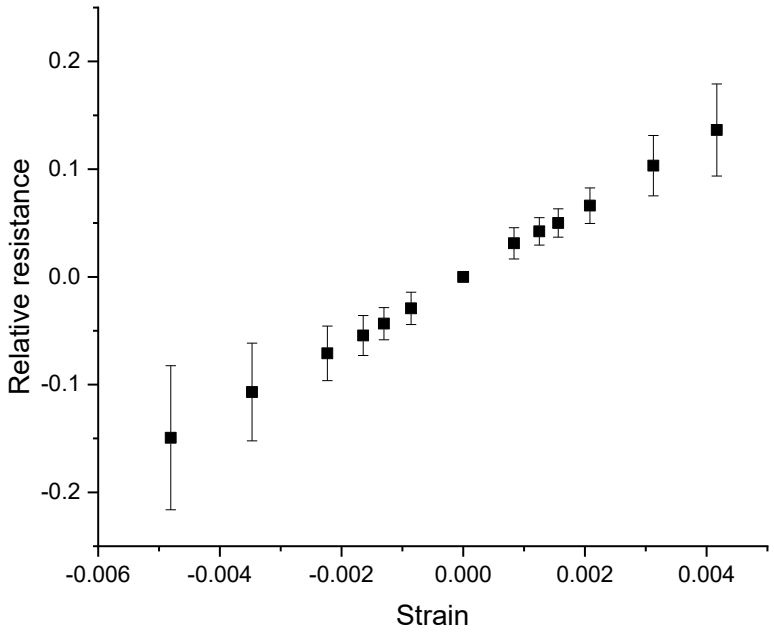

Figure 6-14: Relative resistance versus strain. (Mean value with standard deviation of 9 devices.) **Material**

All chemicals and materials such as poly (4-styrenesulfonic acid) sodium salt, Poly (pyromellitic dianhydride-co-4,4'-oxydianiline), PET film, PF-gel film, silver paste, cooper wire *etc.* were purchased from Sigma-Aldrich without further treatment.

6.3.1.1. Synthesis of gold nanoparticles

The synthesis of AuNPs was accomplished by reduction of gold (III) derivatives by citrate in water, which was introduced by Turkevitch in 1951. This has been for many years the most popular method to produce AuNPs featuring diameters of ca. 20 nm. More recently other methods have been proposed including changing the ratio between reducing/stabilizing agents,[37] two-phase synthesis,[38] seeding growth,[27, 39, 40] and physical methods (*e.g.* photochemistry,[41-43] sonochemistry,[44, 45] radiolysis,[46, 47] and thermolysis[48] *etc.*) as a mean to achieve a better control over the particle composition, size, shape, *etc.*

In this Chapter, the seeding growth method was chosen for the synthesis of AuNPs according to the Ref.[27], to generate monodisperse citrate-stabilized AuNPs with a uniform quasi-spherical shape of up to 30 nm and a narrow size distribution. Focusing on the inhibition of secondary nucleation during the homogeneous growth, AuNPs was enlarged uniformly by the surface-catalyzed reduction of Au^{3+} by sodium citrate.

Synthesis of Au Seeds：

As shown in Figure 6-15, a solution of 2.2 mM sodium citrate in Milli-Q water (150 mL) was warmed up with a heating mantle in a 250 mL three-necked round-bottomed flask with a condenser for 15 min under vigorous stirring. 1 mL of $HAuCl_4$ (25 mM) was injected while the solution was boiling. The color of the solution changed from yellow to bluish gray and then to soft pink in 10 min. The resulting particles (~10 nm, ~3×10^{12} NPs/mL) are coated with negatively charged citrate ions and hence are well suspended in H_2O.

Seeded Growth of AuNPs of Up to 30 nm in Diameter:

Following by the previous step, the solution was cooled to 90 °C. Then, 1 mL of sodium citrate (60 mM) and 1 mL of $HAuCl_4$ solution (25 mM) were sequentially injected (time delay ~2 min). After 30 min, aliquots of 2 mL were extracted for further characterization by transmission electron microscopy (TEM) and UV-vis spectroscopy. By repeating this process twice (sequential addition of 1 mL of 60 mM sodium citrate and 1 mL of 25 mM $HAuCl_4$), gold particles of diameters of 30 nm were synthesized. The concentration of each generation of NPs was approximately the same as the original seed particles (~3×10^{12} NPs/mL).

The as-prepared AuNPs was saved for the next step of functionalization and characterized by UV-Vis spectroscopy, DLS, SEM, and STEM. The characterization results are discussed as follows.

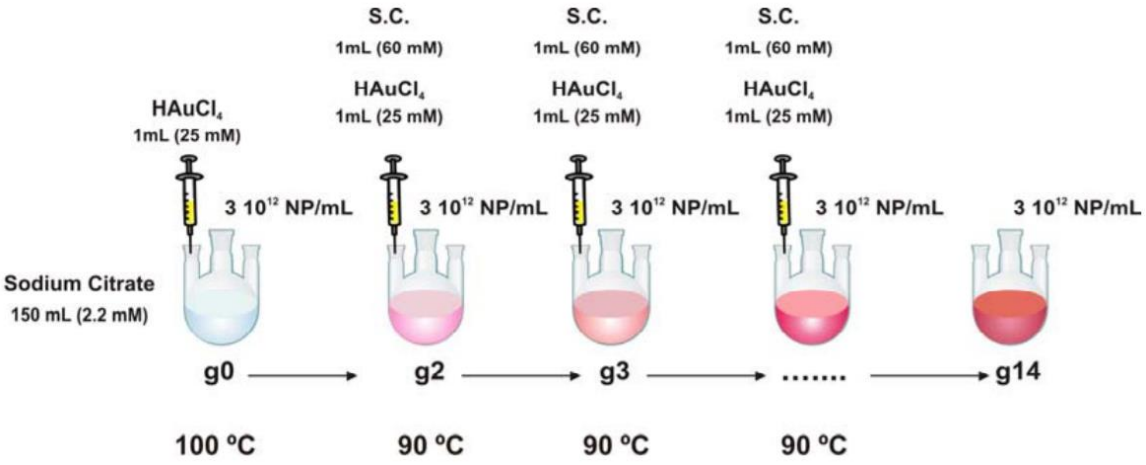

Figure 6-15. Seed growth of AuNPs up to 30 nm in diameter. Reproduced from Ref.[27]

6.3.1.2. Functionalization of gold nanoparticles

Thiol ligands are widely used for the functionalization of AuNPs either through ligand exchange process or by gold nuclei attachment during the reduction process of Au(III).[49-51] In this chapter, AuNPs was functionalized with SH-TEG-SH molecules to form interconnected nanoparticle networks in water solution (Figure 6-16). The ratio between AuNPs and SH-TEG-SH was determined by UV-vis titration, the details of which have been discussed above.

Due to the fast reaction dynamics (finished within 30 min according to UV spectroscopy results), the functionalization process was conducted in a consecutive way. 200 µl of AuNPs solution (0.8 mM) and 5 µl of a 0.5 mM SH-TEG-SH solution were mixed in a vial and drop casted immediately onto the interdigitated gold electrode supported on PI substrate. After 30 min, the solution was removed, and this step was repeated for 10 cycles.

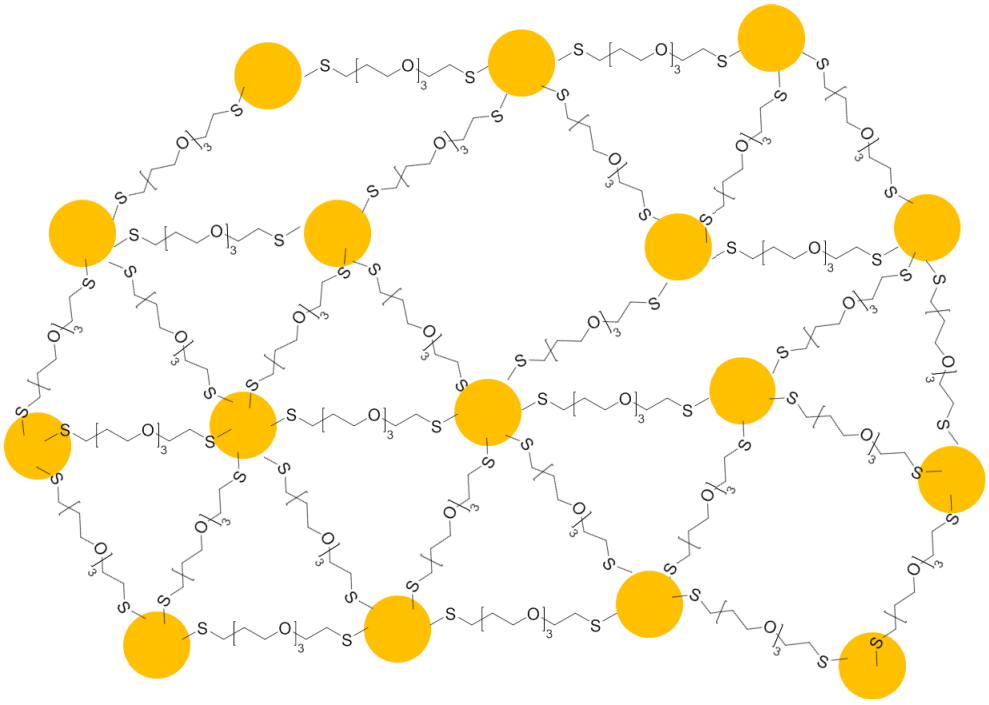

Figure 6-16. Illustration of AuNPs-TEG network. (Gold sphere: AuNPs)

6.3.2. Device fabrication

An overview of the device fabrication is provided in Figure 6-17. The fabrication process, including the electrode preparation, AuNPs-TEG network growth and electrical connection are discussed below.

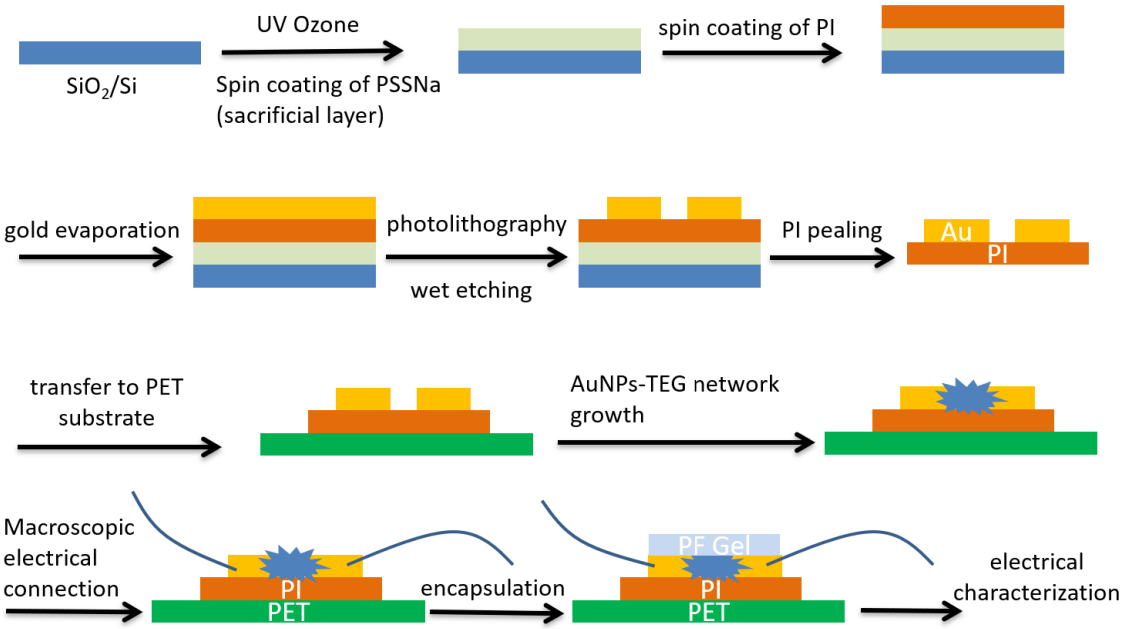

Figure 6-17: Fabrication process of strain sensor (side view).

6.3.2.1. Electrode fabrication

A sacrificial layer of poly (4-styrenesulfonic acid) sodium salt (PSSNa) was firstly spin coated onto SiO_2/Si substrate, followed by the formation of the polyimide (PI) based substrate layer, on which a 60 nm thick gold layer was evaporated. Micropattern of electrode were lithographed by photolithography and wet etching to form an interdigitated electrodes (IDEs). The as-prepared electrodes were investigated with a light microscope a multimeter to prevent any potential short circuit. Details of step-by-step fabrication are provided below:

Substrate cleaning: Silicon substrate was cleaned in an ultrasonic bath for 20 minutes in acetone and 20 minutes in isopropanol. To make the surface hydrophilic for spin coating of aqueous solution of PSSNa, the substrate was activated in UV ozone cleaner for 20 minutes.

Fabrication of scarification layer and flexible substrate: A solution of 30 wt% PSSNa (Mw = 200 000 Da) was diluted in a ratio of 1:3 with Milli-Q water. The solution was filtered with a PTFE filter (pore size: 0.2 µm) and then spin-coated at 2000 rpm with an acceleration

of 1000 rpm/s for 30 seconds. After annealing the polymer for 30 minutes at 150 °C, a layer poly (pyromellitic dianhydride-*co*-4-4'-oxydianiline) (amic acid solution) was spin coated at 2000 rpm with an acceleration of 1000 rpm/s for 120 seconds. The polyimide (PI) based substrate was formed by the annealing step which is ramping to 180 °C for 1 hour and to 300 °C for 2 hours.

Electrode layer deposition: gold layer (60 nm) has been deposited on PI substrate by physical vapour deposition (PVD).

Photolithography: The substrate acquired by the last step was firstly thermally treated on the hot plate under 100°C for 2 min to remove the surface moisture layer. Then photoresist (AZ1505) was spin coated at 3000 rpm with an acceleration of 3000 rpm/s for 45 seconds. The annealing step was performed at 120 °C for 60 seconds. Photolithography was conducted by a) direct laser writer and 2) mask aligner respectively. Afterwards, the photoresist was developed, and the accessible gold layer was wet etched with KI/I_2 according to following reaction:

$$2\,Au_{(s)} + I_{2(aq)} \rightarrow 2\,AuI_{(aq)} \qquad (6-8)$$

a) **Direct laser writing**: After spin coating the photoresist (AZ1505), the substrate was placed in the laser writer and well aligned, the IDEs pattern with channel length of 5 μm was written on the positive photoresist. The pattern used for direct laser writing can be seen in Figure 6-18. Afterwards the substrate was placed in the developer (MIF 726) for 30 seconds, washed carefully with MilliQ water and dried with nitrogen. The exposed part of the device was wet etched in a solution of KI/I_2 for 45 seconds. To remove the photoresist on the electrode after developing and etching, the substrate was placed in acetone in the ultrasonic bath for 1 minute. The substrate was finally checked with multimeter to prevent possible short circuit.

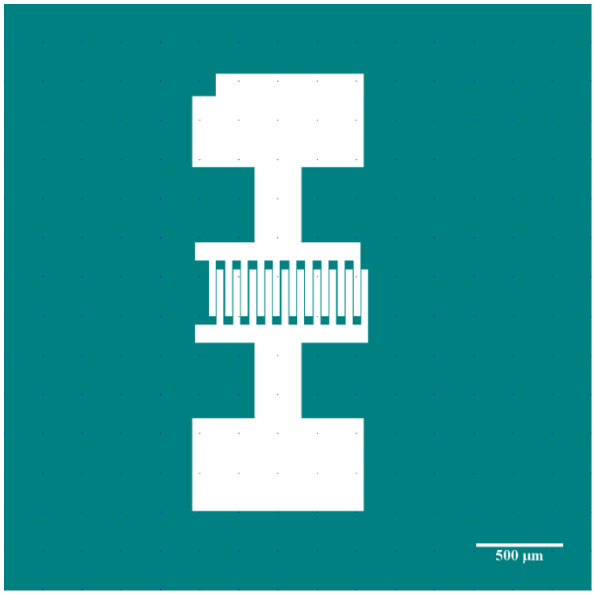

Figure 6-18: IDEs pattern for direct laser writing.

b) **Mask aligner method**: To increase the fabrication efficiency and ensure a constant quality of the IDEs, a chromium-gold mask was fabricated by direct writing lithography.

Mask fabrication: On a clean quartz substrate (ultra-sonication: two times 20 minutes in 5 % NaOH solution and 10 minutes in MilliQ water, 20 minutes in acetone and 20 minutes in isopropanol) 5 nm of chromium and 50 nm of gold were evaporated. Afterwards photoresist AZ1505 was spin coated with the same parameters as in direct laser writing of the devices (see above). IDEs with a channel length of 3 µm were patterned and the substrate was developed for 30 seconds in the developer (MIF 726). The gold was wet etched in the KI/I_2 solution for 20 seconds and the chromium layer was etched with chromium etchant (diammonium hexanitratocerate and nitric acid) for 10 seconds.

Substrate fabrication: photoresist (AZ1505) was spin coated on the substrate after gold deposition, and the mask was placed on top of it with the gold and chromium side facing downwards. Then the substrate and mask were exposed for 15 seconds under UV light and the photoresist was developed for 30 seconds with the same method. Afterwards the gold was etched in KI/I solution within 10 seconds.

Substrate releasing: In the last step the substrates were immersed in Milli-Q water. With the sacrificial layer of PSSNa dissolved, the PI substrate was released on the water surface.

Post-check: The optical characterization was performed with a light microscope. The optical characterization was used to ensure open channels of the IDEs and to investigate the presence of any blockages, which would cause short circuit. In addition, the channel length was investigated under the optical microscope. For both fabrication methods, direct laser writing and mask aligner based photolithography, channel length between 6 and 7 µm were obtained (see Figure 6-19).

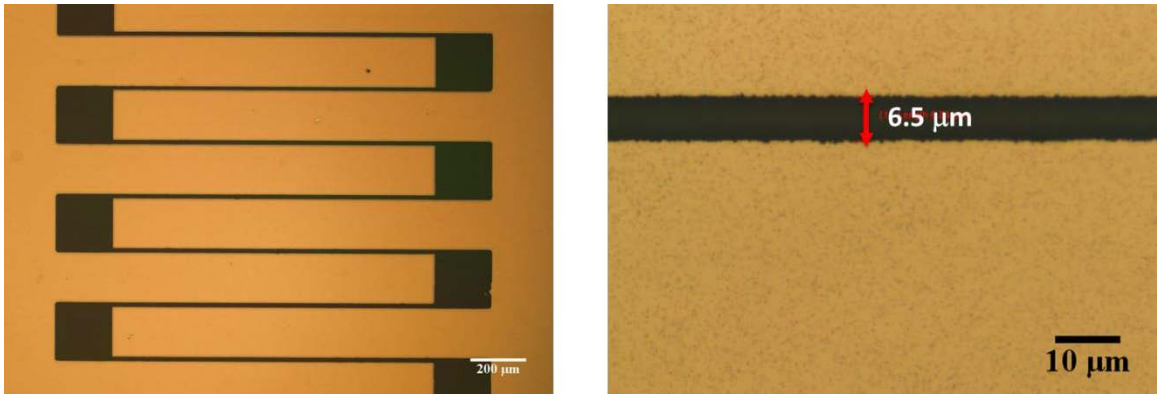

Figure 6-19: Interdigitated electrode, obtained through mask-based photolithography.

6.3.2.2. AuNPs-TEG network fabrication

The careful fabrication of AuNPs-TEG network is of great importance to strain sensor. To enable a uniform and homogenous growth of the 3D AuNPs-TEG network, (3-Aminopropyl) triethoxysilane (APTES) was drop casted onto the substrate, to create a "wetting" self-assembled monolayer ensuring efficient anchoring to the substrate as a prerequisite for the further growth of the network.

The micro patterned substrate was fixed on a PET sheet (dimension: 2 cm✕10 cm✕125 µm) with a double face tape and firstly treated by UV ozone to have a hydrophilic surface. The APTES solution (43 mM) was drop casted onto the substrate. After 30 minutes, the solution was removed, and the substrate was washed thoroughly with Milli-Q water. In the next step, 200 µl of AuNP solution was drop casted on the substrate and placed in a sealed container to avoid evaporation. After 12 hours the devices were washed with Milli-Q. At last, 200 µl of AuNPs solution (0.8 mM) and 5 µl of a 0.5 mM SH-TEG-SH solution were mixed and dropped on the electrode immediately. After 30 minutes the excess solution was removed, and the device was dried with nitrogen. The drop casting was repeated for 10 cycles.

6.3.2.3. Electrical connection

The AuNPs-TEG network being present around the interdigital part of the electrodes was carefully wiped, making sure that the network was only present in between the IDEs. The pads of the electrodes were connected to copper wires (0.1 mm diameter) with silver paste. The connections were fixed with adhesive tape. The electrodes were encapsulated by placing a PF gel film on the interdigital part and placed in the vacuum evaporator to remove trapped air in the network.

6.3.3. Characterization

6.3.3.1. Temperature dependent electrical conductivity measurement

Electrical characterization of the devices at cryogenic temperature were done by using a Nitrogen cryostat Oxford Instrument OptistatDN-V working between 80 K and 300 K (temperature steps of 10 K), controlled via an ITC503S Cryogenic Temperature Controller. The whole setup is interfaced with a dual channel Keithley 2636A source meter and controlled with a homemade LabVIEW program. The electrical conductance of AuNPs has been measured at each temperature, from -2 V to 2 V (0.05 V steps), in a planar geometry device based. This device is composed by a SiO_2 substrates and IDEs (L = 20 μm, W = 1 cm) where the AuNPs network is bridging these two electrodes.

6.3.3.2. Electrical characterization

The electrical characterization was performed with a source meter (Keithley 2635 B System Source Meter) and the software LabTracer 2.0. The baseline current was measured by keeping the PET substrate relaxed and flat. Afterwards, tensile strain and compressive strain was tested through bending the PET sheets upwards and downwards respectively. Also, the effect of vibration of the device on the current was tested by tapping one end of the PET sheet while fixing the other one. The sensor was wrapped around cylinders with different well-known diameters (Figure 6-20a) to measure the gauge factor. This procedure was used for both tensile and compressive strain. The stability and the robustness of pressure sensors has been investigated by fatigue test, in which the periodic press and release on the sensor surface was generated by a digital force gauge (Mark-10, M7-025E, ~25 N) equipped with a motorized test stand (Mark-10, ESM-303E) as shown in Figure 6-20b. All the above-mentioned tests were performed by applying a bias voltage (0.2 V) and measuring the current over time.

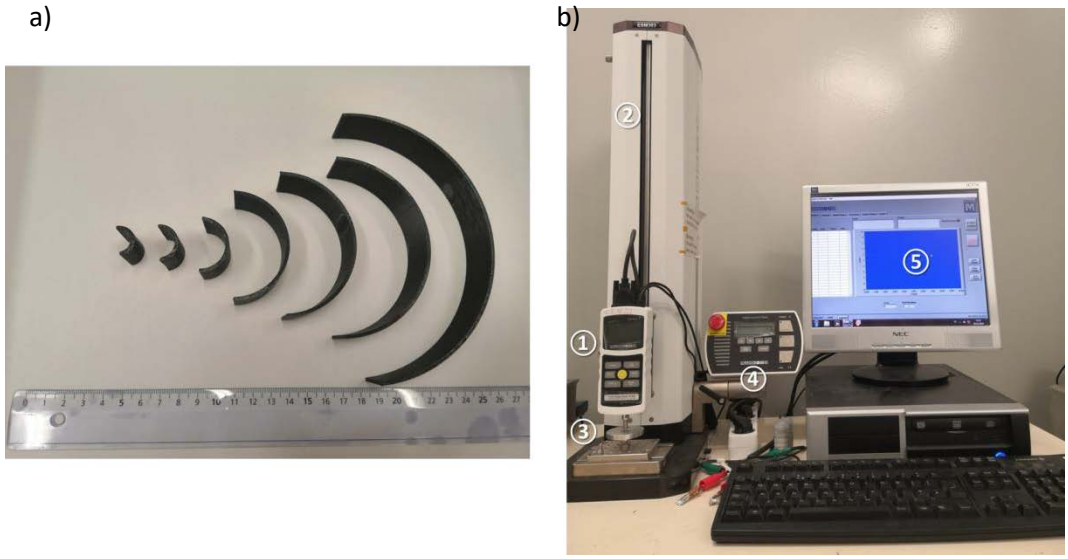

Figure 6-20. a) 3D printed half-cylinders with different radius. b) Mark-10 force test system (①force gauge ②motorized stand ③sample stage ④control panel ⑤MASURGauge software).

6.4. Conclusion

In conclusion, a novel flexible strain sensor has been designed and fabricated, in which AuNPs-TEG network has been used as active sensing material. AuNPs have been synthesized by seed growth method with the diameter of 30 nm. The flexible electrode with PI substrate was fabricated by photolithography, and mask aligner method was used to increase the fabrication efficiency. The AuNPs-TEG network was formed by layer-by-layer deposition on the gold electrode. The channels of the IDEs were covered by AuNPs network uniformly which is crucial for the detection of efficient charge transport. The strain sensing properties have been tested and the device revealed a high sensitivity and fast response to both compressive and tensile strain. The gauge factor has been calculated to be 30.29 in the low strain range (-0.005 to 0.005). These excellent sensing properties have provided unambiguous evidence that the AuNPs-TEG network based strain sensors represent promising devices in the applications of electronic skin, motion detector and health monitoring.

6.5. References

1. Sikarwar, S.; Singh, S. S.; Yadav, B. C., Review on Pressure Sensors for Structural Health Monitoring. *Photonic Sens.* **2017,** *7*, 294-304.
2. Zhang, J.; Tian, G. Y.; Marindra, A. M. J.; Sunny, A. I.; Zhao, A. B., A Review of Passive RFID Tag Antenna-Based Sensors and Systems for Structural Health Monitoring Applications. *Sensors* **2017,** *17*, 265.
3. Park, M.; Park, Y. J.; Chen, X.; Park, Y. K.; Kim, M. S.; Ahn, J. H., MoS2-Based Tactile Sensor for Electronic Skin Applications. *Adv. Mater.* **2016,** *28*, 2556-+.
4. Lee, J.; Kim, S.; Lee, J.; Yang, D.; Park, B. C.; Ryu, S.; Park, I., A stretchable strain sensor based on a metal nanoparticle thin film for human motion detection. *Nanoscale* **2014,** *6*, 11932-11939.
5. Wu, Y.; Karakurt, I.; Beker, L.; Kubota, Y.; Xu, R.; Ho, K. Y.; Zhao, S.; Zhong, J.; Zhang, M.; Wang, X.; Lin, L., Piezoresistive stretchable strain sensors with human machine interface demonstrations. *Sens. Actuator A Phys.* **2018,** *279*, 46-52.
6. Roh, E.; Hwang, B.-U.; Kim, D.; Kim, B.-Y.; Lee, N.-E., Stretchable, Transparent, Ultrasensitive, and Patchable Strain Sensor for Human–Machine Interfaces Comprising a Nanohybrid of Carbon Nanotubes and Conductive Elastomers. *ACS Nano* **2015,** *9*, 6252-6261.
7. Lim, S.; Son, D.; Kim, J.; Lee, Y. B.; Song, J.-K.; Choi, S.; Lee, D. J.; Kim, J. H.; Lee, M.; Hyeon, T.; Kim, D.-H., Transparent and Stretchable Interactive Human Machine Interface Based on Patterned Graphene Heterostructures. *Adv. Funct. Mater.* **2015,** *25*, 375-383.
8. Yeo, J. C.; Yap, H. K.; Xi, W.; Wang, Z.; Yeow, C.-H.; Lim, C. T., Flexible and Stretchable Strain Sensing Actuator for Wearable Soft Robotic Applications. *Adv. Mater. Technol.* **2016,** *1*, 1600018.
9. Flexible and Stretchable Electronics Paving the Way for Soft Robotics. *Soft Robot.* **2014,** *1*, 53-62.
10. Sangeetha, N. M.; Decorde, N.; Viallet, B.; Viau, G.; Ressier, L., Nanoparticle-Based Strain Gauges Fabricated by Convective Self Assembly: Strain Sensitivity and Hysteresis with Respect to Nanoparticle Sizes. *J. Phys. Chem. C* **2013,** *117*, 1935-1940.
11. Zheng, M.; Li, W.; Xu, M.; Xu, N.; Chen, P.; Han, M.; Xie, B., Strain sensors based on chromium nanoparticle arrays. *Nanoscale* **2014,** *6*, 3930-3933.
12. Shi, X.; Liu, S.; Sun, Y.; Liang, J.; Chen, Y., Lowering Internal Friction of 0D–1D–2D Ternary Nanocomposite-Based Strain Sensor by Fullerene to Boost the Sensing Performance. *Adv. Funct. Mater.* **2018,** *28*, 1800850.
13. Lipomi, D. J.; Vosgueritchian, M.; Tee, B. C. K.; Hellstrom, S. L.; Lee, J. A.; Fox, C. H.; Bao, Z. N., Skin-Like Pressure and Strain Sensors Based on Transparent Elastic Films of Carbon Nanotubes. *Nat. Nanotechnol.* **2011,** *6*, 788-792.
14. A stretchable carbon nanotube strain sensor for human-motion detection. *Nat. Nanotechnol.* **2011,** *6*, 296.
15. Shin, U.-H.; Jeong, D.-W.; Park, S.-M.; Kim, S.-H.; Lee, H. W.; Kim, J.-M., Highly stretchable conductors and piezocapacitive strain gauges based on simple contact-transfer patterning of carbon nanotube forests. *Carbon* **2014,** *80*, 396-404.
16. Kundu, S.; Sriramdas, R.; Rafsanjani Amin, K.; Bid, A.; Pratap, R.; Ravishankar, N., Crumpled sheets of reduced graphene oxide as a highly sensitive, robust and versatile strain/pressure sensor. *Nanoscale* **2017,** *9*, 9581-9588.
17. Ameri, S. K.; Ho, R.; Jang, H. W.; Tao, L.; Wang, Y. H.; Wang, L.; Schnyer, D. M.; Akinwande, D.; Lu, N. S., Graphene Electronic Tattoo Sensors. *ACS Nano* **2017,** *11*, 7634-7641.
18. Tang, Y.; Zhao, Z.; Hu, H.; Liu, Y.; Wang, X.; Zhou, S.; Qiu, J., Highly Stretchable and Ultrasensitive Strain Sensor Based on Reduced Graphene Oxide Microtubes–Elastomer Composite. *ACS Appl. Mater.* **2015,** *7*, 27432-27439.

19. Segev-Bar, M.; Haick, H., Flexible Sensors Based on Nanoparticles. *ACS Nano* **2013,** *7*, 8366-8378.
20. Olichwer, N.; Leib, E. W.; Halfar, A. H.; Petrov, A.; Vossmeyer, T., Cross-Linked Gold Nanoparticles on Polyethylene: Resistive Responses to Tensile Strain and Vapors. *ACS Appl. Mater.* **2012,** *4*, 6151-6161.
21. Yi, L.; Jiao, W.; Wu, K.; Qian, L.; Yu, X.; Xia, Q.; Mao, K.; Yuan, S.; Wang, S.; Jiang, Y., Nanoparticle monolayer-based flexible strain gauge with ultrafast dynamic response for acoustic vibration detection. *Nano Res.* **2015,** *8*, 2978-2987.
22. Squillaci, M. A.; Zhong, X.; Peyruchat, L.; Genet, C.; Ebbesen, T. W.; Samorì, P., 2D hybrid networks of gold nanoparticles: mechanoresponsive optical humidity sensors. *Nanoscale* **2019,** *11*, 19315-19318.
23. Squillaci, M. A.; Stoeckel, M.-A.; Samorì, P., 3D hybrid networks of gold nanoparticles: mechanoresponsive electrical humidity sensors with on-demand performances. *Nanoscale* **2019,** *11*, 19319-19326.
24. Caizzone, S.; DiGiampaolo, E., Wireless Passive RFID Crack Width Sensor for Structural Health Monitoring. *IEEE Sens. J.* **2015,** *15*, 6767-6774.
25. Sun, C., Application of RFID Technology for Logistics on Internet of Things. *AASRI Procedia* **2012,** *1*, 106-111.
26. Darianian, M.; Michael, M. P. In *Smart Home Mobile RFID-Based Internet-of-Things Systems and Services*, 2008 International Conference on Advanced Computer Theory and Engineering, 20-22 Dec. 2008; 2008; pp 116-120.
27. Bastús, N. G.; Comenge, J.; Puntes, V., Kinetically Controlled Seeded Growth Synthesis of Citrate-Stabilized Gold Nanoparticles of up to 200 nm: Size Focusing versus Ostwald Ripening. *Langmuir* **2011,** *27*, 11098-11105.
28. Haiss, W.; Thanh, N. T. K.; Aveyard, J.; Fernig, D. G., Determination of Size and Concentration of Gold Nanoparticles from UV−Vis Spectra. *Anal. Chem.* **2007,** *79*, 4215-4221.
29. Zhang, X.; Huang, C.; Wang, M.; Huang, P.; He, X.; Wei, Z., Transient localized surface plasmon induced by femtosecond interband excitation in gold nanoparticles. *Sci. Rep.* **2018,** *8*, 10499.
30. Rodríguez-Fernández, J.; Pérez-Juste, J.; García de Abajo, F. J.; Liz-Marzán, L. M., Seeded Growth of Submicron Au Colloids with Quadrupole Plasmon Resonance Modes. *Langmuir* **2006,** *22*, 7007-7010.
31. Huang, X.; El-Sayed, M. A., Gold nanoparticles: Optical properties and implementations in cancer diagnosis and photothermal therapy. *J. Adv. Res.* **2010,** *1*, 13-28.
32. Paredes-Madrid, L.; Palacio, C. A.; Matute, A.; Parra Vargas, C. A., Underlying Physics of Conductive Polymer Composites and Force Sensing Resistors (FSRs) under Static Loading Conditions. *Sensors* **2017,** *17*, 2108.
33. Kimling, J.; Maier, M.; Okenve, B.; Kotaidis, V.; Ballot, H.; Plech, A., Turkevich Method for Gold Nanoparticle Synthesis Revisited. *J. Phys. Chem. B* **2006,** *110*, 15700-15707.
34. Zheng, T.; Choy, W. C. H.; Sun, Y., Hybrid Nanoparticle/Organic Devices with Strong Resonant Tunneling Behaviors. *Adv. Funct. Mater.* **2009,** *19*, 2648-2653.
35. Chen, S.; Wei, Y.; Wei, S.; Lin, Y.; Liu, L., Ultrasensitive Cracking-Assisted Strain Sensors Based on Silver Nanowires/Graphene Hybrid Particles. *ACS Appl. Mater.* **2016,** *8*, 25563-25570.
36. Vossmeyer, T.; Stolte, C.; Ijeh, M.; Kornowski, A.; Weller, H., Networked Gold-Nanoparticle Coatings on Polyethylene: Charge Transport and Strain Sensitivity. *Adv. Funct. Mater.* **2008,** *18*, 1611-1616.
37. Watson, K. J.; Zhu, J.; Nguyen, S. T.; Mirkin, C. A., Hybrid Nanoparticles with Block Copolymer Shell Structures. *J. Am. Chem. Soc.* **1999,** *121*, 462-463.

38. Brust, M.; Walker, M.; Bethell, D.; Schiffrin, D. J.; Whyman, R., Synthesis of thiol-derivatised gold nanoparticles in a two-phase Liquid–Liquid system. *J. Chem. Soc. Chem. Commun.* **1994**, 801-802.
39. Jana, N. R.; Gearheart, L.; Murphy, C. J., Evidence for Seed-Mediated Nucleation in the Chemical Reduction of Gold Salts to Gold Nanoparticles. *Chem. Mater.* **2001,** *13*, 2313-2322.
40. Meltzer, S.; Resch, R.; Koel, B. E.; Thompson, M. E.; Madhukar, A.; Requicha, A. A. G.; Will, P., Fabrication of Nanostructures by Hydroxylamine Seeding of Gold Nanoparticle Templates. *Langmuir* **2001,** *17*, 1713-1718.
41. Mössmer, S.; Spatz, J. P.; Möller, M.; Aberle, T.; Schmidt, J.; Burchard, W., Solution Behavior of Poly(styrene)-block-poly(2-vinylpyridine) Micelles Containing Gold Nanoparticles. *Macromolecules* **2000,** *33*, 4791-4798.
42. Mallick, K.; Wang, Z. L.; Pal, T., Seed-mediated successive growth of gold particles accomplished by UV irradiation: a photochemical approach for size-controlled synthesis. *J. Photoch. Photobio. A* **2001,** *140*, 75-80.
43. Zhou, Y.; Wang, C. Y.; Zhu, Y. R.; Chen, Z. Y., A Novel Ultraviolet Irradiation Technique for Shape-Controlled Synthesis of Gold Nanoparticles at Room Temperature. *Chem. Mater.* **1999,** *11*, 2310-2312.
44. Reed, J. A.; Cook, A.; Halaas, D. J.; Parazzoli, P.; Robinson, A.; Matula, T. J.; Grieser, F., The effects of microgravity on nanoparticle size distributions generated by the ultrasonic reduction of an aqueous gold-chloride solution. *Ultrason. Sonochem.* **2003,** *10*, 285-289.
45. Okitsu, K.; Yue, A.; Tanabe, S.; Matsumoto, H.; Yobiko, Y., Formation of Colloidal Gold Nanoparticles in an Ultrasonic Field: Control of Rate of Gold(III) Reduction and Size of Formed Gold Particles. *Langmuir* **2001,** *17*, 7717-7720.
46. Henglein, A.; Meisel, D., Radiolytic Control of the Size of Colloidal Gold Nanoparticles. *Langmuir* **1998,** *14*, 7392-7396.
47. Dawson, A.; Kamat, P. V., Complexation of Gold Nanoparticles with Radiolytically Generated Thiocyanate Radicals ((SCN)2•-). *J. Phys. Chem. B* **2000,** *104*, 11842-11846.
48. Nakamoto, M.; Yamamoto, M.; Fukusumi, M., Thermolysis of gold(i) thiolate complexes producing novel gold nanoparticles passivated by alkyl groups. *Chem. Commun.* **2002**, 1622-1623.
49. Woehrle, G. H.; Brown, L. O.; Hutchison, J. E., Thiol-Functionalized, 1.5-nm Gold Nanoparticles through Ligand Exchange Reactions: Scope and Mechanism of Ligand Exchange. *J. Am. Chem. Soc.* **2005,** *127*, 2172-2183.
50. Pensa, E.; Cortés, E.; Corthey, G.; Carro, P.; Vericat, C.; Fonticelli, M. H.; Benítez, G.; Rubert, A. A.; Salvarezza, R. C., The Chemistry of the Sulfur–Gold Interface: In Search of a Unified Model. *Acc. Chem. Res.* **2012,** *45*, 1183-1192.
51. Yang, H. Y.; Wang, Y.; Huang, H. Q.; Gell, L.; Lehtovaara, L.; Malola, S.; Hakkinen, H.; Zheng, N. F., All-thiol-stabilized Ag-44 and Au12Ag32 nanoparticles with single-crystal structures. *Nat. Commun.* **2013,** *4*, 8.

Chapter 7

Graphene-photoresist hybrid based pressure sensor with tunable sensitivity by UV

In this Chapter, a novel kind of pressure sensor whose sensitivity can be tuned with UV light is presented. By employing photosensitive polymer and grafting it to graphene flakes, the rigidity of the hybrid structure can be modulated with UV light as a result of photo-induced polymerization. The current passing through the hybrid materials is directly ruled by the distance between adjacent graphene flakes, which is controlled by the applied pressure. By irradiating with UV light at different power/time, the degree of cross-link of the photosensitive polymer can be tuned which ultimately to a modulation of the hybrid's compressibility. The latter determines the device sensitivity. In this Chapter, a prototypical negative photoresist SU-8 2002 was chosen to form hybrid material with graphene. Negative photoresist is a kind of polymer widely used in photo lithography, whose rigidity will increase as a result of the polymerization triggered by UV. SU-8 2002 is a high contrast, epoxy based photoresist designed for micromachining and other microelectronic applications. In this Chapter, the as-prepared hybrids have been blended with SU-8 2002 and irradiated with UV light to trigger polymerization between graphene flakes. The synthesis of active material and the fabrication of devices have been accomplished, and the characterization of sensing properties is under testing.

7.1. Introduction

Graphene based pressure sensors, which play an important role in the field of electronic skin, health motoring or other applications have been discussed in Chapter 3. In Chapter 5, we introduced a radically new generation of pressure sensors whose sensitivity is modulated by flexible molecular linkers placed in between graphene layers. Sensitivity of the pressure sensor can be effectively improved by chemical modification of graphene with highly flexible molecular ligands. Inspired by this rigidity modulation method, we have designed a new type of pressure sensor, of which the sensitivity can be tuned by UV light.

Bing present in sunlight, UV light is an electromagnetic radiation with wavelength from 10 nm to 380 nm, which has a wide application of photolithography technique in electronic industry. Triggered by UV, negative photoresist undergoes photo-induced polymerization process, in which the polymer precursors start to be polymerized or cross-linked to form a more rigid layer.

In this Chapter, a prototypical negative photoresist, *i.e.* SU-8 2002, is chosen to form composite material with graphene. SU-8 2002 is a high contrast, epoxy based photoresist designed for micromachining and other microelectronic applications.[1] The exposed and subsequently thermally cross-linked portions of the film are rendered insoluble to liquid developers. Upon exposure, cross-linking proceeds in two steps (1) formation of a strong acid during the exposure step, followed by (2) acid-catalyzed, thermally driven epoxy cross-linking during the post exposure bake (PEB) step. The stiffness of SU-8 2002 was determined by AFM nano indentation method, which is commonly used to gain quantitative insight into the mechanical properties of soft matter like cells.[2-4]

The fabrication process of pressure sensor is similar to the one discussed in Chapter 5. As-prepared GO based hybrids dispersions were spray coated onto ITO coated PET substrates, followed by face-to-face assembly and wiring out by cooper wire and silver paste. The pressure sensing properties have been tested by recording the current vs bias voltage while applying a vertical pressure. Prior to the device characterization, the active material was placed under UV irradiation (365 nm) for different time to investigate the effect of UV irradiation on the device sensitivity.

7.2. Results and discussions

Before the fabrication of graphene photoresist hybrid, the relationship between polymer rigidity and UV irradiation time needs to be investigated. In this part, negative photoresist (SU-8 2002) was spin coated onto a Si substrate followed by UV irradiation for a certain time. The Young's modulus of SU-8 2002 membranes was measured by means of AFM. As shown in the equation below (Figure 7-1), the Young's modulus (E) can be extracted directly from the build-in software of Veeco/Bruker Dimension 3100 (AFM model) by indentation experiment with known parameters including Poisson's ratio (sample dependent) and the radius of the indenter (AFM tip). SU-8 2002 is a commercially available photoresist and its Poisson's ratio is reported as 0.22.[5]

Hertzian model:

$$F = \frac{4}{3}\frac{E}{(1-\nu^2)}\sqrt{R}\,\delta^{\frac{3}{2}}$$

where
F = force (from force curve)
E = Young's modulus (fit parameter)
ν = Poisson's ratio (sample dependent, typically 0.2 - 0.5)
R = radius of the indenter (tip)
δ = indentation

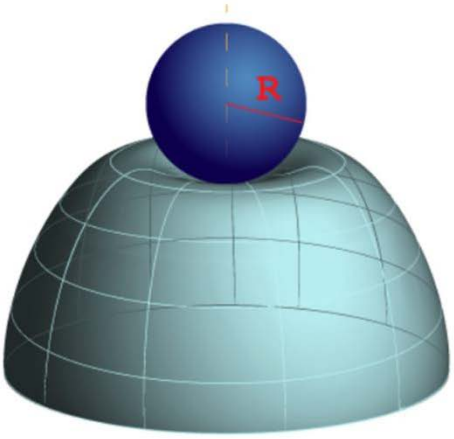

Figure 7-1. Hertz model for contact between a sphere and an elastic half space.

The indenter radius, *i.e.* the radius of AFM tip (BRUKER, SCM-PIC), is 20 nm as provided by the supplier. The radius of a new AFM tip has been measured by SEM (Figure 7-2) revealing a size of 20 nm, in accordance with the value given by the provider. A spherical end appears on top of the pyramid-like tip from the side view of a new AFM tip.

During the indentation experiment, the radius of AFM tip increases with time due to the surface contamination. As shown in Figure 7-3, the surface of a used AFM tip has been checked by SEM. It clearly shows the increased radius (44 nm) of the tip either from the side-view or top-view. This radius measurement is an essential step to acquire an accurate Young's modulus of SU-8 2002. The results have been plotted in Figure 7-4, in which the Young's modulus of SU-8 2002 increases linearly with UV irradiation time. Modified radius value increases the R square value from 0.90 to 0.96 effectively, indicating a more accurate linear

fitting. Above results have demonstrated that the mechanical properties of SU-8 2002 can be finely tuned by UV light in a linear way.

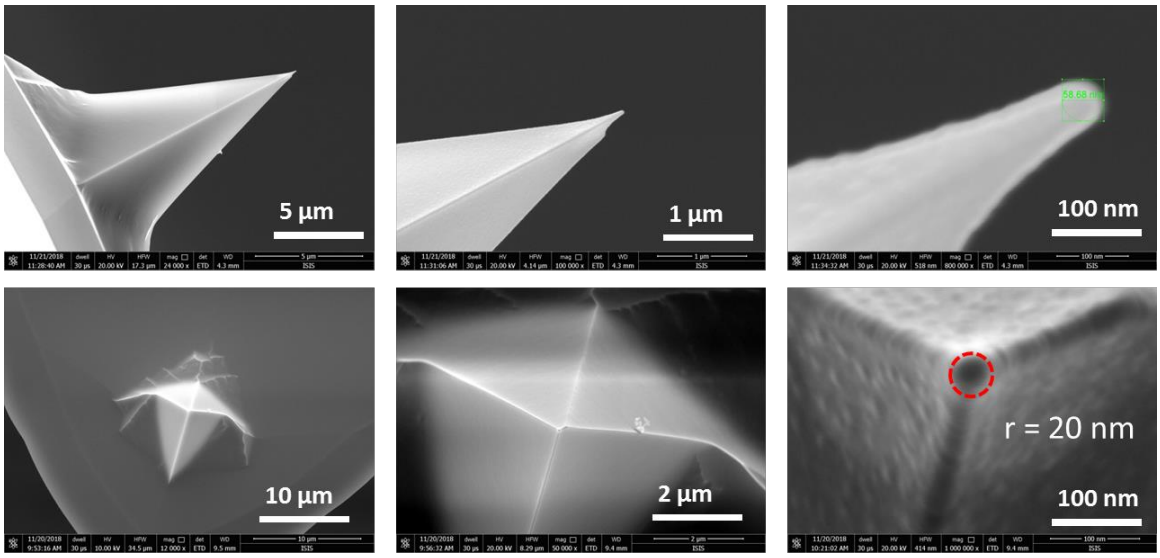

Figure 7-2. SEM images of a new AFM tip (model: SCM-PIC, spring constant: 0.2 N/m). Top: side-view; Bottom: top-view.

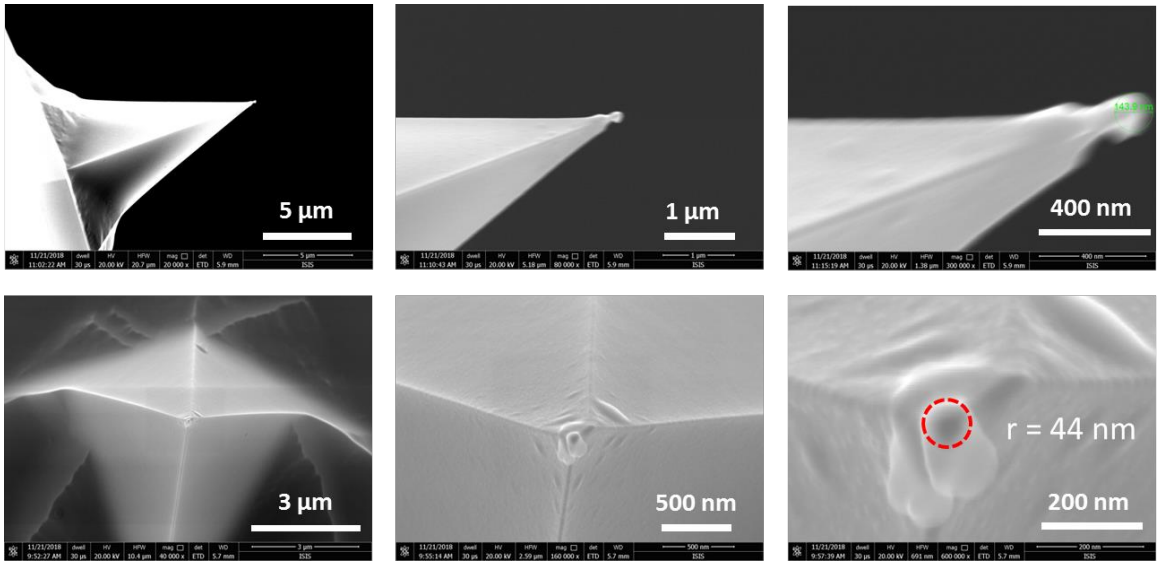

Figure 7-3. SEM images of a used AFM tip (model: SCM-PIC, spring constant: 0.2 N/m). Top: side-view; Bottom: top-view.

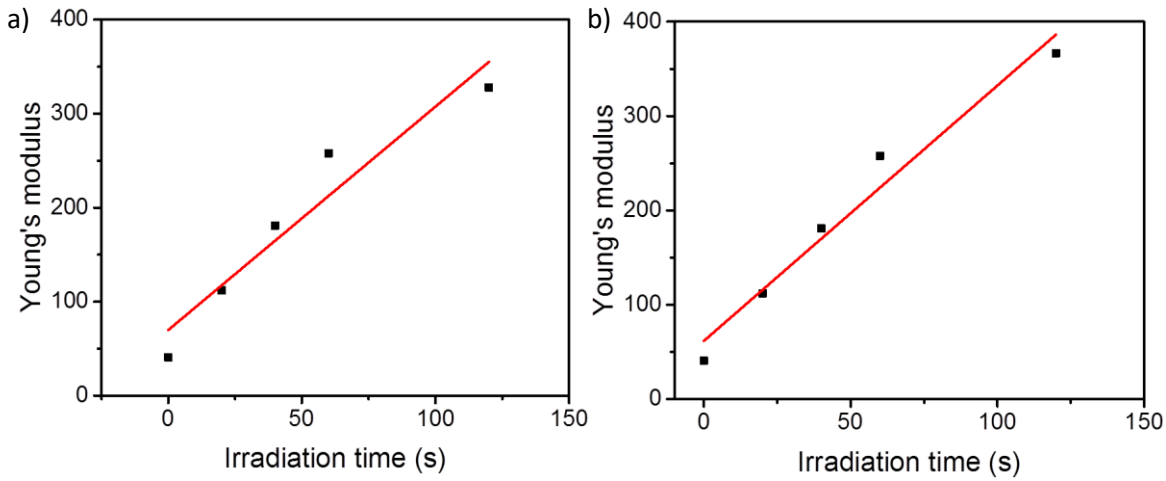

Figure 7-4. Relationship between Young's modulus and UV irradiation time with a) unmodified and b) modified radius value.

After the research on the mechanical properties of SU-8 2002, the active pressure sensing material has been synthesized. As shown in Figure 7-5, starting from graphene oxide (GO), the first step was to functionalize its surface with ethylene diamine to create reactive sites for the grafting of SU-8 2002 polymer. After a reduction step conducted by hydrazine to restore the conductivity of graphene flakes, SU-8 2002 was cross-linked with graphene oxide through the substitution reaction of epoxy groups of SU-8 2002 with the primary amines exposed in the functionalized rGO. The details on the synthesis are provided in the *Experimental methods*.

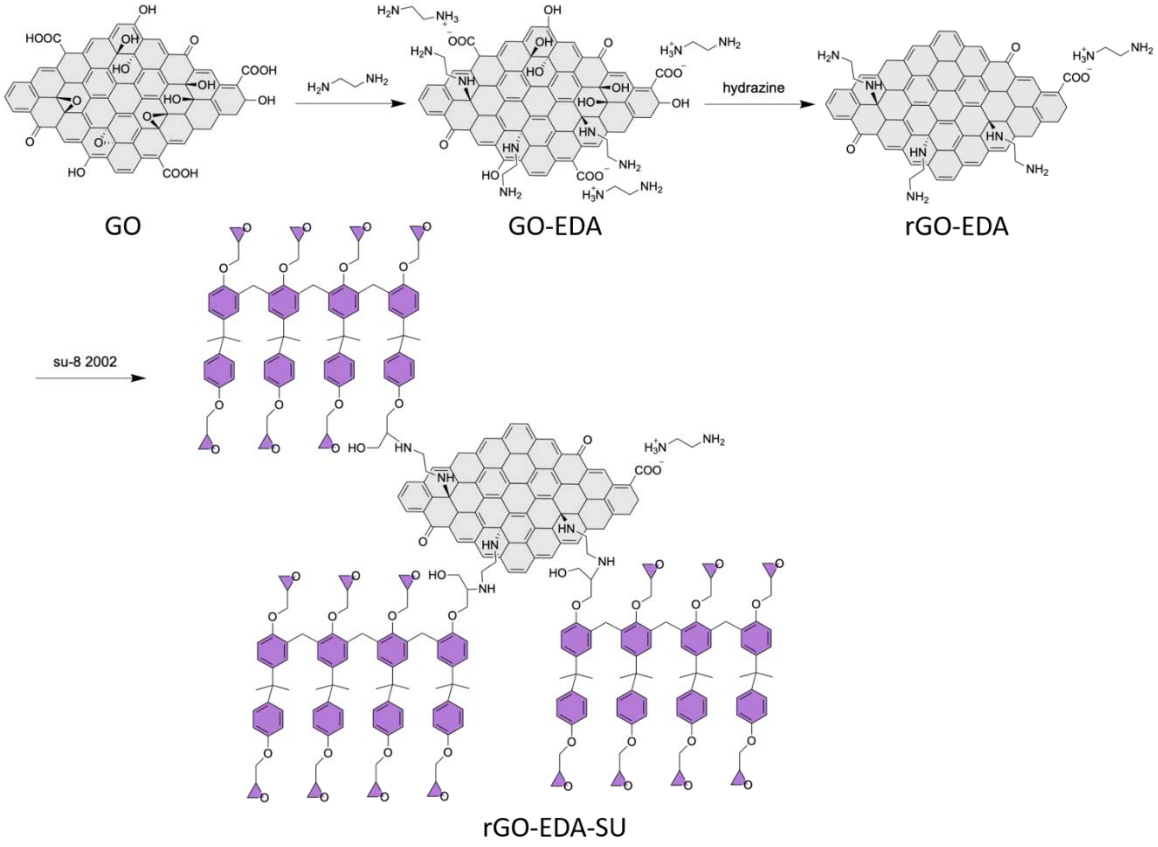

Figure 7-5. Synthesis of active material rGO-EDA-SU.

XPS was used to characterize the composition of the product in each step. As shown in Table 7-1, the N content increased to 8.06% in GO-EDA compared to the negligible amount in GO, which indicates the successful functionalization of ethylene diamine onto graphene. After the reduction step, the oxygen content was clearly decreased from 14.37% to 10.30%, indicating a successful reduction step. The last step of the active sensing material synthesis consists in the reaction between rGO-EDA and SU-8 2002. Upon addition of polymer that comprises only carbon and oxygen atoms, the N1s signal of the final product decreases from 7.42% to 2.56%. Detailed analysis of XPS results are discussed in the *Experimental methods*.

Table 7-1: survey of XPS results of GO, GO-EDA, rGO-EDA, rGO-EDA-SU

	Name	Peak BE	FWHM eV	Area (P) CPS.eV	Atomic %
GO	C1s	286,45	4,26	1697077,80	67,40
	O1s	532,94	2,91	1953047,15	32,08
	N1s (negligible)	402,14	3,78	20152,85	0,52
GO-EDA	C1s	285,21	3,27	1683357,60	77,57
	O1s	532,19	3,58	753691,31	14,37
	N1s	399,96	3,40	271537,89	8,06
rGO-EDA	C1s	285,11	3,08	1871892,79	82,28
	O1s	532,14	3,91	566190,50	10,30
	N1s	399,91	3,53	262029,29	7,42
rGO-EDA-SU	C1s	285,01	3,35	1381176,13	82,50
	O1s	532,86	2,79	603995,42	14,94
	N1s	399,40	3,84	66506,09	2,56

To test the pressure sensing characteristics of the functionalized graphene oxide, the pressure sensor devices were fabricated with the same method presented in Chapter 5. Commercially available ITO coated PET was selected as flexible electrode, on which the rGO-EDA-SU dispersion was spray coated as sensing layer. Two substrates were assembled in a face-to-face manner and wired out by cooper wire and silver paste. The whole device was encapsulated by transparent scotch tape to pass through UV light and to avoid the interference of humidity in the air. Electrical test has been conducted by applying bias voltage (0.2 V) between the electrodes while measuring the current simultaneously to the application of pressure to the system. The electrical response as a result of the applied pressure is shown in the Figure 7-6. The black line represents the electrical signal of the as-prepared pressure sensor without any UV light treatment. Upon pressing continuously with a finger, the device shows certain electrical response which is however very unstable and irregular. All the peaks having

different intensity in the three current vs time plots are the results of continuous finger pressing. The device was irradiated with UV lamp (365 nm) for 2 min and 4 min to trigger the polymerization process. Yet the signal displayed with red and green lines in Figure 7-6 still show irregularities. Considering the morphology of rGO-EDA-SU, the heterogeneous stacking of aggregated graphene hybrid during spray coating might be the reason of the unstable electrical response.

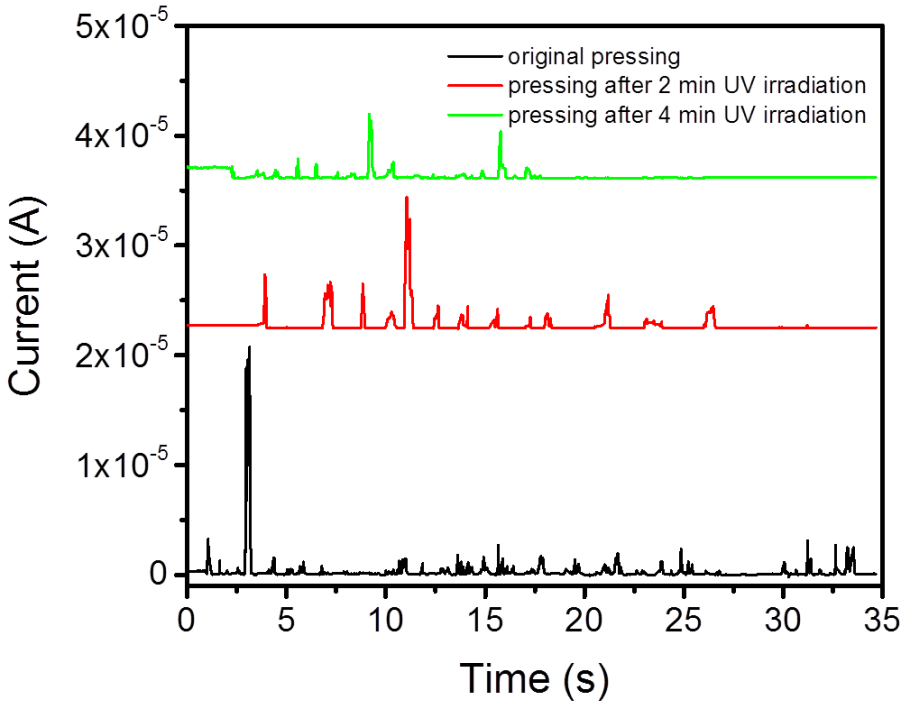

Figure 7-6. Electrical response to dynamic pressure simulation under different conditions. Black: original device without UV irradiation; Red: pressing after 2 min of UV irradiation; Green: pressing after 4 min of UV irradiation.

7.3. Experimental Methods

7.3.1. Materials

To achieve a good understanding and control over rigidity of the layer-by-layer structure, the responsivity of single layer of photoresist to UV needs to be investigated firstly. The photoresist used in this work is SU-8 2002, which is an acid-catalyzed negative photoresist. It is made by dissolving EPON® SU-8 resin in an organic solvent such as propylene glycol methyl ether acetate (PGMEA), cyclopentanone, or gamma-butyrolactone (GBL) and by adding up to 10 wt% of triarylsulfonium hexafluoroantimonate salt as a photoinitiator. The EPON resist is a highly branched epoxy derivative that consists of bisphenol-A novolac glycidyl ether. On average, a single molecule contains eight epoxy groups which explains the "8" in the name SU-8 2002 (Figure 7-7). SU-8 2002 cross-linking starts upon the UV irradiation of the photoresist. In the exposed areas, the photoinitiator decomposes to form hexafluoroantimonic acid that protonates the epoxides on the oligomer. These protonated oxonium ions are conversely able to react with neutral epoxides in a series of cross-linking reactions after application of heat. In other words, irradiation generates a low concentration of a strong acid that opens the epoxide rings and acts as a catalyst of the chemically amplified cross-linking process that gets further activated upon applying heat.

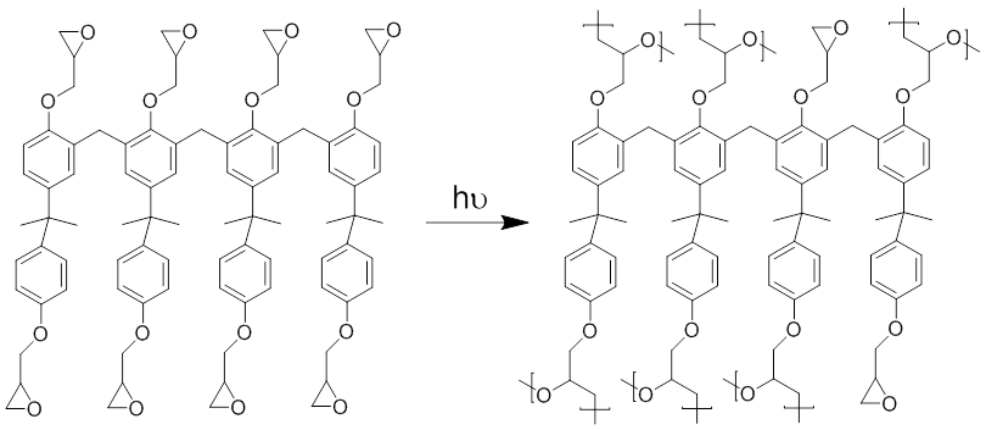

Figure 7-7. Working principle of SU-8 2002 upon exposure of UV.

Synthesis details of rGO-EDA-SU:

25 ml water dispersion of GO (4 mg/ml) was diluted with 100 ml ethanol in a 250 ml round-bottom flask and sonicated for 30 min. Then 500 mg of ethylene diamine (EDA) was weighed into a 10 mL glass vial and dissolved in 5 ml ethanol. The amine solution was then added into the GO dispersion and refluxed while stirring overnight at 90 °C under N_2 atmosphere. After cooling down the solution to room temperature, the dispersion was centrifuged for 10 min at 2000 rpm. Then the supernatant was removed and 200 ml of ethanol were added to the black sludge. The mixture was sonicated for 10 min and centrifuged again. The sonication-centrifugation process was repeated 3 times. After the last centrifugation the black sludge (GO-EDA) was dispersed in 200 ml ethanol and sonicated 10 min.

The reduction process of GO-EDA was carried out by adding 2 ml of hydrazine hydrate to GO-EDA ethanolic dispersion followed by refluxing overnight at 90 °C under N_2 atmosphere. The purification was performed through sonication-centrifugation cycles as described above for GO-EDA. The resulting dispersion (200 ml) of rGO-EDA was decanted and used for the next step synthesis.

The final synthesis step was carried out by the reaction of rGO-EDA and SU-8 2002. 10 ml rGO-EDA dispersion from the previous step was diluted with 15 ml ethanol and 25 ml acetone in a 100 ml round-bottom flask to increase the solubility of SU-8 2002. Then 1 ml SU-8 2002 (solid content: 29%) was added into the dispersion and refluxed while stirring overnight at 90 °C under N_2 atmosphere. After cooling down the solution to room temperature, the dispersion was centrifuged for 10 min at 2000 rpm. Then the supernatant was removed and 100 ml of ethanol were added to the black sludge. The mixture was sonicated for 10 min and centrifuged again. The sonication-centrifugation process was repeated three times. After the last centrifugation the black sludge (rGO-EDA-SU) was dispersed in 10 ml ethanol and sonicated 10 min. The functionalized graphene material has been finalized and ready to be integrated into pressure sensor devices.

7.3.2. Device fabrication

The device fabrication process (shown in Figure 7-8) is the same as the one detailed in chapter 5. rGO-EDA-SU ethanol dispersion was spray coated onto the ITO coated PET substrates. Then two substrates were assembled together in a face-to-face manner with the active material sandwiched in between the electrodes. The only difference with the case discussed in Chapter 5 is that transparent scotch tape instead of PI tape was used as encapsulating material for a better transmission of UV light to enable efficient light driven polymerization. Finally the device was wire up with cooper wires and silver paste for electrical test.

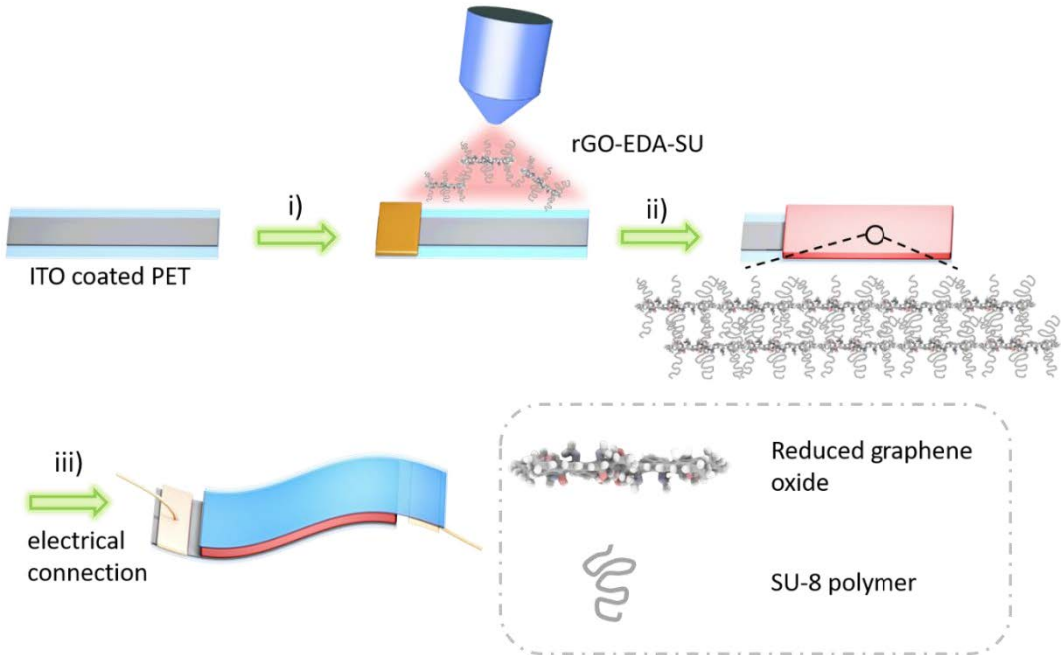

Figure 7-8. Pressure sensor device fabrication process.

7.3.3. Characterization

After the synthesis of GO-EDA, rGO-EDA, rGO-EDA-SU, the materials were thoroughly characterized by means of SEM, XPS, and Raman spectroscopy to have a comprehensive understanding of the material structure.

7.3.3.1. Scanning Electron Microscopy

SEM was firstly used to study the morphology of the active materials. The silicon substrates were firstly cleaned by sonication bath in acetone and IPA for 20 min respectively, followed by UV ozone treatment for 20 min. Then the ethanol dispersions of three materials, which are GO-EDA, rGO-EDA, rGO-EDA-SU, were drop casted on the Si substrates. As shown in Figure 7-9, 7-10, 7-11, the morphologies of GO-EDA, rGO-EDA, rGO-EDA-SU are very different. GO-EDA and rGO-EDA have demonstrated wrinkled layered structure, which is in accordance with reported structures.[6, 7] Yet the SU-8 2002 functionalized graphene rGO-EDA-SU (Figure 7-11) has revealed a totally different morphology, in which the graphene layers have aggregated into small particles featuring a size of dozens of micrometers. This might be caused by the interaction among the SU-8 2002 polymers forcing the graphene layers to adopt a more aggregated state.

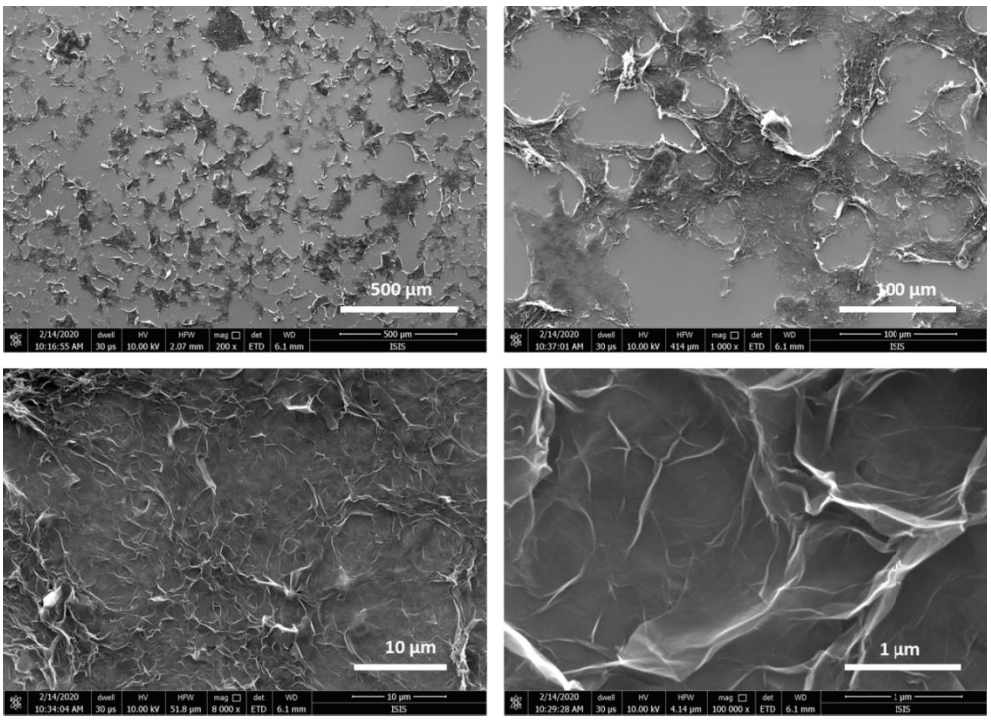

Figure 7-9. SEM images of GO-EDA.

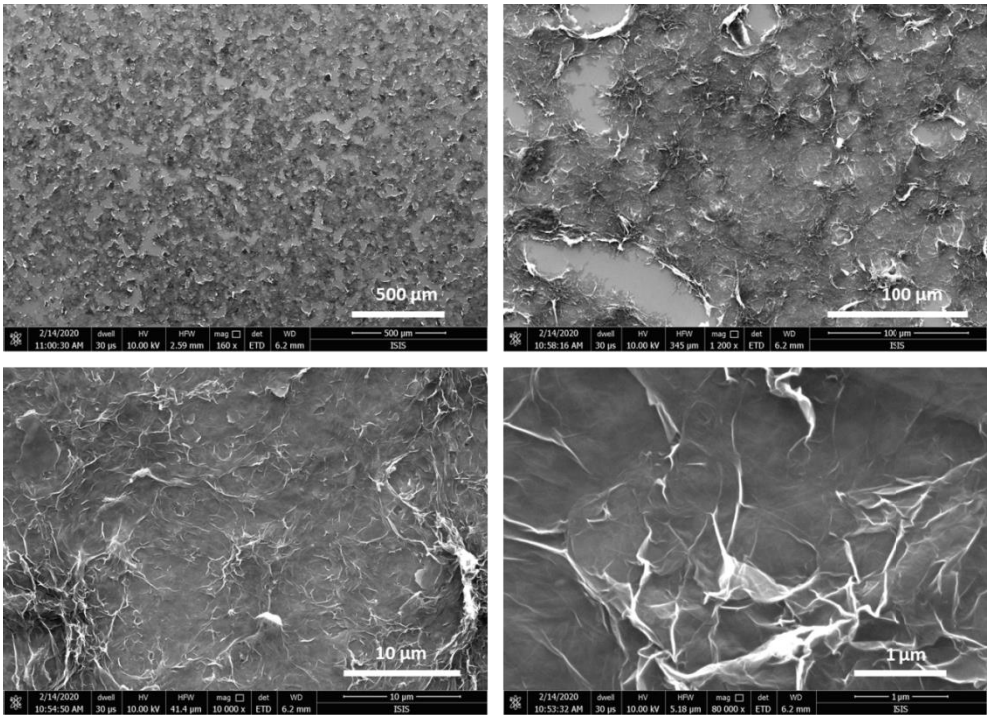

Figure 7-10. SEM images of rGO-EDA.

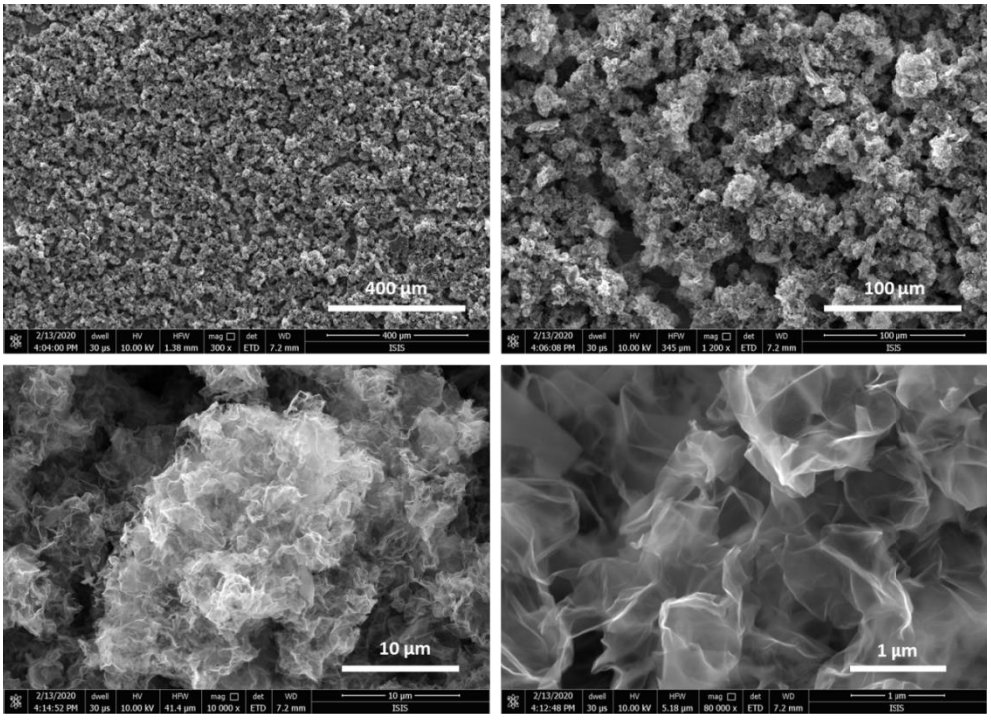

Figure 7-11. SEM images of rGO-EDA-SU.

7.3.3.2. Atomic Force Microscopy

A single layer of SU-8 2002 was firstly deposited on the silicon substrate to test its mechanical response to UV exposure (Figure 7-12). Before deposition, a SiO_2/Si substrate was washed by sonication bath in acetone and IPA. Then a post treatment was carried out by oxygen plasma to further remove the contaminant, providing a hydrophilic character to the surface which is particularly suitable for postdeposition by spin coating. Spin coating process was carried out with a spin speed of 2000 rap min^{-1} and then the sample was transferred to a hot plate at 100°C for a soft bake. The film thickness was measured by profilometer which demonstrated a uniform film with a thickness of 2.100 µm. The substrate was placed under UV light (λ=365 nm) to trigger the polymerization process followed by soft bake at 100℃ for 1 min. The samples were irradiated for different time to understand its effect on the mechanical properties of SU-8 2002. The substrate was cut into small pieces after UV treatment for AFM test.

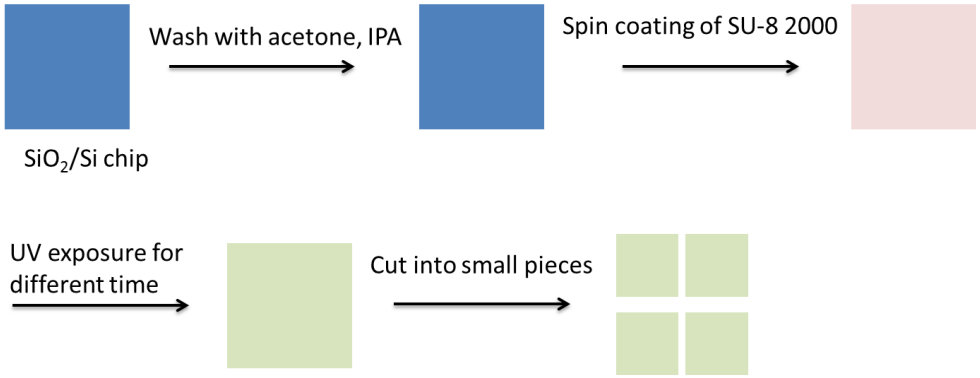

Figure 7-12. Sample preparation process for AFM test.

Nano indentation experiment was conducted with a Bruker Dimension Icon set up operating in air. The operation details have been discussed in Chapter 4.

7.3.3.3. X-ray Photoelectron Spectroscopy

The chemical bonding of each functionalization step of GO was analyzed by X-ray photoelectron spectroscopy (XPS). The full range spectra shown in Figure 7-13 indicates the occurrence of N 1s peak at 400.11 eV after the functionalization step of EDA. The analysis of high resolution spectra of N 1s in Figure 7-14b, d, f (as well as Table 7-2, and Table 7-3) reveals the three types of nitrogen bonding at 398.85 eV, 399.85 eV and 401.67 eV, which could be assigned to be primary amine (C-NH_2), secondary amine (C-NH-C), and protonated primary amine (C-NH_3^+). After the reduction by hydrazine, the oxidation degree of GO has shown a prominent decrease from 14.37% to 10.30% with the amount of nitrogen species remains unchanged. The high resolution C1s spectra in Figure 7-14a, c display that the C=O (288.1 eV) and C-O (286.34 eV) of rGO-EDA drops from 17.07% to 10.17% and from 24.84 % to 21.25 %, respectively, implying the successful reduction. The C-N peak at 285.62 eV has witnessed a slight increase from 5.85% to 7.96% as a result of losing oxygen atoms during reduction. Further connection with the SU-8 2002 results in the drastically decrease of nitrogen atomic percentage to a negligible amount (0.94%) and an enhanced oxygen and carbon content as shown in Figure 7-14e. The disappearance of C-N peak and C=O peak is due to the screening of long chains of functionalized SU-8 2002 and thereby overwhelmingly relative increased of C-C and C-O, which make the signals of C-N and C=O undetectable in XPS. However, the last functionalization step has been confirmed by the high resolution N 1s spectrum as demonstrated in Figure 7-14f, in which rGO-EDA-SU converts to a major C-NH-C peak (76.83 % atom) accompanied by a decrease of the contribution from C-NH_2 and C-NH_3^+, which could be explained by the conversion of C-CH_2 to C-NH-C upon addition of the epoxy group of SU-8 2002. On the other hand, the evident increase in C-O peak in Figure 7-14f further justifies the success of functionalization of rGO-EDA with SU-8 2002 that took advantage of the abundance in epoxy groups.

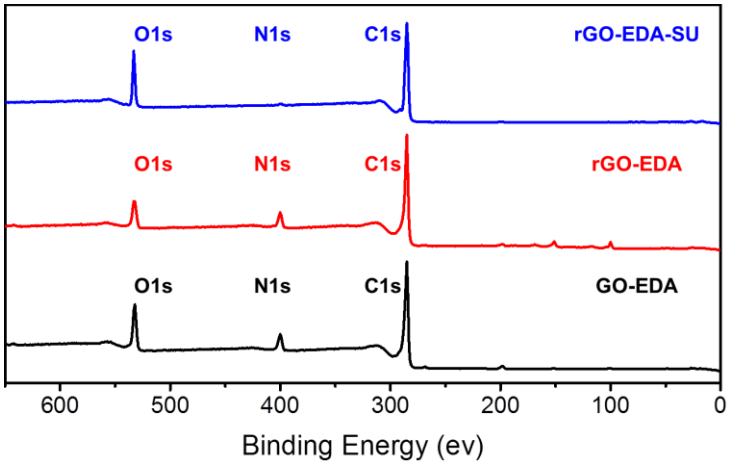

Figure 7-13: Survey spectra of GO-EDA, rGO-EDA, rGO-EDA-SU.

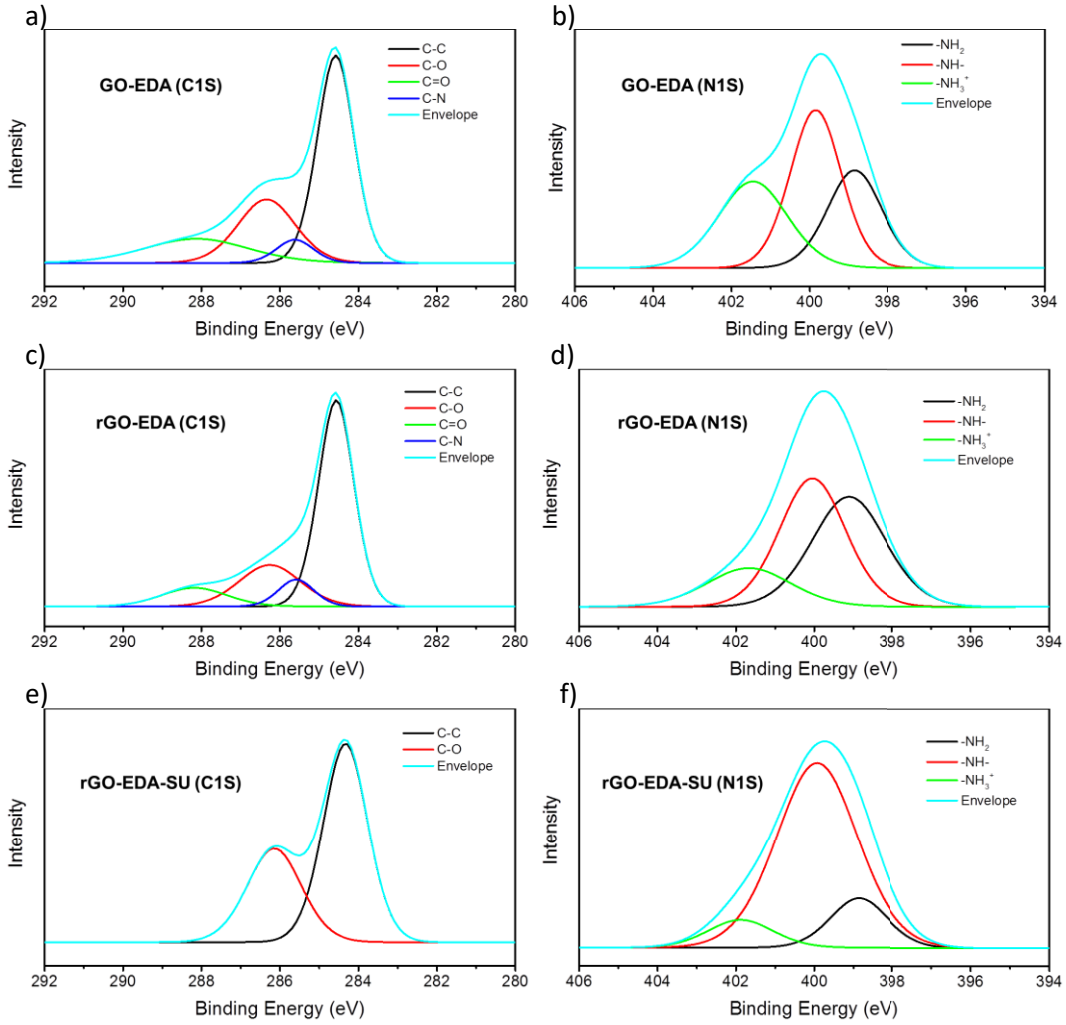

Figure 7-14: C 1s spectra (left column: a, c, e) and N 1s spectra (right column: b, d, f) of GO-EDA, rGO-EDA, rGO-EDA-SU.

Table 7-2. C1s survey of GO-EDA, rGO-EDA, rGO-EDA-SU.

C1s	Name	Peak BE	FWHM eV	Area (P) CPS.eV	Atomic %
GO-EDA	C-C	284,58	1,11	106853,1	52,25
	C-O	286,34	1,72	50731,11	24,84
	C=O	288,13	3,11	34824,02	17,07
	C-N	285,62	1,11	11947,16	5,85
rGO-EDA	C-C	284,57	1,07	120526,2	60,62
	C-O	286,26	1,85	42211,8	21,25
	C=O	288,19	1,96	20176,52	10,17
	C-N	285,59	1,07	15812,88	7,96
rGO-EDA-SU	C-C	284,33	1,33	122358	64,38
	C-O	286,15	1,56	67630,23	35,62

Table 7-3. N1s survey of GO-EDA, rGO-EDA, rGO-EDA-SU.

N1s	Name	Peak BE	FWHM eV	Area (P) CPS.eV	Atomic %
GO-EDA	-NH-	399,9	1,54	14376,05	41,82
	$-NH_2$	398,91	1,75	10606,78	30,84
	$-NH_3^+$	401,51	1,75	9387,92	27,34
rGO-EDA	-NH-	400,05	1,98	13923,38	42,64
	$-NH_2$	399,11	2,22	13368,39	40,91
	$-NH_3^+$	401,67	2,54	5363,66	16,45
rGO-EDA-SU	-NH-	399,93	2,42	2828,47	76,38
	$-NH_2$	398,86	1,72	533,95	14,41
	$-NH_3^+$	401,88	1,96	340,55	9,21

7.3.3.4. Raman spectroscopy

The degrees of disorder in GO in each step of functionalization was monitored by Raman spectroscopy.[8] Typical Raman peaks of GO consist of D band at 1358 cm^{-1} and G band at 1603 cm^{-1}. As is shown in Figure 7-15, these two peaks correspond to the structural disorder in the carbon hexagonal lattice which commonly originates from defects/oxidations and the sp^2 C-C tangential vibrations, respectively. The pristine GO shows similar intensities in D and G peak with I_D/I_G ratio being 0.98. This ratio is similar to EDA functionalization (I_D/I_G=0.99), indicating that the covalent functionalization with EDA does not introduce extra structural defects in GO. In contrast, the subsequent step of GO reduction with hydrazine enhances the I_D/I_G ratio to 1.12, which is similar to the reported observations of successful hydrazine reduction.[9] The final functionalization step of rGO-EDA-SU includes the addition of SU-8 2002 polymer, epoxy based molecules with aromatic substituents which also possess Raman signatures (Figure 7-15), shows an intense peak at 1606 cm^{-1} and a series of weak peaks at around 1100~1500 cm^{-1}. The spectra of rGO-EDA-SU shows an evident decrease of I_D/I_G ratio to 0.74, because of an overlap of Raman bands at 1603~1603 cm^{-1} in both rGO-EDA and SU-8 2002.

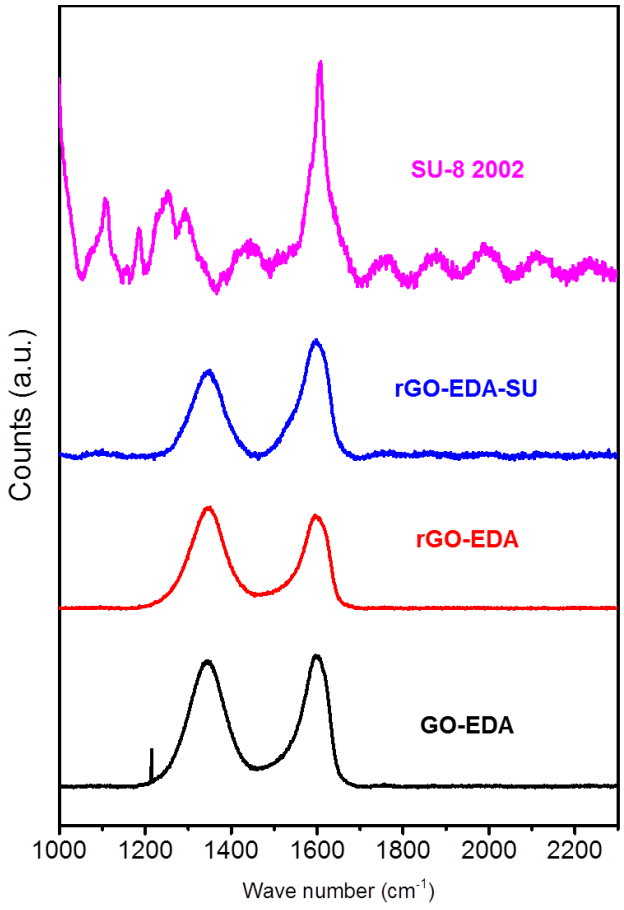

Figure 7-15. Raman spectra of GO-EDA, rGO-EDA, rGO-EDA-SU, and SU-8 2002.

7.4. Conclusion

In this Chapter, we have designed and synthesized a new functionalized graphene oxide material for pressure sensing application. Negative photoresist SU-8 2002 was used as elastic material which was covalently grafted to graphene oxide. Prior to the synthesis of the hybrid material, the mechanical properties of SU-8 2002 have been investigated by AFM-based nano indentation experiment, showing a linear increase of the Young's modulus with the UV irradiation time. Then the hybrid material was successfully synthesized and well characterized by XPS, Raman spectroscopy, and SEM. The pressure sensor device was fabricated by spray coating of the rGO-EDA-SU hybrid onto the commercially available ITO coated PET substrates, after which two substrates were assembled in a face-to-face manner to form a sandwich structure. Electrical response of the pressure sensing device was tested by recording the current change under bias voltage of 0.2 V. Unfortunately, we were not able to generate stable electrical signals under pressure simulation when rGO-EDA-SU hybrid was employed as active material. As revealed by SEM imaging of the hybrid material forms large aggregates instead of layered structures which might be characterized by a heterogeneous stacking during the deposition step. When subjected to pressure, these aggregates could undergo irregular dislocation movement which causes unstable electrical response. A stable electrical signal could be acquired by achieving a greater control onto the assembly of the hybrid materials into a layer-by-layer architecture or by depositing these dispersed aggregates into polymer matrix *etc.* Further modification of pressure sensor structure design is under way.

7.5. References

1. Xu, T.; Yoo, J. H.; Babu, S.; Roy, S.; Lee, J.-B.; Lu, H., Characterization of the mechanical behavior of SU-8 at microscale by viscoelastic analysis. *J. Micromech. Microeng.* **2016,** *26*, 105001.
2. Cross, S. E.; Jin, Y.-S.; Rao, J.; Gimzewski, J. K., Nanomechanical analysis of cells from cancer patients. *Nat. Nanotechnol.* **2007,** *2*, 780-783.
3. Li, Q. S.; Lee, G. Y. H.; Ong, C. N.; Lim, C. T., AFM indentation study of breast cancer cells. *Biochem. Biophys. Res. Commun* **2008,** *374*, 609-613.
4. Nikkhah, M.; Strobl, J. S.; Schmelz, E. M.; Agah, M., Evaluation of the influence of growth medium composition on cell elasticity. *J. Biomech.* **2011,** *44*, 762-766.
5. Chiou, D.-Y.; Chen, M.-Y.; Chang, M.-W.; Deng, H.-C., Characterization and Optimization Design of the Polymer-Based Capacitive Micro-Arrayed Ultrasonic Transducer. *Jpn. J. Appl. Phys* **2007,** *46*, 7496-7503.
6. Ma, H. L.; Zhang, Y. W.; Hu, Q. H.; Yan, D.; Yu, Z. Z.; Zhai, M. L., Chemical reduction and removal of Cr(VI) from acidic aqueous solution by ethylenediamine-reduced graphene oxide. *J. Mater. Chem.* **2012,** *22*, 5914-5916.
7. Wang, S.; Wang, J.; Zhang, W.; Ji, J.; Li, Y.; Zhang, G.; Zhang, F.; Fan, X., Ethylenediamine Modified Graphene and Its Chemically Responsive Supramolecular Hydrogels. *Ind. Eng. Chem. Res.* **2014,** *53*, 13205-13209.
8. Ferrari, A. C.; Robertson, J., Interpretation of Raman spectra of disordered and amorphous carbon. *Phys. Rev. B* **2000,** *61*, 14095-14107.
9. Kanygin, M. A.; Stolyarova, S. G.; Dorojkin, K. V.; Korovin, E. Y.; Suslyaev, V. I.; Bulusheva, L. G.; Okotrub, A. V., Electromagnetic Properties of Reduced Graphene Oxide Buckypapers Obtained by Different Reduction Procedures. *Phys. Status Solidi B Basic Res.* **2018,** *255*, 1700271.

Chapter 8

Conclusions and perspectives

In this Chapter, we draw some general conclusions from each sub-project and provide some short-term and long-term perspectives based on our approaches and on this field of science.

8.1. Conclusions

This Thesis work has been focused on the design and fabrication of low-dimensional nanomaterials (*i.e.* graphene and gold nanoparticles) based flexible pressure and strain sensors featuring high sensitivity, high flexibility, fast response, *etc.* which can be applied in the field of human health monitoring.

The first research project discussed in Chapter 5 has been based on the design and fabrication of pressure sensors with functionalized graphene as the active sensing materials. A novel and simple method has been developed to drastically improve the sensitivity of a piezoresistive pressure sensor. The active material has been assembled by reacting commercially available GO with amino functionalized molecules in order to form covalent bonds onto the basal plane of GO through the epoxy ring-opening reaction. Three organic molecules characterized by a similar contour length and increasing rigidity, namely triethylene glycol (TEG) amine (**R1**), 1-octylamine (**R2**) and 4-aminobiphenyl (**R3**) were chosen as the molecular units. Upon condensation of **R1-R3** with GO, hybrid structures have been obtained in the form of ink dispersed in ethanol. Such chemically modified GOs (CMGOs) have been chemically reduced with hydrazine to restore high electrical conductivity. The as-obtained dispersion can be deposited onto arbitrary substrates by spray-coating, yielding multilayer structures with spacing between adjacent GO sheets which are dictated by the employed molecular pillars, *i.e.* **R1-R3** molecules. Significantly, the latter possess different compressibility, resulting from the intrinsic flexibility of the chosen molecules. The CMGO containing molecules possessing the highest flexibility should display the largest compressibility at a given pressure, thus leading to the highest sensitivity to detect changes of pressure. In analogy to the Hooke's law ruling the compressibility of macroscopic springs, we demonstrated that the sensitivity of the pressure sensor can be improved from **rGO-R$_3$** (0.32 kPa^{-1}) to **rGO-R$_1$** (0.82 kPa^{-1}) by using more flexible linkers acting as molecular springs separating rGO layers. Apart from high sensitivity, the pressure sensor (**rGO-R$_1$**) also demonstrated high flexibility, fast response (less than 24 ms), and good robustness (over 2000 cycles). By taking advantage of the compatibility of graphene for on-the-skin applications, we have demonstrated how our hybrid multilayer architecture can be employed for health monitoring and can be easily transformed into a matrix, which allows a 3D mapping of the pressure exerted by different object thus providing also spatial information. The device additional features such low power consumption (0.2 V operating voltage), large-scale fabrication process, commercially available raw material and low cost, makes it an appealing candidate for the technological applications in wearable health monitoring device, multimotion detection robotic and internet

of functions. Furthermore, our pressure sensor is fabricated by solution processing, thus it is compatible with printed electronics solutions.

The second research project discussed in Chapter 6 has been based on the design and fabrication of a flexible strain sensor in which gold nanoparticles featuring a size of dozens nanometers were employed as conductive nanostructures in an active hybrid material. The working principle of the strain sensor was the electron tunneling through gold nanoparticles under bias voltages. Gold nanoparticles are interconnected by tetra (ethylene glycol) dithiol (TEG) to form 3D networks deposited directly in between flexible interdigitated electrodes. Without applied strain, AuNPs are separated by insulated organic ligands which can effectively define the charge transfer among gold nanoparticles at a certain range. Upon applied strain, the active material is either compressed (under compressive strain) or stretched (under tensile strain) thus having the organic ligands undergoing conformational change ruled by its flexibility. The interparticle distance, which can be seen as the insulating barrier for charge transport, will be decreased/increased under compressive/tensile strain respectively, thus increasing/decreasing the tunneling current exponentially when voltage is applied. The strain sensing properties have been tested and the device demonstrated high sensitivity and fast response to both compressive and tensile strain. The gauge factor has been calculated to be 30.29 in the low strain range (-0.005 to 0.005). Our results show that the developed strain sensor displays high gauge factor and highly sensitive response both to tensile strain and compressive strain as well as to the mixed motion and even vibrations. Apart from the superior strain sensing properties of the strain sensor, the wireless data transmission method (*i.e.* RFID) has been employed to construct a wireless strain sensing system with AuNPs-TEG networks being active sensing material. The system is consisting of two circuits, which are the chip circuit and the measure circuit, respectively. The strain sensor was integrated into the chip circuit as a variable resistor, in which the resistance changes with strain thus affecting the current in the measure circuit through mutual inductance. The fabrication and measurement of strain sensor have been accomplished while the wireless sensing is under testing (see *Perspectives*).

In the third research project, a novel pressure sensor whose sensitivity can be tuned with UV light irradiation has been reported. The working principle is similar to the one of the first project. By employing photosensitive polymers and grafting them onto graphene flakes, the rigidity of the hybrid structure can be modulated with UV light irradiation as a result of photo-induced polymerization. The current passing through the hybrid materials is directly ruled by the distance between adjacent graphene flakes, which is controlled by the applied pressure. By irradiating with UV light at different power/time, the degree of cross-link of the photosensitive polymer can be tuned yielding ultimately to a modulation of the hybrid's

compressibility. The latter determines the device sensitivity. In this project, a prototypical negative photoresist SU-8 2002 was chosen to form hybrid material with graphene. Negative photoresist is a kind of polymer widely used in photo lithography, whose rigidity will increase as a result of the polymerization triggered by UV. Prior to the synthesis of the hybrid material, the mechanical properties of SU-8 2002 have been investigated by AFM based nano indentation experiment, showing a linear increase of the Young's modulus with the UV irradiation time. Then the hybrid material was successfully synthesized and well characterized by XPS, Raman spectroscopy, and SEM. The pressure sensor device was fabricated by spray coating of the rGO-EDA-SU hybrid onto the commercially available ITO coated PET substrates, after which two substrates were assembled in a face-to-face manner to form a sandwich structure. Electrical response of the pressure sensing device was tested by recording the current change under bias voltage of 0.2 V. Unfortunately, the pressure sensors were not able to generate stable electrical signals under pressure simulation. As revealed by the SEM results, the hybrid material forms aggregates instead of layered structures which might be characterized by a heterogeneous stacking during the deposition step. When subjected to pressure, these aggregates could undergo irregular dislocation movement which causes unstable electrical response. A stable electrical signal could be acquired by achieving a greater control onto the assembly of the hybrid materials into a layer-by-layer architecture or by depositing these dispersed aggregates into polymer matrix *etc.* Further modification of pressure sensor structure design is under way (see *Perspectives*).

8.2. Perspectives

8.2.1. Short-term perspectives

Short-term attentions will be focused on the open projects which were discussed in Chapter 6 and Chapter 7.

In Chapter 6, the design and fabrication of AuNPs-TEG network based strain sensor has been accomplished and the electrical strain sensing properties under dynamic and static stimulations have been fully studied. With the high sensitivity, fast response, and high flexibility, the strain sensor is very promising for the applications of human health monitoring as demonstrated in Chapter 5. The strain sensor can be attached on the wrist or neck of subject to monitor the pulse signal by recording the current change under bias voltages. Noteworthy, the difference with the functionalized graphene based pressure sensor is that the current change of the strain sensor is caused by the subtle strain change, in which higher flexibility and conformability is needed during the sensing process. For this reason, PET substrate might not be suitable in this case due to the lack of stretchability. In the following on-skin test, thin PDMS film (~2 mm thick) could be employed as substrate for a better attachment of the device. Efforts should also be paid on the fabrication of wireless data transmission setup of the strain sensing system. RFID technique has been employed in this project, in which the strain sensor was integrated in the chip circuit as a variable resistor. Based on the preliminary research results, the use of commercially available RFID chip is more promising due to the complexity of the circuit design and adjustment. Realization of wireless strain sensing with multi-discipline cooperation will be one of the key goals in the following research and will largely improve the practicability and efficiency of the strain sensor.

In Chapter 7, a pressure sensor featuring tunable sensitivity by UV light was designed and fabricated. Functionalized graphene oxide with SU-8 2002 (positive photoresist) was synthesized and characterized as active sensing material of the device. The graphene hybrid materials were spray coated on ITO coated PET substrates and the substrates were assembled in a face-to-face manner with active sensing materials sandwiched in between. The major problem of this project is the unstable electrical response to pressure simulations, which is caused by the irregular stack of the aggregated hybrid materials. Dispersion of the graphene hybrid into polymer matrix could be a promising method to prevent the irregular dislocation movement of the aggregates under pressure. SU-8 2002 is a very viscous liquid photoresist in which the epoxy-based molecule SU-8 is dissolved in organic solvents such as propylene glycol methyl ether acetate (PGMEA), cyclopentanone, or gamma-butyrolactone (GBL). To improve the deposition quality of the active sensing materials, the functionalized graphene

oxide aggregates can be dispersed into SU-8 2002 to form a hybrid ink which can be spray/spin coated onto the flexible substrate. Polymerization triggered by UV light can not only modulate the rigidity of the active sensing layer, but also fix the aggregates inside the polymer matrix to form a more stable stacking structure. The pressure sensor with tunable sensitivity by UV light can be fabricated with this method.

8.2.2. Long-term perspectives:

Long-term and more visionary perspective could include:

Development of pressure/strain sensors with the on-demand molecular linkers will enable to further improve the sensing properties such as sensitivity, detection range, response time, *etc.* In Chapter 5, we have proved that the use of highly flexible molecular linkers can improve the sensitivity of pressure sensor. In the following research, different molecular linkers featuring high flexibility (*e.g.* long-chain polymers, dendrimers, *etc.*) will be investigated to achieve better pressure or strain sensing properties. Natural macromolecules such as DNA, proteins, cellulose, polysaccharide, *etc.* can also be employed to improve the biocompatibility and biodegradability of the sensing devices.

Other sensing devices such as humidity sensor, ion sensor, pH sensor, *etc.* will be developed with the space-interval engineering concept, *i.e.* molecular springs. In Chapter 2, the existence of molecular springs with different stimuli responsive properties was discussed, which can be integrated into pressure and strain sensing devices serving as dynamic sensing unit. Different molecular springs can be employed to serve as space interval between conductive units such as graphene flakes, CNTs, metal nanoparticles or nano wires, *etc.* For example, molecular springs featuring specific ion combination sites can be integrated with gold nanoparticles, in which the tunneling current can be monitored to give the information of the present and concentration of target ions. With the instruction of this design principle, different sensors featuring superior sensing properties can be developed.

In addition, the development of wireless pressure and strain sensing is also an important long-term goal. In 2019, Bao and coworkers[1] reported a flexible wireless pressure sensor which can be used to monitor arterial blood flow and other various surgical operations. Capacitive pressure sensor was integrated into the RFID chip as a variable capacitor, in which the change of pressure will cause a shift of the resonant frequency of the inductor-capacitor-resistor (LCR) circuit. Resistive pressure sensor has also been employed in the wireless sensing system to analyze a person's pulse, breath and body movement.[2] In our design in Chapter 6, flexible strain sensor was integrated into the RFID chip as variable resistor. Instead of monitoring the resonance frequency of the LCR circuit, the induced current was recorded as a

function of strain. Future work will focus on the integration of the pressure and strain sensors into RFID system to achieve wireless sensing. The development of corresponding software or APP will be implemented through inter-discipline corporations.

The development of 4G (the fourth generation wireless technology) enabled us to have high speed internet connections, high quality video calls, and stable connections in the past 10 years (~2009-2019). With the higher demand of *Internet of Things*, 4G is no longer capable of connecting the huge number of smart electronic devices. 5G (the fifth generation wireless technology) has given birth paving the way towards greater speed in the transmissions, a lower latency, greater number of connected devices and network slicing, in which the life-changing applications including autonomous vehicles, smart city infrastructure and traffic management, and smart wearables *etc.* can become a reality. Electronic sensing devices, as the core components of IoT, will meet a great increasing consequently in the following decades.

8.3. References

1. Boutry, C. M.; Beker, L.; Kaizawa, Y.; Vassos, C.; Tran, H.; Hinckley, A. C.; Pfattner, R.; Niu, S.; Li, J.; Claverie, J.; Wang, Z.; Chang, J.; Fox, P. M.; Bao, Z. Biodegradable and flexible arterial-pulse sensor for the wireless monitoring of blood flow. *Nature Biomedical Engineering* **2019,** *3*, 47-57.
2. Niu, S.; Matsuhisa, N.; Beker, L.; Li, J.; Wang, S.; Wang, J.; Jiang, Y.; Yan, X.; Yun, Y.; Burnett, W.; Poon, A. S. Y.; Tok, J. B. H.; Chen, X.; Bao, Z. A wireless body area sensor network based on stretchable passive tags. *Nature Electronics* **2019,** *2*, 361-368.

Closing remarks

All the experimental data reported in this thesis were performed and collected by the author (Chang-Bo HUANG) except from the following:

1) **Chapter 5**: The XRD, IR and BET spectra were collected by S. Witomska; The synthesis of triethylene glycol amine was carried out by Dr. A. Aliprandi; The Raman spectra and temperature dependent electrical conductivity were collected by Dr. M.-A. Stoeckel; The Laser Scanning Confocal Microscopy (LSCM) analysis was conducted through collaboration with Prof. M. Bonini from University of Florence.
2) **Chapter 6**: The design of RFID wireless sensing system was performed with the help of Minghao LI from Nanostructure Lab and Irene BURAIOLI; The temperature dependent electrical conductivity was collected by Dr. M.-A. Stoeckel; The statistic study of strain sensor was performed by Miriam von Holst.
3) **Chapter 7**: The XPS and Raman spectra were collected by Ye WANG.

All the images displayed in this thesis were designed by the author (Chang-Bo HUANG) except the pictures which clearly indicated the source references and Figure 5-2 which was designed by Dr. Yifan YAO.

All the original projects reported in this thesis were designed and developed by Chang-Bo HUANG, Dr. Artur CIESIELSKI and Prof. Paolo SAMORÌ.

List of publications

1. **Chang-Bo Huang**, Aatur Ciesielski*, Paolo Samorì*, Molecular Springs: Integration of Complex Dynamic Architectures into Functional Devices, *Angew. Chem. Int. Ed.*, **2020**, (in press) (doi.org/10.1002/anie.201914931)

2. **Chang-Bo Huang**, Samanta Witomska, Alessandro Aliprandi, Marc-Antoine Stoeckel, Artur Ciesielski*, and Paolo Samorì*. Molecule-graphene hybrids with tunable mechanoresponse: highly-sensitive pressure sensors for health monitoring. *Adv. Mater.*, **2019**, *31*, 1804600. (doi.org/10.1002/adma.201804600)

3. **Chang-Bo Huang**, Minghao Li, Ye Wang, Marc-Antoine Stoeckel, Miriam von Holst, Artur Ciesielski*, and Paolo Samorì*. Gold nanoparticles based highly sensitive strain sensor for wireless human health monitoring applications. (Manuscript in preparation)

List of presentations

1. Oral Presentation:

Chang-Bo Huang, Artur Ciesielski*, Paolo Samorì*

Molecule-Graphene hybrid materials with tunable mechanoresponse: highly sensitive pressure sensors for health monitoring.

GRAPHENE WEEK 2019, Helsinki, Finland, Sep 23-27, 2019

2. Poster Presentation:

Chang-Bo Huang, Samanta Witomska, Fanny Richard, Artur Ciesielski*, Paolo Samorì*

Pressure Sensors Based on Functionalized Graphene Oxide.

1st European Conference on Chemistry of Two-Dimensional Materials (Chem2DMat), Strasbourg, France, Aug 22-26, 2017

Acknowledgements

At this special moment, I would like to express my highest gratitude to all the medical staffs and researchers all over the world who are fighting against COVID-19 in the frontline.

I would like to thank my jury members: Prof. David BELJONNE, Prof. Marta MAS-TORRENT, Prof. Yves H. GEERTS, and Prof. Alberto BIANCO for their acceptance and valuable time to evaluate my work.

High gratitude has been dedicated to Solvay for the valuable support of my PhD research. I am very grateful to Dr. Patrick. MAESTRO for his kind concern of my research work, and many thanks to his invitation of Solvay lab visit both in Lyon and Shanghai.

Since I stepped on the foreign land for the first time on 2016.09.27, my life has started a brand-new chapter. I want to firstly thank my supervisor Prof. Paolo SAMORÌ for accepting me as a PhD student in his group, and for his valuable guidance during my PhD. With his encouragement, professional guidance and unlimited support, I was guided into the fascinating nanochemistry world and able to carry out independent research. I am very thankful to be guided by a world class scientist and I am very proud of working in this top-notch lab.

I also would like to express my gratitude to Dr. Artur CIESIELSKI. He is not only my co-supervisor, but also a big bro who is always willing to help and to cultivate my confidence. He is a great model for us with his intelligence and profession for work, responsibility and love for family, optimism and enthusiasm for life.

Nanochemistry lab has always been an international group, in which I enjoy the multi-cultural environment very much. I would like to thank all my lovely colleagues (also including those who have already left this lab) for your kind help, in particular the *Losers Support Team* (with Yifan, Yuda, Zhaoyang), Minghao (the most talented friend of me), Ye, Verónica, Irene, Matilde, Lili, Samanta, Miriam, Haixin, Sara, Can, Rafael, Agostino, Marco S., Stafano I., Alessandro, Lei, Tim, Cosimo, Pietro, Dawid, Haijun, Daniel, Stafano C. Stefano D-B., Marco C., Xiaoyan. I will always remember those great moments we shared in Christmas dinners, annual barbecues, music festivals, and dinners at 6th floor for reasons and for no reason. I will always remember our amazing trips in Easter holidays, summer holidays, and ski seasons. I will always remember our great Friday football nights. I would like also to thanks Corinne, Fanny, and Nicolas for their kind help during the past years.

It would take another chapter to list all the great and crazy moments with my best friend, Marc-Antoine. Thank you for your help and for introducing me a bunch of nice friends: Justine, Nicolas, Chaudière, Romain, Maxim, Justin… And yes, it's just a start...

I am deeply thankful to my family, in particularly my parents, for their endless love and support. This debt will never be paid, and I will love you until the end of my life. I also would like to thank Erika & Gunther BERL who treated me as family for the past years. These great moments will always be kept in my mind.

At the end, this thesis is dedicated to my wife, Ying, on the occasion of our 10 years anniversary of love. She is the meaning of my life. With the long distance (8971 km) and the long separation (1265 days), our love never fades away.

"执子之手，与子偕老"

Changbo

2020.03.16

Chang-Bo HUANG

Nanomatériaux fonctionnels à faible dimensionnalité pour la détection de pression et de tension

Résumé

L'objectif de cette thèse a été la conception chimique et la fabrication de capteurs de pression/déformation avec des matériaux actifs pour une détection fine afin de surveiller la santé humaine. L'ingénierie de la compressibilité du matériau actif à travers des molécules modulables (telles un ressort moléculaire ou un polymère photorésistant) est la principale nouveauté de cette thèse. L'hybride graphène-molécule a d'abord été utilisé comme matériau actif de détection de pression dans lequel la sensibilité peut être réglée en modifiant la rigidité des ressorts moléculaires. Une stratégie de conception similaire a été appliquée au capteur de déformation basé sur le réseau AuNPs-TEG, dans lequel le signal de détection peut être transmis via un système RFID sans fil. Dans le dernier projet, la résine photosensible a été utilisée pour fabriquer un capteur de pression hybride à base de graphène possédant une sensibilité réglable par irradiation UV. Dans l'ensemble, cette nouvelle conception de matériau de détection de pression/déformation a fourni une méthode efficace pour fabriquer des capteurs de pression/déformation très sensibles. Les caractéristiques supplémentaires de l'appareil telles que la faible consommation énergétique (tension de fonctionnement de 0.2 V), le processus de fabrication à grande échelle, les matières premières disponibles commercialement, le faible coût de production et, plus important encore, la détection sans fil, en font un candidat attrayant pour les applications technologiques portatives contrôlant la santé, pour des dispositif de surveillance, dans la robotique de détection multi-mouvement et pour l'IoT.

Mots-Clés : graphène, capteur de pression, capteur de déformation, ressort moléculaire, Surveillance de la santé

Résumé en anglais

The aim of this Thesis is the chemical design and fabrication of pressure/strain sensor with delicately designed active sensing materials for human health monitoring applications. Engineering of compressibility of active material through tunable molecules (*e.g.* molecular spring, photoresist polymer) is the main novelty in this thesis. Graphene-molecule hybrid has been firstly employed as active pressure sensing material in which the sensitivity can be tuned by changing the rigidity of molecular springs. Similar design strategy has been applied on the AuNPs-TEG network-based strain sensor, in which the sensing signal can be transmitted through RFID system in a wireless manner. In the last project, photoresist has been utilized to fabricate hybrid graphene material-based pressure sensor possessing tunable sensitivity by UV irradiation. Overall, this novel design of pressure/strain sensing material has provided an effective method to fabricate highly sensitive pressure/strain sensors. The additional device features such as low power consumption (0.2 V operating voltage), large-scale fabrication process, commercially available raw material, low cost, and more importantly, the wireless sensing, make it an appealing candidate for the technological applications in wearable health monitoring device, multimotion detection robotic and IoT.

Key words: graphene, pressure sensor, strain sensor, molecular spring, health monitoring